Internal Report
DESY H1-96-01
March 1996

The H1 Detector at HERA

H1 Collaboration

Abt, I.

To be submitted to Nuclear Instruments and Methods
(this is an updated version of DESY report 93-103)

Internal Report
DESY H1-96-01
March 1996

The H1 Detector at HERA

H1 Collaboration

Abstract:

Technical aspects of the H1 detector at the electron-proton storage ring HERA are described. This paper covers the detector status up to the end of 1994 when a major upgrading of some of its elements was undertaken. Some performance figures from luminosity runs at HERA during 1993 and 1994 are given.

To be submitted to Nuclear Instruments and Methods
(this is an updated version of DESY report 93-103)

H1 Collaboration

I. Abt[8], T. Ahmed[4], S. Aid[14], V. Andreev[26], B. Andrieu[29], R.-D. Appuhn[12], C. Arnault[28], M. Arpagaus[37], A. Babaev[25], H. Bärwolff[36], J. Bán[18], E. Banas[7,12], P. Baranov[26], E. Barrelet[30], W. Bartel[12], U. Bassler[30], F. Basti[33], D.E. Baynham[6], J.-M. Baze[10], G.A. Beck[21], H.P. Beck[38], D. Bederede[10], H.-J. Behrend[12], C. Beigbeder[28], A. Belousov[26], Ch. Berger[1], H. Bergstein[1], R. Bernard[10], G. Bernardi[30], R. Bernet[37], R. Bernier[28], U. Berthon[29], G. Bertrand-Coremans[5], M. Besançon[10], R. Beyer[12], J.-C. Biasci[28], P. Biddulph[23], V. Bidoli[33], E. Binder[12], P. Binko[12], J.-C. Bizot[28], V. Blobel[14], F. Blouzon[30], H. Blume[27], K. Borras[9], V. Boudry[29], C. Bourdarios[28], F. Brasse[12], W. Braunschweig[1], D. Breton[28], H. Brettel[27], V. Brisson[28], D. Bruncko[18], C. Brune[16], U. Buchner[9], L. Büngener[14], J. Bürger[12], F.W. Büsser[14], A. Buniatian[12,40], S. Burke[20], P. Burmeister[12], A. Busata[29], G. Buschhorn[27], A.J. Campbell[11], T. Carli[27], F. Charles[30], M. Charlet[12], R. Chase[28], D. Clarke[6], A.B. Clegg[19], M. Colombo[9], V. Commichau[2], J.F. Connolly[6], U. Cornett[12], J.A. Coughlan[6], A. Courau[28], M.-C. Cousinou[24], Ch. Coutures[10], A. Coville[27], G. Cozzika[10], D.A. Cragg[6], L. Criegee[12], H.I. Cronström[22], N.H. Cunliffe[6], J. Cvach[29], A. Cyz[7], S. Dagoret[30], J.B. Dainton[20], M. Danilov[25], A.W.E. Dann[23], D. Darvill[2], W.D. Dau[17], J. David[30], M. David[10], R.J. Day[6], E. Deffur[12], B. Delcourt[28], L. Del Buono[30], F. Descamps[30], M. Devel[28], J. P. Dewulf[5], A. De Roeck[12], P. Dingus[29], K. Djidi[10], C. Dollfus[38], J.D. Dowell[4], H.B. Dreis[2], A. Drescher[9], U. Dretzler[9], J. Duboc[30], A. Ducorps[28], D. Düllmann[14], O. Dünger[14], H. Duhm[13], B. Dulny[27], F. Dupont[28], R. Ebbinghaus[9], M. Eberle[13], J. Ebert[35], T.R. Ebert[20], G. Eckerlin[12], B.W.H. Edwards[6], V. Efremenko[25], S. Egli[38], S. Eichenberger[38], R. Eichler[37], F. Eisele[15], E. Eisenhandler[21], N.N. Ellis[4], R.J. Ellison[23], E. Elsen[12], A. Epifantsev[25], M. Erdmann[15], W. Erdmann[37], G. Ernst[9], E. Evrard[5], G. Falley[12], A. Fedotov[25], D. Feeken[14], R. Felst[12], J. Feltesse[10], Z.Y. Feng[30], I.F. Fensome[4], J. Fent[27], J. Ferencei[12], F. Ferrarotto[33], K. Finke[12], K. Flamm[12], W. Flauger[12,†], M. Fleischer[12], M. Flieser[27], P.S. Flower[6], G. Flügge[2], A. Fomenko[26], B. Fominykh[25], M. Forbush[8], J. Formánek[32], J.M. Foster[23], G. Franke[12], E. Fretwurst[13], W. Fröchtenicht[27], P. Fuhrmann[1], E. Gabathuler[20], K. Gabathuler[34], K. Gadow[12], K. Gamerdinger[27], J. Garvey[4], J. Gayler[12], E. Gažo[12], A. Gellrich[14], M. Gennis[12], U. Gensch[36], H. Genzel[1], R. Gerhards[12], K. Geske[14], I. Giesgen[2], D. Gillespie[20], W. Glasgow[6], L. Godfrey[8], J. Godlewski[7], U. Goerlach[12], L. Goerlich[7], N. Gogitidze[26], M. Goldberg[30], A.M. Goodall[20], I. Gorelov[25], P. Goritchev[25], L. Gosset[10], C. Grab[37], H. Grässler[2], R. Grässler[2], T. Greenshaw[20], C. Gregory[29], H. Greif[27], M. Grewe[9], G. Grindhammer[27], A. Gruber[27], C. Gruber[17], S. Günther[36], J. Haack[36], M. Haguenauer[29], D. Haidt[12], L. Hajduk[7], D. Hammer[12], O. Hamon[30], D. Handschuh[12], K. Hangarter[2], E.M. Hanlon[19], M. Hapke[12], U. Harder[36], J. Harjes[12], P. Hartz[9], P.E. Hatton[6], R. Haydar[28], W.J. Haynes[6], J. Heatherington[21], V. Hedberg[22], C.R. Hedgecock[6], G. Heinzelmann[14], R.C.W. Henderson[19], H. Henschel[36], R. Herma[1], I. Herynek[31], W. Hildesheim[13,30], P. Hill[12], D.L. Hill[6], C.D. Hilton[23], J. Hladký[31], K.C. Hoeger[23], R.B. Hopes[6], R. Horisberger[34], A. Hrisoho[28], J. Huber[27], Ph. Huet[5], H. Hufnagel[15], N. Huot[30], J.-F. Huppert[30], M. Ibbotson[23], D. Imbault[30], H. Itterbeck[1], M.-A. Jabiol[10], A. Jacholkowska[28], C. Jacobsson[22], M. Jaffré[28], J. Janoth[16], T. Jansen[12], P. Jean[28], J. Jeanjean[28], L. Jönsson[22], K. Johannsen[14], D.P. Johnson[5], L. Johnson[19], P. Jovanovic[4], H. Jung[2], P.I.P. Kalmus[21], D. Kant[21], G. Kantel[12], S. Karstensen[6,12], S. Kasarian[12], R. Kaschowitz[2], P. Kasselmann[13], U. Kathage[17], H.H. Kaufmann[36], G. Kemmerling[2], I.R. Kenyon[4], S. Kermiche[24], C. Kenker[1], C. Kiesling[27], M. Klein[36], C. Kleinwort[14], G. Knies[12], W. Ko[8], T. Kobler[27], J. Koch[13], T. Köhler[1], M. Kolander[9], H. Kolanoski[3], F. Kole[8], J. Koll[12], S.D. Kolya[23], B. Koppitz[14], V. Korbel[12], M. Korn[9], P. Kostka[36], S.K. Kotelnikov[26], M.W. Krasny[7,30], H. Krehbiel[12], F. Krivan[18], D. Krücker[2], U. Krüger[12], U. Krüner-Marquis[12], M. Kubantsev[25], J.P. Kubenka[27], T. Külper[12], H.-J. Küsel[12], H. Küster[2], M. Kuhlen[27], T. Kurča[18], J. Kurzhöfer[9], B. Kuznik[35], B. Laforge[10], F. Lamarche[29], R. Lander[8], M.P.J. Landon[21], W. Lange[12], W. Lange[36], R. Langkau[13], P. Lanius[27], J.-F. Laporte[10], L. Laptin[25], H. Laskus[27], A. Lebedev[26], M. Lemler[7,12],

U. Lenhardt[9], A. Leuschner[12], C. Leverenz[12], S. Levonian[12,26], D. Lewin[12], Ch. Ley[2], A. Lindner[9], G. Lindström[13], F. Linsel[12], J. Lipinski[14], B. Liss[12], P. Loch[12], A.B. Lodge[6], H. Lohmander[22], G.C. Lopez[21], J.-P. Lottin[10], V. Lubimov[25], K. Ludwig[12], D. Lüers[27,†], N. Lugetski[25], B. Lundberg[22], K. Maeshima[8], N. Magnussen[35], E. Malinovski[26], S. Mani[8], P. Marage[5], J. Marks[24], R. Marshall[23], J. Martens[35], F. Martin[30], G. Martin[28], R. Martin[20], H.-U. Martyn[1], J. Martyniak[7], V. Masbender[12], S. Masson[2], A. Mavroidis[21], S.J. Maxfield[20], S.J. McMahon[20], A. Mehta[23], K. Meier[16], J. Meissner[36], D. Mercer[23], T. Merz[12], C.A. Meyer[38], H. Meyer[35], J. Meyer[12], S. Mikocki[7,28], J.L. Mills[6], V. Milone[33,†], J. Möck[27], E. Monnier[30], B. Montés[29], F. Moreau[29], J. Moreels[5], B. Morgan[21], J.V. Morris[6], J.M. Morton[20], K. Müller[38], P. Murín[18], S.A. Murray[23], V. Nagovizin[25], B. Naroska[14], Th. Naumann[36], P. Nayman[30], A. Nepeipivo[25], D. Newman-Coburn[21], D. Newton[19], D. Neyret[30], H.K. Nguyen[30], F. Niebergall[14], C. Niebuhr[12], R. Nisius[1], T. Novák[31], H. Nováková[31], G. Nowak[7], G.W. Noyes[6], M. Nyberg[22], H. Oberlack[27], U. Obrock[9], J.E. Olsson[12], J. Olszowska[7,12], S. Orenstein[29], F. Ould-Saada[14], P. Pailler[10], S. Palanque[10], E. Panaro[12], A. Panitch[5], J.-Y. Parey[29], C. Pascaud[28], G.D. Patel[20], A. Patoux[10], C. Paulot[28], U. Pein[13], E. Peppel[12], E. Perez[10], P. Perrodo[29], A. Perus[28], S. Peters[27], J.-P. Pharabod[29], H.T. Phillips[4], J.P. Phillips[23], Ch. Pichler[13], A. Pieuchot[24], W. Pimpl[27], D. Pitzl[37], A. Porrovecchio[33], S. Prell[12], R. Prosi[12], H. Quehl[12], G. Rädel[12], F. Raupach[1], K. Rauschnabel[9], A. Reboux[28], P. Reimer[31], G. Reinmuth[28], S. Reinshagen[12], P. Ribarics[27], V. Riech[13], J. Riedlberger[37], H. Riege[14], S. Riess[14], M. Rietz[2], S.M. Robertson[4], P. Robmann[38], P. Röpnack[12], R. Roosen[5], A. Rostovtsev[25], C. Royon[10], A. Rudge[8], K. Rüter[27], M. Rudowicz[27], M. Ruffer[13], S. Rusakov[26], V. Rusinov[25], K. Rybicki[7], J. Sacton[5], N. Sahlmann[2], E. Sanchez[27], D.P.C. Sankey[6], M. Savitski[12,25], P. Schacht[27], S. Schiek[14], N. Schirm[13], S. Schleif[16], P. Schleper[15], W. von Schlippe[21], C. Schmidt[12], D. Schmidt[35], G. Schmidt[14], W. Schmitz[2], H. Schmücker[27], V. Schröder[12], J. Schütt[14], E. Schuhmann[27], M. Schulz[12], A. Schwind[36], W. Scobel[13], U. Seehausen[14], F. Sefkow[12], R. Sell[12], M. Seman[18], A. Semenov[25], P. Shatalov[25], V. Shekelyan[25], I. Sheviakov[26], H. Shooshtari[33], L.N. Shtarkov[26], G. Siegmon[17], U. Siewert[17], Y. Sirois[29], A. Sirous[12], I.O. Skillicorn[11], P. Škvařil[31], P. Smirnov[26], J.R. Smith[8], L. Smolik[12], D. Sole[6], Y. Soloviev[26], J. Špalek[18], H. Spitzer[14], R. von Staa[14], J. Staeck[2], P. Staroba[31], J. Šťastný[31], M. Steenbock[14], P. Štefan[18], P. Steffen[12], R. Steinberg[2], H. Steiner[30], B. Stella[33], K. Stephens[23], J. Stier[12], J. Stiewe[16], U. Stösslein[36], J. Strachota[12], U. Straumann[38], A. Strowbridge[6], W. Struczinski[2], J.P. Sutton[4], Z. Szkutnik[12], G. Tappern[6], S. Tapprogge[16], R.E. Taylor[28,39], V. Tchernyshov[25], V. Tchudakov[25], C. Thiebaux[29], K. Thiele[12], G. Thompson[21], R.J. Thompson[23], I. Tichomirov[25], C. Trenkel[17], W. Tribanek[27], K. Tröger[12], P. Truöl[38], M. Turiot[30], J. Turnau[7], J. Tutas[15], L. Urban[27], M. Urban[29], A. Usik[26], Š. Valkár[32], A. Valkárová[32], C. Vallée[24], G. Van Beek[5], M. Vanderkelen[5], L. Van Lancker[5], A. Vartapetian[12,40], Y. Vazdik[26], M. Vecko[31], P. Verrecchia[10], R. Vick[14], G. Villet[10], E. Vogel[1], K. Wacker[9], M. Wagener[34], I.W. Walker[19], A. Walther[9], G. Weber[14], D. Wegener[9], A. Wegner[27], P. Weissbach[27], H. P.Wellisch[27], L. West[4], D. White[6], S. Willard[8], M. Winde[36], G.-G. Winter[12], Th. Wolff[37], L.A. Womersley[20], A.E. Wright[23], E. Wünsch[12], N. Wulff[12], B.E. Wyborn[6], T.P. Yiou[30], J. Žáček[32], D. Zarbock[13], P. Závada[31], C. Zeitnitz[13], Z. Zhang[28], H. Ziaeepour[28], M. Zimmer[12], W. Zimmermann[12], F. Zomer[28] and K. Zuber[16]

[1] *I. Physikalisches Institut der RWTH, Aachen, Germany*[a]
[2] *III. Physikalisches Institut der RWTH, Aachen, Germany*[a]
[3] *Institut für Physik, Humboldt-Universität, Berlin, Germany*[a]
[4] *School of Physics and Space Research, University of Birmingham, Birmingham, UK*[b]
[5] *Inter-University Institute for High Energies ULB-VUB, Brussels; Universitaire Instelling Antwerpen, Wilrijk; Belgium*[c]
[6] *Rutherford Appleton Laboratory, Chilton, Didcot, UK*[b]
[7] *Institute for Nuclear Physics, Cracow, Poland*[d]
[8] *Physics Department and IIRPA, University of California, Davis, California, USA*[e]

[9] *Institut für Physik, Universität Dortmund, Dortmund, Germany*[a]
[10] *CEA, DSM/DAPNIA, CE-Saclay, Gif-sur-Yvette, France*
[11] *Department of Physics and Astronomy, University of Glasgow, Glasgow, UK*[b]
[12] *DESY, Hamburg, Germany*[a]
[13] *I. Institut für Experimentalphysik, Universität Hamburg, Hamburg, Germany*[a]
[14] *II. Institut für Experimentalphysik, Universität Hamburg, Hamburg, Germany*[a]
[15] *Physikalisches Institut, Universität Heidelberg, Heidelberg, Germany*[a]
[16] *Institut für Hochenergiephysik, Universität Heidelberg, Heidelberg, Germany*[a]
[17] *Institut für Reine und Angewandte Kernphysik, Universität Kiel, Kiel, Germany*[a]
[18] *Institute of Experimental Physics, Slovak Academy of Sciences, Košice, Slovak Republic*[f]
[19] *School of Physics and Chemistry, University of Lancaster, Lancaster, UK*[b]
[20] *Department of Physics, University of Liverpool, Liverpool, UK*[b]
[21] *Queen Mary and Westfield College, London, UK*[b]
[22] *Physics Department, University of Lund, Lund, Sweden*[g]
[23] *Physics Department, University of Manchester, Manchester, UK*[b]
[24] *CPPM, Université d'Aix-Marseille II, IN2P3-CNRS, Marseille, France*
[25] *Institute for Theoretical and Experimental Physics, Moscow, Russia*
[26] *Lebedev Physical Institute, Moscow, Russia*[f]
[27] *Max-Planck-Institut für Physik, München, Germany*[a]
[28] *LAL, Université de Paris-Sud, IN2P3-CNRS, Orsay, France*
[29] *LPNHE, Ecole Polytechnique, IN2P3-CNRS, Palaiseau, France*
[30] *LPNHE, Universités Paris VI and VII, IN2P3-CNRS, Paris, France*
[31] *Institute of Physics, Czech Academy of Sciences, Praha, Czech Republic*[f,h]
[32] *Nuclear Center, Charles University, Praha, Czech Republic*[f,h]
[33] *INFN Roma and Dipartimento di Fisica, Universita "La Sapienza", Roma, Italy*
[34] *Paul Scherrer Institut, Villigen, Switzerland*
[35] *Fachbereich Physik, Bergische Universität Gesamthochschule Wuppertal, Wuppertal, Germany*[a]
[36] *DESY, Institut für Hochenergiephysik, Zeuthen, Germany*[a]
[37] *Institut für Teilchenphysik, ETH, Zürich, Switzerland*[i]
[38] *Physik-Institut der Universität Zürich, Zürich, Switzerland*[i]
[39] *Stanford Linear Accelerator Center, Stanford California, USA*
[40] *Visitor from Yerevan Phys.Inst., Armenia*
[†] *Deceased*

[a] *Supported by the Bundesministerium für Forschung und Technologie, FRG under contract numbers 6AC17P, 6AC47P, 6DO57I, 6HH17P, 6HH27I, 6HD17I, 6HD27I, 6KI17P, 6MP17I, and 6WT87P*
[b] *Supported by the UK Particle Physics and Astronomy Research Council, and formerly by the UK Science and Engineering Research Council*
[c] *Supported by FNRS-NFWO, IISN-IIKW*
[d] *Supported by the Polish State Committee for Scientific Research, grant Nos. SPUB/P3/202/94 and 2 PO3B 237 08, and Stiftung fuer Deutsch-Polnische Zusammenarbeit, project no.506/92*
[e] *Supported in part by USDOE grant DE F603 91ER40674*
[f] *Supported by the Deutsche Forschungsgemeinschaft*
[g] *Supported by the Swedish Natural Science Research Council*
[h] *Supported by GA ČR, grant no. 202/93/2423, GA AV ČR, grant no. 19095 and GA UK, grant no. 342*
[i] *Supported by the Swiss National Science Foundation*

Contents

List of Figures

List of Tables

1 Introduction

The H1 detector described in this paper is one of the two detectors built around the interaction regions of the first ever constructed electron-proton storage ring – HERA at the DESY laboratory in Hamburg, Germany. In this accelerator 27.5 GeV electrons collide with 820 GeV protons at a centre of mass energy of 300 GeV. At HERA a new kinematic region becomes accessible for deep inelastic lepton scattering. Such experiments have played a crucial role in understanding the fundamental forces of nature and in providing first evidence for the pointlike constituents of the nucleons [1]. Compared to previous fixed target conditions, [2], experiments at HERA provide an increase by one order of magnitude in resolving power, with values of the momentum transfer squared Q^2 reaching 4×10^4 GeV^2, an increase of at least two orders of magnitude. In contrast to previous experiments the unique kinematics at HERA makes it possible to observe the hadronic recoil and to study the weak neutral and charged currents at high momentum transfer.

The extensive discussions of all aspects of HERA physics at the three workshops held before the experimental program started [3, 4, 5] led to a detector designed for good identification of leptons (especially electrons), high granularity and resolution for jets and good hermiticity to recognize missing transverse energy. These requirements follow from the fact that the final states will contain several leptons accompanied by quark and gluon jets. The inclusive measurements of neutral and charged current interactions also demand the best possible hadron calorimeter. In addition electron identification and charged particle reconstruction within jets require a high-resolution, large solid angle tracking system. The efficient use of all these tools must rely on a sophisticated trigger system to overcome the adverse background conditions met at an electron-proton machine.

The differential cross-section measurement at a collider such as HERA requires the reconstruction of kinematic variables as close as possible to the parton level. The most relevant kinematic quantities in the deep inelastic electron scattering process are Q^2, the fraction x (Bjorken scaling variable) of the proton momentum carried by the struck quark and the fractional energy loss y of the electron. These are given in terms of the energies of the incoming electron E_e, the scattered electron E'_e, the incoming proton E_p, the hadronic recoil jet E_h and the corresponding polar angles θ_e and θ_h (both measured relative to the proton direction $\theta = 0$, positive $z-$direction) as:

$$Q^2 = 4E_eE'_e\cos^2\frac{\theta_e}{2}\ ;\ \ x = \frac{Q^2}{4E_eE_py} = \frac{E_eE'_e(1+\cos\theta_e)}{E_p(2E_e - E'_e(1-\cos\theta_e))}\ ;\ \ y \equiv y_e = 1 - \frac{E'_e}{E_e}\sin^2\frac{\theta_e}{2}$$

$$Q^2 = \frac{E_h^2\sin^2\theta_h}{1-y_h} = \frac{(\sum_{h,i}\vec{p}_{th,i})^2}{1-y_h}\ ;\ \ y \equiv y_h = \sum_{h,i}\frac{E_{h,i}-p_{zh,i}}{2E_e}$$

Q^2 and x can be reconstructed from measured electron or hadronic quantities or a combination of both. Figure 1.1 shows contour plots of fixed θ_e and E'_e in the x, Q^2 plane for $E_e = 30$ GeV and $E_p = 820$ GeV and illustrates the influence of finite angle and energy resolution using the actual design values of the H1 detector. The resolution in Q^2 is determined by the electron energy resolution except for large scattering angles, where the angular resolution becomes the dominant term. The latter term only influences the x resolution for large x and small Q^2. At low y the x resolution is quite poor. The areas in the x, Q^2 plane where a reliable structure function measurement is possible are also indicated in Figure 1.1. Here the effects of migration and the systematic errors are also included. Migration is the process where a fraction of events move from one bin in x, Q^2 into a neighbouring bin as a result of measurement errors. For the control of systematic errors the energy calibration, and its stability are of particular importance. Since event rates at high Q^2 are quite low, long term stability is clearly required.

Systematic shifts of the outgoing electron energy measurement can generate large shifts in the differential cross-section because there is an amplification factor roughly proportional to y^{-1}, e. g. for $y \approx 0.1, x < 0.5$ an energy shift of 1 % results in 10 % cross-section change. Since angles are measured both by the calorimeter and the tracker, alignment errors influencing angle measurements are less important.

On the hadron side the above formulae implicitly make use of the Jacquet–Blondel method [6]. It is possible to measure x and Q^2 by using only the outgoing hadrons, without using jet identification or assumptions concerning the proton structure. Furthermore, for HERA kinematics y and Q^2 are more suitably expressed in terms of laboratory variables using the energy-momentum balance between the leptonic and the hadronic system (as done above) and then deducing x. Because hadrons emitted in the forward direction contribute little to y_h or Q^2, the unavoidable dead areas along the beam pipe have only a minor impact. Reconstruction errors depend on the size of the beam hole, the uncertainties on the angles and the energies of the outgoing hadrons. Use of the hadron information alone or in combination with the electron information, e. g. by using θ_e and θ_h without direct energy information as in the so-called double angle method [7], extends the measurable regions to considerably lower values of y as shown in Figure 1.1.

The largest contribution to the event rates at HERA stems from low Q^2 photoproduction. For example the high cross-section for producing charmed quark-antiquark pairs makes HERA a prolific source of $D-$mesons with cleaner background conditions than obtained with hadron beams. This makes the study of rare and forbidden decays feasible. The momentum of a tagged $D^{*\pm}$ is correlated with that of the charmed quark produced in γ gluon fusion [8, 7] so that the gluon momentum can be reconstructed knowing y_h. Thus the gluon density within the proton may be measured. If forbidden decays such as $D^0 \rightarrow \mu^+\mu^-$ or e^+e^- are to be studied it is important to have good muon identification, and good electron identification at momenta near 1 GeV/c, because the D meson spectrum peaks at rather low energies in particular in the central rapidity region, where these low multiplicity events can be reconstructed.

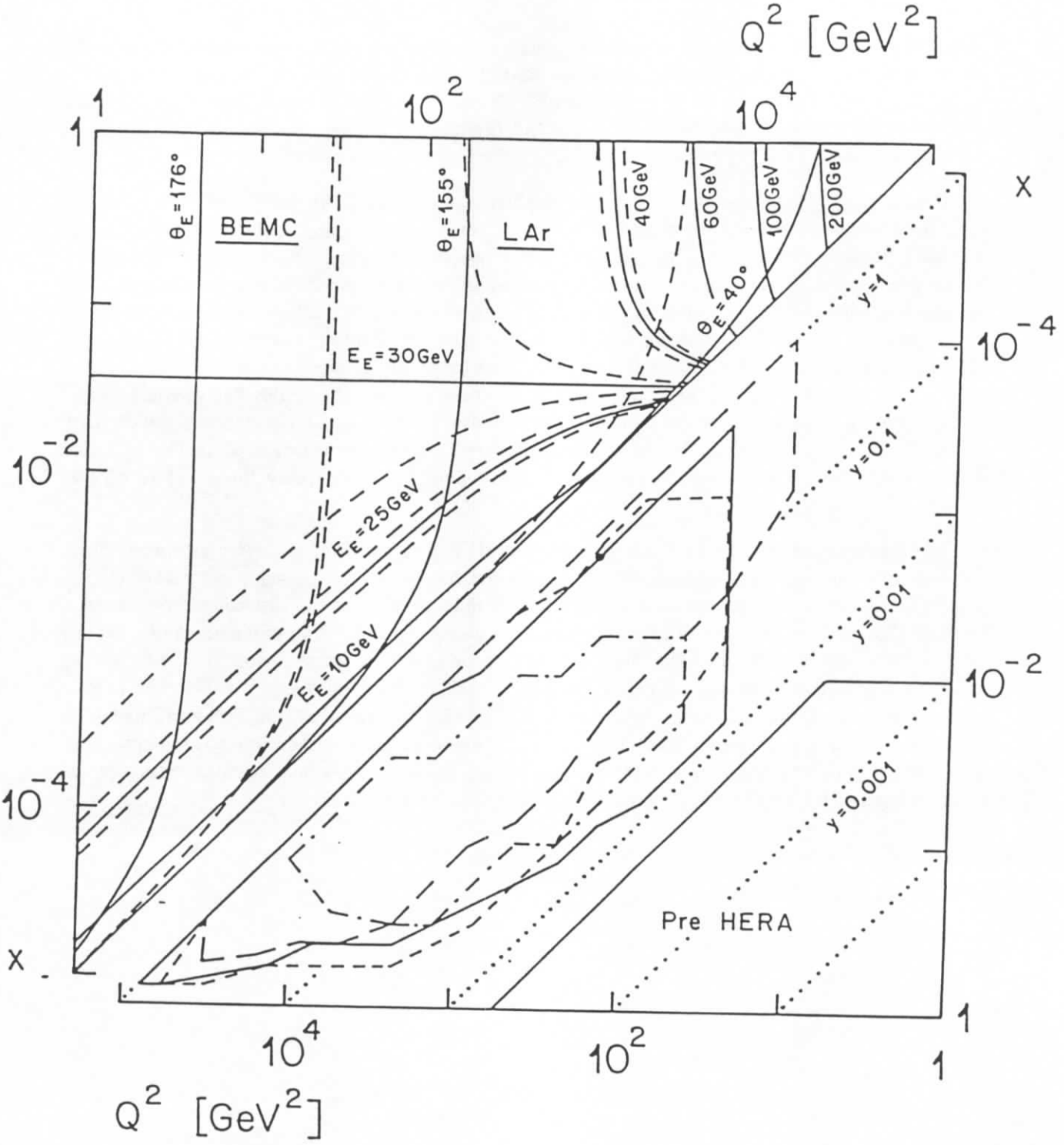

Figure 1.1: Top left: contour plots of fixed θ_e and E'_e in the x, Q^2 plane for $E_e = 30$ GeV and $E_p = 820$ GeV. The dashed lines bracketing the isoenergy lines at $E'_e = 30$ and $E'_e = 25$ GeV show the energy resolution of the backward electromagnetic calorimeter (BEMC, $151° < \theta_e < 176°$) at these energies, the dashed lines bracketing the isoenergy line at $E'_e = 40$ GeV the resolution of the liquid argon calorimeter (LAr, $4° < \theta_e < 153°$). Similarly the dashed isoangle lines indicate the angular resolution at $\theta_e = 165°$ and $\theta_e = 90°$, respectively. Bottom right: domains in the Q^2, x plane, where the systematic errors on $d^2\sigma/(dxdQ^2)$ are below 10%. The dotted lines correspond to constant y. The contours correspond to areas where different kinematic reconstruction methods have been used (from reference [9]). The area in the lower right corner corresponds to the range accessible to previous experiments.

2 General description of the H1 detector

In the design of the H1 detector prime attention has been given to the clean identification of electrons and to their energy measurement. To facilitate this we opted for a large coil, which encloses the electromagnetic and the hadronic calorimeters. With this choice the amount of dead material in front of the calorimeter and its total weight are minimised. Choosing a liquid Argon calorimeter we further benefit from the proven stability of this technique, the ease of its calibration, and the fine granularity which allows to separate electrons from pions to a high degree. Lastly the homogeneity of the response and overall hermiticity are helpful for energy flow measurements as well as missing energy detection. The calorimeter is supplemented by high resolution tracking on the inside and an instrumented iron yoke on the outside for muon detection. In these aspects the H1 detector does not differ strongly from the detectors at e^+e^- colliders, or $p\bar{p}$ colliders built in the past. Specific at HERA are however the high resolution required for hadronic calorimetry as well as the imbalance in the energy of the two colliding beams, which requires an asymmetric detector. Different also is the microstructure of the two beams, which leads to short intervals (96 ns) between two subsequent bunch crossings, and also the high background level, as proton induced background arises from beam line vacuum conditions.

The main elements of the detector are shown in Figure 2.1. This figure shows as well the reference frame adopted in this experiment.

Since the centre of mass for $e-p$ collisions at HERA is boosted along the proton direction with $\gamma_{cm} = 2.86$ the H1 detector is considerably more massive and highly segmented in this direction. This is apparent from Figure 2.2, which shows a cut along the beam axis. In the following we often refer to electron direction as the backward direction (negative $z-$values relative to the center of the interaction region and $\theta = \pi$), and the proton direction as the forward direction (positive z and $\theta = 0$).

Starting the description outward from the interaction vertex the detector consists of a central and a forward tracking system, each containing different layers of drift chambers and trigger proportional chambers. The liquid argon cryostat surrounds the trackers. It houses the lead absorber plates and readout gaps of the electromagnetic section, which are followed by the steel plates of the hadronic section with their readout gaps. A superconducting cylindrical coil with a diameter of 6 m and a length of 5.75 m provides the analysing field of 1.15 T. The iron return yoke of the magnet is laminated and filled with limited streamer tubes. The small fraction of hadronic energy leaking out of the back of the calorimeter is registered there, and muon tracks are measured. Muon identification further benefits from additional chambers inside and outside of the iron. Stiff muon tracks in the forward direction are analysed in a supplementary toroidal magnet sandwiched between drift chambers. The remaining holes in the liquid argon (LAr) calorimeter are closed with warm calorimeters, a silicon-copper plug at very forward angles, a Lead-scintillator calorimeter backed by a tail catcher (part of the muon system) in the backward direction and lastly an electron tagger at $z = -33$ m from the interaction point not shown in Figure 2.2. The tagger marks the energy of an electron with very small scattering angle inducing a photoproduction event and, taken in coincidence with a corresponding photon detector at $z = -103$ m upstream from the interaction point, monitors the luminosity by the bremsstrahlung process. Two scintillator walls in backward direction are installed to recognize background produced by the proton beam upstream of the H1 detector. A survey of detector parameters is given in Table 2.1.

2.1 Electron detection

Scattered electrons are observed in the backward electromagnetic calorimeter (BEMC) for $Q^2 \leq 100$ GeV^2, in the LAr calorimeter for larger values of Q^2, and for photoproduction events

Calorimetry		
Main calorimeter: liquid Argon (LAr)	Electromagnetic part	Hadronic part
Granularity	10 to 100 cm^2	50 to 2000 cm^2
Depth (number of channels)	20 to 30 X_0 (30784)	4.7 to 7 λ_{abs} (13568)
Resolution $\sigma(E_{e,h})/E_{e,h}$	$\approx 11\%/\sqrt{E_e} \oplus 1\%$	$\approx 50\%/\sqrt{E_h} \oplus 2\%$
Stability of electronic calibration	$\leq 0.2\%$ over one month	
LAr purity (decrease of signal)	$\leq 0.2\%$ over one year	
Noise per channel	10 to 30 MeV	
Angular coverage – dead channels	$4° < \theta < 153°$	$< 0.3\%$
Backward calorimeter: Pb–scintillator		
Angular coverage – granularity	$151° < \theta < 176°$	16×16 cm^2
Depth – resolution $\sigma(E_e)/E_e$	21.7 X_0 (1 λ_{abs})	$10\%/\sqrt{E_e} \oplus 1.7$ [1]%
Tail catcher: iron–streamer tubes		
Angular coverage	$4° < \theta < 176°$	
Depth – resolution $\sigma(E_h)/E_h$	4.5 λ_{abs}	$100\%/\sqrt{E_h}$
PLUG calorimeter: Cu–Si		
Angular coverage – granularity	$0.7° < \theta < 3.3°$	5×5 cm^2
Depth – resolution $\sigma(E_h)/E_h$	4.25 λ (44.6 X_0)	$\approx 150\%/\sqrt{E_h}$
Electron tagger: Tl(Cl/Br)		
Angular coverage – granularity	$\theta > 179.7°$	2.2×2.2 cm^2
Depth – resolution $\sigma(E_e)/E_e$	21 X_0	$\approx 10\%/\sqrt{E_e} \oplus 1\%$
Tracking		
Coil: radius – field	3 m – $B = 1.15$ T, $\Delta B/B \leq 2\%$	
Central tracking		
Angular – radial coverage	$25° < \theta < 155°$	$150 < r < 850$ mm
Jet chamber: spatial resolution	$\sigma_{r\phi} = 170\,\mu$m	$\sigma_z = 22.0$ mm
z-chambers: spatial resolution	$\sigma_{r\phi} = 25$ and 58 mm	$\sigma_z \approx 350\,\mu$m
Momentum – dE/dx resolution	$\sigma_p/p^2 < 0.01$ [0.003] GeV^{-1}	$\sigma(dE)/dE = 10$ [6]%
Forward/backward tracking		
Angular – radial coverage (f)	$7° < \theta < 25°$	$120 < r < 800$ mm
Spatial resolution (f)	$\sigma_{r\phi} = 170\,\mu$m ($\sigma_r = 29$ mm)	$\sigma_{x,y} = 210\,\mu$m
Angular coverage – resolution (b)	$155° < \theta < 175°$	$\sigma_{x,y} = 1$ mm
Trigger proportional chambers		
Angular coverage – channels	$7° < \theta < 175°$	3936
Muon detection		
Instrumented iron		
Angular coverage – total area	$4° < \theta < 171°$	4000 m^2
Number of channels	wires: 103700, strips: 28700, pads: 4000	
Spatial resolution	$\sigma_{wire} = 3 - 4$ mm	$\sigma_{strip} = 10 - 15$ mm
Angular – momentum resolution barrel	$\sigma_\theta(\sigma_\phi) = 15(10)$ mrad	$[\sigma_p/p \approx 0.35]$
Forward muon toroid		
Angular coverage – resolution	$3° < \theta < 17°$	$[0.25 < \sigma_p/p < 0.32]$
Overall size (x, y, z) – weight	$12 \times 15 \times 10$ m^3	2800 t

Table 2.1: Summary of H1 detector parameters.
Alternatively, design and test beam figures are given in brackets [ ]. Energies are given in GeV.

($Q^2 \approx 0$) in an electron tagger which is part of the luminosity measuring device.

The BEMC is a conventional lead-scintillator sandwich calorimeter with photodiode readout, providing an energy resolution sampling term of $10\%/\sqrt{E}$. The diodes are located in the ≈ 1 T magnetic field. The backward proportional chamber (BPC) located just in front of the BEMC provides the angular measurement of the electron together with track and vertex data given by the central tracker. The kinematic peak in the energy spectrum of the scattered electron at a value corresponding to the electron beam energy allows a precise overall calibration.

The LAr calorimeter covers the polar angular range $4° \leq \theta \leq 153°$ in a single cryostat. The electromagnetic calorimeter with lead absorber plates of total depth of 20 to 30 radiation lengths provides an energy resolution $\sigma/\mathrm{E} \approx 12\ \%/\sqrt{E}$. Electron identification is based on fine transverse and longitudinal shower shape measurement and a cross-check of the absolute energy calibration of the calorimeters is provided by comparing the calorimetric energy measurement of electrons to the corresponding momentum measurement in the central tracking chambers.

Further electron pion discrimination is available by a dE/dX measurement in the central jet chamber (CJC) and by using the transition radiation detectors incorporated into the forward tracker.

2.2 Hadron and jet detection

The hadronic calorimeter with stainless steel absorber is located within the same cryostat as the electromagnetic calorimeter and supports the latter. Both calorimeters together provide the energy measurements of hadrons. Their total depth ranges between 5 and 7 absorption lengths, depending on the polar angle θ. Events with energy leaking out of the LAr calorimeter are efficiently tagged by the tail catcher consisting of the analog readout of the pads of the limited streamer tube system in the iron instrumentation to improve the calorimeter energy resolution. Measurements in a test beam show that the expected resolution $\sigma/\mathrm{E} = 50\ \%/\sqrt{E}$ has been achieved, with an energy independent term of 2%. Here too combining the calorimetric information with the momentum information from the central tracking chambers provides a cross-check of the absolute energy calibration. Further intercalibration between calorimeters is possible by checking the balance in transverse momentum between the electrons and the hadrons.

Low energy hadrons may also be identified by the dE/dX of the CJC.

2.3 Muon detection

An important source of prompt muons at HERA is semileptonic decays of charm- and bottom mesons, therefore the muon system was designed to identify muons within jets. In the large coil solution of H1 the calorimeter serves to absorb the hadronic activity. It moreover allows to detect penetrating single ionizing tracks while the high field provides sufficient bending power for a momentum measurement. The necessary spatial resolution, matched to the dispersion due to the multiple scattering in the material in front of the instrumented iron, is reached with a total of sixteen streamer tube layers with a basic cell size of 10×10 mm^2, a triple layer each in front and after the iron, a double layer after four iron sheets of 75 mm thickness, and eight single layers in the remaining gaps in between the ten iron sheets. The multiple layers are equipped with pads and cathode strips for the measurement of the coordinate perpendicular to the wires.

In the barrel part muons with energies below 1.2 GeV do not reach the first layer, while muons with energies below 2.0 GeV stop within the iron. In the forward direction the effective threshold is 2.5 GeV, but here the muon energy is usually large enough for muons to traverse all 16 layers of chambers. An independent track segment is then measured which can be linked

to forward tracker segments. The comparison between momentum measurement in the tracker and through the muon system reduces misidentification and also allows to discriminate against muons from π and K-decay.

In the extreme forward direction the central tracker and the chamber system in the flux return iron are not adequate for measuring muon momenta with sufficient accuracy. This is why a toroidal magnet with an average field of 1.6 T was added. The driftchambers are constructed in such a way, that correlated angle and position measurements are possible. This is needed because the hadronic activity from secondary interactions of the target jet is quite high. The spectrometer is useful in the momentum range between 5 and 200 GeV/c. The lower limit is determined by the amount of material traversed, while beyond the upper limit the muon charge can no longer be measured unambiguously.

2.4 HERA beam features

The electron-proton colliding beam facility HERA consists of two independent accelerators storing respectively 820 GeV protons and 27.5 GeV electrons and colliding the two counter-rotating beams head on in four interaction points spaced evenly along its 6.3 km circumference. Electrons are injected at 12 GeV and are guided by a warm magnet system at 0.165 T, while protons are injected at 40 GeV into a ring with superconducting dipole magnets at 4.68 T. The accelerator was designed for 210 circulating bunches with 760 μA protons and 290 μA electrons each [10, 11] and a luminosity of 1.5×10^{31} cm^{-2}s^{-1}. The bunches are separated in time by 96 ns. In the early phases of operation in 1992 and 1993 only 10 and 90 bunches were circulating, respectively. An indication of the HERA performance in 1992, 1993 and 1994 is given in Figure 2.5. Since July 1994 the electron beam has been replaced by a positron beam which has considerably improved the beam lifetime at high currents.

Between the last two beam focussing quadrupoles 11.3 m of free space is available for the detector. The beams pass the detector at a height of 5.9 m above floor level ($\approx$ 20 m below ground) at an inclination of 5.88 mrad. Presently a 190 mm inner diameter beam pipe is installed, with a wall of 150 μ Al on the inside backed by 2 mm carbon fibre reinforced plastic comprising 1 % radiation length. Details of the beam line are shown in Figure 2.4. The beam pipe is cooled with nitrogen gas, which also circulates on the outside of the central tracker to avoid buildup of larger amounts of inflammable gases leaking from the chambers. Incorporated into the beam pipe are a capacitively coupled proton position monitor [12], synchrotron radiation shielding masks (see below), getter pump connections and a flexible bellow to absorb temperature dependent variations of the beam pipe. For the future upgrade of the tracking near the beam pipe [13, 14] a smaller beam pipe with an inner diameter of 90 mm (150 μm Al backed by 0.75 mm carbon fibre) will be installed.

While the radial extension of the beams is small, the finite time spread of the bunches and the zero degree crossing leads to total length of the interaction zone of $\approx \pm 50$ cm. The zero degree crossing was chosen to reduce $e - p$ beam coupling, which could result in beam blow up. The width of the interaction zone is apparent from Figure 2.5, which shows the projection of central drift chambers tracks onto the beam axis for a background free sample of photoproduction data. Typical vacuum conditions in the beam pipe during the initial running phase lead to a residual gas pressure of $\approx 1 - 2 \times 10^{-9}$ hPa primarily consisting of atomic hydrogen and carbon monoxyde. Assuming nitrogen as an average representation of the residual gas and a reaction cross-section for protons at 820 GeV ($\sqrt{s} = 39$ GeV) of ≈ 200 mb [15] one expects one proton nitrogen interaction in 10^4 bunch crossings at design luminosity along the interaction region (1 m) compared to one genuine $e-p$ event every 10^5 bunch crossings. The physics rate is dominated by photoproduction giving a visible event rate of about 200 Hz at design luminosity, the beam gas rate given above corresponds to $\approx$ 1 kHz. Beam gas background is not restricted to the

interaction zone proper and can originate from the whole proton path through the detector. Furthermore beam halo protons hitting apertures contribute, too. Monte Carlo simulations and measurements from the first data taking period indicate roughly a factor 50 higher rate for the latter process than for beam gas events from the interaction zone. These contributions are however more easily removed in the different trigger and filter levels.

The actual tuning of the luminosity optics for the two beams relies partly on the H1 luminosity system. It makes use of the $ep \rightarrow ep\gamma$ bremsstrahlung process and hence is sensitive to electron interactions with the residual gas. By filling both electron and proton bunch sequences in such a way that there is always at least one bunch of each type with no partner for a collision (pilot bunches) background subtraction can be made. During the filling phase the trigger scintillators of the time-of-flight wall can be remotely removed from the beam pipe. The integrated rate in these counters provides an efficient means for monitoring the quality of the beam tune. Only when a lower value for this rate has been reached the counters are moved back in, and the high voltage on all drift and proportional chambers is raised. While proton fill lifetimes well exceeding 24 h have been reached, the lifetime of the electron ring fills during the HERA startup phase was limited to about 6 hours; since July 1994 when positrons were used, this lifetime has increased by a factor ≈ 2.

2.4.1 Synchrotron radiation shielding

The e^- beam is accompanied by a strong flux of synchrotron radiation photons which are produced in the last bending magnet before the interaction point. Synchrotron radiation from the arcs is absorbed before the H1 detector and need not be considered. At a beam energy of 30 GeV and a stored current of 60 mA we expect a flux of 10^{18} photons per second with an energy above 5 keV into the interaction region. This flux represents a radiated power of 3.6 kW. The critical energy is 42.4 keV. In order to protect the detector elements a system of masks inside the beam pipe is installed.

The synchrotron radiation absorbers were designed such that only photons which have undergone at least two scatters can reach the central detector region. In order to reduce the photon flux the aperture of the collimators should be as small as possible. The width is thus determined by the requirement for sufficient aperture at injection. Masks which are hit by synchrotron radiation are sources of secondary photons. Therefore the albedo of all surfaces has been reduced by coating the tungsten absorbers with 0.5 mm silver and 0.2 mm copper. For 100 keV photons the albedo is reduced from 10% for pure tungsten to 1% with the appropriate coating. The geometry of the absorbers is shown in Figure 2.6. The collimators C_1, C_2 and C_3 are hit by direct synchrotron light and have to stand a radiated power of about 1 kW each. These collimators are movable and water-cooled. The synchrotron radiation which misses C_3 passes through the detector area and hits an absorber 24 m behind the interaction point. The collimators C_4, and C_5 have a fixed horizontal aperture of +30 mm -25 mm and $\pm$ 50 mm, respectively. They protect the detector elements against secondary photons originating from edge scattering at the collimators C_1 – C_3 and backscattered photons from the absorber at 24 m. The collimator C_6 is movable and provides an additional shield against photons from 24 m downstream. The aperture can be set between 65 mm and 25 mm with respect to the beam.

The present arrangement of synchrotron radiation masks cuts down the number of photons which enter the central part of the detector to a level of 10^6 photons per second with an energy above 20 keV. Thus at nominal beam conditions we expect about 10^{-1} spurious synchrotron hits in the central tracking chamber per bunch crossing. Due to the low currents and the reduced electron energy of 27.5 GeV we did not observe synchrotron radiation hits in the tracking chambers, consistent with the estimates.

2.5 Detector upgrade

This paper describes the H1 detector as it was up to the end of 1994. During the HERA winter shutdown of 1994-1995 some major upgrade work was done to the detector. It is not the scope of this paper to describe these upgrades, but the subdetectors involved will be enumerated at the end and appropriate references given.

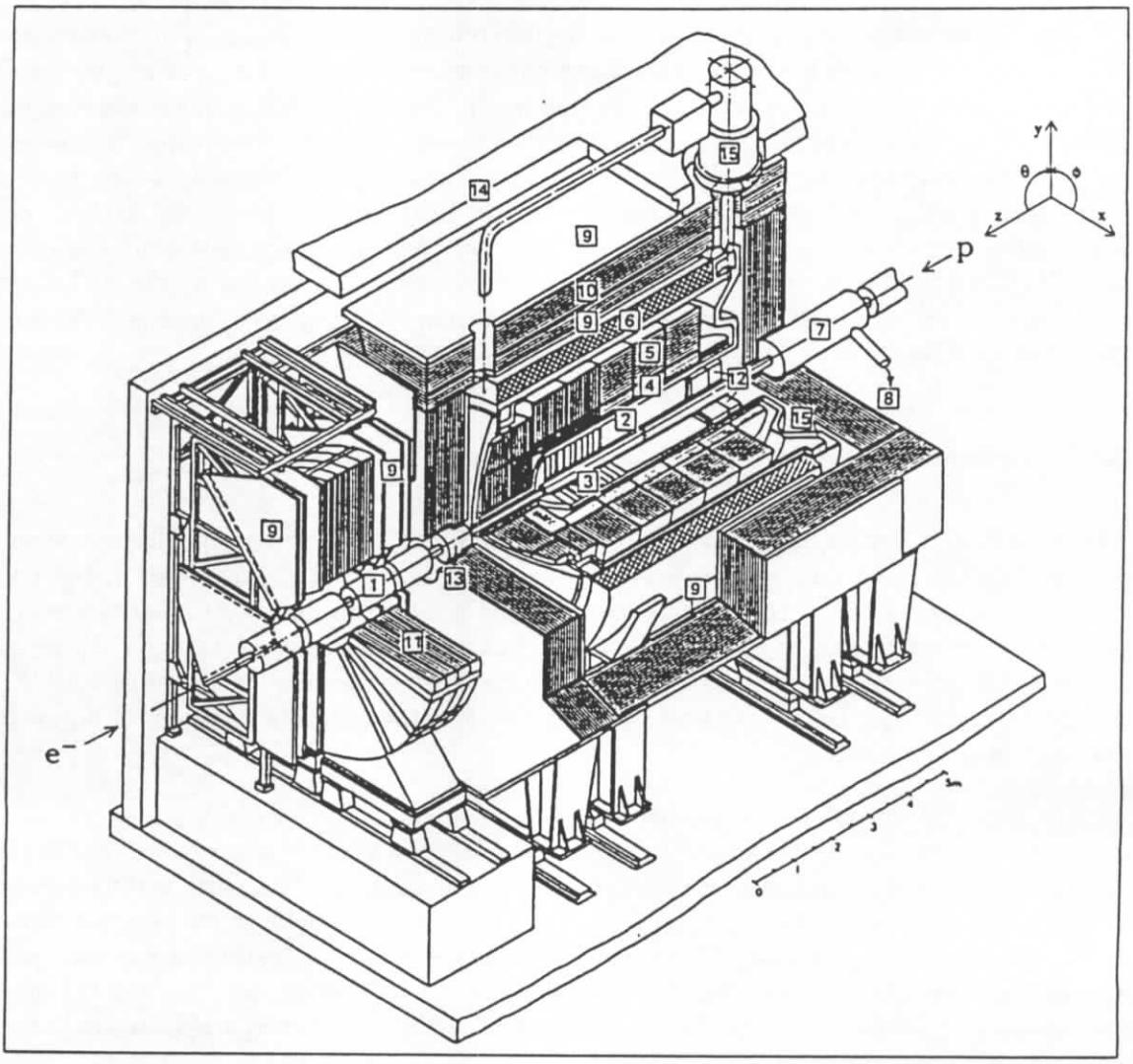

1 Beam pipe and beam magnets	9 Muon chambers
2 Central tracking device	10 Instrumented iron yoke
3 Forward tracking device	11 Forward muon toroid
4 Electromagnetic LAr calorimeter	12 Backw. electromagn. calorimeter (BEMC)
5 Hadronic LAr calorimeter	13 PLUG calorimeter
6 Superconducting coil (1.15 T)	14 Concrete shielding
7 Compensating magnet	15 Liquid argon cryostat
8 Helium supply for 7	

Figure 2.1: Schematic layout of the H1 detector.

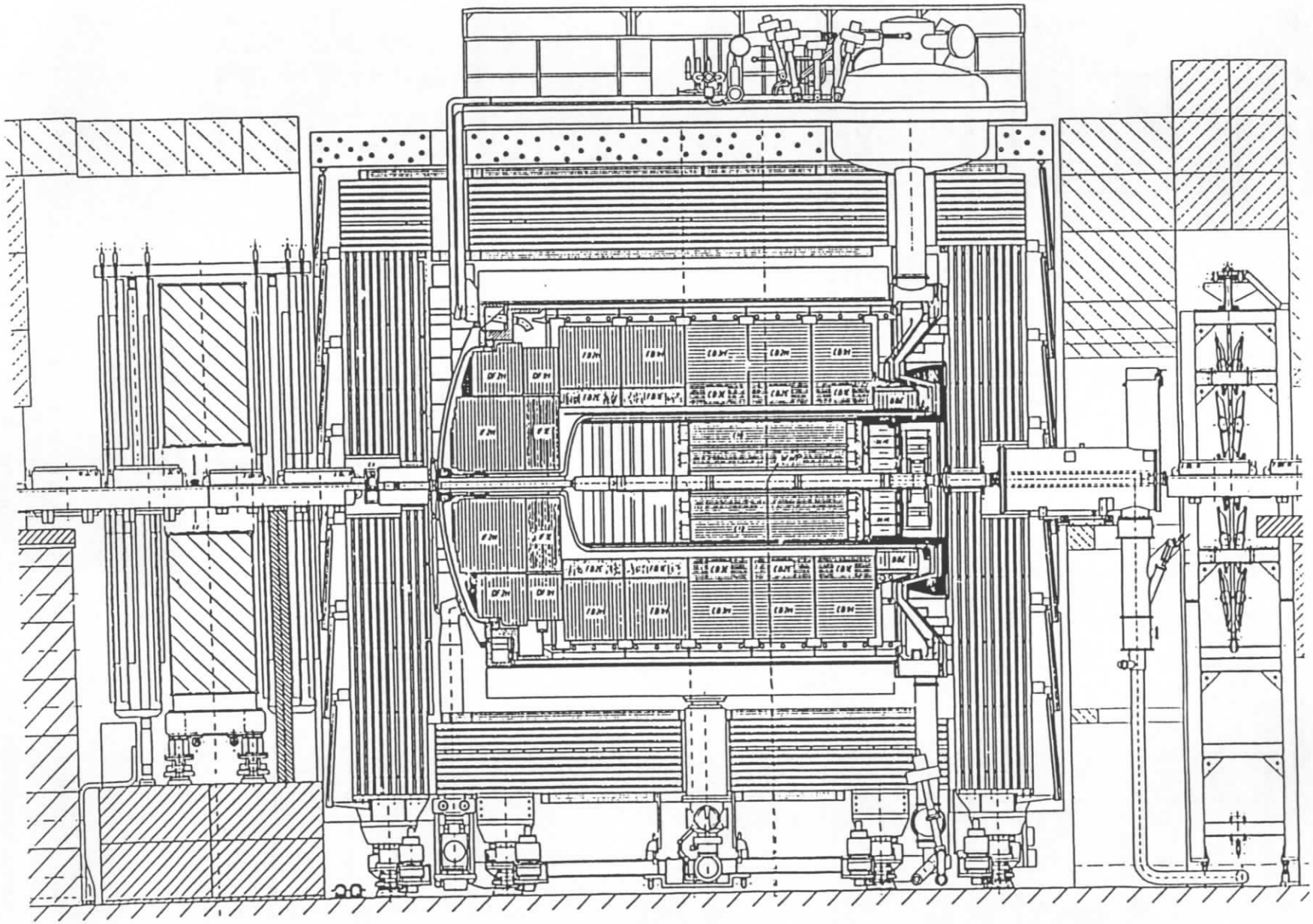

Figure 2.2: Longitudinal cut through the H1 detector along the beam line.

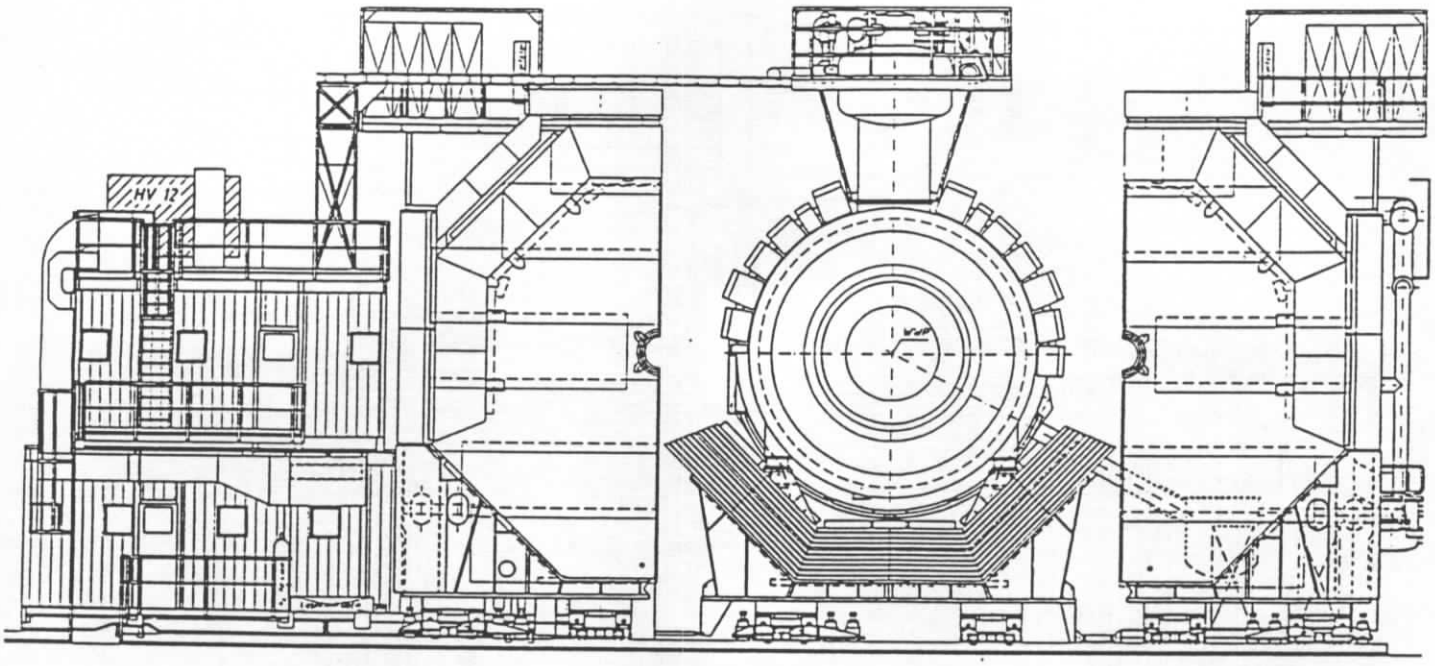

Figure 2.3: Front view of the H1 detector with the southern and the northern shells of the iron yoke opened.

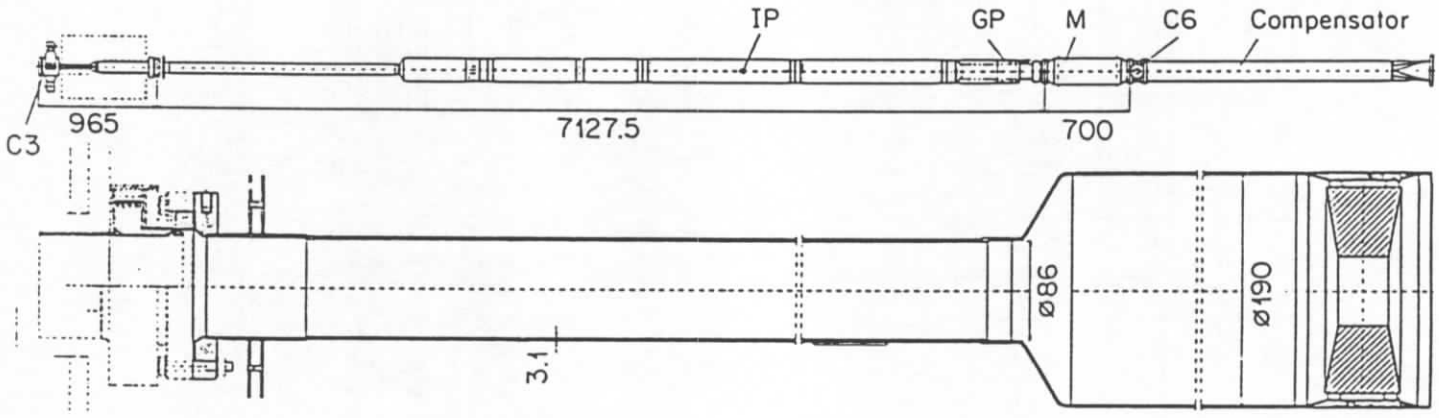

Figure 2.4: Cross section of the beam pipe in the H1 detector. IP: interaction point, GP: getter pump, M: beam profile monitor, C6: synchrotron radiation mask (see also Figure 2.6). The lower part shows an enlarged view of the forward part with the flexible bellow connections and synchrotron radiation mask C4 (right).

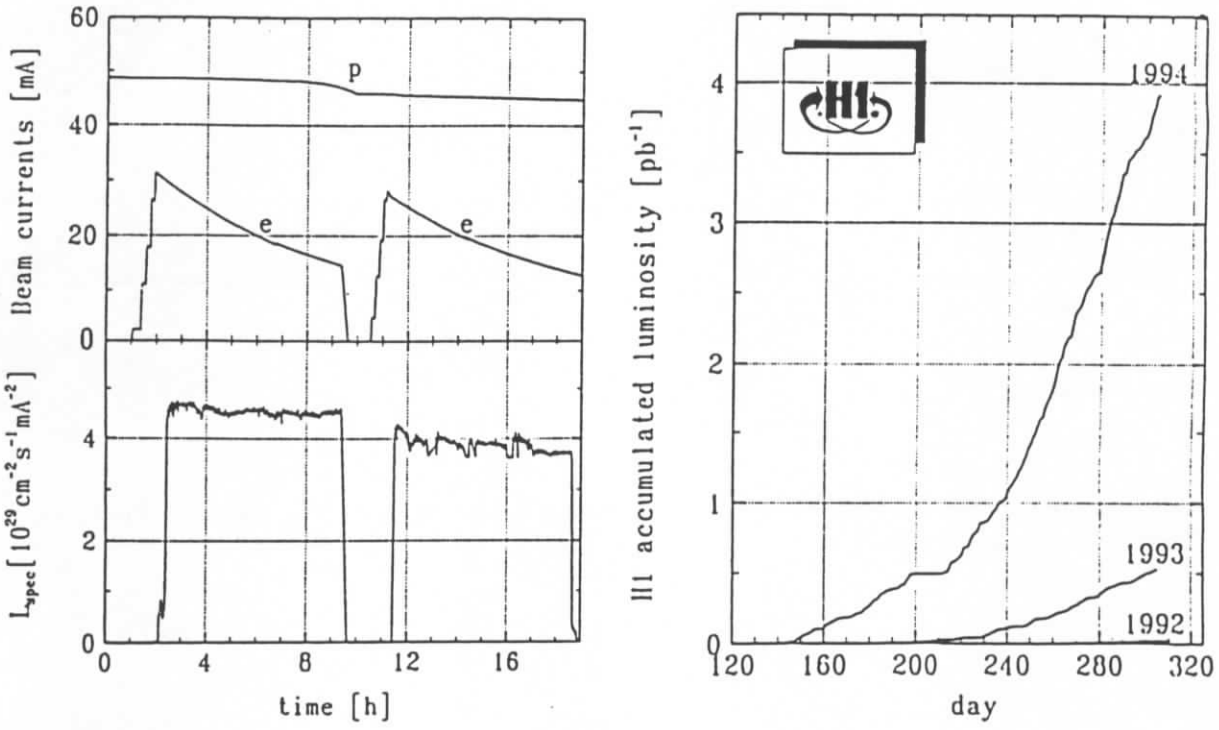

Figure 2.5: Performance of the HERA storage ring in the first three years of operation. Left: beam currents (top) and luminosity (bottom) measured during a typical run. Right: integrated luminosity accumulated by H1 over the running periods 1992 - 1994.

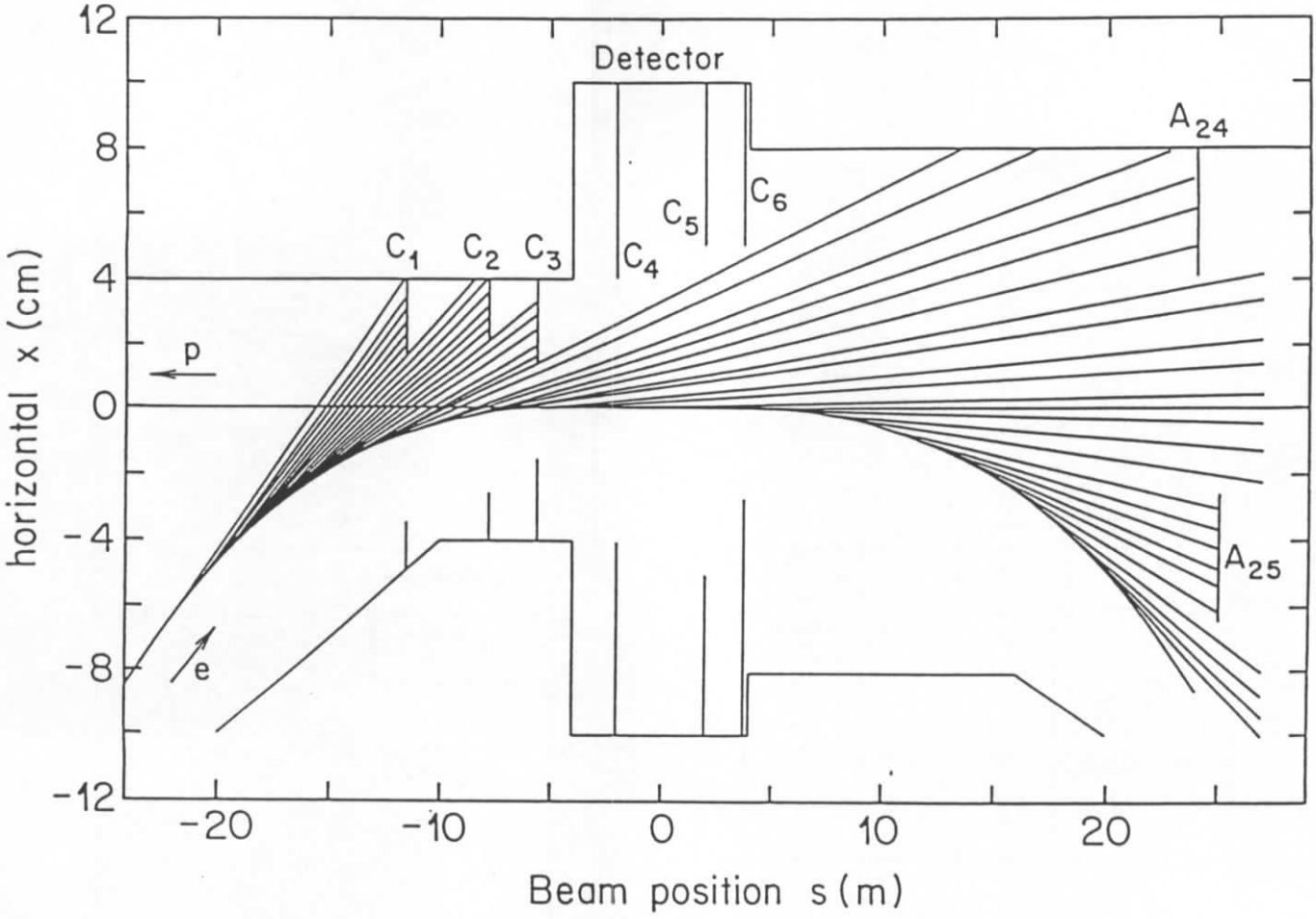

Figure 2.6: Arrangement of synchrotron masks shielding the H1 detector from direct synchrotron radiation (from reference [16]).

3 Magnet

The magnet consists of a superconducting solenoid and an iron yoke producing an almost uniform field parallel to the HERA beams. The field has only a few percent variation over the region of the tracking chambers. Within that region, 3600 mm in length and 1600 mm in diameter, the field has an average value 1.15 T.

3.1 The iron yoke

The iron yoke has the shape of an octagonal barrel with its axis parallel to the beam axis and to that of the solenoid which it encloses, plus flat end caps. In overall size it is similar to the ALEPH [17] and DELPHI [18] magnets at CERN. The requirements on uniformity of field are less stringent than for those experiments, which have chambers very sensitive to radial field components. Thus reentrant end caps are not needed for the H1 magnet and a much simpler opening mechanism is possible.

The yoke of the H1 magnet is separated into three parts, the northern and southern shells and the base structure (see Figure 2.3). The latter consists of the three lower faces of the octagonal barrel, and supports the superconducting coil. The northern and southern shells are mirror images of each other, symmetric about a vertical plane through the beam. Together they form all the rest of the octagonal barrel and the two end caps. Thus each shell is a rigid structure consisting of half of the western endcap and half of the eastern endcap, connected by 2.5 of the 8 faces of the octagonal barrel. Each of the three parts of the iron yoke moves independently on rails.

The iron of the octagonal barrel is made of 10 laminations each 75 mm thick, separated by air gaps of 25 mm accommodating a single layer of limited streamer tubes (LST), except for one air gap of 50 mm to accommodate a double layer of LSTs. The iron of the end caps is made up of 10 laminations each of 75 mm, separated by air gaps of 35 mm except for one air gap of 50 mm.

3.2 The superconducting coil

The main solenoid consists of four separate coaxial coils powered in series, symmetrically placed about the median vertical plane. The two coils nearest to the median plane ('central') are single layers, each of 201 turns, extending from 400 mm to 1420 mm from the median plane. The two coils farthest from the median plane ('peripheral') are double layers and have each 418 turns, extending from 1520 mm to 2580 mm from the median plane. All four of these windings are housed in one cryogenic envelope with an overall length 5750 mm, inner diameter 5180 mm, outer diameter 6080 mm. The superconductor, bonded into its aluminium substrate, was manufactured in industry [19]. The coils were fabricated from this conductor in modular form of length up to 1.5 m for both double and single layers on a custom built machine using the inside winding technique [20]. Liquid helium is supplied by the central plant at DESY. The parameters of this superconducting coil assembly are given in Table 3.1.

3.3 The magnetic field measurements

The general similarity in size and shape of the H1 magnet to those of the ALEPH and DELPHI magnets [17, 18] made it possible to use the same apparatus for the field measurements throughout a cylindrical volume of radius $r = 1775$ mm and length $L = 5200$ mm. The tracking

chambers occupy only a smaller volume (r = 800 mm, L = 3600 mm, $-1125 < z < 2500$ mm) asymmetric to the median plane of the magnet (z = 1100 mm). The axial component B_z which needs to be known over the tracker volume with an accuracy of 0.3 % is shown in Figure 3.1 as function of radius and axial distance to the median plane. The average value over the volume is 1.15 T at the nominal magnet current of 5514 A, and the maximum departure from this value is 4.5% at the extreme backward end of the central tracker.

The longitudinal field integral $\int B_z dz$ for the H1 magnet was evaluated to be 8.32 T.m at the nominal current.

3.4 The forward muon toroid

The toroidal magnet for the forward muon detector consists of 8 solid iron modules built into two mobile half-toroids for access purposes. The inner radius of the toroid is 0.65 m, the outer radius 2.90 m, and the length between the flat ends 1.20 m. The weight is 250 tons.

There are 12 coils wound on the toroid, each consisting of 15 turns of water-cooled copper, carrying a current of 150 A. The copper windings are square in cross-section with side 11.5 mm, with a 8.5 mm diameter hole for water-cooling.

The magnetic field within the iron toroid has been measured by the change in flux, as the magnet is turned on or off, through loops of wire threaded through small holes in the iron. The field varies with radius, from 1.75 T at a radius of 0.65 m to 1.5 T at a radius of 2.90 m.

3.5 Compensating magnet

The compensating coil is located at the proton entrance side of the H1 magnet with its center at 4.4 m from the interaction point. Its purpose is to provide a longitudinal field integral $\int B_z dz$ equal and opposite to that of the main H1 magnet. This is required if longitudinal polarization of the electron beam is to be achieved. It also avoids horizontal-vertical coupling and minimises closed orbit shifts in HERA due to any misalignment of the H1 magnet [21]. Its downstream end extends into the endcap of the main magnet. This 1.8 m long superconducting coil was manufactured in industry [22] from NbTi cable embedded into a copper matrix insulated by glass fiber epoxy. The magnetic field is shielded by an iron yoke, with both iron and coil mounted inside a pressure vessel, which is cooled by liquid He from the main DESY transfer line. The relevant parameters are also given in Table 3.1. The field integral and the magnetic field axis have been determined by means of a rotatable Hall probe described in detail in ref. [23].

Solenoid parameters	Main H1 magnet	Compensating magnet
Superconductor		
Dimensions	26×4.5 mm^2	3.1×2.1 mm^2
Type	Rutherford cable on high purity Al (RRR 500) substrate	ABB-Zürich cable
Length (weight)	22.5 km (7.7 t)	4.5/4.5 km (0.49 t)
Winding geometry		
# of coils	2 ('central')/ 2 ('peripheral')	1
# of layers (turns)	1 (201)/2 (209)	14 (534)
# of turns: total	1238	7576
Inner radius	2750/2750 mm	320 mm
Outer radius	2800/2850 mm	429 mm
Cooling	support cylinder, forced flow	cryostat bath cooled
Vacuum chamber		
Inner/outer diameter	5200/6080 mm	238/870 mm
Length/thickness	5750/10 mm	2270/6 mm
Material	stainless steel	stainless steel
Radiation shield (50 K)		
Inner/outer diameter	5330/5950 mm	268/800 mm
Length/thickness/material	5370 mm/5 mm/Al	2135 mm/1.2 mm/Cu
Overall weight (rad. length)	74.5 t for coil (1.2 X_0)	6.8 t
Operational performance		
Power supply voltage	12 V	7 V
Current nominal (max.)	5517 (6000) A	870 (1000) A
Run up (down) time	80 (120) min	40 (40) min
Cooling time	168 h	168 h
He flow (4.5/50 K)	40/3 gs^{-1}	1.3/1.3 gs^{-1}
Cryogenic losses (4.5/50 K)	60/420 W	12.2/34.6 W
Total stored energy	120 MJ	1.87 MJ
Fast discharge time constant	60 s	40 ms
Fast discharge voltage	750 V	860 V
Field on axis (integral)	1.15 T (8.32 T.m)	4.83 T (8.74 T.m)

Table 3.1: Parameters of the superconducting magnets.

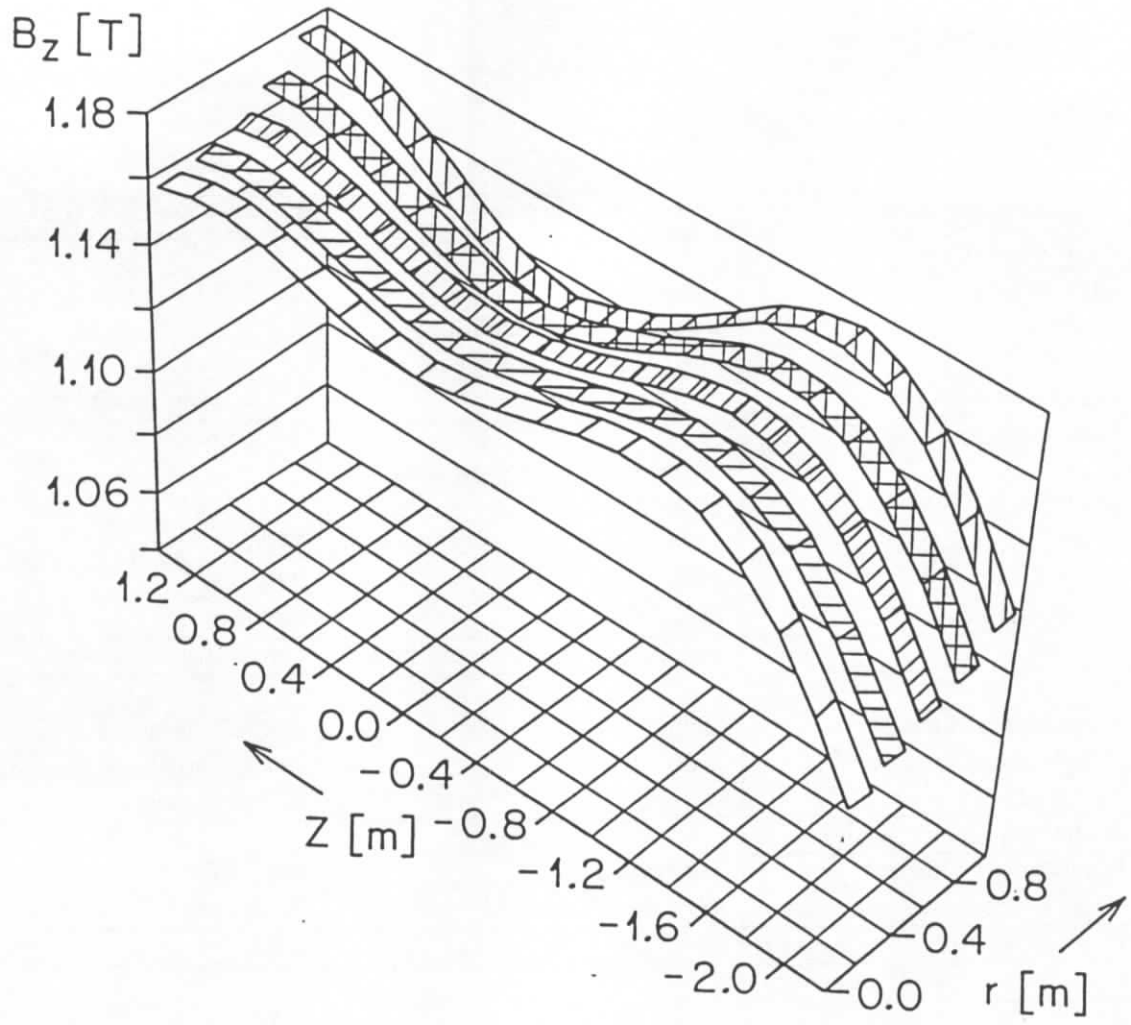

Figure 3.1: Main coil field map over the tracking volume. Here z denotes the distance to median plane, see text.

4 Tracking

The tracking system of H1 provides simultaneous track triggering, reconstruction and particle identification for the event topology particular to HERA electron proton collisions. It has been designed to reconstruct jets with high particle densities and to measure the momentum and angles of charged particles to a precision of $\sigma_p/p^2 \approx 3 \times 10^{-3}$ GeV^{-1} and $\sigma_\vartheta \approx 1$ mrad.

Because of the asymmetry between the electron and proton beam energies many charged particles are produced at small angles θ to the incident proton (forward) direction. To maintain good efficiency for triggering and reconstruction over the whole solid angle, we divide the tracking system between the central and forward regions (see Figure 4.1). Two mechanically distinct tracking detectors have been constructed, the central (CTD) and forward (FTD) tracking devices respectively. Each is optimised for tracking and triggering in its angular region.

Track reconstruction in the central region (see Figure 4.2) is based on two large concentric drift chambers, CJC1 and CJC2. The chambers have wires strung parallel to the beam axes (z-direction) with the drift cells inclined with respect to the radial direction. We have measured a space point resolution of 170 μm in the drift coordinate ($r\phi$ plane) and can, by comparing signals read out at both wire ends, achieve a resolution of one percent of the wire length in z. From the signals recorded in these chambers the transverse track momentum is determined and in addition the specific energy loss dE/dx is used to improve particle identification.

Two thin drift chambers, the central inner (CIZ) and central outer (COZ) z-chambers measure the z coordinates with better accuracy than charge division and complement the measurement of charged track momenta in the central chambers. The CIZ chamber fits inside CJC1, and the COZ chamber fits in between CJC1 and CJC2. These two chambers deliver track elements with typically 300 μm resolution in z and 1 to 2% of 2π in ϕ. This requires a drift direction parallel to, and sense wires perpendicular to the beam axis.

Triggering over the full solid angle is based on multiwire proportional chambers with pad readout in the central and forward region and wire readout in the backward direction. They provide a fast first level (L1) trigger decision which can be used to distinguish between successive beam crossings. Furthermore, in the central and forward region, combinations of pads hit in the central inner proportional chamber (CIP), the central outer proportional chamber (COP) and the forward proportional chambers (FWPC) are used to trigger on tracks coming from a nominal interaction vertex. First level track triggers are also derived from the central drift chambers.

Each of the central chambers has an independent gas volume and separate electrostatic shielding. They were built and tested separately, and then assembled and locked to one mechanical unit. The detector walls are thin to reduce photon conversion, and in particular its effect on identification of primary electrons. Neighbouring volumes share a thin (1.5 mm) cylinder of carbon fiber reinforced epoxy with a 50 μm aluminium coating on each side. The complete system of central tracking detectors is housed in a single aluminium cylinder of 4 mm wall thickness. The assembly also provides a precise alignment of the chambers relative to the outside support.

Charged tracks produced at polar angles θ close to the beam axis (forward $\theta < 30°$, backward $\theta > 150°$) no longer traverse the full bending ($r\phi$) plane radius of the solenoid magnetic field. Consequently in the CTD both track pattern recognition and accuracy of track reconstruction deteriorate as the measured track length and the number of precision space points decrease. A way of rectifying this loss is to compensate for the reductions in track length and the number of points in the central region by means of a higher radial density of accurate space points obtained using wires strung in the bending plane closely spaced in z. This is provided by the forward tracking detector which consists of an integrated assembly of three nearly identical

supermodules. Each supermodule includes, in increasing z: three different orientations of planar wire drift chambers designed to provide accurate θ measurements, a multiwire proportional chamber (FWPC) for fast triggering, a passive transition radiator and a radial wire drift chamber which provides accurate $r\phi$ (drift coordinate) information, moderate radius measurement by charge division and limited particle identification by measuring the transition radiation produced immediately upstream.

The FTD and CTD are linked together, aligned and surveyed prior to installation into the calorimeter cryostat.

The description of the individual components of the tracking detector below is followed by sections which describe the features common to all drift chambers, namely the readout and pulse shape analysis and the gas systems used for all chambers.

4.1 Central jet chambers: CJC1 and CJC2

4.1.1 Design criteria

The design of CJC1 and CJC2 [24, 25] follows that of the jet chamber used in the JADE experiment at PETRA [26]. The wire pattern characteristic for a jet chamber is a plane of anode sense wires parallel to the beam line with two adjacent cathode planes shaping the drift field. In the CJC's the latter planes are also made of wires.

A jet chamber cell extends azimuthally from the sense wire plane to both adjacent cathode wire planes, and radially over the full radial span of CJC1 or CJC2 each with no further subdivision, as shown in Fig. 4.2. This minimises the disturbing influence of field shaping wires at the inner and outer radii.

The jet cells are tilted by about 30° such that in the presence of the magnetic field the ionization electrons drift approximately perpendicular to stiff, high momentum tracks originating from the center. This not only gives optimum track resolution, but also leads to additional advantages. The usual drift chamber ambiguity is easily resolved by connecting track segments of different cells. The wrong mirror track segments do not match, as demonstrated in Figure 4.3. They also do not point to the event vertex and therefore obstruct only small parts of a real track in the opposite half cell. Each stiff track crosses the sense wire plane at least once in CJC1 and in CJC2. From the fine match at the crossing, the passing time of a particle can be determined to an accuracy σ of ~ 0.5 ns. This allows an easy separation of tracks coming from a different bunch crossing. The drifting electrons from stiff tracks arrive at neighbouring sense wires with a time shift of about 100 ns, and therefore produce only negligible disturbance by cross-talk. Every track traverses several regions of uniform driftfield inside the cells. Systematic errors of drift time measurement, which are known to arise in the nonuniform fields near the cathode and sense wire planes, reverse sign at the crossing, and therefore cancel in good approximation.

Adjacent sense wires are separated by two potential wires (see Figures 4.2 and 4.3). This reduces both the surface field and the cross-talk by nearly a factor of two as compared to a single potential wire. Most important, it allows to adjust drift field and gas amplification nearly independently. The actual positions of the sense wires are staggered off the nominal sense wire plane by ± 150 μm, such that adjacent wires are pulled by the electric field to definite positions on opposite sides of the plane.

A cell is azimuthally limited by two cathode wire planes, and at the inner and outer radius by the field wires. The cathode wires are set to a voltage proportional to the distance from the sense wire plane in order to create an uniform drift field and hence a constant drift velocity over almost all the cell. The voltages for the cathode wires are supplied by a resistor network

(cathode chain) on the adapter cards connected to the cathode wires. The field wires shape the field at the inner and outer end of the cell such that the deviations from a uniform drift field are minimal. The sense wires are connected to a positive voltage and are AC coupled to the amplifiers. The potential wires are set to ground. To prevent ageing of the chambers due to high electric surface fields, the diameters of the potential, cathode and field wires were chosen conservatively large : 127, 180 and 500 μm. This limits the surface field to $\leq$ 2KV/mm. The anodes are 20 μm (25 μm at the cell ends) gold plated tungsten wires with 3 % rhenium, having a resistivity of 300 Ω/m.

The electrostatics of the cells have been studied in detail by computer simulations. Figure 4.3 shows drift lines and isochrones in CJC1 for a Lorentz angle of 30°. In most of the drift region the electric field is constant to better than 1 %. At the first and the last sense wires the wire geometry produces local distortions of the field which, however, do not exceed 2 %. This introduces only negligible variations of the drift velocity, in particular around the maximum of the drift velocity.

The parameters of the jet chamber are listed in Table 4.1. All sense wires are read out at both ends and yield via charge division a $z-$measurement.

4.1.2 Mechanics

The volume of each jet chamber is defined by two endwalls perpendicular to the beam line and an inner and outer cylinder concentric to the beamline. The volume has to be gas tight and to support small overpressure with respect to the atmosphere.

The bulk material of the endwalls was chosen to be 10 mm glass fiber reinforced epoxy [27], combining excellent insulation with good mechanical properties. The fact that there are two jet chambers allowed relatively thin endwalls, because the support lengths between inner and outer cylinders are small and thus the bending under the summed wire tension could be kept below 1 mm.

To facilitate installation, insulation and HV testing of all connections, the signal- and HV leads are integrated into the endwall structure by means of multilayer printed circuit (PC) boards. One board (2 mm thick) covers one drift cell. Of its four layers, one provides a nearly complete electric shield of the chamber, while the others make the contacts between the wire feedthroughs and the (signal and HV) connector sockets. A second PC board inside the chamber, 0.8 mm thick, carries strips for shaping the end fields.

Optimum precision of the wire positions is achieved by first gluing 3 mm thick massive brass pins into pre-bored holes in the endwalls, and then drilling precision holes into the brass. The precision of the sense wire positions, $\pm$15 μm within one cell is determined by small excentric holes in the brass. Details of the wire supports can be found in ref. [24].

The endwalls are kept apart by four cylinders. For the inner and the outer cylinder of CJC1 and the inner cylinder of CJC2 carbon fiber reinforced epoxy (1.5 mm thick) has been chosen because of its excellent mechanical stability (Young's modulus ϵ = 80 kN/mm^2) and very long radiation length (X_0 = 230 mm). The chamber volume forms a Faraday cage in order to be screened against external electromagnetic noise. Since the conductivity of the carbon fibers is not sufficient in all directions, an aluminium coating of the inner and outer surface was mandatory. The thickness of 50 μm of the Al surface liner was a compromise between electromagnetic screening down to low frequencies (skin depth at 20 MHz in Al is $\approx$ 20 μm) and minimum material. The outer cylinder of CJC2 is made of aluminium (4 mm thick) and is the main support vessel for all tracking detectors. It has feet which slide on rails positioned on the inner warm wall of the liquid argon cryostat and which are the mechanical link to the rest of the H1 detector. At both ends the Al cylinder has thicker flanges (Δr = 12 mm), which are machined to 0.1 mm tolerances in order to house the endwalls precisely. At final assembly the stability and shape of the Al cylinder is guaranteed by the insertion of the endwalls.

	unit	CJC1	CJC2	CIZ	COZ
active length Δz	mm	2200		1800	2160
active zone starts at z	mm	-1125		-1080	-1105
total length Δz[1]	mm	2500		2467	2590
mechanical length Δz	mm	2230		2254	2230
inner radius R_i	mm	203	530	173.5	460
outer radius R_o	mm	451	844	200	485
active radial length	mm	224	296	20	24
number of cells (rings)		30	60	15	24
number of sense wires per cell (ring)		24	32	4	4
number of potential wires per cell (ring)		50	66	3	6
number of field wires per cell		10	10		
number of cathode wires per cell		49	65		
sense wire distance	mm	10.16		5.6(7.0)	6.0
maximum drift distance at R_i	mm	22.9	28.5	61.25	45
maximum drift distance at R_o	mm	44.5	43.1		
sense wire tension	N	0.65		0.2	0.9
mean wire length	mm	2200		1120	2970
drift velocity [2]	mm/μs	$\approx$ 50		52	48.5
$\sigma_{r\phi}$	mm	0.170		28	58
σ_z	mm	22		0.26	0.20
double hit resolution	mm	2		4.6	3.5

Table 4.1: Central jet and $z-$ chamber parameters.
[1] Incl. preamplifiers; [2] for the gas mixtures given in Table 4.6.

4.1.3 Calibration and performance

The accurate measurement of the track parameters is limited by the intrinsic resolutions, namely $\sigma_{r\phi} \approx 150$ μm for drift time measurements with a gas mixture of Ar-CO_2-CH_4 (89.5 : 9.5 : 1.0), $\sigma_z \approx 1\%$ of the wirelength for the charge division measurements (limited by pulseheight and noise), and $\sigma_{dE/dx} \approx 6\%$. With this gas the drift velocity at nominal HV is 50 mm/μs.

A large variety of constants is involved to determine the coordinates of a hit from the timing (t) and pulse-integral (Q) of a drift chamber signal (see Section 4.4.5 for (Q,t) analysis). We distinguish overall and wire dependent constants.

The overall constants – event timing, average drift velocity and average Lorentz angle – are sufficient to determine the track parameters with moderate accuracy, e.g. $\sigma_{r\phi} \approx 350$ μm. They are determined and continuously monitored by fitting them as additional parameters to long, high momentum tracks (see Section 4.1.4). The use of an average effective wire length and gain gives resolutions of $\sigma_z \approx 5$ cm and $\sigma_{dE/dx} \approx 17\%$.

The wire dependent constants – timing, signal propagation, absolute gain, relative gain and position of both wire ends – have been determined in two steps. The first step consists of the evaluation of data where the 4 odd/even wires of an 8-channel amplifier card on both chamber ends are pulsed separately and simultaneously. This gives the relative timing of the 4-wire groups, the timing difference, and the relative gain at the two wire ends. The start values for the effective wire length are determined, apart from an overall factor. In the second step the residuals of hits for reconstructed and fitted tracks are evaluated to obtain the absolute values of the individual wire constants. This improves the resolution to $\sigma_{r\phi} = 170$ μm, $\sigma_z = 2.2(3.3)$ cm for protons (pions) and $\sigma_{dE/dx} = 10\%$ (see Figures 4.4 and 4.5 and Table 4.1).

The resolution achieved in the $z-$coordinate depends on the deposited ionization (Figure 4.4). Data from ep collisions were analysed [28]. The dependence of the specific ionization on

the particle momentum is show in Figure 4.5. There are clearly visible bands for pions, proton and deuterons , where the latter two particle species are mainly produced by protons colliding with the residual gas in the beam pipe.

4.1.4 Track reconstruction

4.1.4.1 Track parametrization Tracks of charged particles are characterized by the five helix parameters: the signed curvature ($\kappa = \pm r^{-1}$, positive if the direction ϕ coincides with a counter-clockwise propagation along the circle), the signed closest distance from the $z-$axis in the $(x, y)-$plane d_{ca}, positive if the vector to the point of closest approach and the trajectory direction form a right-handed system), azimuth and polar angle (ϕ and θ), and the $z-$position (z_0) at the point of closest approach. The first three parameters are determined by a circle fit to the data in the xy-projection using the non-iterative algorithm of Karimäki [29]. The circle equation is expressed in polar coordinates (r, φ) as

$$\frac{1}{2}\kappa\left(r^2 + d_{ca}^2\right) + (1 - \kappa d_{ca})\, r \sin(\phi - \varphi) - d_{ca} = 0$$

For a track traversing both rings of the CJC a single parametrization for both rings is usually sufficiently accurate. Due to multiple scattering in the material between the two rings (2 % X_0) for some tracks two separate sets of parameters are determined, which are constrained to join in a point between the two rings under an angle compatible with the mean multiple scattering angle.

The other two parameters are determined by a linear least-squares fit of $z_i = z_0 + S_i^{xy}(dz/dS)$, where S_i^{xy} is the track length for the point z_i in the xy-projection, with $S^{xy} = 0$ at d_{ca}. The slope parameter (dz/dS) determined by the fit is converted to the angle θ by $\theta = \arctan(1/(dz/dS))$.

The track finding is followed by further modules to determine the xy-vertex for a given run, and to perform track fits to the primary and secondary vertices. The track parameters in this stage are κ, ϕ and θ, together with the xyz-coordinates of the vertex and the error matrix.

4.1.4.2 Track finding Two versions are used for the track finding and fitting. A fast version, efficient for tracks originating from the primary vertex with a momentum > 100 MeV/c, is used on the fourth trigger level filter farm (see Section 8.5) for background rejection and fast classification of events. It is roughly a factor ten faster than the standard version, which is efficient for all kinds of tracks and is used within the normal reconstruction.

The first phase of track finding, the search for short track elements (curvature negligible), is done independently in the angular cells with 24 (CJC1) and 32 (CJC2) radial wires. Within angular sectors track-element finding does not depend on parameters like the Lorentz angle or the drift velocity. However accurate values of these parameters are necessary when hits from more than one angular cell are combined. Track finding is based almost exclusively on drift time data in the xy-plane and includes removal of outliers, which would distort the circle fit. Only in a later stage the measured z-values are used; here it is again necessary to remove outliers before the data are fitted.

For the fast track finding it is sufficient to determine the bunch crossing time t_0 for an event from the threshold in the drift time histogram. The first step involves the search for track elements defined by three hits within angular cells found on three wires with a wire distance of two. The algorithm starts by trying all pairs of hits at wires $n \pm 2$ (n = wire index). Possible values of drift distances $\bar{d}^n$ at the wire n are calculated by $(d_i^{n-2} + d_k^{n+2})/2$ and/or $|d_i^{n-2} - d_k^{n+2}|/2$ (i, k = hit indices) and stored in a list, if the direction of the pair does not deviate too much

from the radial direction. Very dense regions with many hits are not analysed. This list is then compared with the measured values d_j^n and for small differences $|d_j^n - \bar{d}^n|$ the indices of the hits at the three wires are stored as a possible track element. From these hit triplets the curvature κ and the angle ϕ_m can already be determined with sufficient accuracy assuming $d_{ca} \equiv 0$. The parameter ϕ_m is the track angle at the mean radius r_m of the CJC1 and the CJC2, respectively. No attempt is made at this stage to resolve the drift sign ambiguity; triplets with a large value of $|\kappa|$ are rejected, otherwise both solutions are kept. A z-value and a value for dE/dx are assigned to the triplets from the median of the three single-hit values and later used to determine the z-slope and -intercept z_0 and the mean dE/dx value of the track.

Tracks from the origin cluster in the plane of the two parameters κ and ϕ_m of the triplets, with a width of typically only one degree for ϕ_m. These clusters are sufficiently separated, that after finding them a first track definition is achieved. The coordinates of triplets within the clusters are then used in a circle fit, now allowing $d_{ca} \neq 0$, and by a z-fit. Track candidates with large $|d_{ca}|$ and $|\kappa|$ values are rejected.

The track candidates are then checked in the order of decreasing number of triplets (decreasing significance) rejecting tracks with several triplets already used before for an accepted track. Drift sign ambiguities are normally resolved at this stage, since most tracks traverse several cells and the correct solution has a much larger number of triplets than the wrong one. The fast track finding is in general efficient enough to allow sensitive recognition of background or classification of physics events.

The standard track finding starts from the results of the fast track finding and first improves the time reference value t_0 for an event by fits to the drift length values of long tracks. For a given track the values of the circle parameters are used to calculate the expected drift length for all possible wires. The difference between the measured and the expected drift length is then calculated for all hits, taking into account the sign of the drift length. To these differences an expression is fitted, which in addition to a parabolic dependence on the track length (to allow for a small inaccuracy in the track parameters) parametrizes the effect of a t_0 difference (which depends on the sign of the drift length) and of a small difference of the drift velocity. This fit yields an accurate value for t_0 and allows in addition to detect changes of the drift velocity. At the same time the method improves the definition of tracks, since often the range of the hits found is extended. Another circle fit is performed to all long tracks traversing more than one cell (drift sign ambiguity resolved). If the χ^2 value of the track fit (after removing single bad hits eventually) is acceptable the complete set of track parameters is stored already at this stage, the hits assigned to the track are flagged and not used in the following steps.

The first phase of standard track finding again searches for track elements defined by three hits, but now on adjacent wires. All possible wires are considered, except for very dense regions. Triples with common hits are connected by pointers and when all hits of an angular cell are analysed, chains of hits are extracted. These chains of hits are then checked by a fit to the drift times for effects like kinks; eventually long chains of hits are split into two shorter chains. For long chains the staggering of wires sometimes allows already to resolve the drift sign ambiguity; otherwise both solutions are kept. Chains accepted at this stage are stored as track elements with parameters from the fit.

Short track elements are merged to larger ones first within the same or neighbouring angular cells, then within one ring and lastly from both CJC1 and CJC2. The merging algorithm starts with a comparison of pairs of track elements with similar helix parameters. If the distance between them is not so large that they could belong to the same track, a χ^2-fit in the xy-plane is performed. The list of all acceptable pairs is sorted in the order of an increasing "distance", assigned to each pair. The distance is constructed from the χ^2-value and other parameters (e. g. the length of the track element). The list of pairs is then checked sequentially, starting with

the "close" pairs. Two elements from a pair are combined to a new (longer) track element, if acceptable. If in this sequence one element of a pair has already been used in the construction of a new element, the fit to the modified element(s) is repeated and rejected eventually. By this process longer and more accurate track elements are formed, starting with the simple and clear cases, thus avoiding with high probability a wrong combination of short track elements.

For the final improvement of the track finding efficiency and precision the expected drift length is calculated for all possible wires and for all track elements ordered by their length. Hits at the expected wires which are not already used by another track are collected. The differences between measured and expected drift length are analysed to reject incompatible hits. Tracks found are allowed to contain rather large gaps of several wires, since parts of tracks may be invisible, especially within jets, due to the limited double track resolution. The fits for the track parameters are repeated using all acceptable hits.

Very short track candidates are rejected, unless they start with the first few wires of a ring. The energy loss dE/dx for a given track is determined from the mean of single-hit values $1/\sqrt{k_i} = 1/\sqrt{(dE/dx)_i}$, excluding hits which are close to another track. An analysis based on a likelihood method has improved the dE/dX to below 10 % (see [30]).

4.1.4.3 Vertex determination The $e-p-$interaction vertex region in the xy-plane extends over a few hundred μm with a rather stable mean position for a sequence of runs. The mean vertex coordinates (x_v, y_v) are determined using long high momentum tracks with a small value of d_{ca} from a few hundred events and minimizing the sum of squares of the distance of the tracks to the vertex.

The known (x_v, y_v) position of the run vertex can be used as a constraint to improve the parameters of tracks originating from this vertex, if the effect of multiple scattering in the beam pipe and the CJC wall for low-momentum tracks is taken into account. Since the standard deviation of the curvature value is roughly inversely proportional to the track length squared, the track precision is significantly improved by this vertex fit in the xy-plane. A z-value of the primary interaction vertex in an event is determined from all tracks fitting to the xy-vertex. The polar angle θ for these tracks is changed accordingly .

Within the standard reconstruction program a search is made for neutral particles decaying into a pair of oppositely charged particles with tracks in the CJC; in addition to K_S^0, Λ and $\bar{\Lambda}$ particles also e^+e^--pairs from conversion are found by this module. Candidate pairs are determined using simple geometrical cuts. For each candidate pair a fit is performed applying geometrical (common secondary vertex of the charged particles) and kinematic constraints. Use is made of the known position of the primary vertex. Momentum balance perpendicular to the direction of the neutral particle is used as kinematic constraint, but no masses are assumed. For a very small opening angle of the pair the transverse momenta in the xy-plane are both constrained to zero, to improve the stability of the fit for e^+e^--pairs. Pairs with an acceptable χ^2-probability are stored.

At later stages of the analysis alternative methods for reconstructing secondary vertices are also employed (see references [31, 32] and Figure 12.5). Kalman filtering techniques have also been shown to be useful [33].

4.2 Central $z-$ chambers

The central inner and outer $z-$chambers (CIZ, COZ) surround the inner half of the jet chamber and complement the measurement of charged track momenta in the latter chamber. These two chambers deliver track elements with typically 300 μm resolution in z, which can be linked to

those obtained from the jet chamber for the final accuracy on both the longitudinal as well as the transverse momentum components. The polar angles covered by CIZ and COZ are $16° < \theta < 169°$ and $25° < \theta < 156°$, respectively. Since the CIZ uses the inner carbon fiber wall of the CJC for closing its gas volume, and the COZ uses the outer carbon fiber cylinder for its basic structural element, the thickness of both chambers could be kept small, namely 0.6 % X_0 for CIZ and 0.7 % X_0 for COZ in the active zones and 1.2 % and 1.5 %, respectively averaging over the cell wall material. Furthermore the total amount of dead zones in azimuth imposed by readout channels and wire supports is only 7.7 % and 5.3 % of 2π respectively. The basic parameters of both chambers are given in Table 4.1 and the gas mixtures used are given in Table 4.6. A first level, background rejecting trigger [34] combines CIZ and COZ hits to trigger on straight tracks pointing to the interaction region (see Section 8.3.1.7).

4.2.1 CIZ

For CIZ a laminar construction technique similar to that described below for CIP was used, starting from a steel mandril with an inner diameter of 347 mm. Successive layers include 25 μm Kapton with a 2.5 μm Al coating for electrical shielding, a 6 mm thick Rohacell [35] cylinder with its outer surface machined and polished to produce 16 flat surfaces forming a regular polygon in cross-section (see Figure 4.2), and a 25 μm Kapton foil with 10 μm Cu field forming strips on both sides. The 15 independent cells are separated by printed circuit boards, 1.6 mm thick with 5 μm Cu on each side serving as cathode planes. The cells are closed electrically with another Kapton foil identical to that on the bottom of the cell, here backed by 1 mm Rohacell. The end flanges of the CIZ are sealed against the CJC end plates with O-rings. Further constructional details, e. g. on the specially designed wire feedthroughs, can be found in references [36, 37, 38].

Figure 4.6 shows the geometry of the drift cell. The sense wire planes are tilted by 45° with respect to the normal to the chamber axis, with the first nine cells in the backward direction tilted backward and the last six in the forward direction tilted forward, i.e. following the direction of the tracks crossing the respective cells. As explained in ref. [36] this tilt produces a distortion of the equipotential lines resulting in a non-uniform distribution of the charge collected on the four wires and an equivalent tilt of the isochrones. This unusual wire arrangement solves the left-right ambiguity automatically without a need for wire staggering and furthermore eliminates the dependence of the resolution on the crossing angle. The wires are soldered to both side walls of a 23 mm wide cable channel at $\phi = 0°$. Here the signal wires are connected to line drivers and the potential wires to HV cables. The line drivers provide the impedance matching to the preamplifiers mounted on the end plate. A high resistivity alloy (Elgiloy [39], 3 kΩ/m) was selected as sense wire material (Ø 20 μm) to improve the measurement of the ϕ coordinate along the wire by charge division. The potential wires are made from Au (Ø 120 μm). To save space the HV cables to the electrodes and cathodes are buried in the Rohacell chamber body and the miniaturized 10 MΩ resistors (1.25 mm × 2 mm × 0.5 mm), which supply the field forming strips are embedded in the printed circuit board chamber partitions. The structure of the field shaping electrodes is indicated in Figure 4.6. For the gas mixture listed in Table 4.6 the chamber is operated with a cathode voltage of 4500 V, a potential wire voltage of 2250 V and a field gradient of 53 V/mm.

Since the CIZ is the drift chamber closest to the interaction point, a dedicated current monitoring system (see ref. [40] for details) was included into each potential wire supply line. It allows to measure the currents in the nA range. These wires control the gas amplification in the chamber. In this way the activity introduced by interaction products or stray beam can be monitored. Typically we found 10 nA current increase per ring for a luminosity of 20 $mb^{-1}s^{-1}$. This corresponds to an accumulated charge of 10 Cb/m per wire for an integrated luminosity of 100 pb^{-1}.

Apart from a narrow strip near the cell walls the chamber efficiency was measured to 98 % in test beams at PSI [37]. From test beam data the resolution was found to be $\sigma_z = 320$ μm independent of the drift distance and the crossing angle in the range $10° < \theta < 110°$. These results could be confirmed with cosmics ray data, where central jet chamber tracks were extrapolated into the z-chambers and then linked to the corresponding track elements. The average deviation from a straight line fit (in the $r - z$ plane) is $\sigma_z = 260$ μm for CIZ internal track elements and 400 μm for linked tracks. For the $\phi-$projection a resolution of 2.4 % of the wire length was measured. Double pulses can be resolved, if their separation exceeds 90 ns, which converts into 4.6 mm spatial separation in z [37].

4.2.2 COZ

This chamber was also built on a Rohacell body with the cross-section of a regular 24-edge polygon (Figure 4.2), but resting on a cylinder of carbon fiber reinforced plastics. The Kapton foils with field shaping copper strips were glued to the Rohacell surfaces. Guided by a mechanical positioning device the wire supporting rods (G10 with Cu strips, double sided) were placed and soldered to the Kapton foil. Between these rods planar cathodes were introduced made of G10/Cu with holes to enable the gas flow through the chamber. The top cover of the drift cell structure consists of a Kapton-Rohacell sandwich which is fixed at the cathodes. The chamber has a cylindrical shape due to its G10-Cu gas cover held by the endflanges. Further details can be found in references [38, 41]. Figure 4.7 shows a schematic view of the COZ. The dead zones for the wire readout are distributed in azimuth which allows a corresponding distribution of the preamplifiers at the end flanges and minimises the dead area of the chamber. The anode signals are transmitted by twin readout lines (signal-ground signal, length 20 to 120 cm) from the wire ends to the preamplifiers on both chamber ends.

Each drift cell is 24 mm high, the maximum drift length is 46 mm which limits the drift time to about 1 μs. Each cell has four sense wires (Stablohm [39], Ø 48 μm, 0.6 kΩ/m) in the symmetry plane of the cell and three pairs of potential wires (CuBe, Ø 127 μm). The wire feedthroughs in the supporting rods are kept in their nominal position to about 30 μm (σ). No wire stagger is implemented. Mirror tracks can be removed in the analysis since they do not point to the vertex.

The COZ is typically operated with a cathode voltage of 3000 V, a potential wire voltage of 2250 V and field gradient of 82 V/mm. For the gas mixture listed in Table 4.6 this gives a drift velocity of 48.5 mm/μsec, as determined from tracks crossing the sense wire plane and the cathode plane, respectively.

Inefficiencies along the cell walls and other performance parameters were studied in test beams (3 GeV electrons at DESY and low energy pions and electrons at PSI, see references [42, 41]). Apart from a small region near the sense wire feedthroughs the efficiency was determined to be 98 % over the full drift cell. For a 90° crossing angle the resolution measured at HERA is about 200 μm, deteriorating to 500 μm for low crossing angles. The azimuthal angle is determined by charge division to an averaged accuracy of 7.2 °, i.e. 2 % of the wire length. Double pulses can be resolved if their separation is larger than 70 ns which corresponds to 3.5 mm distance. For a discussion of the optimum method to resolve double tracks and a comparison of different algorithms for (Q, t) analysis we refer to [41, 42, 43].

4.3 Forward tracking detector

The forward tracking system is designed to provide an accurate measurement of charged particles in the forward direction (momentum resolution $\sigma_p/p^2 < 0.003$ GeV^{-1} and track angular

resolution $\sigma_{\theta,\phi} < 1$ mrad), track information on individual particles within jets, electron identification by means of transition radiation detection and a fast forward ray track trigger. Details about track finding and fitting can be found in [44].

The layout of the FTD is illustrated in Figures 4.8 and 4.9. Key parameters are listed in Table 4.2. The drift chambers have different wire geometries - the planar ones contain parallel wires whereas the radial ones have wires radiating outwards from the beam pipe – all wires being strung perpendicular to the beam direction. The planar module consists of three drift chambers, each four wires deep in z and rotated at 60° to each other in azimuth. It is located closest to the central tracker in each supermodule, since its homogeneous spatial precision in x and y is most suitable for linking to tracks in the center. For practical reasons the FWPC (Section 4.5.1) is mounted directly behind the planar drift chambers in order to share the same gas mixture and maximise the geometrical trigger efficiency of the FTD. After the FWPC the particles traverse a transition radiator consisting of 400 polypropylene foils contained in its own gas volume. The transition radiation photons pass through a thin mylar window and are detected in the radial chamber which produces up to 12 accurate space points from ionization drift timing and charge division. To improve double track resolution the second and third radial modules are rotated by 3.75° and 2.5° (1/2 and 1/3 of a wedge) relative to the first. The interleaving of planar and radial chambers provides the optimum lever arm for momentum measurement.

The individual chambers were assembled and tested separately. The components for a single supermodule were installed into a three section tank consisting of aluminium outer cylinders ($\emptyset_{max}$ = 1700 mm) and glass free carbon fiber inner cylinders ($\emptyset_{min}$ = 243 mm, 4 mm thick, lined with Al foil), each tank section forming an independent gas volume and electrically isolated environment. Each chamber is bolted to the rigid central U-shaped outer cylinder using a set of precision dowels for alignment. Assembly was carried out on high quality surface tables with dimensional tolerances kept to $< 30\,\mu$m throughout the build sequence. After commissioning each supermodule on a cosmic ray test facility the three supermodules were then bolted together, separated by thin gas tight Kapton windows, and the end faces closed with stiff plates made from a sandwich of 1.2 mm thick Al alloy and 17.6 mm thick Nomex honeycomb [45]. The final alignment of the whole FTD was measured using cosmic rays after installation into the H1 experiment. Water at constant temperature (±1 °C) is circulated around each tank section through copper pipes in order to maintain dimensional stability and provide cooling for the preamplifiers. As well as maintaining the relative alignment of the tracker elements and support for the various services – water, gas, cables, preamplifiers, position monitors etc., the tank provides an electromagnetically sealed environment and serves as the common ground for the chambers. The HV and signal cables access the tracker volume via the outer cylinder using hermetically sealed feedthroughs where they are grounded. The HV cables are also filtered before entering the tank.

Three different gas mixtures are used, two working gases for the chambers and one purge gas for the transition radiation (TR) volumes. Gas is fed into each supermodule volume via the U-shaped channels in the outer cylinder, two feed pipes and one pipe for local pressure sensing, a total of nine pipes per supermodule. Gas tightness is maintained by rubber O-ring seals at the outer and inner flanges. The gas is supplied at atmospheric pressure from three computer controlled closed loop gas circuits (see Section 4.6) which maintain gas purity and provide the accurate pressure control, $\pm 10\,\mu$bar required in order to prevent damage to the fragile TR windows. During HERA operation the oxygen level in all volumes has been kept to < 50 ppm.

The whole tracker is mounted on four insulated feet and rests on the cryostat rails in stress-free condition. It is electrically isolated from the central tracker and the cryostat.

Parameter	unit	Radials	Planars
number of cells per supermodule		48	32
inner (outer) active radius	mm	150 (750)	$\approx$ 150 (750)
total number of sense wires (per cell)		1728 (12)	1152 (4)
sense wire diameter (resistance)	μm (Ω)	50 (450)	40
sense wire material		Stablohm[1]	W (Au plated)
sense wire spacing Δz (stagger)	mm	10 (0.28)	6 (0.30)
sense wire tension	N	1.75[2]	1.20[2]
total number of grid wires (per cell)		1584 (11)	2880 (10)
grid wire [Cu-Be(2%)] diameter	μm	125	125
grid wire tension (surface field)	N (kV/cm)	2.80[2] (170)	4.00[2] 135)
sense voltage	V	+2228	+1575
bulk (grid) field gradient	kV/cm	1.2 (-6.9)	1.0 (-5.0)
maximum drift distance (B = 0 T)	mm	50	28
drift velocity (B = 0/1.14 T)	mm/μs	$\sqrt{3} \times 37/37$	43.5/42
Lorentz angle (B = 1.14 T)	$^\circ$	45	41.8
z planar (x), module 0/1/2 [3]	mm	1324.4/1746.4/2168.4	
z planar (u), module 0/1/2 [3]	mm	1367.0/1789.0/2211.0	
z planar (v), module 0/1/2 [3]	mm	1409.6/1831.6/2253.6	
$z-$ radial, module 0/1/2 [3]	mm	1593.0/2015.0/2437.0	
$\sigma_{r\phi}(\sigma_r)/\sigma_{x,y}$ from track segments	μm (cm)	180 – 200 (3)	150 – 170
double track resolution	mm	2	2

Table 4.2: Forward tracker drift chamber parameters and positions.
[1] alloy from ref. [39]; [2] 60 % of the limit of proportionality; [3] position of first wire in plane.

4.3.1 Planar drift chambers

Each chamber is constructed as a self-supporting module containing 32 drift cells of identical rectangular cross-section with wire lengths between 460 mm and 1410 mm as shown in Figure 4.9. The chamber walls are formed from two circular discs with an outer diameter of 1.57 m and a central aperture of 280 mm diameter. They are composed of a low mass composite of Fibredux skinned Nomex honeycomb 3.4 mm thick, manufactured to be parallel and flat to within 100 μm. A 0.8 mm thick double sided printed circuit board carrying the drift field forming strips and voltage bus on opposite faces is bonded onto one side of the honeycomb laminate. the drift cells are defined by parallel sets of copper clad PCB's, 0.8 mm thick by 32 mm high, mounted perpendicularly and bonded at 57 mm intervals into precisely machined slots in the honeycomb panels, resulting in a multiple box section structure of high mechanical strength and rigidity. The vertical PCB's constitute the cathode planes and define the maximum drift distance as 28.1 mm (for B = 0). Each cell contains four sense wires uniformly spaced in z and staggered alternately 300 μm each side of the median plane of the cell. Each sense wire is surrounded by four grid wires Cu-Be arranged on a 6 mm square matrix. Significant benefits arise from the double grid design including reduced cross talk, lower wire tensions, improved cell isochronicity, and reduced grid wire surface fields. All wires are crimped under tension in pins which are held in position by means of high precision extruded Noryl templates at each end of the cell. The principal source of error in the wire position ($\approx$ 20 μm) arises from the inherent inaccuracies in the crimping technique. The cell ends are closed by PCB's containing electrodes which cleanly terminate the electrostatic field of the cell. Aluminium foils covering the outer surfaces and connected to the tank provide electromagnetic isolation between the individual planes. A set of precision dowels fix the relative orientation of each plane (to $<$ 0.06 mrad), the orientation of the planar supermodule with respect to the FWPC and the planar chamber/FWPC combination with respect to the tank.

The cell electric field distribution is controlled by seven different voltages: the sense voltage defines the gas amplification, the central strip voltage affects the sense field homogeneity, four drift strips and the cathode voltages determine the field gradient. The grid wires are grounded. All voltages are supplied directly from the HV supplies, after suitable fan out, without the use of resistor chains at the chamber. Field optimization and chamber operation are considerably aided by the fact that the double grid geometry produces a strong decoupling between the sense field (gas amplification) and the drift field. The operating conditions of the chambers for the gas mixture given in Table 4.6 are listed in Table 4.2.

The outer end of each sense wire is AC coupled into a current sensitive preamplifier (two drift cells per preamplifier) and the signals transmitted via 40 m of 50 Ω coaxial cable to the FADCs. Pulse profile (Q,t) analysis in the front end data acquisition system yields one drift time coordinate measurement perpendicular to the sense wire and one pulse integral measurement. Resolutions achieved on $e-p$ data are typically $150-170\,\mu$m for the single point spatial resolution and < 2 mm for the double track resolution.

4.3.2 Radial chambers

The radial wire drift chambers cover 360° in ϕ with 48 separate sectors of 7.5° width. Each sector is a drift cell having 12 sense wires staggered alternately 287 μm each side of a plane which bisects the sector. The sense wires, which are all parallel within one of these cells, are separated by 10 mm. Between adjacent sense wires, and positioned on the plane which bisects the sector, are field wires parallel to the sense wires and half way between them. All these wires are supported by crimp pins. At the small radius end (r = 152 mm), the crimp pins are mounted in a cylindrical Noryl hub, and at the large radius end (r = 760 mm), in Noryl templates precision bonded into the cylindrical wall of the composite structure which contains the whole 48 cells of the radial chamber as one rigid unit. The structure of these radial drift chambers has been described in references [46, 47, 48].

The wedge-shaped drift cells are separated from each other by cathode planes which consist of voltage graded copper strips on each side of thin paper-epoxy material (PCB technology). The electrostatic field cage for each drift cell is completed by voltage graded shaped conducting strips bonded onto the plane inner surface of the composite structure (for the high z end of the wedge), and onto a complex window assembly, described below, which is affixed as a lid to the composite structure (for the low z end of the wedge).

Detailed design of this window, forming the plane surface of the radial chamber towards low z was determined by the requirement to detect the transition radiation (TR) entering the radial drift chamber. The X-ray component of TR produced by an ultra relativistic charged particle contributes to an enhanced track ionization, hence to enhanced charge collected on one or more of the sense wires, provided that all ionization deposited anywhere in the cell is collected onto the sense wires and not onto field wires. The window of the radial chamber is thus designed to be as X-ray transparent as possible, and to ensure maximum X-ray detection efficiency as close as possible to it inside the drift cell. Because of the imperfect nature of the field grading close to the V shaped strips, ionization deposited within about 2 mm of the window cannot be collected onto the first sense wire. Such a loss of X-ray sensitivity is significant at the TR entry (low z) side of the radial chamber, where most of the X-ray photons photo-ionize the chamber gas. For this reason the V shaped strips to create the drift field are of aluminium on mylar and are supported on Rohacell [35] spacers which position them 5 mm from the thin mylar window which isolates the chamber gas volume. The effect of this window assembly on the electrostatics is to move the drift field inhomogeneities out of the sensitive gas volume. Then at the mylar wall closing the gas volume the drift field is uniform and parallel to the surface, except directly opposite the sense wire. Charging effects on the mylar window are then minimal,

and the ionization collection efficiency on the first sense wire is optimal right to the edge of the gas volume.

Because all the sense wires are in the radial direction, a coarse determination of the radial position of a track may be made from charge division if a wire is read out at both ends. However it is not physically possible to have preamplifier cards at the small radius end. For this reason the sense wires of one 7.5° sector drift cell are connected at the inner hub to the sense wires of another 7.5° sector drift cell, actually 105° away in azimuth, so that when sense wires are read out at the outer radius charge division is possible along this double length of radial wire. Current sensitive preamplifiers are at each end of these sense wire pairs, each channel of which drives approximately 40 m of cable to the FADC system. Pulse profile (Q, t) analysis gives the drift coordinate perpendicular to the sense wire plane, and two pulse integral measurements Q_L and Q_R from the two ends give the radial position by charge division.

The spacing in the z direction between the sense wires of the radial chambers, between the three modules, and the sets of planar drift chambers and the radial drift chambers may be seen from Table 4.2. Concerning the azimuthal position of the radial chambers, the plane which bisects a 7.5° sector cell (and about which the sense wires are staggered) is at $\phi = 3.75°$ in the first module, at $\phi = 7.5°$ in the second module and at $\phi = 6.25°$ in the third module. The resolution achieved with the 50 % argon, 50 % ethane gas mixture used so far is $150 - 200$ μm. The gas mixture which is intended to use for optimal detection of transition radiation is given in the following section.

4.3.3 Transition radiators

A passive array of polypropylene layers provides a sufficient number of dielectric interfaces for useful transition radiation (TR) X-ray emission. The dielectric constant, the layer thickness and the mark to space ratio of the polypropylene sheets determine the X-ray yield and the energy spectrum. For the values chosen the spectrum peaks around 6 keV for 20 GeV electrons. The interface between the TR and the radial wire drift chambers has been optimised for transmission of these X-rays. As described in the previous section the radial wire drift chambers are designed and operated both for optimal track point measurement and efficient X-ray detection. The combination of TR and radial wire drift chamber is designed for electron-pion discrimination, at the level of 90% electron acceptance with less than 10% pion contamination, up to 80 GeV for tracks passing through all three modules of the FTD. To achieve this, it is planned to operate the radial wire chambers with a gas containing xenon which has a high photoionization cross-section at 6 keV. A 20 % xenon, 40 % helium, 40 % ethane mixture satisfies the requirements of TR detection with acceptable charged track dE/dx ionization density, and also suitable drift velocity for the requirements of the drift chamber. Data taken with a radial drift chamber in a test beam at CERN have shown that the design discrimination between electrons and pions can be achieved with this gas [49, 50].

The assembly of polypropylene sheets is self supporting but is enclosed in its own gas envelope in order to isolate it from the gases used in the rest of the FTD. The helium-ethane mixture surrounding the polypropylene sheets is chosen to give the same partial pressure of helium as in the radial drift chamber. This is important because the interface is the thin mylar TR window of the radial drift chamber section which could be damaged by pressure differences in excess of about 100 μbar.

4.4 Drift chamber electronics, readout, and front end data processing

4.4.1 Introduction

All drift chambers in H1 are connected to one of the three independent branches of the central data acquisition system (CDAQ). The analog signals are digitized and processed in a number of

Chamber	Branch #	# of crates	# of channels	Raw data [Kbyte]	(Q,t) data [Kbyte]
Radial	5	9	1728	20.5	2.4
Planar	5	6	1152	28.5	4.1
CJC1 and CJC2	4	23	2640	33.2	5.4
COZ	4	1	96	3.41	0.5
CIZ	4	1	60	5.14	0.9
Forward muons θ	6	4	1024		

Table 4.3: Summary of drift chamber readout data.

front end crates, the trigger connection is based on the H1 standard subsystem trigger controller crate and interface cards and local logic produces and distributes control signals to the front end crates. A master crate collects the complete data from the branch and sends it to the CDAQ. Crates for local data monitoring can be added. Figure 4.10 shows the general layout of each drift chamber branch.

The drift chambers are distributed between the branches according to position in the detector. The inner and outer jet chambers and the inner and outer z chambers form branch 4 (CTD). The forward radial and planar chambers form branch 5 (FTD). The $\theta-$ and $\phi-$ chambers of the forward muon spectrometer form branch 6 (FMu). Table 4.3 shows the sizes of the various components, and the typical size of the zero suppressed digitizations (raw data) and processed summary data ((Q,t) data).

4.4.2 Operation of the readout

The analog signals from the preamplifiers mounted on the detector are received by 104 MHz FADC cards which continually digitize and store the data - at this point we are recording data at a rate of over 600 Gbyte/s over all drift chambers. On receipt of a first level trigger (L1) signal the digitization is stopped so that the data recorded in the FADC card memory includes, for each detector, all digitizations which could have occured between the time of the event and the maximum possible drift time for that chamber.

At a second level trigger (L2) signal the full 2.5 Mbytes of raw data for an event is copied by the scanner controller cards into the second level buffer at a speed of 3.3 Gbyte/s. At a third level trigger (L3) signal, the processor card in the FADC crate reads the data from the scanner, and writes an off-line format data bank into an intermediate buffer which contains blocks of significant, zero suppressed data with an event size of approximately 100 Kbyte. The output is written into a triple ported buffer memory on the intercrate connection (VIC8251 [51]). When a complete event is available from all front end crates the master processor collects the data from this buffer memory and writes the complete event to the multi-event buffer of the optical fiber VMEtaxi link (see Section 10.1.2).

4.4.3 Amplifier and FADC

The sense wires of the tracking drift chambers are connected to amplifiers either at one or at both wire ends. The eight-channel amplifier cards are mounted directly on the chamber vessel. The sense wire and the grounded potential wires serve as differential input. The sense wire is at positive HV and therefore it is coupled to the amplifier via a capacitor (1.5 nF). The sense wires (in some chambers) and amplifier are protected by a spark gap, and a pair of crossed diodes to

ground. Each amplifier channel consists of two stages of video amplifiers. The amplification is large enough so that no further amplification is needed on the readout card. This gives optimum noise rejection and minimises the influence of pick-up on the cable to the readout card. The amplifier card has two test inputs which allow the application of test pulse signals to the inputs of odd or even amplifier channels.

The 9520 signals from the drift chamber are digitized by F1001-FADCs [52]. The sampling frequency is 104 MHz, generated by an oscillator phase locked to the bunch crossing clock of the HERA storage ring of 10.4 MHz. The differential outputs of the amplifiers are connected to the FADC cards with multi-coaxial cable of about 28 m length. This cable also carries the power and test lines to the preamplifiers. The FADC-chips used have a resolution of eight bits [52]. The combined signal is fed to the FADC chip through a transformer eliminating DC offsets and via a resistor network that includes feedback of the input signal to the voltage reference, providing a non linear response with 8 bit accuracy for small signal amplitudes and a 10 bit dynamic range. Each FADC-chip is connected to one 256 byte deep memory which serves as circular buffer. During the active sampling phase of the FADC system signals are continuously digitized and stored in the memories. This recording process is stopped by a trigger signal that freezes the history over 2.5 μs in the memory. Sixteen FADC-channels are housed on one F1001-card and up to 16 F1001 cards are housed in a F1000 crate. It has a VME backplane used for fast 32-bit wide readout of the digitized signals from the FADC-memories. The signal risetime at the sense wire is a few ns. It is deliberately degraded by the amplifier band width, cables, and coupling transformer to 18 ns (20 % to 80 % of pulse amplitude) at the input of the digitizing FADC. This is the optimum for a time measurement with a FADC sampling at 100 MHz.

4.4.4 The scanner and the front end processor

In each F1000 front end crate there is an M1070 scanner card that acts as a sample controller for the FADCs, and provides fast readout and zero suppression of the FADC data. The scanner supplies the 104 MHz clock to the FADC cards, and at a L1 trigger gates this clock such that the circular buffers of the F1001 cards contain the required time segment. At a L2 trigger signal it copies the data from the FADCs into a local buffer in a series of synchronous bursts over the VME bus, in this way a transfer speed of 80 Mbyte/s is achieved, and the data for a full crate can be copied within the 800 μs requirement of H1. During the copy the data is compared with programmable thresholds and any significant transition (presently two subsequent time bins above or below threshold) is recorded in the hit table.

At a L3 trigger signal the scanner interrupts the front end processor (24 MHz FIC 8231 [53]) present in each F1000 crate. The interrupt handler reads the hit table from the scanner, calculates the required blocks of raw data, and copies these blocks into a multievent raw data buffer in an off-line format data bank. Each block includes four pre-samples before the hit starts to allow dynamic calculation of the pedestal, and blocks are merged in cases where a block would influence a subsequent block on the same wire. An output bank is written into a multievent output buffer in the memory of the VIC 8251 interconnect card, using the VSB bus connecting the processor and the interconnect, since the VME bus may be occupied by the scanner reading a subsequent event. The input raw buffer and output buffer both typically hold 30–40 events, and this allows derandomization over many events of the large range in processing times caused by localised high track density.

4.4.5 Determination of charge and time (Q, t)

The relevant parameters of a signal pulse from a drift chamber wire are signal timing (t) and the pulse integral (Q). These signal parameters are determined by a program which runs on the

L4 farm (see section 8.5). In this way the amount of raw data is reduced by a factor of about five. The zero suppressed data provided by the scanner are treated in several steps. For the CJC, CIZ, COZ and the radial chambers the first three steps consider the data of both wire ends separately, while the further steps use the combined information.

In the (Q,t)−algorithm the FADC data are first linearised. The leading edge of a new pulse is found by a search for a maximum in the difference of successive samples above the threshold. The average of the six digitizations before the pulse start is used to evaluate the pedestal to be subtracted from the pulse. Hits from the two ends of a wire are combined if the leading edges differ by less than or equal to two clock bins.

The essential information for the drift time determination comes from those electrons which arrive first at the sense wire and which are produced along the track in the region tangential to the isochrones. These electrons contribute to the sharp rise of the pulse, which is, however, smeared out by diffusion, chamber capacity, and amplifying electronics. The remaining off-tangential electrons arrive at later times and fluctuations of their ionization density influence only the trailing edge of the pulse, otherwise determined by the differentiating electronics.

The drift time is determined by chamber specific algorithms. For the CJC e. g. the time at half the full amplitude is determined by linear interpolation, averaged over both wire ends and used with the average risetime to extrapolate to the arrival time of the first electrons, taken at 10 % of the pulse amplitude. The average pulse consists of about 20 digitizations, while 10.4 MHz noise pulses extend typically over 5 bins and can therefore partly be rejected at the scanner level. The pulse integral is determined by summing some fraction of these digitizations. Most important for the CJC (and radial drift chambers) is the relative error of the integral for the $z(r)$ determination. It is minimised by choosing a rather short integration interval of eight time bins. The timings of the pulses from the two wire ends differ because of different cable length and signal propagation along the wire. Therefore the phase of the integration interval has to be properly adjusted in order to guarantee the integration over the same part of the pulse on both wire ends.

If a pulse is recognized on the tail of a previous one it is analysed after effects from the previous pulse have been subtracted on the two wire ends independently. For this subtraction a standard pulse shape is determined by averaging a large number of pulses, and then matched in phase and normalised in height to the preceding pulse.

4.4.6 Implementation

The subsystem trigger controller crate (STC, [54]) provides a standard interface to the central trigger electronics (see also Section 8.3.5). The STC in the DC readout is supplemented by a 104 MHz phase locked loop (PLL) card providing an accurate ($\pm$1 ns) clock and a logic card acting as sequence controller. Although responses from the scanner could by simple combination be used directly to respond to the central trigger, inclusion of the logic card in the path allows better overall performance by overlapping some stages of processing with refill and other delays of subsequent events. This places much of the response time of the DC systems in second or even third order dead time, and allows the DC systems to be run at almost full throughput with little or no actual dead time.

The master crate contains interfaces to the CDAQ (VMEtaxi link) and to other crates in that branch (VIC8251) consistent with the common H1 architecture (see Section 10.2.1). On startup, the master processor loads all other processors with code and data stored in non volatile ram. Once the other processors are running, all communication is made through the buffer memory of the VIC boards connected to each of the remote processors. During a run the master processor

operates asynchronously, waiting for an event to be signalled by the trigger processor, and then polling the front end processors until the complete event is ready to be built. The events are not buffered or processed by the master processor.

A monitoring crate provides access to the readout branch for chamber specific control and monitoring systems. A small fraction of the event data can be passed to the monitoring crate for local monitoring, especially that which requires raw data that might be unavailable in the CDAQ monitoring systems. Data is collected from a dedicated memory in the master crate using a differential VSB extension [55] – the VIC8251 connection is not used for technical reasons. Data may also be fed back from the monitoring system into the data stream, to allow important slow control information (e. g. HV, currents) to be recorded together with the event.

The drift chamber readout uses processors of the Motorola 68000 family throughout. These CISC processors are relatively easily programmed at the native instruction level, and all the readout code was written in assembler. By splitting the workload between many processors each fulfilling a specific task it has been possible to avoid the use of an operating system on any of the readout processors. This has minimised response times and maximised performance.

4.5 Proportional chambers

Between 5° and 175° the solid angle seen from the interaction region is completely covered by multiwire proportional chambers. Six independent planes in the forward direction, four in the central and also in the backward direction serve three different functions: to deliver a fast timing signal with a time resolution better than the separation of two succeeding HERA bunch crossings, to provide moderately accurate space points for charged particle track reconstruction at the first level trigger and lastly to add an accurate track element in the backward direction, where the drift chambers fail to provide enough space points.

The planar forward chambers (FWPC) are interspaced between the driftchambers of the FTD described above and are exposed to high particle rates increasing towards the beam pipe. Hence minimum overall thickness and minimal amount of material traversed, sufficient ageing prospects, and cathode pad size adapted to increasing rates near the beam pipe became the primary design criteria. These points do also apply for the two cylindrical chambers in the central region. The inner one (CIP) is closest to the interaction region and covers the largest solid angle. In order not to degrade the track reconstruction of the surrounding drift chambers, the CIP and its outer partner (COP), were fabricated with low mass materials and a narrow active gap. Since the main purpose of the FWPC, COP and CIP is to provide space points for the first level trigger, a pad segmented cathode readout was chosen with graphited surfaces as in other chambers built for high rates [56, 57]. From the reconstructed tracks the event vertex can be deduced and other detector data such as calorimeter and muon information can be validated. Since the trigger logic requests three space points per track, spurious background hits from uncorrelated noise and synchrotron radiation are removed.

In the backward direction the reconstruction of the scattered electron in low momentum transfer events calls for an accurate track segment. This is given by the signals from the four differently oriented anode wire planes of the backward chamber (BWPC). Several wires can be combined for triggering purposes. Standard planar chamber construction techniques sufficed here, since more than one radiation length of electronics and cables from the central tracker separate the BWPC from the interaction region. The BWPC covers the front surface of the backward electromagnetic calorimeter (BEMC) and hence also serves to discriminate electrons and photons.

The properties of all four chamber types are summarized in Table 4.4. The front end electronics and readout system is identical for all chambers.

	unit	CIP inner/outer	COP inner/outer	FWPC # 1/# 2/# 3	BWPC
active length $\Delta z/\Delta r$[3]	mm	2190	2172	583	515
active zone starts at z/r[3]	mm	-1125	-1107	167	135
mechanical length $\Delta z/\Delta r$[3]	mm	2254	2262	665	597
total length $\Delta z/\Delta r$[1,3]	mm	2467	2360	665	708
thickness $\Delta r/\Delta z$[3,6]	mm	21.5 (25)	30 (34)	40	52 (60)
chamber starts at z/r[1,3]	mm	-1376	-1270	135	110
position of first anode r/z[3]	mm	157/166	501/514	1451/1874/2297	-1423
number of anode planes		1	1	2	4[5]
number of wires		480	1574/1615	724	2496
wire separation	mm	2.1/2.2	2.0	2.5	2.5
gap width	mm	3.0	4.0	4.0	4.0
number of cathode pads		480	288	384	
cathode resistivity	kΩ/□	≈400	≈ 200	≈300	≈400
length of pad $\Delta z/\Delta r$[3]	mm	36.6	120	13 to 54[4]	
width of pad $\Delta\phi$	°	45	22.5	45 (22.5)[2]	
anode wire tension	N	0.63	0.60	1.5	0.98
plateau length	V	200/250	200	300	200
plateau starts at	V	2425/2375	2900	1900	2800

Table 4.4: Proportional chamber parameters. The separate columns for CIP and COP refer to the two planes, for the FWPC to the whole module containing two planes.
[1] Inclusive preamplifiers; [2] only for the four outermost of the 20 radial pads;
[3] first coordinate for CIP and COP, second for FWPC and BWPC; [4] width increases with radius, $\Delta r_i = 0.0782 r_i$, where r_i is the inner radius of the pad; [5] the anode wire of each successive plane are rotated by 45°; [7] in active zone (and at end flanges).

4.5.1 Forward proportional chambers (FWPC)

Each of the three chambers in the forward tracker volume consists of two wire planes interleaved with three cathode planes. The gap between the two adjacent cathode planes is 4 mm wide, as indicated in Figure 4.9. All chamber frames are made of glass fiber epoxy. To reduce the mass in the active area a laminated structure consisting of the following layers is used: 100 μm graphited mylar foil serving as cathode plane, 250 μm printed circuit board carrying 10 μm Cu readout pads, 3.3 mm Nomex [45] mesh, another 250 μm printed circuit board covered with 10 μm Cu for the strips leading from each pad to the preamplifiers on the chamber ends, a further 100 μm of graphited mylar foil in the central plane or aluminized mylar foil on the external planes for electromagnetic shielding. The graphite layers are produced by spraying a mixture of DAG 5466/DAG 213 [58] at 5 bars giving an initial surface resistivity of 1 MΩ/□, which was reduced to 300 kΩ/□ by polishing. Each chamber is strengthened by a backplane, 12 mm thick, with two layers of 250 μm glass fiber epoxy sandwiching 11.5 mm Nomex. The overall thickness is 1.7 % of a radiation length. The mechanical tensions of the wires and the foils are supported by 24 and 8 axial rods on the external and internal frames, respectively. The anode planes contain gold plated tungsten wires (Ø 25 μm) spaced by 2.5 mm. They are crimped on pins fixed on the frames. Each wire is connected to the following one through 1 MΩ resistors and to ground through 330 nF capacitors. Groups of 15 wires are connected to separate HV lines, which allows degrading of malfunctioning sectors if necessary. The cathode pads are ring shaped and cover an azimuthal angle of $\pi/8$ each, except for the four outermost of the 20 rings where they cover $\pi/16$. The radial pad width increases with radius in geometrical progression from 18 to 37 mm. Two consecutive cathode planes are offset by one half of a ring, such that the effective polar angle resolution is halved: $r_{min,i+1} = r_{min,i} \times 1.0382$ with $167.5 \leq r \leq 750$ mm.

The Pluto gas mixture (see Table 4.6) was chosen, because the FWPC share their gas volume with the forward drift chambers and transition radiation detectors.

A track crossing all three or at least two modules of the FWPC has to fall into the polar angle range $6.6° \leq \theta \leq 18.0°$ or $5.1° \leq \theta \leq 21.6°$, respectively. For such tracks an effective timing resolution of 20 ns (FWHM) and 47 ns (base width at 10 % of the maximum) was measured using H1 data, well below the required resolution to separate two bunches.

4.5.2 Central proportional chambers

4.5.2.1 CIP The laminar structure of the CIP called for special construction techniques which are described in detail in reference [59].

The double layer of chambers consists of three concentric cylinders. During construction each chamber cylinder was formed on a steel mandril milled to a precision of 25 μm over the full length. The innermost layer of the first cylinder, a 25 μm thick Al-foil provides the electromagnetic shielding. The next layer – 2 mm thick Rohacell foam [35] glued onto the Al-foil with 20 g/m^2 epoxy-glue [60] – gives the chambers the necessary rigidity. The Rohacell surface was polished, and a second 25 μm Al-foil glued to it served as the inner cathode. After cutting the cylinder to the right length the Al-foils were connected to Cu-foils, at the ends and the glass fiber epoxy [27] end flanges were added. These carry the printed circuit boards for the anode wires, which are supported further by glass fiber epoxy rings at 1/3 and 2/3 of the chamber length. The active gap is 6 mm wide. The anode wires (gold plated tungsten, Ø 25 μm) were transfered to the axially prestressed cylinder from planar frames.

The middle cylinder forms the outer cathode of the inner chamber and the inner cathode of the outer chamber. Here the innermost layer, a 20 μm Kapton foil is coated with high resistive graphite (400 k$\Omega/\Box$) on one side and 0.5 μm Al on the other side. The Al layer is segmented into pads on which the induced charge on the cathode is collected. The graphite layer in front guarantees a fast disappearance of the accumulated ion charge. This has the advantage, that the readout wires of the pads can be mounted outside the gas volume. After several tests on prototypes [59] the graphite layer in the final chamber was produced by spraying a mixture of DAG213, DAG305 [58] and isobutylmethylketon (IBMK) in a ratio of 20 : 1 : 7 onto the Kapton foil with 3 bar. The cathode foils are again backed by 2 mm Rohacell. The readout wires (150 μm Al) are embedded into 250 μm deep grooves in the Rohacell running along the $z-$axis from the chamber end ($-z$ side) to a hole centered over the pads. The wires were contacted onto the pads with silver paint and soldered at the flange end. Another 20 μm thick Kapton foil with Al-coating is glued onto the Rohacell, which forms together with the wires a wave guide of $\sim 70\ \Omega$ impedance. The Kapton foil again backed by 1 mm Rohacell with a polished surface is covered by another 25 μm Al foil serving as the cathode for the outer chamber. End flanges and connections are similar to those of the first cylinder and the sequence of layers for the third cylinder is identical to that of the second.

Gas sealing is provided by two O-rings at the end flanges (2 mm Ø). The overpressure in the chambers has to be kept small and needs to be monitored carefully in order not to distort the gap. The two chambers have independent gas distributions and are rotated by $\pi/16$ in ϕ with respect to each other, thus halving the eightfold segmentation of each chamber at the trigger level by requiring coincidence of two planes. In z there are 60 pads of 36 mm width in each ϕ sector.

With the gas mixture given in Table 4.6 the single pad efficiency measured in a test beam was 99 %, while at HERA 94 $\pm$ 2 % was measured with extrapolated jet chamber tracks. From the measured pulse height distributions the gap variations for this light chamber were deduced to be

less than 0.2 mm. The measured test beam time resolution (FWHM 21 ns) compares well with the results at HERA. This result converts into a 2 % probability to register a given pad with the wrong (neighbouring) bunch crossing. The probability for crosstalk, i.e. the probability to register signals also in neighbouring pads in z and ϕ and the inefficiencies across the pad boundaries are discussed in detail in reference [59]. The average number of active pads for crossing angles larger than $\theta = 40°$ in a test beam (1.4) compares well with what is observed at HERA.

4.5.2.2 COP The construction of the COP follows closely that of CIP in those aspects concerning the sandwich structure (see Figure 4.11). Steel mandrils machined to a precision of 60 μm and appropriate to the larger chamber radii were used. To improve the stability of the sandwich structure, the thickness of the core material (Rohacell) was increased to 4 mm. The graphite cathodes (7 m^2 area per chamber) are produced with a screenprinting technique using a resistor ink solution, rather than spraying . The ink [61] has a resistivity of 170 K$\Omega/\Box$ for a 15 μm layer and was diluted with a solvent monobutylic ether of ethylene glycol in a ratio of 1 : 3. A surface resistivity of 200 K$\Omega/\Box$ was obtained after polymerization at 120 °C during 1 hour. The cathode pad structure is provided by gluing patches of 25 μm Kapton coated with 1 μm Cu to the back side of the graphite cathodes, giving an 18–fold segmentation in z and 16–fold segmentation in ϕ. The cathode layer is backed by 3 mm Rohacell, in which 50 μm diameter Cu wires are embedded. A 25 μm Kapton foil coated with 1 μm Cu put on top of the previous layer constitutes with the copper wires the transmission line that carries the chamber signals to the $-z$ end of the chamber. This layer is then backed by 2 mm Rohacell. The Vetronite (G10) end flanges of the chamber support the printed circuit boards to which the anode wires ($\approx$ 1600 per chamber) are soldered and assure the 8 mm chamber gap size. They form the only rigid structure to which the gas distribution and preamplifiers are connected. The three cylinder sandwiches are assembled in vertical position. Pulse height measurements showed that the gapsize variation is of the order of 0.3 mm [62].

Despite its three times larger radius the COP is only moderately thicker than CIP (0.18 % radiation length instead of 0.14 %). The efficiency plateau is reached at 500 V above the CIP plateau with the same gas mixture, a consequence of the larger gap. While in test beams CIP and COP behaved similarly, at HERA the noise level in COP is slightly higher due to more difficult grounding. This requires a higher threshold setting and leads to a typical efficiency of 92 $\pm$ 2 %. The timing resolution is similar to that of the other chambers.

4.5.3 Backward proportional chamber (BWPC)

The BWPC is equipped with five graphited cathode planes (50 μm Mylar foil) and four anode wire planes. It is the only chamber in H1 in which the cathodes are not segmented and the anodes are read out. The graphite coating was fabricated with the same technique as described for CIP. The wires and the foils are stretched between a 23 mm wide inner and a 67 mm wide outer ring of glass fiber epoxy (G10). These rings are 4 mm thick and sustain the active gap of 8 mm per chamber, as indicated in Figure 4.12. The wires are strung every 2.5 mm, but signals from two neighbouring wires are fed to one preamplifier. The wire orientations are vertical, horizontal and $\pm 45°$ for the four layers. Gas sealing and structural support for the assembly is provided by G10 front and back planes of 10 mm thickness milled down to 6 mm in the active zone. The latter starts at an inner radius of 135 mm and ends at 650 mm, while the whole chamber occupies the region betweenn $r = 110$ mm and $r = 818$ mm. The BWPC therefore covers polar angles of $174.5 \geq \theta \geq 155.5°$. The space points given by the BWPC contribute 0.5 mrad to the angular resolution, of the same order as the multiple scattering in the material in front of it. For high energy electrons an efficiency of 87 % per plane was measured from extrapolated CJC chamber tracks. When requiring three out of four planes to be hit in coincidence with the BEMC an efficiency of 98 % is obtained.

4.5.4 Proportional chamber electronics and readout

Preamplifier		Amplifier–Shaper	
Differential gain	65 nV/e	Max. differential gain	400
Rise time (10–90)%	2 ns	Rise time	9 ns
Fall time (10–90)%	20 ns	Pulse width (FWHM)	16 ns
Input impedance	64 Ω	Max. output voltage	3.2 V
Output load	2 × 50 Ω	Overload recovery:	
Dynamic range	± 300 mV (≈ 10^7 e)	$V_{in} < 5 \times V_{in,sat}$	70 ns
Power supply	± 3.5 V (22 mW)	$V_{in} = 30 \times V_{in,sat}$	170 ns
Size	25 × 10 × 2 mm^3	Power supply	+5, -5.2 V (320 mW)
		Size	36 × 3 × 6 mm^3

Table 4.5: Characteristics of the MWPC preamplifier and amplifier–shaper.

A schematic picture of the frontend electronics is shown in Figure 4.13. The cathode pad signals (CIP, COP, FWPC) and anode wires (BWPC), respectively are preamplified directly on the chambers. A differential signal is then transmitted through a 35 m long cable to the electronic trailer. Each cable contains 16 signal pairs and is connected to a receiver card containing shaping amplifiers, followed by discriminators with computer controllable thresholds. The characteristics of the preamplifier-shaper chain are listed in Table 4.5. The overall gain can be adjusted to chamber pulse height between 1.3 μV/e and 26 μV/e by means of a resistor on the receiver card. A typical equivalent noise charge is about 3800 e, for a chamber capacity of 60 pF.

The digitized signals are synchronized with the HERA clock and stored in a pipeline constructed from the same gate arrays as used in the muon system (see Section 6.1.4). Upon a first level trigger decision (L1-Keep), the pipeline clock is stopped. A second level trigger decision (L2-Keep) then initiates the data readout. The synchronized pad signals are furthermore made directly accessible to the $z-$vertex and forward ray trigger (see Section 8.3.1.3). Test registers allow controlling the readout and trigger chains.

The MWPC readout system, an independent branch (# 7) of the H1 data acquisition system (see Figure 10.3), is responsible for reading 3936 channels, originating from 270 receiver cards in 15 crates, and some decision data from the two first level triggers. In addition to the frontend crates, the system consists of two standard VMEbus crates and one STC crate [54] in a configuration common to all H1 subsystems (see Section 10.2.1).

The frontend crates are equipped with a customised 'EasyBUS', which is essentially a simplified 16 bit wide VME bus with a 64 kWord address space lacking any interrupt capabilities but with added analog and ECL signal lines. The latter are used to distribute the clock and L1-Keep signals. The analog lines allow measuring the digitization thresholds loaded to the discriminators through an ADC located on a crate controller (CC) card. The primary task of the CC's is however to connect the crate to a branch driver card (BDC) residing in the master VME crate. The BDC-CC combination maps the EasyBUS address space into the VME frame [63].

Each BDC is directly connected to the STC and contains a DMA (direct memory access) controller and a 4 Kbyte deep FIFO (first in, first out) buffer. An L2-Keep signal can thus initiate a frontend data transfer to the master crate without processor intervention. The maximum transfer speed is 4.5 Mbyte/s. Each of the six BDC's installed in the MWPC area can control eight frontend crates. The latter are grouped into pairs to make use of the 32 bit wide data path of the VME bus. To optimise readout speed, between two and six crates are connected to one BDC.

The first order dead time is determined by the front-end transfer to the BDC as long as the BDC FIFO are not saturated. The saturation rate is given by the average time spent by the data acquisition processor per event. Details of the data acquisition program are available in references [63]. An average time of 4.2 ms per event is needed. This corresponds to an average of 237 hits in 10 bunch crossings.

4.6 Gas systems

To operate the nine different tracking detectors nine separate gas circuits are necessary, with different gas mixtures, flows, and demands on purity and overpressure control. For the forward chambers and CJC closed circuits are used while CIZ, COZ, CIP, COP and BWPC are flushed with premixed gases in open circuits. The main parameters of the gas systems are given in Table 4.6.

Detector	Gas volume	Gas mixture + additives: volume ratio	Pressure relative to atmosphere		Flow rate		System
			typ.	max.	typ.	max.	circuit type
	[l]	[%]	[hPa]		[l/min]		
Planars+ FWPC	~900	$Ar/C_3H_8+C_2H_5OH$ (90/10)+1	0.15±0.10	1	1.3	3	I closed
Radials	~700	Phase I: Ar/C_2H_6 (48/52) Phase II: $Xe/C_2H_6/He$ $+C_3H_7OH$ (20/40/40)+1	0.15±0.10	1	1.0	2	
Radiators	~500	He/C_2H_6 (60/40)	0.25±0.10	1	0.1	1.5	open
CJC1	~1140	Phase I: $Ar/CO_2/CH_4$ (89.5/9.5/1)	1.5±0.5	5	1.5	3	II closed
CJC2	~3080	Phase II: $Ar/C_2H_6+H_2O$ (50/50)+0.5	1.5±0.5	5	4.5	9	
CIZ	~55	$Ar/C_2H_6+H_2O$ (70/30)+0.2	0.15±0.10	1	0.1	0.6	III open
COZ	~240	$Ar/C_2H_6+C_3H_7OH$ (48/52)+1	0.15±0.10	1	0.2	0.8	
CIP	~30	Ar/C_2H_6/Freon12$+H_2O$ (49.9/49.9/0.2)+0.2	0.15±0.10	1	0.07	0.6	
COP	~150	Ar/C_2H_6/Freon12 (49.9/49.9/0.2)	0.15±0.10	1	0.1	0.6	
BWPC	~120	Ar/C_2H_6/Freon12 (49.9/49.9/0.2)	0.15±0.10	1	0.1	0.6	

Table 4.6: The different circuits of the gas systems.

4.6.1 Gas circuits

The simplified diagram of the gas circuit of the planar chambers shown in Figure 4.14 illustrates the typical features of the gas systems. The system is distributed over three levels, the supply outside the H1 hall, the control room on the first underground floor and finally the distribution rack on top of the electronics trailer near the detector. At the latter point the gas inlet flow for each detector is adjusted by mechanical flow meters and for some chambers split into several

streams for further distribution as shown in Figure 4.14. The static pressure of chambers relative to atmosphere is measured with sensors in the μbar range. In order to avoid too large hydrostatic pressure differences between chambers and sensors, the latter are also located at this point.

From the inlet manifold either pure or premixed gases can be fed into the circuit. Flushing is done by gently filling helium or argon via the two flow meters FL1-1 and FL1-2 into the chambers, while the chamber gas at the same time is sucked out by the membrane pump CP1-1. To hold the chamber pressure during the whole operation within adjustable tolerances of about ± 100 μbar, the solenoid valves SV1-2 and SV1-3 will be either opened or closed depending on the actual pressure inside the detector. As seen from Figure 4.14, the ingoing and outgoing flows of the chamber gas are split into two paths, one of them containing instruments for continuous gas analysis like infrared meters, a hygrometer and a gas chromatograph in combination with an oxygen trace analyzer. The filling of the chambers proceeds in a similar way as the purging either with premixed gas or by introducing approximately the right proportions of first the non-flammable and later the flammable gases. Then inlet and vent valve are closed and the circuit is switched from the open to the closed mode. The gas circulates through the barrel, the purification units, if needed, through an alcohol or water bath, and through the chambers. Since the purification units absorb part of the gas components, particularly hydrocarbons, a readjustment of the mixture is necessary after typically one day of circulation. To maintain the correct mixture gas can be added to the barrel manually. Repeated circulation for several days, especially when additives like water or alcohol are used, leads then to a homogeneous gas mixture constant in time.

So far three types of additives are used. Some mixtures contain 0.2 % Freon 12 as one of the components of the premixed gas. To other delivered mixtures alcohol (typically 1 %) or water (typically 1000 ppm) is added by passing the gas over a bath of the cooled or frozen liquid stored in a refrigerator in temperature controlled reservoirs. The admixture is adjusted by varying the bath temperature.

4.6.2 Purification and analysis

The closed loop circuits are supplied with purification units for removing oxygen, water and low concentrations of higher organic compounds. For oxygen removal 2 kg BTS-catalyst R3-11 [64] in the reduced state is used as an absorption agent and oxygen levels as low as 20 to 40 ppm have been reached over long time periods. Optimal oxygen removal is obtained with catalyst temperatures of 100 °C to 150 °C. However in the case of ethanol admixture, as is foreseen for the planar chambers, the alcohol will be cracked [65, 66]. Working at temperatures below 80 °C circumvents this problem at the cost of a lower oxygen capacity for the purifier of only about 6 to 15 l [O_2/kg (catalyst)]. A similar problem arises when isopropanol is added to the chamber gas, which is recommended for Stablohm wires and the radial chambers [46, 67]. Since the isopropanol molecule is more fragile than the ethanol molecule, it is cracked even at room temperature into hydrogen and acetone by the catalyst [68]. Use of other O_2-purifiers working at low temperature like Oxisorb [69] and palladium-catalyst [70] give similar problems with alcohol-additives, especially with isopropanol, so that up to now isopropanol could not be used in the closed circuit of the radial chambers.

At room temperature water and higher organic compounds are removed by a mixture of 1.5 kg 3 Å and 0.5 kg 5 Å molecular sieves. In case of water or ethanol additives the molecular sieve eventually saturates, but it is still capable of removing other impurities. Both, molecular sieve and BTS-catalyst are regenerated twice per year or whenever necessary.

Continuous control of gas composition is necessary for constant operation. Infrared meters, dedicated to a certain gas type, but with some sensitivity left for the gas additives give permanent

information on changes. Hygrometers in the ppm-range and an O_2-trace analyser allow an early detection of leaks. Complete analysis of the gas composition is performed by an automatic gas chromatograph station, routinely switched into the different circuits. Independently of the use of calibrated gases this instrument gives the different gas portions to an accuracy of ± 2 % of the measured value with an overall sensitivity of about 300 ppm [71, 72].

4.6.3 Electronic control and safety

The concept of the H1 gas system control follows the solution chosen for L3 time expansion chamber (TEC) [73, 74]. A Motorola 68000 CPU serves as a crate master, integrated into a VME-system with the necessary resources for monitoring, logging and control equipment. The instantaneous values of all analog outputs of the measuring devices, especially those for pressure and temperature, but also those for supply voltages are controlled within preset limits. Warnings or alarms are generated if one of the relevant parameter values is exceeded. In case of an alarm the gas circulation is stopped and the HV supplies of the detectors concerned are switched off. A computer independent hard wired logic with a more generous alarm setting protects the chambers against destruction in case of program failures or other accidents. In this case also an alarm is generated and the powerless open solenoid valves in the distribution rack on top of the electronic trailer connect the chambers with an argon flushed reservoir at atmospheric pressure as indicated in Figure 4.14. A set of four independent serial links per gas system monitors all gas parameters and distributes this information to the slow control system (Section 9).

Gas sensors are distributed in the H1 detector region, on the electronic trailer with the distribution rack and in the volume occupied by the trackers, as well as in the rooms where flammable gases are handled.

The tracker volume is flushed with $\simeq 12$ m^3 of nitrogen gas per hour to prevent accumulation of flammable gases in case of a leak. Since the operational pressure of most chambers is as low as 0,15 hPa relative to atmosphere and only 1.5 hPa in case of CJC, the amount of gas which may escape through a sudden leak in the chamber region is at most only a few liters. Small continuous leaks are best controlled in the closed loop circuits by measuring the pressure drop in the barrel over several days. The maximum working pressure in these circuits is limited to 1.6 bar absolute. A typical leakage of about 4 l/day corresponds to a pressure drop of $\sim$40 hPa/day. In the open circuits additional electronic flow controls, in series with FL1-1 and FL1-2, restrict the input flow. In case of a major leak the operational chamber pressure cannot be reached with the low flux adjusted by these controls.

4.7 Scintillators

Both scintillator arrays discussed in this section are located in the backward region (see Figure 2.2) and have been installed to reject proton beam associated background at the first trigger level. The present life time of the stored proton beam in HERA during collisions varies between 10 and 48 h. The stored proton current design value is 160 mA with 2×10^{13} circulating protons in total. These protons are lost by beam gas and beam wall interactions producing background showers of energetic penetrating hadrons and halo muons. With a beam life time of 10 h the H1 sensitive detector volume is hit by this background with a frequency of 2.6 MHz.

4.7.1 Time-of-flight counters

The time of flight hodoscope (ToF) consists of two planes of 3 cm thick NE102A scintillator mounted perpendicular to the beam pipe upstream of the interaction region. Particles from

proton induced background and from $e-p$ collisions are separated in time at this point by ~ 13 ns. The electron bunches have negligible size whereas the proton bunches are spread over 2 to 3 ns FWHM. The plane nearest to the interaction point (ToF1) lies at $z = -1.95$ m and has 16 butted counters, measuring 317×317 mm^2 thus matching the size of four BEMC stacks. The outer plane at $z = -2.25$ m consists of eight larger counters (317×634 mm^2).

In order to operate inside the 1.14 T field, ToF utilises 24 Hamamatsu R2490-01 high field photomultiplier tubes (PM). It is necessary to mount them perpendicular to the planes of ToF, requiring a light collection countersink to be machined into one of the large faces. A corresponding perspex truncated cone is glued to the other side to match the PM sensitive area. The PM's themselves are housed in non-magnetic holders and held in contact with the small light guide by springs.

Each wall of ToF is made up of a sandwich of scintillator and lead (Figure 4.15), mounted on a backing plate of non-magnetic steel to minimise stresses from the large magnetic field. The lead is 6.5 mm thick to absorb synchrotron radiation. Steel is used rather than aluminium to minimise eddy currents produced during a magnet quench.

The six inner counters (four on ToF1, two on ToF0) can be moved horizontally up to 20 cm from the beam pipe using computer controlled pneumatic rams. This removes them from the high radiation fluxes around the beam pipe during injection. With the counters in the open position, ToF can be split in half about the horizontal axis, allowing removal without breaking the vacuum in the beam pipe.

Signals produced by the PM's are amplified ($\times 40$), up to ~ 1 V before travelling down 29 m of cable to a NIM logic located in the electronics trailer. Here the signals are discriminated and strobed in three time windows: background, interaction and global, which are used in the first level trigger decision (see Section 8.3.1.1) available after 250 ns. The device as a whole has a resolution of 4 ns, while individual counters have a resolution of the order of 2 ns. The timing information of all counters is available in the event readout chain.

The setting and width of the time windows greatly affects the performance of ToF, and they are continually updated as offline analysis proceeds. The background window currently starts 18 ns before the centre of the background distribution, and is 25 ns long. The interaction window starts 1 ns after the background window ends and is 13.1 ns long (Figure 4.16). A constant background of cosmic ray hits is present, about 200 entries per bin. Triggers in the interaction window are in fact much dominated by synchrotron radiation.

4.7.2 The veto wall

In addition to the ToF device two double scintillator veto walls are installed at a distance of 6.5 and 8.1 m, respectively upstream from the interaction point (Figure 2.2).

The smaller inner veto wall covers the near beam area (100×90 cm^2) down to a radius of 11 cm (Figure 4.15). The four scintillator pairs (NE 114, thickness 6 mm) are read via two photomultipliers (56 AVP, VALVO) each. The pairs are shielded against electromagnetic showers by lead walls of 4 cm thickness. Penetrating particles are then identified by coincidences between two scintillators with a time resolution of $\pm$ 3 ns. The large outer veto wall with an area of ca. 5×4 m^2 overlaps the inner veto wall and nearly all of the liquid argon calorimeter. The array of 10 counter pairs of up to 2.1×0.90 m^2 area each (Figure 4.15) is grouped around the last upstream HERA quadrupole with a 0.8×0.8 m^2 sized hole. The scintillators (NE 110, 1 cm thick) are coupled to 20 5 inch phototubes of type VALVO XP 2041. These tubes are shielded with thick iron tubes and μ - metal cylinders against the magnetic fringe field (≈ 10 mT).

An iron wall of 5 cm thickness separates the scintillator pairs of the outer wall. The coincidence resolution of such pairs is $\pm$ 8 ns. It is dominated by the light path differences over the large area. The light attenuation length is measured to be larger than 1.5 m and leads to inefficiencies for the detection of minimum ionizing particles of $< 10^{-5}$. (see also references [75, 76, 77]). The time resolution achieved allows a clear time separation between the background of the passing proton beam and event correlated hits during e-bunch passing. A 3 m concrete wall separates the outer veto wall from the main detector and protects it against low energy showers from upstream.

Amplitudes, signal arrival times, rates and efficiencies of all counters are monitored online, and this information is used to study the background condition after each filling and during runs. The time of flight information allows to measure the z position of the $e - p$ interaction point online with a precision of ca. 30 cm. It is used in the first level trigger (Section 8.3.1.1), and is sent to the central data acquisition system for off-line analysis.

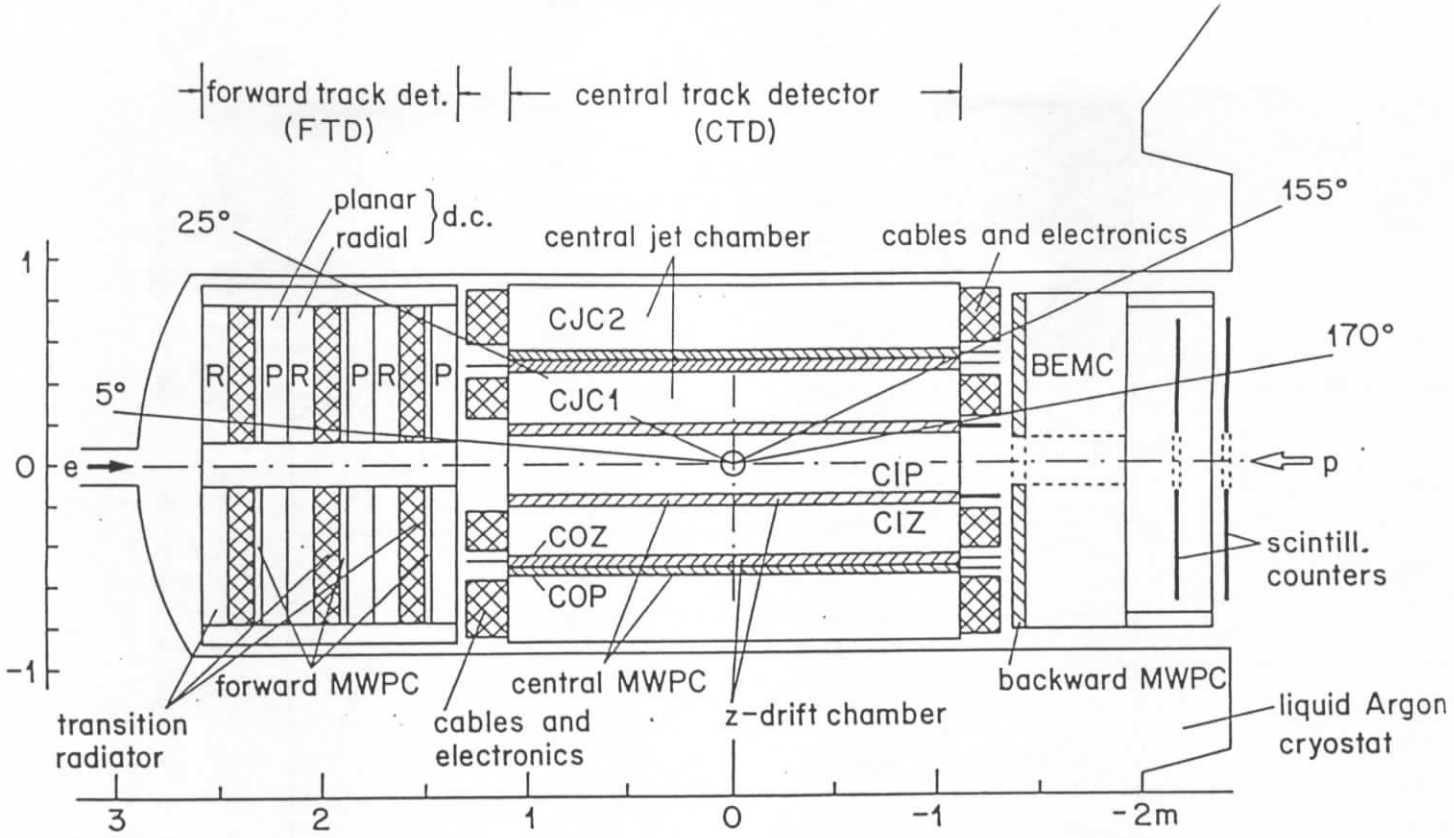

Figure 4.1: The H1 tracking system ($r - z$ view)

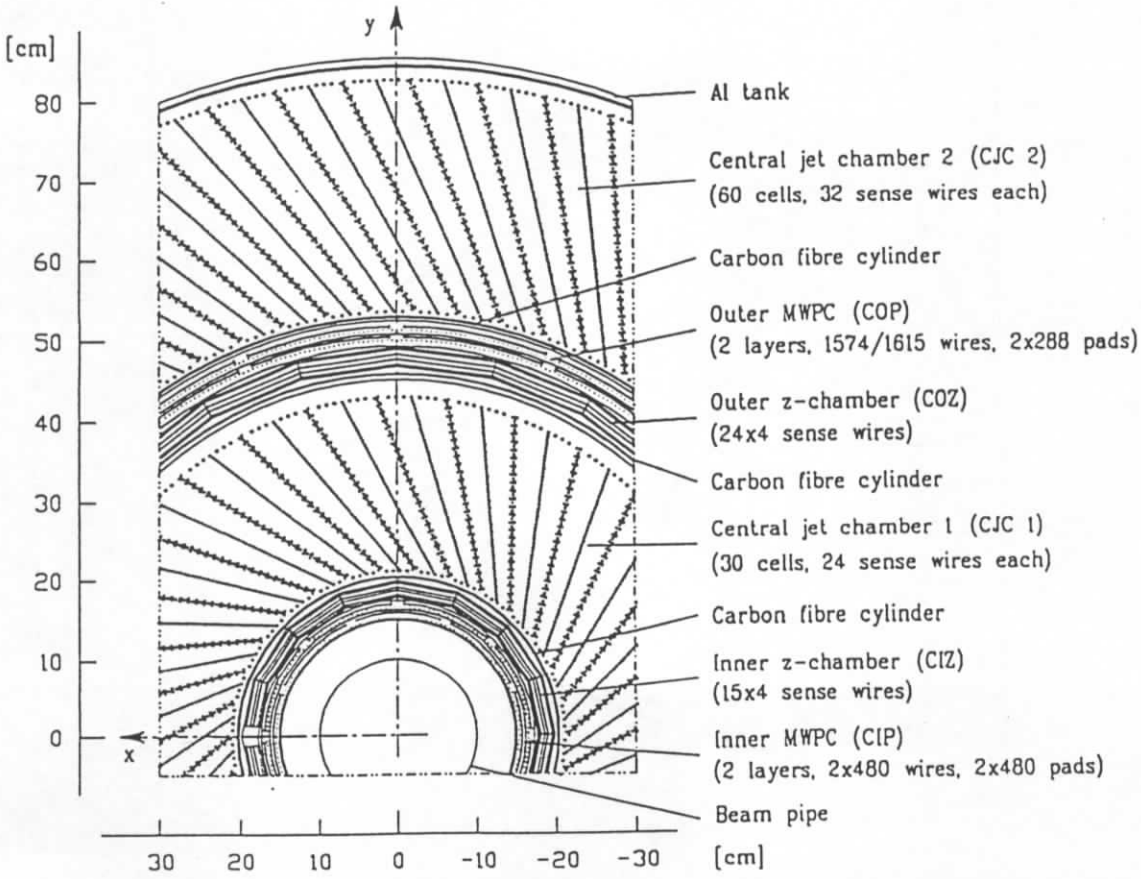

Figure 4.2: Central tracking system, section perpendicular to the beam

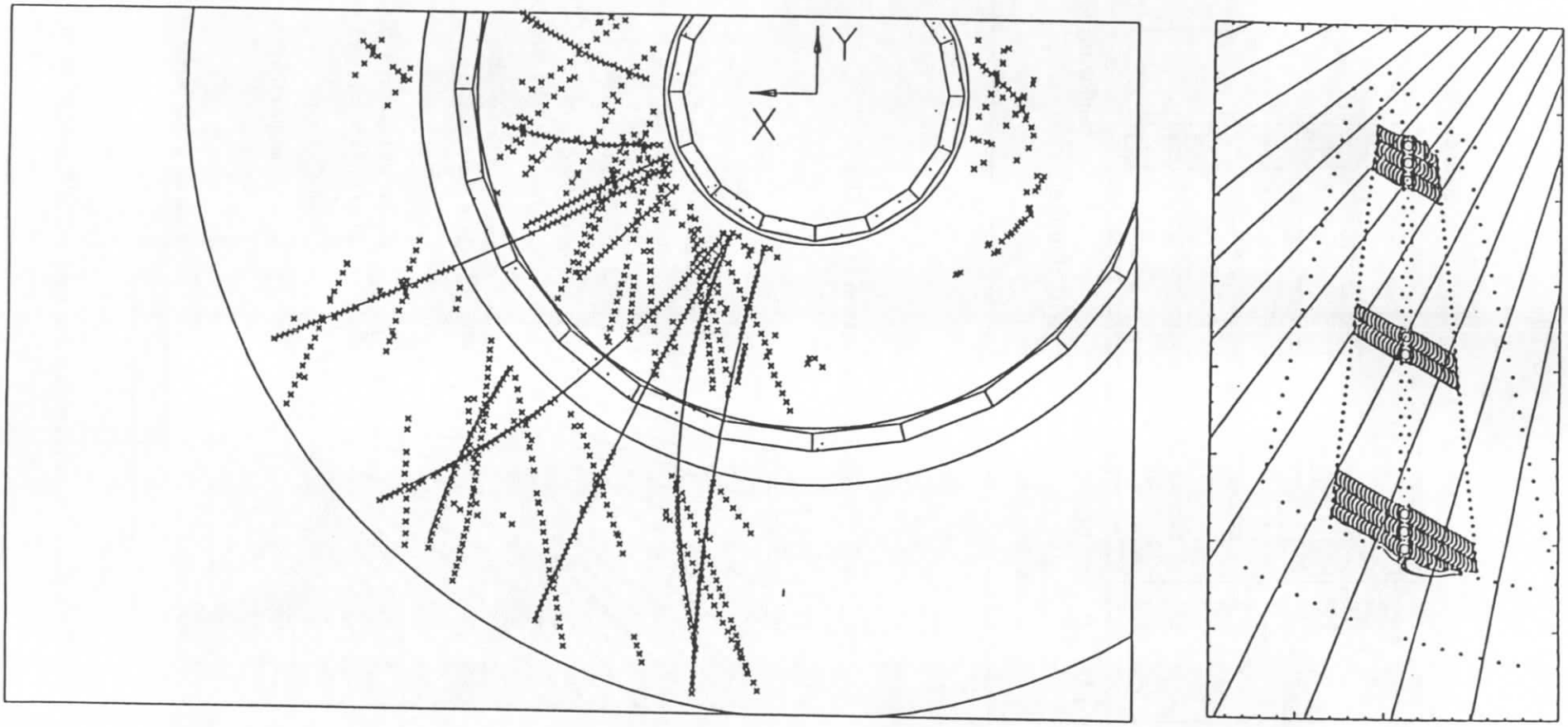

Figure 4.3: Left: Electron-proton scattering event as seen in the CJC showing tracks found by the pattern recognition program and mirror tracks. Right: Simulation of a CJC cell indicating the drift regions of the senses wires, drift lines and isochrones. The straight lines represent infinite momentum tracks from the beam axis.

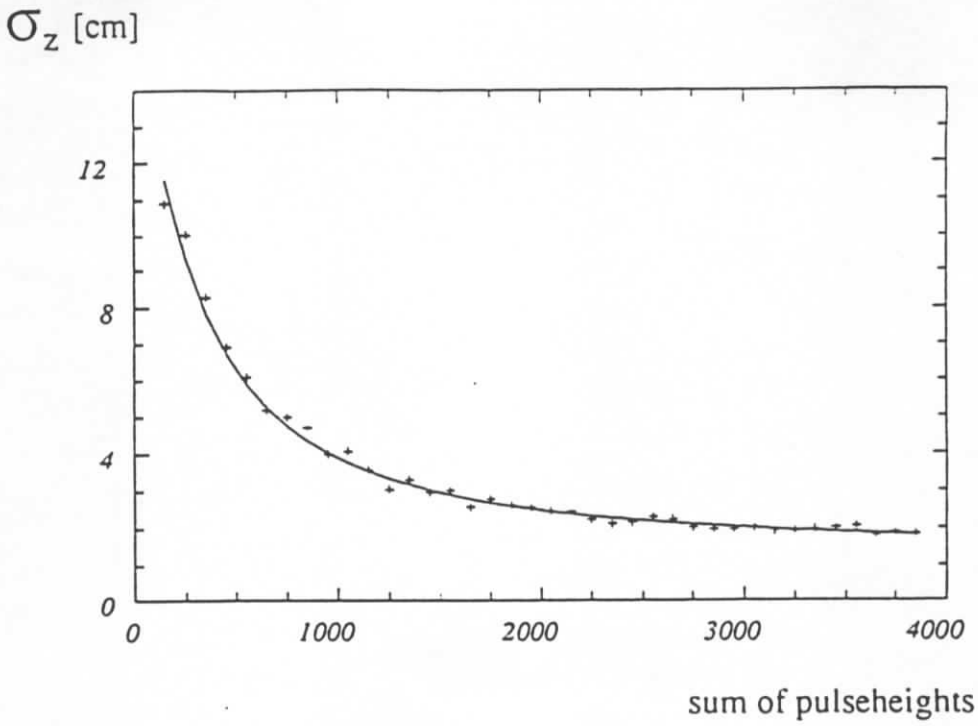

Figure 4.4: Dependence of the CJC $z-$resolution on the amount of ionization. A minimum ionizing particle deposits typically 1000 counts.

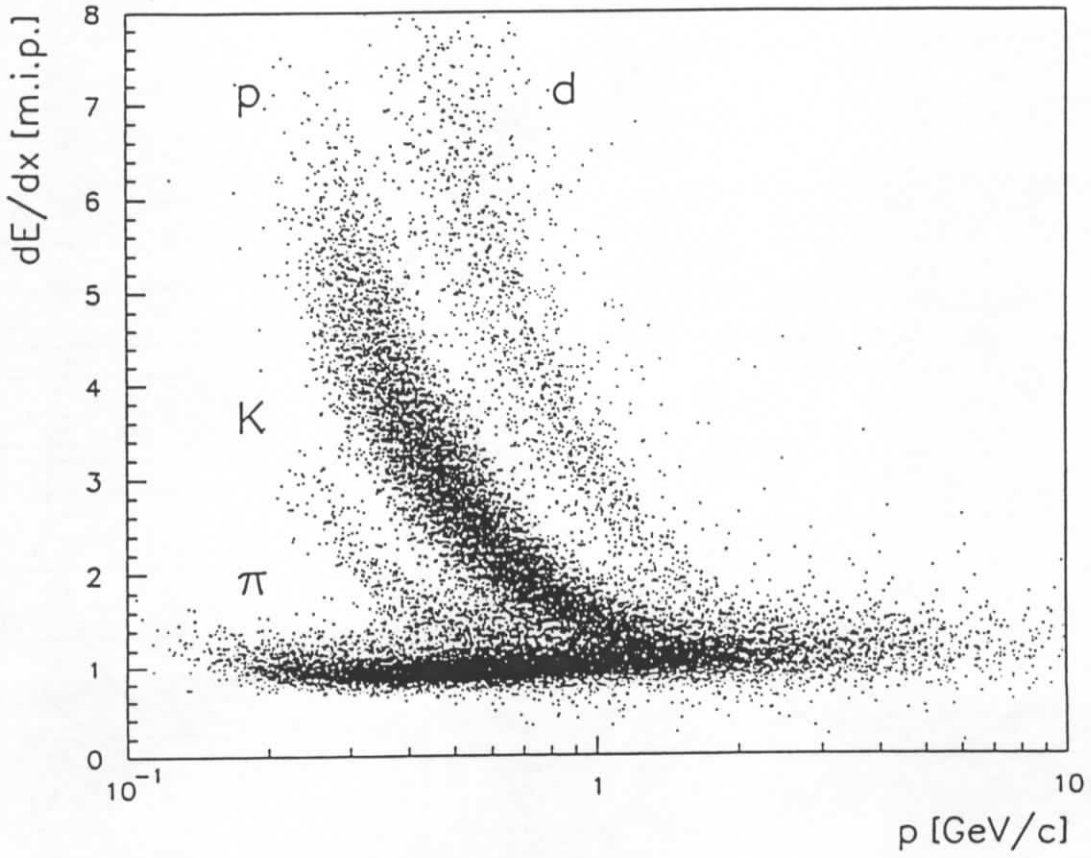

Figure 4.5: Specific ionization versus particle momentum measured in the CJC in HERA runs.

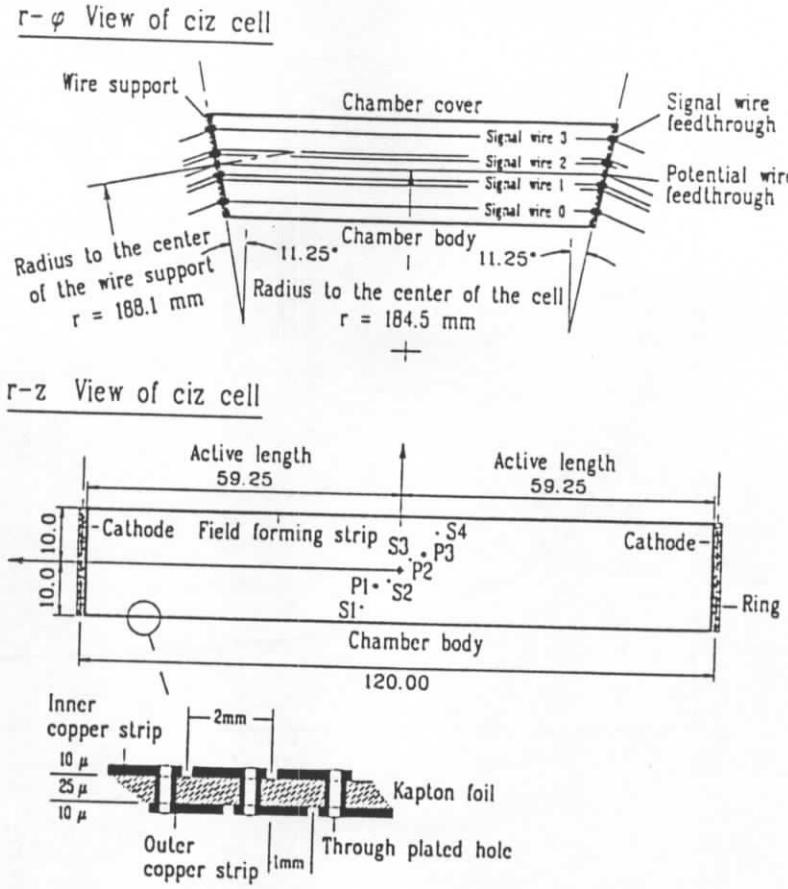

Figure 4.6: Longitudinal and transverse cross-section through a cell of the CIZ. S: signal wires, P: potential wires, the $z-$coordinates are given relative to the center of the cell [mm].

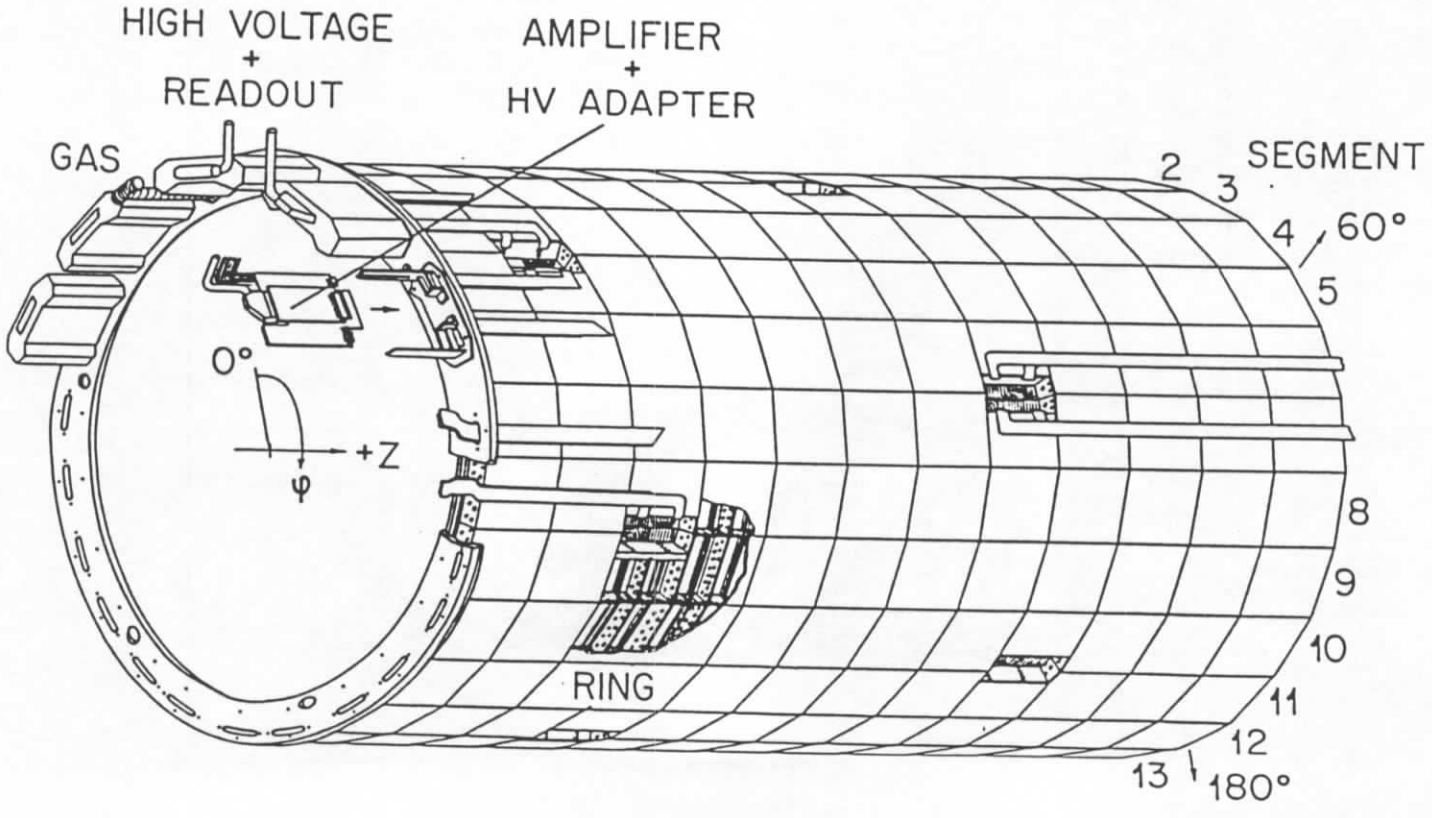

Figure 4.7: Schematic view of the COZ.

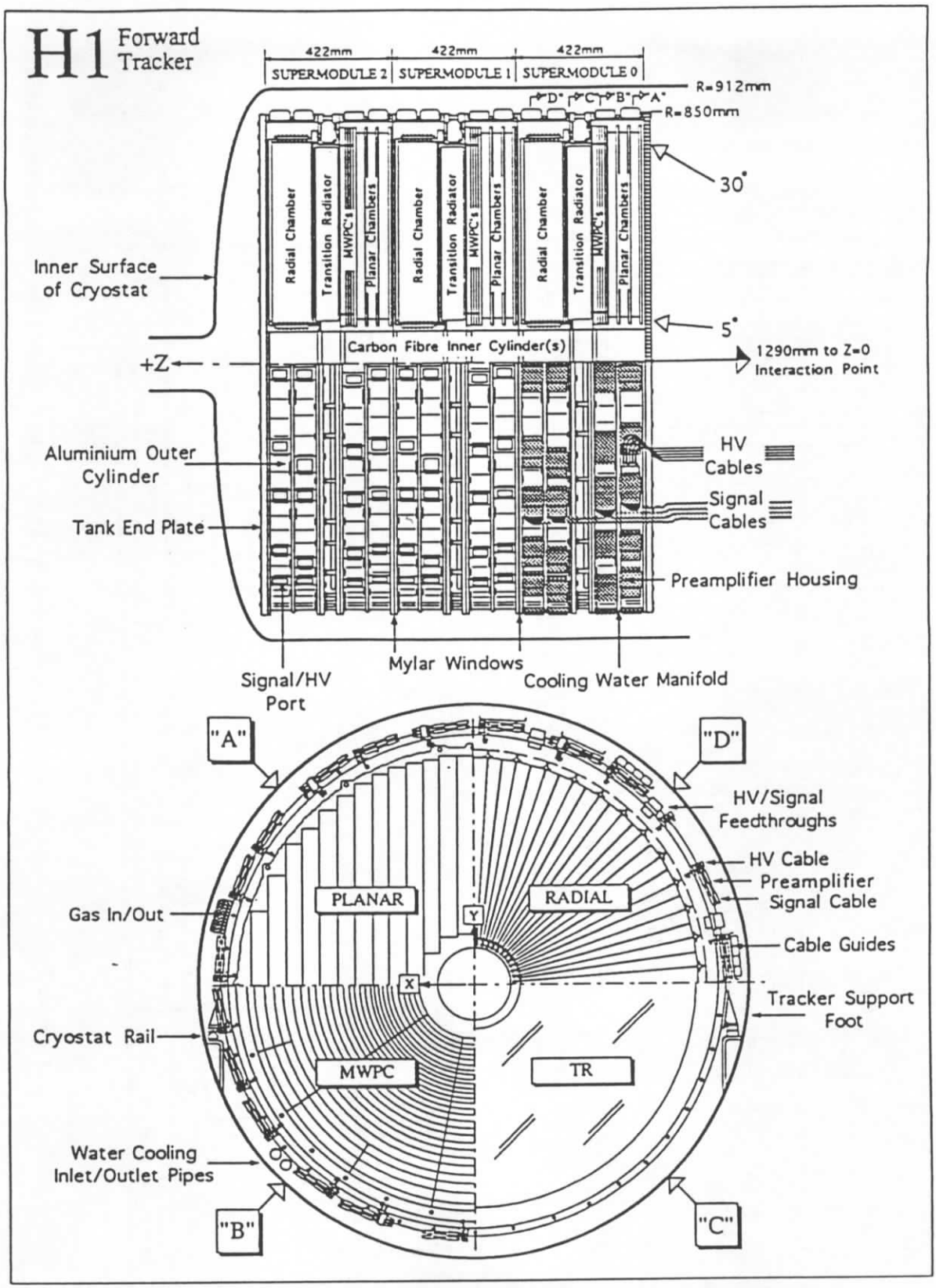

Figure 4.8: Forward tracker overview. Top: cross-section in the $r,z-$plane showing the three supermodules. Bottom: cross-section in the $r,\phi-$plane showing the basic cell structure of each supermodule component in one quadrant (A: planar chamber, B: FWPC, C: TR, D: radial chamber).

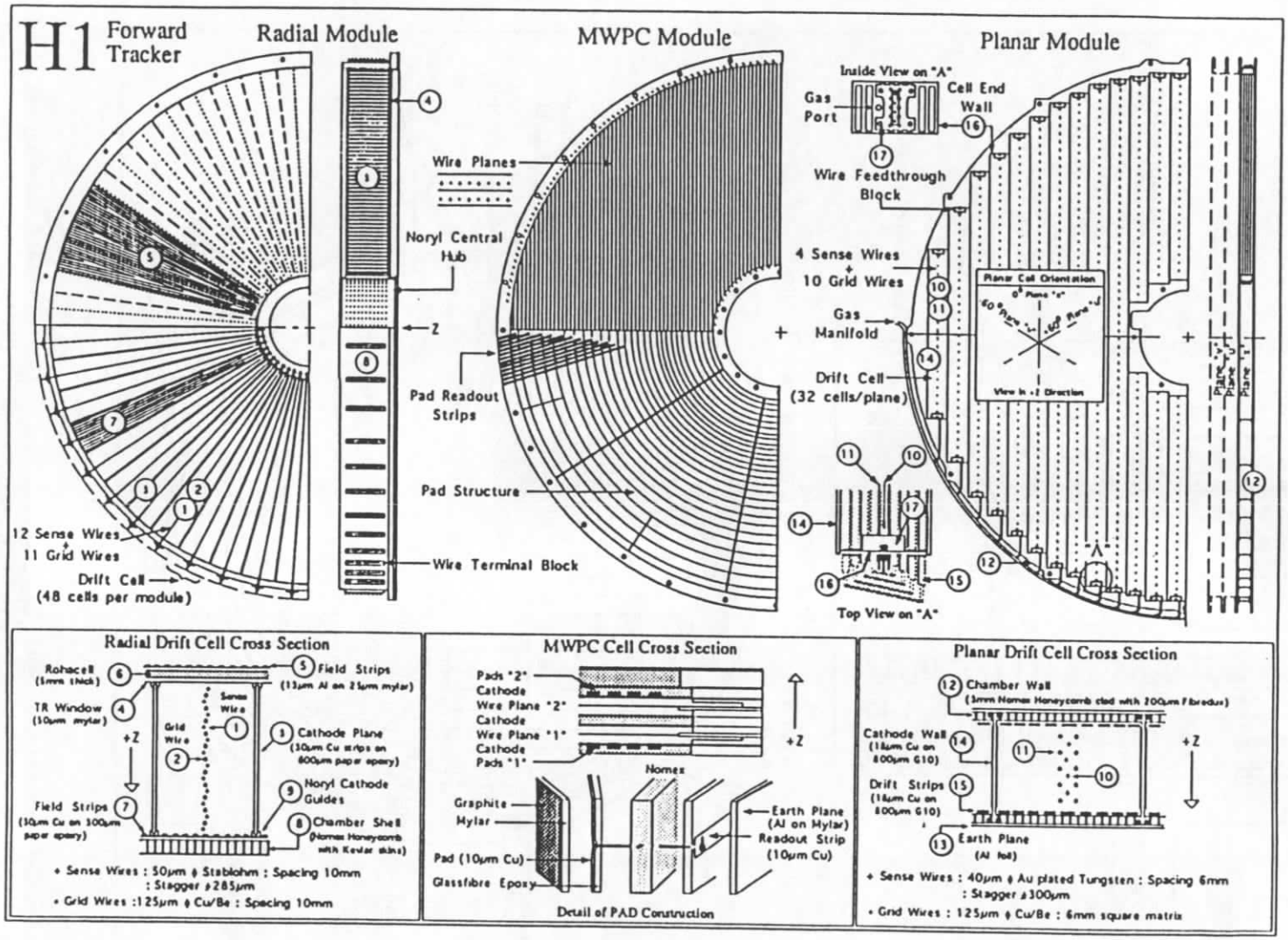

Figure 4.9: Details of the forward tracker construction. Top: cross-section in the $r, z-$plane and in the $r, \phi-$plane showing the overall orientation of cells, wires and pads for each supermodule component. Bottom: details of cell construction.

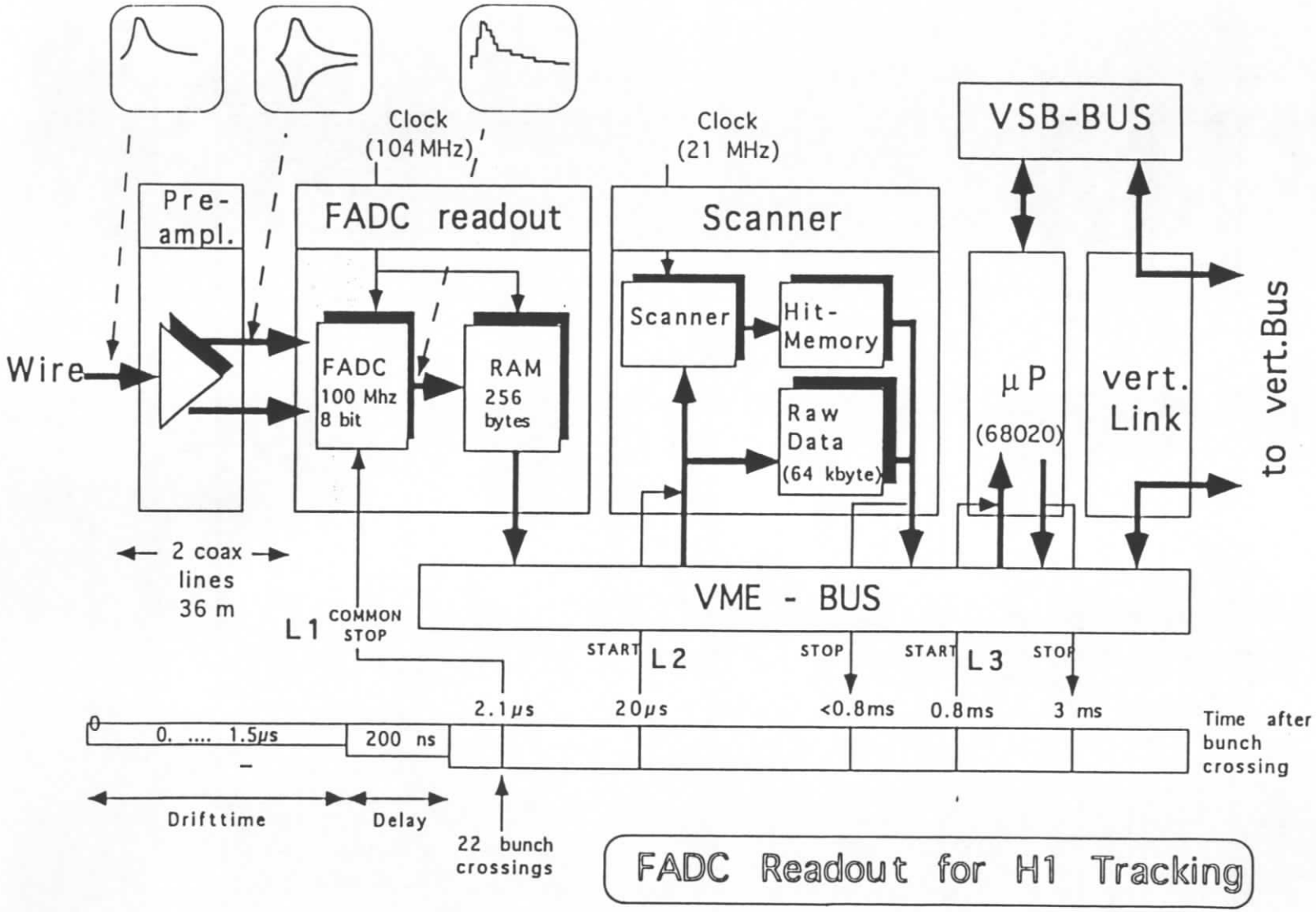

Figure 4.10: FADC readout system for drift chambers

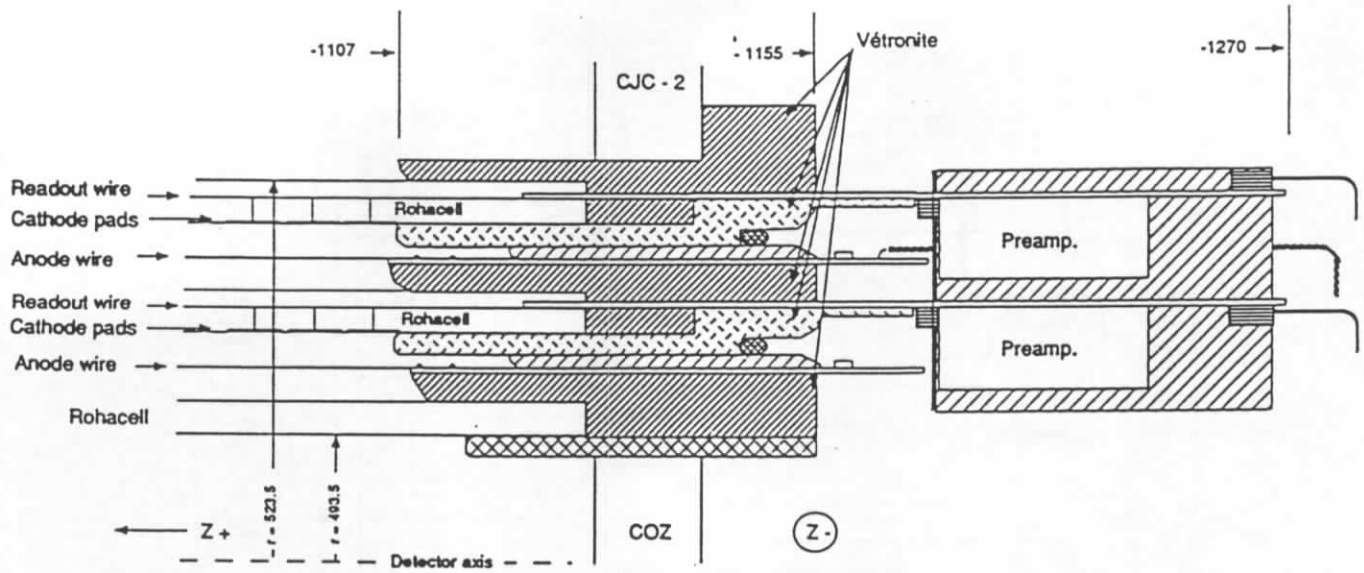

Figure 4.11: Longitudinal cross-section and details of the COP.

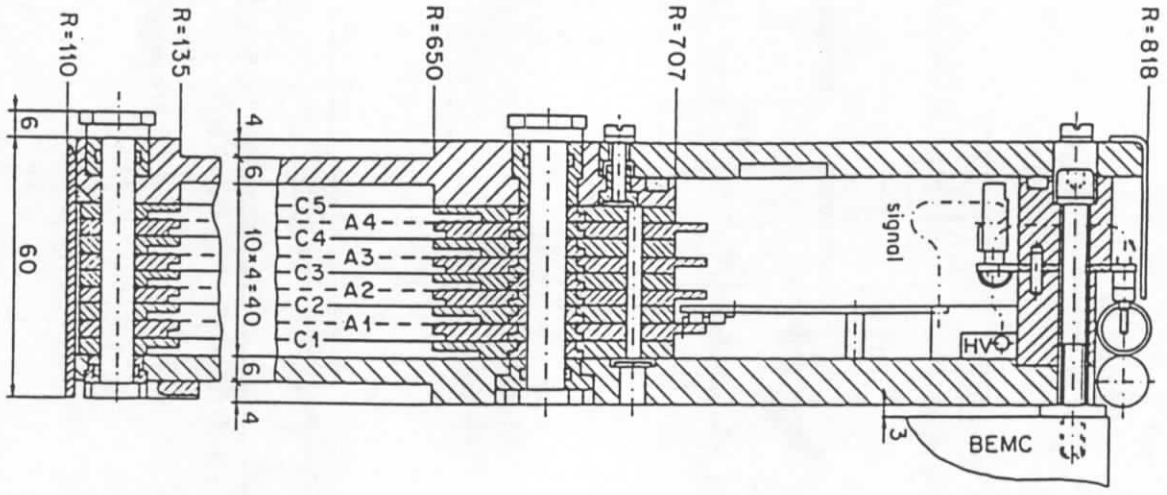

Figure 4.12: Cross section through the backward proportional chamber.

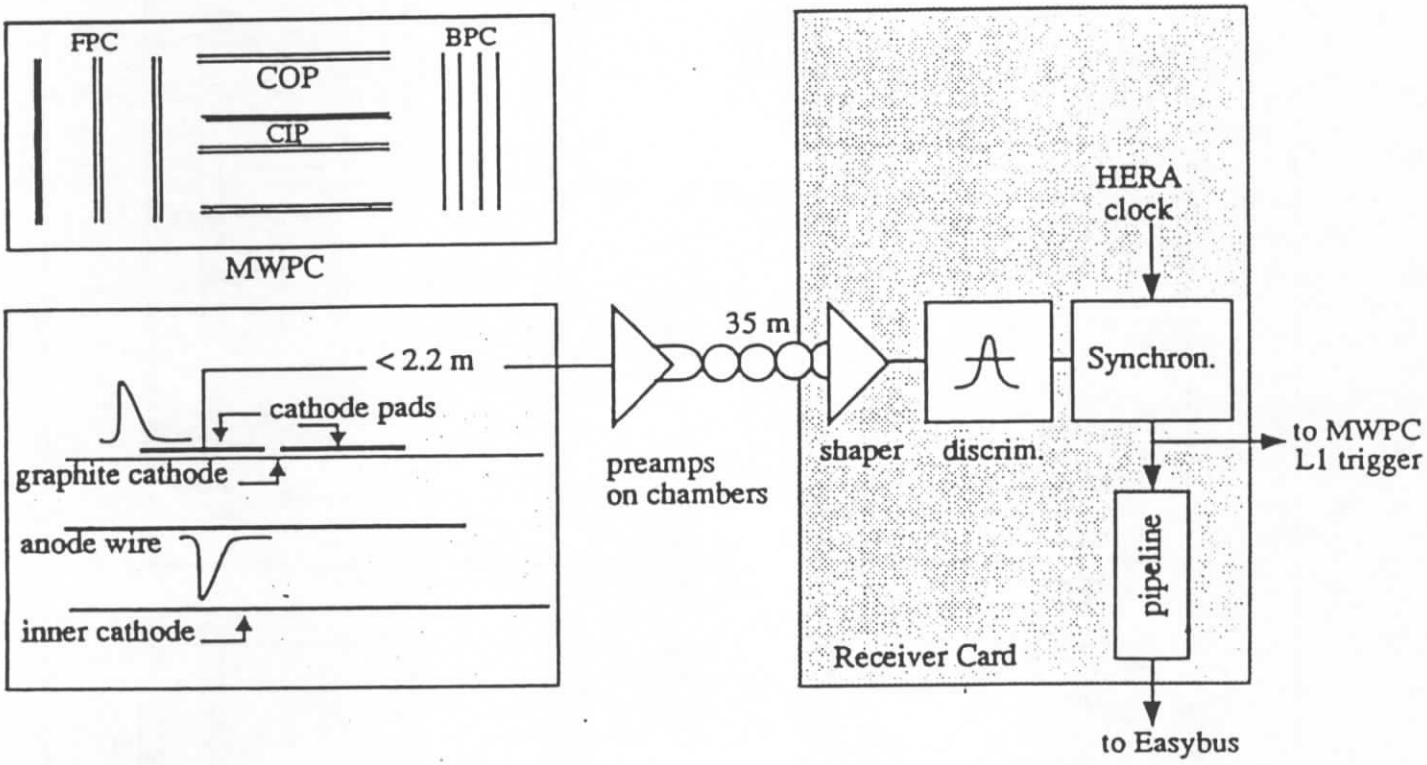

Figure 4.13: MWPC front end electronics and read-out system.

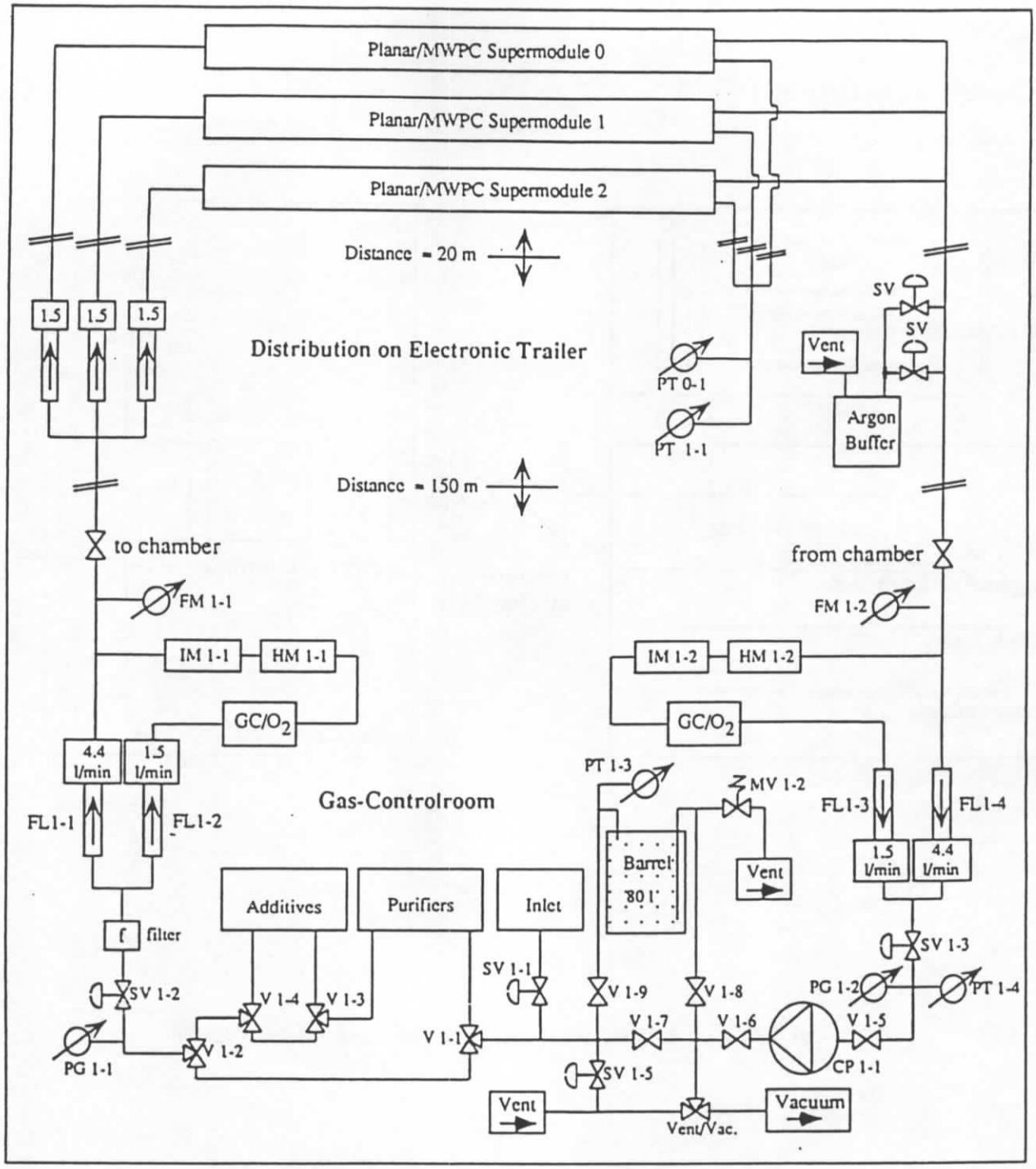

Figure 4.14: Layout of the closed circuit gas system for the planar drift chambers. CP: circuit membrane pump, FL: mechanical flow meter, FM: electronic flow meter, GC: gas chromatograph, HM: hygrometer, IM: infrared meter, MV: mechanical safety valve, O_2: O_2-meter, PG: mechanical pressure gauge, PT: electronic pressure transducer, SV: solenoid valve, V: mechanical two- or three-way valve.

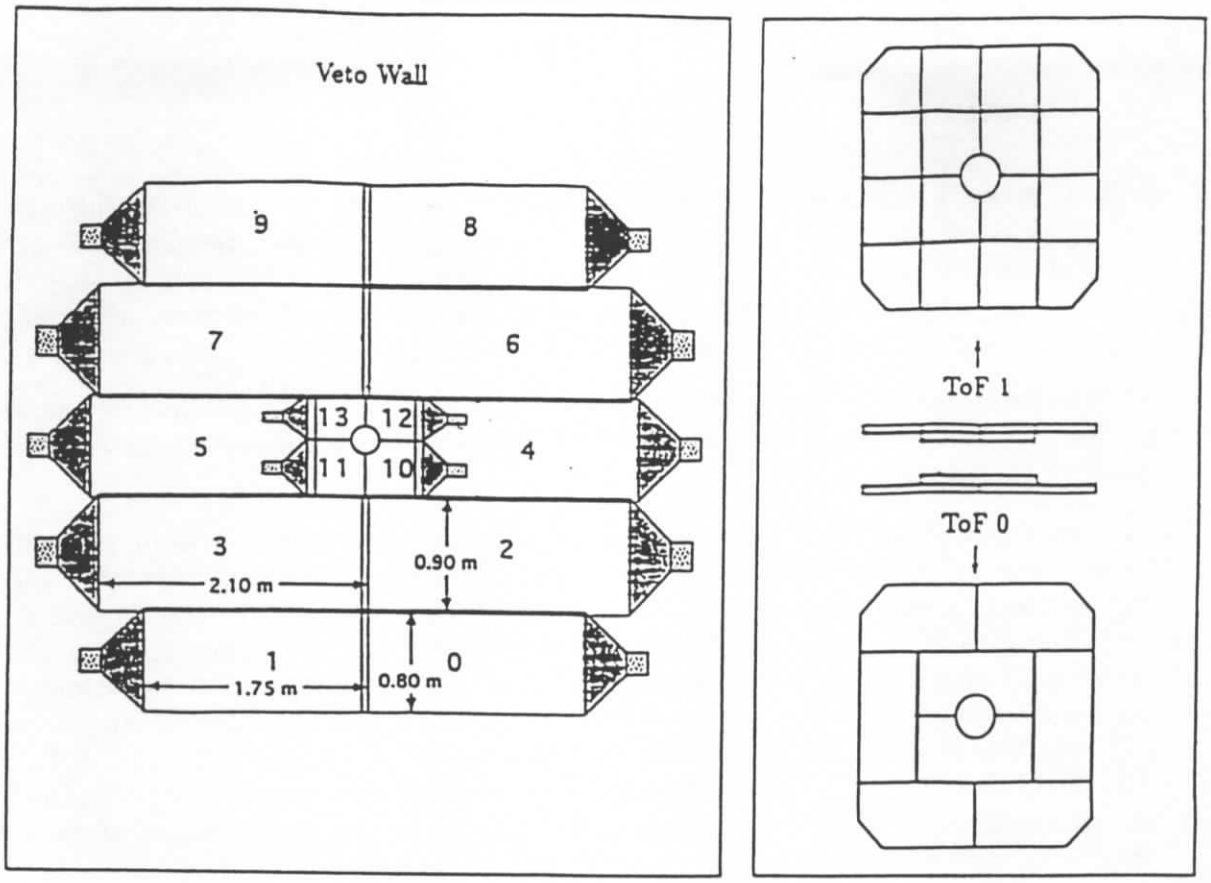

Figure 4.15: Schematic cross-section of the inner and outer veto wall (left) and the ToF counters.

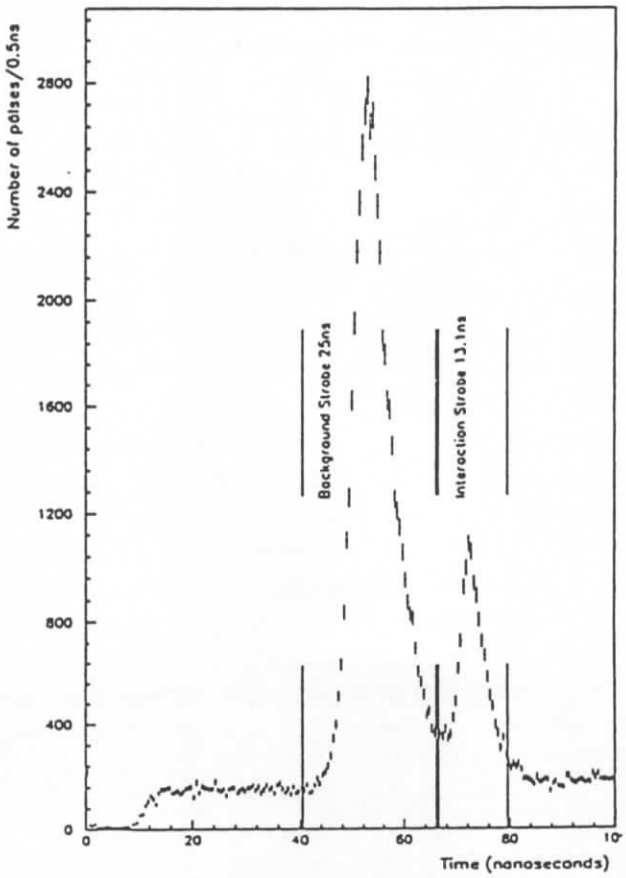

Figure 4.16: Time distribution of hits in a ToF counter.

5 Calorimetry

The H1 detector was designed to provide clear identification and precise measurement of electrons, muons and penetrating neutral particles together with good performance in the measurement of jets with high particle densities. These requirements were best met by a calorimeter inside a large coil to minimise both the amount of dead material in front of the electromagnetic calorimeter and the overall size and weight of the calorimeter [78].

The main reasons for choosing the liquid argon technique were good stability and ease of calibration, fine granularity for e/π separation and energy flow measurements as well as homogeneity of response.

Figure 5.1a shows the longitudinal view of the calorimeters along the beam axis and Figure 5.1b shows a transverse view of the LAr calorimeter with the wheel structure that is described below. The LAr calorimeter covers the polar angular range between $\theta = 4°$ and $\theta \approx 153°$. The calorimetric coverage is completed with a small calorimeter in the proton direction (PLUG) with copper absorber and silicon pad readout, covering the region between the beam-pipe and the liquid argon cryostat ($\theta \leq 4°$) and a lead scintillator backward electromagnetic calorimeter (BEMC) located in the electron direction after the tracker and covering angles $151° \leq \theta \leq 176°$. The tail-catcher system (TC) is used to provide a rough calorimetric measurement of hadronic particles leaking out of the LAr calorimeter and is based on the analog readout of the pads of the limited streamer tubes that instrument the iron yoke.

In the next section the LAr calorimeter is described; descriptions of the BEMC, the PLUG and the TC can be found in sections 5.2, 5.3 and 5.4 respectively. Further details on the instrumentation of the iron yoke are given in the section on the muon detector (see Section 6). For a more detailed description of the LAr calorimeter system we refer to [79].

5.1 The liquid argon (LAr) calorimeter

5.1.1 Cryostat and cryogenic system

All walls are made of stainless steel except for the inner ones of the warm and cold vessels around the beam pipe and the tracker which are made of aluminium alloy, to minimise the dead material in front of the electromagnetic calorimeter (EMC). The cold vessel is able to withstand a maximum pressure of 3 bars and to support the weight of the calorimeter modules (450 t) and of the liquid argon load (53 m^3). Cooling down to LAr temperature is achieved by circulation of helium gas cooled through an external heat exchanger which is removed when no longer needed. The LAr load is transferred from a 70 m^3 storage tank located at ground level (about 20 m above the detector) into the cryostat through the bottom of the cold vessel. A regulated flow of liquid N_2 through heat exchangers located within the cold and expansion vessels ensures temperature and pressure regulation (1.35 bar). Control of all processes, including cool-down/warm-up and filling/emptying is done by a system controlled by VME processors. Since operations started in early 1991 the calorimeter has remained at liquid argon temperature and most of the time full of liquid argon except for the few days needed to move the detector in or out of the beam. For more details to this system we refer to [79].

5.1.2 Liquid argon purity

A liquid argon purity monitoring system has been integrated into the LAr cryostat to check the stability of the ratio of energy loss to collected charge to the level of $< 1\%$. The basic sensor is a

liquid argon ionization chamber to which an electric field of 625 V/mm is applied, corresponding to the nominal field applied to the calorimeter stacks. Its cathode is coated with a ^{207}Bi source of 10^4 Bq activity. The energy spectrum of the radioactive decays is continuously monitored. The data from 11 such probes distributed around the cryostat show that the signal attenuation due to pollution from the stacks is less than 0.5 % per year.

5.1.3 Stack design and construction

The segmentation along the beam axis is done in eight self supporting "wheels" as shown in Figure 5.1, each of them segmented in ϕ into eight identical stacks or octants. The two forward wheels are somewhat similar in the principle but mechanically assembled as two half rings. An effort was made to minimise dead regions due to cracks.

Common features for all active cells are pad readout on the ground side and a high resistive coated high voltage plane (except for the CBH stacks) with integrated decoupling capacitance as described below.

The hadronic stacks are made of stainless steel absorber plates with independent readout cells inserted between the plates. They define the rigid structure on to which the corresponding electromagnetic stacks are mounted. The orientation of the absorber plates is such that particles are incident on the calorimeter with angles not smaller than 45°. The structure of each electromagnetic stack consists in a pile of G10(epoxy+glass fiber)-Pb-G10 sandwiches separated by spacers defining the LAr gaps. The basic sampling cell is shown in Figure 5.2a. It consists of 2.4 mm Pb absorber and 2.35 mm liquid argon as active material with, per gap, one readout plane with pads and one high voltage plane coated with high resistive paint (HRC). The latter is a mixture of carbon and glue with a surface resistance of 1-30 MΩ / □, sieveprinted on a Kapton foil. The high resistivity coating provides the HV protection and serves as a distributed decoupling capacity to keep negative cross-talk small. The hadronic sampling cells, as shown in Figure 5.2b, consist of a total of 19 mm stainless steel, (16 mm absorber from the welded structure and twice 1.5 mm from the plates of the independent readout cells defining the active liquid argon gap) and of a double gap of 2.4 mm liquid argon. They have, in the middle of the active gap, a G10 board with pads on both sides to collect the charges deposited in the gaps. A Kapton foil coated by a layer of HRC (IF2H, FBH, OF stacks) or with copper (CBH) is glued to the inner side of the stainless steel plates, with the same functions as for the electromagnetic modules. The HV is applied to the HRC (or copper for CBH, in which case neon spark gaps mounted close to the gaps act as active protection). For more details we refer to [78, 79]).

The basic calorimetric material constants are given in Table 1 of reference [80]. The granularity of the read-out cells stems from the requirements of a good separation of electromagnetic and of hadronic showers. Longitudinal segmentation is 3– and 4–fold for the EMC over 20 to 30 radiation lengths (X_0) and 4– to 6–fold for the hadronic calorimeter (HAC) over 5 to 8 interaction lengths (λ). Furthermore the tower sizes are such that the channel capacities are kept below 14 nF so that the electronic noise is at a reasonable level, with the additional constraint from the calorimeter trigger that channels belonging to the same trigger tower should have similar capacities within ± 5% for good timing adjustment.

The high voltage distribution is done by 1504 independent lines. Each line feeds a group of non consecutive planes in a stack, interleaved with planes linked to another HV line to reduce the probability that a complete tower segment be dead in case of a high voltage problem in one line. The present operating voltage of the calorimeter is 1.5 kV which corresponds to an electric field of 625 V/mm. The very good purity observed allows high charge collection efficiency (about 94% [79, 81]) at this low field value, thus minimizing HV problems. After 3 years of operation less than 3% of the high voltage lines do not reach the full voltage.

5.1.4 Electronic system

A major constraint in the design of the system, is that large energies may be deposited at short time intervals (96 ns at HERA) into detectors with large capacities and long collection times, and the information has to be stored until the arrival of the trigger signal ($\approx 2.5\ \mu s$). The basic layout of the electronic chain is described in more detail elsewhere [78, 79]. The preamplifiers, each with two shapers, a slow one and a fast one, are located just outside of the cryostat and feed on one hand the analog readout system where the signals of the slow shapers are read out via two multiplexers giving an overall multiplexing factor of 128, and on the other hand the trigger read out system where the outputs of the fast shapers are processed (see Section 8.3.2.1). To extend the dynamic range to 14 bits while using a 12-bit ADC, a double transmission system with two different gains for about 50 % of the channels is used thus increasing the number of channels to be read-out to about 65000 (electronic channels). The signals are sent twice via $\approx$ 30 m twisted pair lines to differential line receivers located in the analog receiving unit (ANRU) which performs analog baseline subtraction [82]. Each ANRU serves 512 calorimeter channels and is connected to an ADC board serving 1024 electronic channels that is controlled and read out by a digital signal processor (DSP) module performing data correction. This read-out system is described below (section 5.1.6). The total amount of channels where no signal reaches the preamplifier because of bad contacts within the cryostat is 0.15 % and has remained stable for about three years after closing the cryostat.

5.1.5 Electronic calibration system

To ensure that the calibration of the electronic chain is known and stable to within a few 10^{-3}, calibration capacitors of 47 pF, selected to be within ± 1 %, are used. They are charged with voltage pulses of precisely ($\approx 10^{-3}$) known amplitude.

Two systems have been built into the calorimeter: the first one (cold calibration) with the calibration capacitors in the liquid argon, as close as possible ($\approx$ 1 m) to the gaps, pulses individual channels (one out of 16) allowing detailed cross talk studies. The second system, with calibration capacitors at the preamplifier level (warm calibration), is used mainly as a backup for calibrating channels with a problem in the calibration line within the cryostat. In this case an extrapolation technique developed during the runs in test beams at CERN is used, and a precision of the order of 1 % in the determination of the calibration constants is achieved. This method is presently applied to less than 1 % of the 45000 calorimeter channels.

A third order fit to the calibration data is performed for each channel [79] from which the constants to be downloaded into the DSPs are determined. At H1 such operations are done once every few weeks. Figure 5.3 shows the stability of the calibration constants over one month.

The calibration constants need no correction for diagonal cross-talk as they are determined by pulsing the cells individually using the high granularity cold calibration system. Non diagonal cross-talk has been determined from the test beam data and was found to be small ($\leq 0.5\%$), mainly affecting the CBH modules.

5.1.6 Calorimeter data acquisition

The calorimeter data acquisition system reads out data from the LAr calorimeter, the BEMC, the PLUG calorimeter and the analog part of the instrumented iron (TC). These detectors have the same readout electronics starting from the ANRU. The LAr calorimeter yields most of the data and its readout is described here. At the preamplifier level the data are split into two paths as mentioned in section 5.1.4. In the analog data path the first level trigger decision samples

the slow shaper pulse at its maximum. At the level 2 trigger (L2), 20 μs after the collision, the analog to digital conversion of the 65000 electronic channels is started (total encoding time is 1.2 ms). The ADC counts of all electronic channels are then converted into calibrated charges by 69 DSPs working in parallel. The DSP boards [83] used here are based on the Motorola DSP56001 and perform for each cell a noise suppression done in parallel to the encoding and an order three polynomial correction. These DSPs provide calibrated charges formatted with the offline numbering of the calorimeter cells. On-board memories are downloaded with the current set of calibration constants (for each channel four parameters and the 1σ noise value are needed). The code contains less than 200 instructions. It is written in assembler language and was optimised to fit into timing specifications and the available program memory space in the DSP chip.

In the trigger data path, the pipelined trigger chain produces digital sums for each of the 22 bunch crossings following the collision. A first level trigger decision (L1) based on total and transversal energies is derived within 2.5 μs. Ten dedicated DSPs read the data of the fast shapers (see Section 8.3.2.1). They verify the timing and the shape integrity of the trigger tower signals, calculate pileup estimators based on charge and time analysis, and report any malfunctionings [84]. They store the signal history of a total of 474 trigger towers over 256 bunch crossings around the trigger time (t_0). From these data, every second sample in the interval ranging from -25 to +25 bunch crossings is read out for pileup studies. The DSP boards used in this path are based on the same DSP chip as for the analog data read out but are of a different design, with a special interface to the trigger data.

The formatted data for both paths, within independent VME branches, are collected by two event builders based on the RISC processor AM29000 running the real time kernel VRTX. The AM29000 event builders, one for the analog data and the other for the trigger data, run on top of the real time kernel VRTX, with minimal system overhead. The data are passed to the event logging task through a circular buffer. The event is then formatted and sent to the central data acquisition through an optical fiber link (see Section 10.1.2).

Presently with an event size for the calorimeter branch of about 20 Kbyte and a first order dead time of 1.2ms the maximum data taking rate has been measured to be 200 Hz (100 % dead time). At a rate of 100 Hz the dead-time is 15 %.

A processor based on the Motorola 68030 chip and operating under an OS9 system is used for run control and as a stand alone facility.

5.1.7 Reconstruction techniques

Input to LAr calorimeter reconstruction are calibrated charges for each calorimeter cell, as provided by the DSPs. The calorimeter reconstruction program converts charges to energies in the calorimeter cells for both hadronic and electromagnetic showers, corrected for the effects of dead material, eliminates electronic noise and forms clusters from groups of cells.

The scaling from charge to energy (electromagnetic scale (see Section 5.1.8)) involves a charge to energy calibration factor (determined for each stack geometry in calibration runs at CERN, see Section 5.1.8), a correction for the charge collection efficiency for operating at 1500 V (derived from HV curves obtained with cosmic muons [79]) and correction factors for local variations of gap and absorber thicknesses (measured during stack construction).

The noise is measured for each channel during electronic calibration. It varies between 15 and 30 MeV equivalent energy depending on the calorimeter region (see Table 5.1). In events recorded with a random trigger 1100 cells out of a total of 45000 cells pass a $+2\sigma$ noise threshold

	CB	IF
EMC	30 MeV/0.25 mips	15 MeV/.15 mips
HAC	30 MeV/0.15 mips	24 MeV/.15 mips

Table 5.1: Approximate energies and minimum ionizing particle equivalents (mips) corresponding to 1σ noise in the electromagnetic and hadronic sections of the central barrel and inner forward modules respectively.

on average. Adding up this energy for the full calorimeter yields an average value of 48 GeV with a standard deviation of 3 GeV (Figure 5.4a). To suppress the noise further we use the negative noise, present in the gaussian distributed noise signals after pedestal subtraction, to compensate the positive noise contribution to the measured signal. We keep cells above $+4\sigma$ (signal seed) and all neighbours in a $3 \times 3 \times 3$ cube around a seed cell ($> +4\sigma$) also to keep small signals at the fringe of showers. In order to compensate for noise picked up in the previous step also cells below -2σ around a signal seed are kept. Cells below -4σ are kept in order to compensate for noise contribution to $+4\sigma$ seed cells. No neighbours are collected around these -4σ cells which are purely noise. After this procedure, the residual noise contribution is 0.1 GeV with a $\sigma = 0.5$ GeV (Figure 5.4b).

The signal loss introduced by the above noise suppression procedure has been studied with simulated low Q^2 DIS events. In these events the hadronic energies are low, with average deposited energies in the barrel region of the calorimeter of about 4.5 GeV, 800 MeV for hadrons and 400 MeV for photons. In this (most difficult) case 17 % of the energy is lost due to this noise suppression. For high Q^2 events ($< Q^2 > \approx 500$ GeV^2) the loss is smaller (5 %). These losses are corrected for in the reconstruction of hadronic energy (see Section 5.1.7.5).

For simulations, noise is included for each cell by using events recorded with random triggers in special runs with no online noise suppression.

5.1.7.1 Clustering All cells passing the cell level reconstruction are subject to clustering. The algorithms used are tuned so that the cells containing energy depositions from an electromagnetic shower initiated by a photon or electron are most probably merged into one cluster. Hadronic showers on the other hand, with their large spatial fluctuations are in general split into several clusters.

5.1.7.2 Further noise suppression Clustering allows further reduction of the noise in the hadronic part of the calorimeter. A hadron penetrating deeply inside the calorimeter usually deposits enough energy to form at least one cluster with a signal well above the noise level. Other small isolated energy depositions which are not distinguishable from noise are correlated in space with this prominent cluster.

Small signals are suppressed if they are in the last layer of EMC or in HAC and far away (> 50 cm) from the direction given by the centre of gravity of any prominent cluster (significance, $\sqrt{\sum(E_i/\sigma_{noise})^2}$ above 8) and the nominal interaction point.

This suppression does not increase the signal loss mentioned in Section 5.1.7. The energy distribution of noise remaining in empty events after the suppression peaks at zero with a sigma of 0.25 GeV, as can be seen in Figure 5.4b.

5.1.7.3 Correction for energy loss in dead material The energy losses in dead material in front of the calorimeter (the beam pipe, the central tracker and the inner cryostat wall) and in cracks between the calorimeter stacks are quite substantial. In low Q^2 DIS events they amount to $\approx$ 10 % of the energy deposited in the calorimeter, dead materials in front of the calorimeter accounting for about 90% of these.

Corrections for the energy loss were derived using Monte Carlo simulations. The event by event corrections are based on the measured calorimetric energies. To reduce the influence of noise on the correction, only cells with energy above $3\sigma_{noise}$ for cells in prominent clusters (see Section 5.1.7.1) and above $5\sigma_{noise}$, otherwise, are considered.

Energy losses in front of the LAr calorimeter are corrected by using the first (inner) layer of cells in the LAr calorimeter. For each cell in the first layer with a signal above the threshold mentioned above, an energy is added according to:

$$E^i_{loss} = \alpha_{fr} f^i_{dead}$$

Here f^i_{dead} is the energy loss of a minimum ionizing particle in the material in front of cell i in projective geometry with respect to the nominal interaction point. A global factor α_{fr} was determined for each half wheel along the beam direction by simulation. For the above energy estimate we use only the fact of the presence of an energetic cell, but not its energy. This approach allows a common correction procedure for losses caused by electrons and hadrons.

The correlation between the estimate of the energy losses in the reconstruction and the true energy lost in front of the calorimeter for simulated low Q^2 DIS events is given in Figure 5.5. An example of the effect of the dead material correction for experimental data is shown in Figure 5.6, where the π^0 peak in the effective mass of two photons (e.m. clusters) is moved by the correction into the region of the π^0 mass.

The correction procedure for energy losses in a crack uses cells in the layers nearest to the crack and on either side of it. Cells on one side of a crack are coupled with cells on the other side and for each such pair an energy loss between them is estimated by

$$E^j_{loss} = \beta f^j_{dead} E^j_l E^j_r / (E^j_l + E^j_r)$$

distributed between the two cells of a pair in proportion to the cell energy. Here E^j_l and E^j_r are energies in a pair j deposited at left and right sides of the crack. The function f^j_{dead} takes into account local inhomogeneities of dead materials. A global factor β was determined for each type of a crack. These factors differ considerably for pions and electrons. For the moment, only corrections of hadronic type are used in the reconstruction because of difficulties in the separation of hadronic and electromagnetic components in ϕ and z crack regions.

Figure 5.7 shows the performance of the dead material correction as function of θ and ϕ for simulated pions of 20 GeV. The crack structure which is clearly seen before the correction nearly vanishes after the correction. The CB2/CB3 z-crack almost pointing to the interaction point was scanned by a pion test beam of 30 GeV at CERN. Results are given in Figure 5.8. The response across the crack is well described in simulation.

5.1.7.4 The hadronic energy scale The LAr calorimeter is non compensating. The charge output for hadrons is about 30 % smaller than for electrons. Therefore an additional correction has to be applied to the signal obtained on the electromagnetic scale.

The fine segmentation of the LAr calorimeter allows to distinguish the primary electromagnetic component of a jet which is already on the correct (electromagnetic) energy scale. It also

allows a high level of compensation within hadronic showers to be reached by weighting signals from individual calorimeter cells (see below).

The primary electromagnetic clusters are filtered using such characteristics as the fraction of cluster energy deposited in EMC (containment in EMC), in the first layer of EMC (early shower development), and in the four most energetic cells of a cluster (compactness); see reference [80]. The filtering is done for clusters with an energy above 1 GeV.

The hadronic objects in the reconstruction are formed by cells which are not included in an electromagnetic cluster and are located within a radius r around the direction given by the nominal interaction point and the centre of gravity of the hadronic cluster ($r < 25$ cm in EMC and $r < 50$ cm in HAC). Here, a cluster is called hadronic if it is prominent (see Section 5.1.7.3) and if it is not recognized in the filtering as an electromagnetic one or, at lower energies, if it is developing deeply inside the calorimeter.

To get the proper hadronic scale for hadrons, a software weighting technique is applied, which was initially proposed by the CCFR Collaboration and used in the CDHS experiment [85]. This method was further developed by H1 on the basis of CERN test runs [86, 87, 88, 89, 90]. The aim is to equalize the response to the electromagnetic and hadronic components of a hadronic shower and, therefore, to suppress the influence of the large fluctuations in the hadronic shower composition on the reconstructed energy. The technique exploits the fact that local energy deposits of high density are mainly of electromagnetic origin while the hadronic component is much more spread out. Thus, in a well segmented calorimeter the amount of energy deposited in the cells can be used for statistical separation of electromagnetic and hadronic energy depositions.

In the reconstruction the weighted energy in a cell i, E^i_{rec}, is calculated from the cell energy on the electromagnetic energy scale, E^i_0, by:

$$E^i_{rec} = \{a_0 + a_1 exp(-\alpha E^i_0/V^i)\}E^i_0$$

where, a_0, a_1, and α are the parameters of the weighting function (different for EMC and for HAC) and V^i is the volume of the cell. These parameters were determined as function of the reconstructed jet energy (calculated inside cones of 10°) using a Monte Carlo simulation of jets [91]. For hadrons with energy below 7 GeV this ansatz is replaced by simple multiplicative factors corresponding to effective e/π ratios in EMC and HAC. In the region 7 to 10 GeV both methods contribute to the correction in order to get a smooth transition from the simple correction factors to the weighting.

The remaining cells not included into electromagnetic clusters or hadronic objects are due to low energy particles depositing energy in the first two (three in the forward region) inner layers of the calorimeter. These leftovers are affected by noise, and the energy correction to be applied depends on particle composition and energy spectra. The corresponding correction factors were defined using simulated low Q^2 DIS events.

5.1.8 Calibration and performance

The most important task in understanding the calorimeter modules is the energy calibration. This was done by putting full scale calorimeter modules in a test beam at CERN. Checks of the calibration quality were done once the H1 detector was fully operational by using various techniques as described below, such as determining the response of the electromagnetic calorimeter to electrons generated by cosmic muons crossing the detector or verifying the P_t balance between the electromagnetic and the hadronic energy in deep inelastic events at HERA.

5.1.8.1 Overview of the test runs at CERN An extensive calibration program with $e-$, $\pi-$ and $\mu-$ beams was performed in the H6 test beam at the CERN SPS with prototypes [86, 87, 92] and with modules installed later in the H1 cryostat at HERA [93, 94]. These beam tests supplied the basic calibration constants of the calorimeter.

Only one of each type of the calorimeter stacks was tested as the very strict mechanical constraints (see references [78, 79]) needed to reach a homogeneity at the 1 % level were achieved during the construction phase, allowing to transfer calibration constants from one module to another.

Eight characteristic stack configurations were tested separately using the same beam setup, calorimeter readout and calibration electronics. These configurations include a full coverage of θ and all important crack configurations [93, 94]. Special modules consisting of half stacks assembled to reproduce a CB2-CB3 ϕ crack (see reference [95] and an FB1-FB2 ϕ crack (see references [96, 97]) were built and put into the test beam in 1992.

The purity of the liquid argon was constantly monitored by probes identical to those used in the detector described in section 5.1.2. The decrease of the signal with time was much faster than in the H1 detector because of polluting agents brought by the stacks. It was not possible to use the same flushing and cool-down procedures for the test set-up as in the final detector. Big variations in the pollution rate from one configuration to the next were attributed to the different cleaning agents used during the construction of the stacks which were built at various institutes.

The same front end electronics scheme and calibration system as at HERA was used as much as possible. Data were taken with beam energies in the range 3.7 to 80 GeV for electrons and 3.7 to 205 GeV for pions.

In some of the data taking periods a tail catcher module was added behind the hadronic calorimeter allowing combined analyses [87, 93]. The tail catcher modules were also calibrated in standalone tests [98].

5.1.8.2 Test beam results For the electromagnetic energy scale two calibration constants (c^{exp}_{EMC}, c^{exp}_{HAC}) were determined for each wheel, which transform the measured electric charge Q_i per cell into energy deposited by electron showers. Corresponding constants (c^{MC}_{EMC}, c^{MC}_{HAC}), transforming visible energy into deposited energy are obtained in Monte Carlo simulations (MC) for electrons (of 30 GeV). These constants are defined to be independent of effects of dead materials in front of the calorimeter, any leakage and analysis cuts.

The corresponding experimental constant c^{exp}_{EMC} is obtained by a comparison (see Figure 5.9) of experimental data with detailed simulation of the test setup and requiring the reconstructed energies to agree:

$$E^{exp}_{rec} = c^{exp}_{EMC} \sum_{i}^{EMC} Q_i = E^{MC}_{rec} = c^{MC}_{EMC} \sum_{j}^{EMC} E^{vis}_j \qquad (1)$$

For the calibration constant a value of $c^{exp}_{EMC} = 3.55$ GeV/pC is obtained on average. For the hadronic stacks no electron data were available and $c^{exp}_{HAC} = 7.1$ GeV/pC was obtained by scaling the value of the EMC by MC.

The resolutions σ/E obtained for various stacks are in the range 10 % to 13 %/$\sqrt{E}$ with constant terms below 1 %. Figure 5.10 shows the results for four different stacks and the parametrization for FB2 according

$$\sigma/E = \sqrt{A^2/E + B^2/E^2 + C^2} \qquad (2)$$

with $A = 11\%\sqrt{E}$, $B = 154$ MeV and $C = 0.6\%$. The measured resolutions differ at low energies due to different handling and influence of electronic noise for the various stacks. The observed non linearities are below 1 % after corrections for effects of dead material and noise by Monte Carlo.

The calibration constants of the various stacks were found to vary by about 2.5 % . This is larger than expected from the known mechanical differences of different wheels. The main error source were impurities in the liquid argon during the CERN test. The variation is consistent with the systematic error of the extrapolations of the high voltage plateau curves by which the charge collection efficiency was determined. Further tests of the energy scale are possible at HERA (see below). For further results on the calibration by test beam electrons and simulations we refer to [94] and for more details to [90, 99, 100, 101, 102, 103, 104].

The response to pions has been extensively studied for the different calorimeter wheels and compared to detailed simulations (compare references [93, 90, 105, 102, 106, 107, 108]). An application of the standard H1 reconstruction code (section 5.1.7) is shown in Figure 5.11, where data and GHEISHA simulation [109, 110] for pions at 80 GeV are compared in 3 different wheels on the electromagnetic scale and after reconstruction of hadronic energies. No attempt is made here to correct for leakage. The effect of the inclusion of the streamer tube tail catcher (see Section 5.4 and reference [111]) which adds at the test beam another 4.5 interaction lengths (λ_{abs}) to the 6 of the IF wheel, can be seen in Figure 5.12. It shows the reconstruction at a pion energy of 205 GeV for all events and for those fully contained in liquid argon. The obtained resolutions are about σ/E = 50 %/$\sqrt{E}$ with an energy independent term of 2 % as shown in Figure 5.13.

5.1.8.3 Performance at HERA Data taken at HERA, since April 1991 with cosmic muons, and since June 1992 with beams, allowed for checks of both the overall electromagnetic and hadronic energy scales.

The orientation of the three CB wheels is especially favourable for the study of the signals from cosmic muons and allowed to check the charge collection, the overall calibration and the time stability. The charge collection efficiency at the operating voltage of 1.5kV was determined by high voltage plateau curves to be .944 ± .014. The electromagnetic energy scale as determined at the CERN beam tests (see above) could be verified to ± 8 % ([81]). More precise tests are possible with electrons (see below).

The overall response to muons of the individual electromagnetic and hadronic sections of the three CB wheels varied from October 91 to November 94 by less than ± 3 %.

A fraction of the cosmic muons traversing the detector generates electrons. Their momentum p can be measured in the central tracker CJC and can be compared with the energy E measured mainly in the CB wheels. A typical event is shown in Figure 5.14 together with the measured E/p distribution for selected electrons with $p > 1$ GeV/c and incident angles below 25° with respect to the normal of the calorimeter plates. The mean (0.96 ± 0.01) and width ($\sigma = 0.15$) agree with the simulation within errors. The width corresponds to a resolution of $\sigma/E = 0.20/\sqrt{E}$, but this value is still influenced at these energies ($< p >= 1.6$ GeV/c) by noise and dead material corrections (section 5.1.7) of about 10 %.

With these techniques the forward wheels cannot be reached, but the performance of IF and FB wheels can be checked by two photon mass spectra as demonstrated in Figure 5.6 which shows a clear π^0 mass peak.

Deep inelastic scattering events where the scattered electron and the hadronic jet are detected both in the LAr calorimeter can be used for a direct comparison of the hadronic and electromagnetic energy measurement exploiting p_t balance. The transverse components p_{te} and p_{th} are calculated by summing vectorially the calorimeter cell energies. Figure 5.15 shows that the measured energy balance is compatible with simulation.

5.2 The backward electromagnetic calorimeter (BEMC)

The backward ($-z$) region of the H1 detector is instrumented with a conventional electromagnetic lead-scintillator sandwich calorimeter.

The primary task of this backward electromagnetic calorimeter is to measure energies and directions of electrons scattered under small angles from DIS processes. In addition the BEMC contributes to the measurement of hadrons emerging from photoproduction and medium to low-x, high-y hadronic final states from DIS.

The kinematics of DIS accessible with this calorimeter is characterised by moderate four-momentum transfers 5 GeV^2 $< Q^2 <$ 100 GeV^2. Such processes dominate by far the DIS cross section-observed in the H1 detector and provide the only access to the low-x part of the proton structure ($x \approx 10^{-4}$). At the same time the calorimeter has to operate in a very high rate environment caused by the illumination of the rear side with secondary hadrons originating from beam-gas and beam-wall interactions of the 820 GeV proton beam. Due to its location within the large solenoid the BEMC is exposed to the full magnetic field of 1.15 T.

A full description of the BEMC and its associated trigger, the backward single electron trigger (BSET) can be found in [112].

5.2.1 Mechanical layout

The calorimeter elements (stacks) of the BEMC are mounted in an aluminium barrel with a diameter of 162 cm. The front face is located at a distance of 144 cm from the nominal interaction point. Scattering angles θ from 151° to 176° are covered with full azimuthal acceptance. This corresponds to $\approx$ 1.4 units of pseudorapidity η ranging from -2.9 to -1.6

Granularity of the calorimeter is provided by segmentation into 88 calorimeter stacks aligned parallel to the beam line. The transverse structure can be seen in Figure 5.16a. 56 stacks have a square cross-section. The remaining ones are of trapezoidal and triangular shapes in order to provide an approximation to the circular shape of the support barrel.

The stacks are multilayer lead-scintillator sandwich structures with 50 active sampling layers made of SCSN-38 plastic scintillator [113] of 4 mm thickness. The entire structure (figures 5.16b,c) corresponds to a total of 21.7 radiation lengths or $\approx$ 1 λ. The Moliere radius is 3.4 cm. The scintillation light is coupled via a 0.3 mm air gap to Y-7 wavelength shifter bars [113]. Two pairs of 8 cm wide bars cover two opposite sides of a square stack extending over the full active length. The remaining two sides are covered with 16 cm wide bars extending only over the last 15 sampling layers in the stack, thus providing a twofold segmentation in depth.

The light emitted in the wavelength shifter bars is detected by PIN photodiodes (S2575 [114]). Each long bar is equipped with one diode. The short bars are connected to a pair of diodes due to their double width. Special arrangements of wavelength shifters have been made for the non-square stacks. Some of them have a reduced number of readout channels. In total there are 472 read-out channels in the BEMC.

5.2.2 Readout electronics and trigger

The electronics associated with the BEMC must fulfill two main functions. It processes the analog signals from the PIN photodiodes and converts them into digital form with the required speed, precision and stability. It further provides trigger signals.

The signals from the PIN photodiodes are fed into charge sensitive pre-amplifiers mounted directly on the back of each calorimeter stack. The preamplifiers produce fast signals of 100 ns rise time and a fall time of 150 μs. A differential pulse is sent from a line driver through 30 m twisted pair cables to a receiver located in an electronics hut. Here the signals are split to provide input for the calorimetric triggers and for the readout.

Two trigger signals are produced. Firstly the analog signals of the four long wavelength shifter bars within one stack are summed in order to provide input for the high granularity backward single electron trigger (BSET; see Section 8.3.2.2). A second set of stack sums is being formed to feed the overall calorimeter trigger sums with low granularity. The timing and the gain of the BSET stack sums are individually adjusted in order to assign events uniquely to one bunch crossing and to compensate for stack-to-stack variations in energy calibration already on the first trigger level.

The readout of BEMC energies proceeds through a chain of shapers, sample-and-hold circuits and multiplexing similar to the one of the LAr calorimeter described previously. Due to the large cross-section of calorimeter stacks and the high proton beam related background rates the concept of slow shaping to match the trigger level L1 decision after 25 bunch crossings cannot be applied for the BEMC. The probability for a distortion of the energy measurement through pile-up would exceed 50 % for a background rate of 100 kHz. To overcome this problem an analog electronics chain consisting of a fast, unipolar shaper and a subsequent analog delay line is used. The shaper has a time constant of 450 ns (FWHM) in order to reduce the pile-up window to about five bunch crossings. To match the trigger decision time the shaped signal is delayed by an analog delay line with a length of 2.4 μs [115]. The fast shaping requires a precise relative adjustment of all 472 delay lines in order to avoid channel-to-channel gain variations of the signal. Equalization of the delay lines to 60 ns is required to keep the gain variations within 1 %. The equalization achieved is better than 10 ns so that there is no contribution to the energy scale uncertainty from this source.

5.2.3 Calibration

The calibration of the BEMC is based on two contributions. Electronics gain and light collection in the stacks are factorised and monitored independently.

The gain of the electronics chain is determined with a pulser system identical to the one used for the LAr calorimeter. The pulser system measures the response of the entire electronics chain including all cables. It has also been used to transfer the initial absolute calibration from test beams to the final experiment. During data taking periods the entire electronics is calibrated once per week. The stability achieved is better than 0.1 %. This is far below other sources of calibration uncertainties.

The second contribution to BEMC calibration is light collection and detection in the calorimeter stacks. Here the concept is to obtain the initial absolute energy scale from testbeam measurements and to confirm and improve the scale in situ using electrons scattered under small angles from medium/high x_{Bj} partons, i.e. in the kinematic peak.

The initial absolute calibration of individual square stacks has been obtained from measurements with a 5 GeV electron beam at the DESY synchrotron. The individual calibration constants of channels in quadratic stacks differ only slightly with a spread of 6 %. This demonstrates the stable and well reproducible construction procedure for the optical part of the calorimeter.

In the environment of HERA $e-p$ collisions the BEMC is exposed to a cross-section of 100 nb from DIS. Deep inelastic scattering at small angles from medium/high x_{Bj} partons gives rise to a peak in the distribution of scattered electron energies at the value of the electron beam

energy. A method has been devised to use this peak for a precise determination of the calorimeter energy scale for electrons. The method has been successfully applied to the high statistics data sample collected in the 1993 and 1994 running periods [116]. The calibrated energy distribution observed in the BEMC is shown in Figure 5.17. The data points are compared to a simulation program taking into account energy losses in dead material as well as spatial inhomogeneities and all known contributions to the energy resolution.

5.2.4 Performance

The overall electromagnetic energy scale of the BEMC has been determined using the data taken in the 1994 run period. In figure 5.17 a comparison of the measured energy distribution of the leading cluster with a simulated one (shaded area) using the GRV structure function is shown after adjustment of the calibration for each individual stack using the kinematic peak method. Good matching of the data and the simulation proves the quality of the BEMC calibration and of the understanding of the detector response. In the 1994 luminosity period the global energy scale for electrons in DIS was adjusted using the kinematic peak method with a precision corresponding to 1 % dominated by systematical errors.

The energy resolution of the BEMC has initially been determined in test beam studies carried out with electron beams ranging from 1 GeV to 60 GeV. A sampling term of $10\%/\sqrt{E}$ has been found in agreement with expectations from the mechanical design. The average noise per calorimeter stack was measured to be 130 MeV in the real H1 environment. Energy clustering is carried out over stack nonets giving rise to a contribution of 390 MeV from noise for each cluster. The constant term in energy resolution for a single stack was found to be 1.7 %. Using the observed shape of the kinematic peak the residual stack-to-stack calibration uncertainty has been determined to be 0.3% for electrons depositing more than 95% of their energy in a single stack.

The inherent mechanical non-uniformities in the stack construction due to the wavelength shifters cause an impact point dependent response to electromagnetic showers. Extensive studies carried out with test beam data and shower simulations exhibit a regular pattern of inhomogeneities with losses up to 8 % close to the wavelength shifters. A look-up table has been created to correct this impact point dependence. Electrons sharing their energy among many stacks receive an additional contribution of 3 % to their effective resolution caused by imperfections in the correction procedure.

The matching of electron tracks measured in the tracking detectors to the cluster position reconstructed in the BEMC has been determined from DIS events with the electron scattered into the BEMC. Based on the known attenuation properties of light in the scintillator plates a position resolution of 7 mm transverse to the beam has been achieved.

Interacting hadrons deposit typically 45 % of their energy in the BEMC. A satisfactory hadronic resolution of $\approx 80\%/\sqrt{E}$ has been estimated in detector simulations by combining the measurements in the BEMC and in the instrumented iron structure behind it with proper weighting.

5.3 The plug calorimeter.

The plug calorimeter (PLUG) has been designed to close the gap of acceptance for the energy flow measurements between the beam pipe ($\theta \approx 0.6$ °) and the forward part of the LAr calorimeter ($\theta \approx 3.5$ °). Its main task is to minimise the missing part of the total transverse momentum due to hadrons emitted close to the beam pipe. In addition the energy, emitted into a narrow cone

Position	$+476 \leq z \leq +545$ cm
Overall radius	$6 \leq r \leq 32$ cm
Radius of detector planes	$6 \leq r \leq 25$ cm
Polar angular range	$12.5 \leq \theta \leq 58$ mrad
Number of detectors	$8 \times 84 = 672$
Number of electronic channels	$4 \times 84 = 336$
Total length	69 cm $\equiv 4.25\lambda_{abs} \equiv 44.6X_0$
Weight	1.48 t

Table 5.2: Global parameters of the PLUG calorimeter

around the beam pipe can be used to separate the proton jet as well as to veto beam gas and beam wall background.

Owing to the geometrical constraints – the available space inside the return yoke of the H1 magnet was restricted to a cylindrical hole of ≈ 0.7 m length and a diameter of ≈ 0.7 m around the beam axis – only a most compact calorimeter could fit. Facing the physical requirements of good angular resolution, nearly full containment and linearity, the solution was a sampling calorimeter consisting of nine copper absorber plates interleaved with eight sensitive layers of large area silicon detectors [78]. The most important construction parameters are given in Table 5.2.

Figure 5.18 shows a schematic view of one of the two half-cylindrical parts of the PLUG calorimeter, each mounted in one half of the return yoke. The detector modules are placed within 15 mm wide slots between the absorber plates. These are sealed and easy to replace entities, which contain one half of a detector plane each. Between two 5 mm copper plates a G10 readout board, equipped with 42 silicon detectors of 400 μm thickness, is placed (Figure 5.18, left part). A detailed description of the detector technology can be found in [117]. Typical characteristics of single silicon detectors, as measured in the laboratory, are given in Figure 5.19. Due to a special edge-protection procedure 32 quadratic (5×5 cm^2), six triangular and four rectangular detectors cover one half of the detector plane in a mosaic structure nearly completely, leaving only 4% of the total area inactive. A total of 672 detectors have been installed.

The readout electronics of the PLUG are included in the analog chain of the H1 calorimeters and use the same components (see Section 5.1.6). The 672 detectors are read out in 336 pairs of channels. Trigger towers are built by merging the signals from subsequent channels in the $z-$direction.

The calibration of the ADC output in units of visible energy rests on an absolute energy measurement using α-particles. Its conversion into total absorbed energy is based on detailed MC-simulation studies of electromagnetic and hadronic shower developments in silicon instrumented calorimeters in comparison with test measurements [118, 119, 120, 121, 122].

Since March 1994 the PLUG was operated with 8 instrumented detector planes. During luminosity operation sharp increases of detector dark currents up to 15 % were observed which could be correlated with failures of HERA machine components and consequential increase in proton-related backgrounds (see references [123, 124]).

The energy resolution of the PLUG calorimeter suffers from both the amount of dead material in front of the device and the energy leakage. Nevertheless its value of about $150\%/\sqrt{E}$, evaluated from experiment supported MC-calculations [121], turns out to be sufficient for the tasks within the H1 experiment. As an illustration of the PLUG-calorimeter response to selected low-Q^2 events the distribution of the total energy is shown in Figure 5.20. It compares remarkably well with MC-simulations produced using the Colour Dipole Model (LEPTO 6.1 MEAR, see reference [125]).

5.4 The tail catcher (TC)

In order to measure the hadronic energy leaking out of the LAr calorimeter and BEMC, eleven of the sixteen limited streamer tube (LST) layers of the instrumented iron are equipped with readout electrodes (pads, see also Section 6). Here we describe the features of the LST tail catcher (TC) relevant for the energy measurement which is based on the analog readout of the pad signals. For more details see reference [126].

The pad sizes vary from 28×28 cm^2 in the endcaps up to about 50×40 cm^2 in the barrel region. The pad signals from the five inner (six outer) layers are summed up by tower builders (TB) to form the front (back) tower signals. The differential analog signals from the TB's are then relayed in groups of 12 to the cable stations (CS) which reorganise the signals from the towers into groups of 16. From there the signals are sent to the analog superboards (SB) whose function is to amplify, integrate and store the analog signals in groups of 128 channels each. The geometry of the tower structure is briefly described in Table 5.3.

Region	θ range	Segmentation	# of channels
Forward end cap	$6° \leq \theta \leq 33°$	x and y	552
Central barrel	$33° \leq \theta \leq 137°$	ϕ and z	2784
Backward end cap	$137° \leq \theta \leq 172°$	x and y	552

Table 5.3: Layout of the pad readout of the iron instrumentation.

5.4.1 Electronics

The amplifier used on the TB-boards allows for the measurement of single muons as well as hadronic showers without saturation. The signals have a dynamic range of 0.75 mV to 1 V. Each superboard accepts the input of 128 channels which are individually processed by a line receiver, shaper and sample & hold. The line receiver and shaper are modified versions of the LAr calorimeter system cards, while the sample & hold cards are identical to those used in the LAr readout system. The signals are multiplexed and held in the output buffer to be read by the analog receiving unit (ANRU). The data are then zero suppressed and corrected in the DSP and read out (see Section 5.1.6).

The calibration of the superboards is done by sending calibration pulses through the analog readout chain beginning at the tower builder board. The calibration constants are downloaded into the DSPs to correct for the channel to channel variations and non-linearities. Channel to channel variations are less than 2% for 3888 channels .

During data taking and calibration, acquisition is controlled by the LAr calorimeter OS9 system. Normal data and calibration results can also be collected in stand-alone mode, in which case the local TC test station is used.

5.4.2 Energy calibration

The conversion of the signal charge Q_i, as measured in a tower i, to hadronic energy $E_{had,i}$ is given by [127]:

$$E_{had,i} = c_1 c_{3,i} \frac{Q_{had,i}}{c_2}$$

The general hadronic energy calibration constant c_1 has been determined in test measurements at CERN using pion and muon beams [128]. The parameter c_2 gives the tower charge of an average minimum ionizing particle, i.e. a muon, at an angle of incidence of 0° with respect to

the normal of the LST chambers. The intercalibration factor for each tower, $c_{3,i}$, describes the tower to tower variations of the measured charge.

The constant c_1 is derived from the linear relationship between the incident pion energy and the ratio Q_π/Q_μ of the measured charge for pions and muons. Defined in this way c_1 is essentially determined by the sampling fraction of the calorimeter and the gas used in the chambers. It does not depend on the angle of incidence of the hadrons and is also insensitive (in wide limits) to the operating conditions [128]. The parameter c_2 and the charge $Q_{had,i}$ on the other hand vary with high voltage, pressure, gas composition and temperature. Since the atmospheric pressure is the only one of these operating parameters which can change rather quickly, we compensate for this effect by regulating the high voltage (see section 6.1.3 of the muon system).

The transformation of ADC counts into charge is done online during the readout process according to

$$Q_i = p_{1,i}(ADC_i - p_{0,i})$$

The pedestals $p_{0,i}$ are obtained from random triggers and the gains $p_{1,i}$ are given by the slope of the test pulser response curves of the electronic calibration. Both varied by < 2 % over the whole data taking period. Zero suppression allows to read out only pads above a certain threshold.

The parameters c_2 and $c_{3,i}$ are determined from cosmic muons [129], triggered by opposite pairs of barrel or endcap modules in special cosmic runs. The data have to be corrected for non-normal incidence with respect to the chamber plane. In order to keep the corrections small, only tracks with $\tan\theta < 0.8$ are considered in the calibration procedure. The intercalibration constants $c_{3,i}$ vary by $\sim 10\%$ within one module. There are larger module to module variations depending on the module location in the iron yoke, mainly due to different gas temperatures and pad sizes.

5.4.3 Performance

The performance of the tail catcher has been studied in test measurements at CERN with π and μ beams of 10 to 80 GeV [128]. The energy response for single pions is linear up to at least 40 GeV and the energy resolution is $\sigma/E \simeq 100\%/\sqrt{E}$.

The calibration of the tail catcher at HERA is done by cosmic muons as described above and taking the energy scale from the CERN test results as $c_1 = (0.233 \pm 0.002)$ GeV. Figure 5.21 shows representative muon spectra of a complete module for the inner and outer towers. Clean muon signals can be seen with mean values far beyond the pedestals. The widths relative to the most probable values are ~ 35 %. The ratio of the mean values of inner and outer towers corresponds to the expected value of 0.8. We do not observe any effect of the magnetic field in the iron yoke on the muon signal. The intercalibration constants vary among the detector by $\sim 20\%$ (mostly due to a vertical temperature gradient within H1) with a long term stability of $\sim 10\%$. They are regularly measured with cosmic muons.

Important for energy measurements with the H1 detector is the combination of the tail catcher with the LAr calorimeter. The energy response can be symmetrized and the energy resolution can be improved by including the information of the tail catcher [87, 111, 93]. Corrections for energy losses in dead materials have to be done for each event. Inside the tail catcher dead material appears as cracks between towers, in particular in the transition region between the end cap and barrel yoke. Corrections between adjacent towers are calculated using the ratio of the tower areas with and without the crack as correction factor. More involved corrections are necessary for the material between the calorimeters, e.g. the cryostat wall and coil between the LAr calorimeter and the TC. For this purpose a hadronic object in the LAr calorimeter is geometrically linked with a TC cluster into a generalized cluster. The energy

losses are estimated [111] by a linear interpolation of the energy deposit in the last layer of the LAr calorimeter $E_{LAr,last}$, and the first layer of the tail catcher, $E_{TC,first}$:

$$E_{loss} = \alpha(\theta)(E_{LAr,last} + 0.5E_{TC,first})$$

The calculated energy loss is distributed among the cells in proportion to their energy contents. The function α depends on the polar angle θ of the shower or, more precisely, on the thickness Δt_{dead} of the material between the two calorimeters and are almost independent of the energy over a large range. It has been determined as a function of Δt_{dead} from dedicated test measurements at CERN [111]. At H1 Δt_{dead} varies from 0.5 up to 2.4 interaction lengths depending on the polar angle θ. The corresponding values for α range from 0.1 up to 1.1. The uncertainty of the energy correction was estimated to $\sim 20\%$. Figure 5.12 shows the effect of the combined LAr and TC measurements with energy loss corrections from test beam results.

Calibration and correction procedures have been successfully transferred from the test beam measurements to the H1 detector at HERA, where the balance of the transverse hadronic energy p_{th} and the transverse electron energy p_{te} in neutral current events can be used to check the overall hadronic calibration. Figure 5.22 shows the ratio p_{th}/p_{te} of p_{th} as measured with the hadronic section of the LAr calorimeter and the TC (including the above mentioned corrections) and p_{te} as measured with the electromagnetic section of the LAr (or BEMC) versus the energy fraction deposited in the TC. The distribution is flat, demonstrating that calibration and corrections have been treated properly.

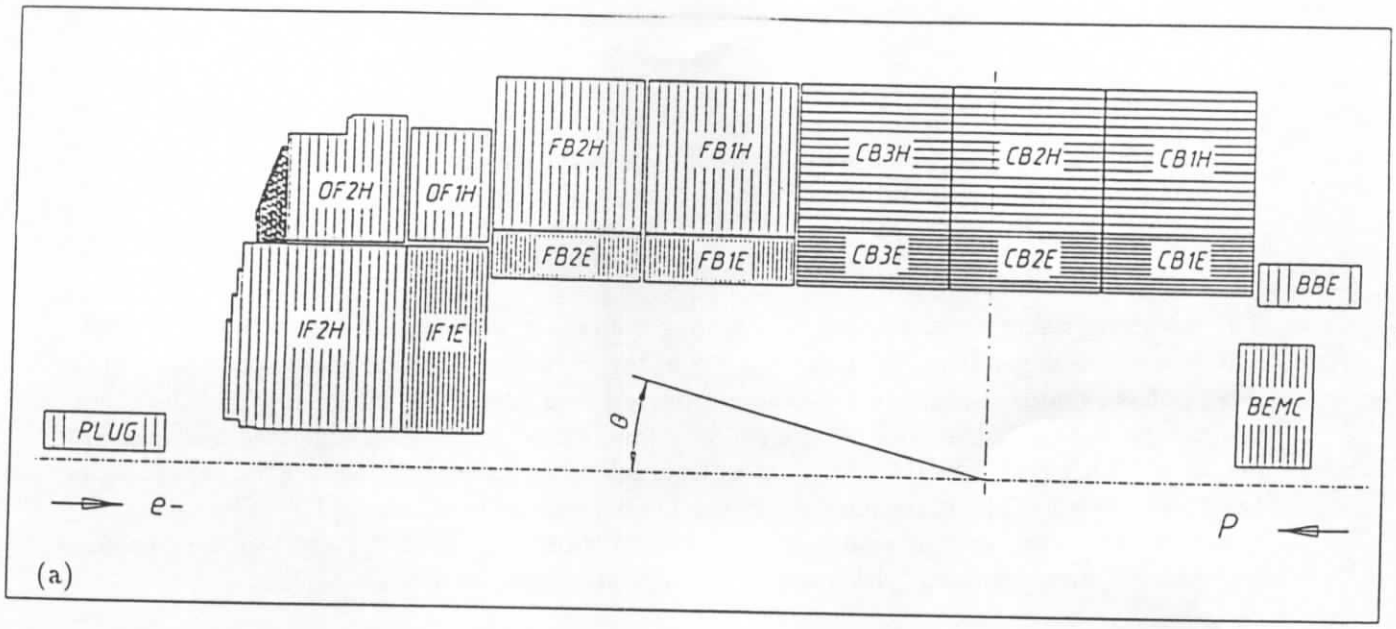

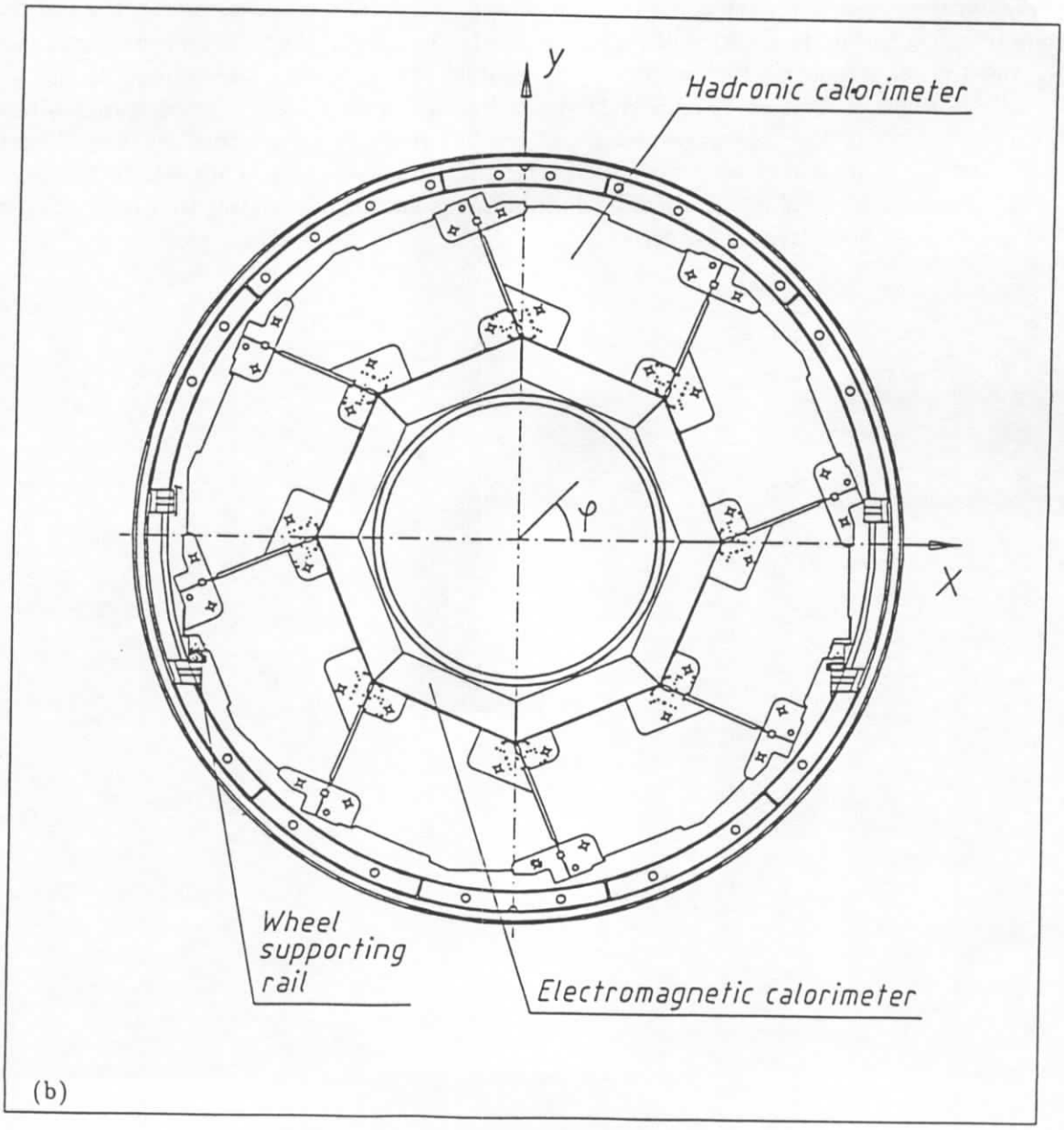

Figure 5.1: a) Longitudinal view of calorimeters. b) Radial view of a LAr calorimeter wheel.

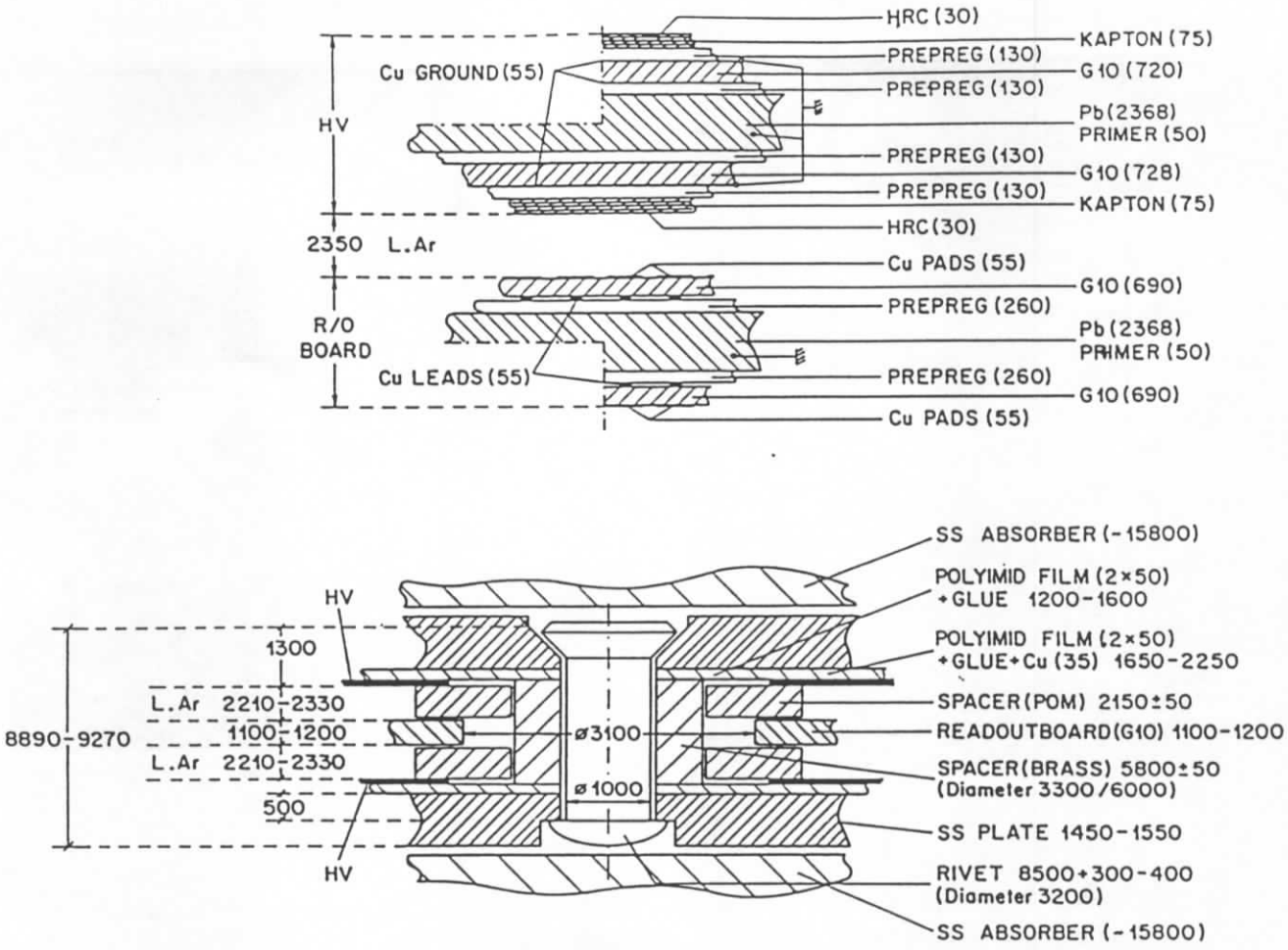

Figure 5.2: Schematic structure of the readout cell: a) e.m. cell, b) hadronic cell. All dimensions given in μm.

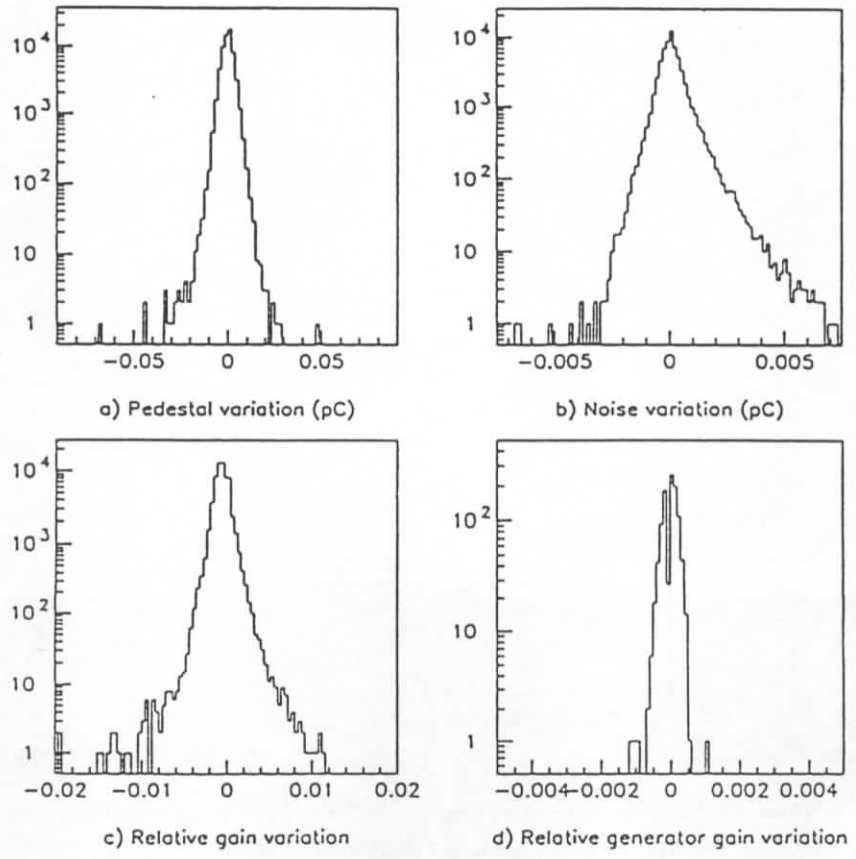

Figure 5.3: Relative stability of the electronic chain over one month.

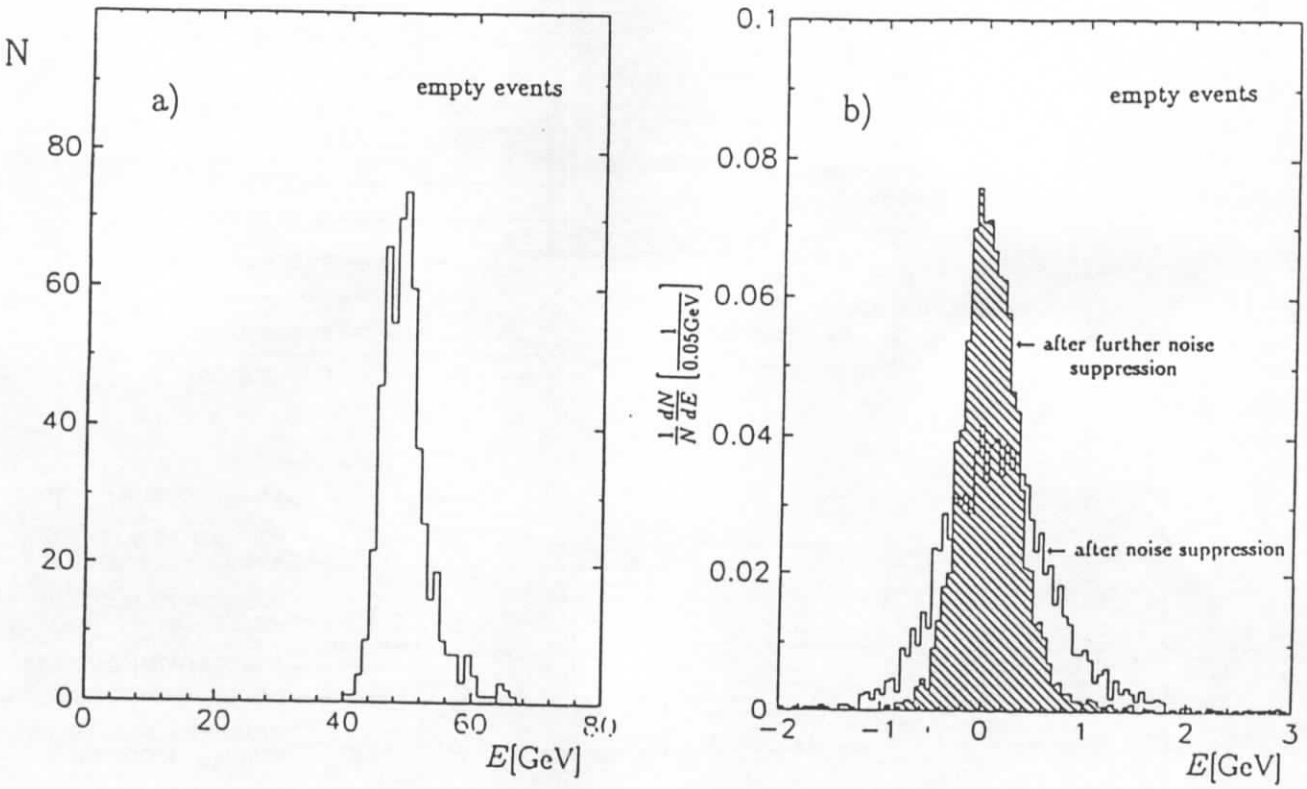

Figure 5.4: Noise contribution summed over all channels of the LAr calorimeter: a) after applying a $+2\sigma$ noise threshold, b) after noise suppression.

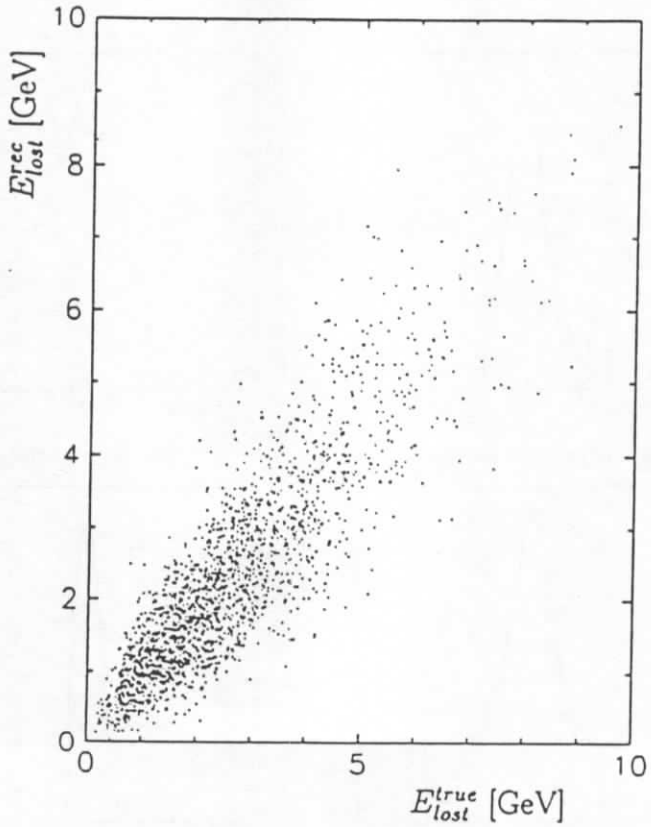

Figure 5.5: Correlation between the true energy lost in front of the calorimeter (E^{true}_{lost}) and its estimation in the reconstruction (E^{rec}_{lost}) for simulated low Q^2 DIS.

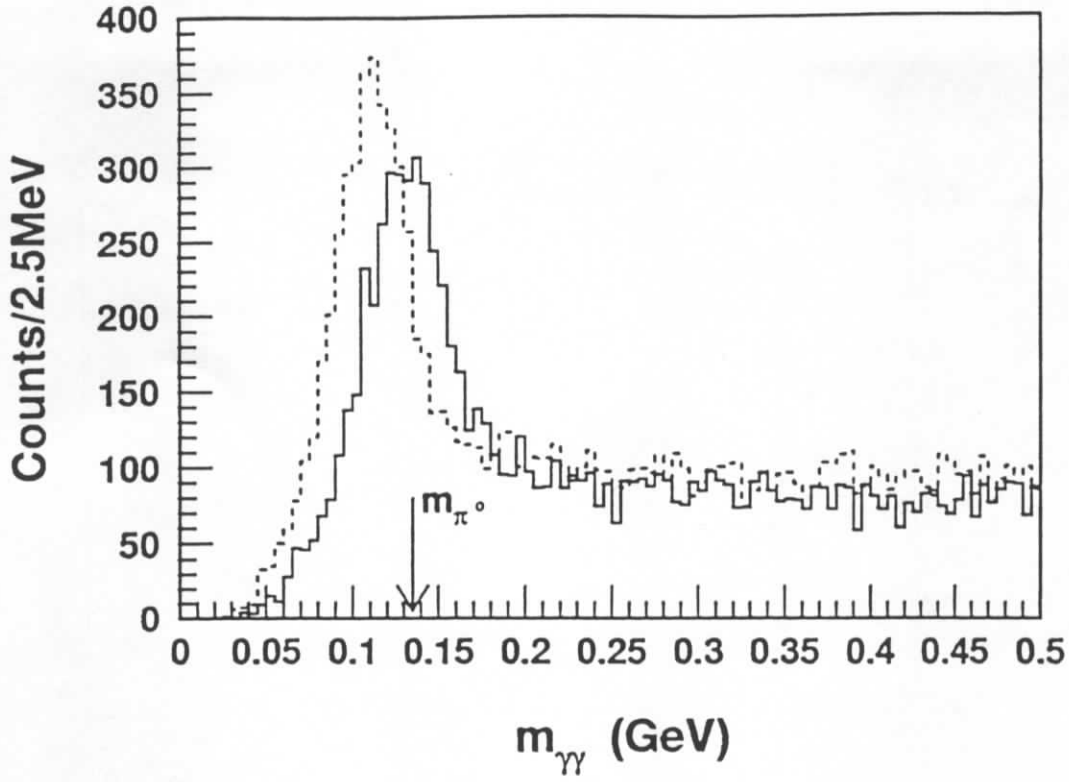

Figure 5.6: The effective mass of two photons before (dashed histogram) and after (hatched one) the dead material correction.

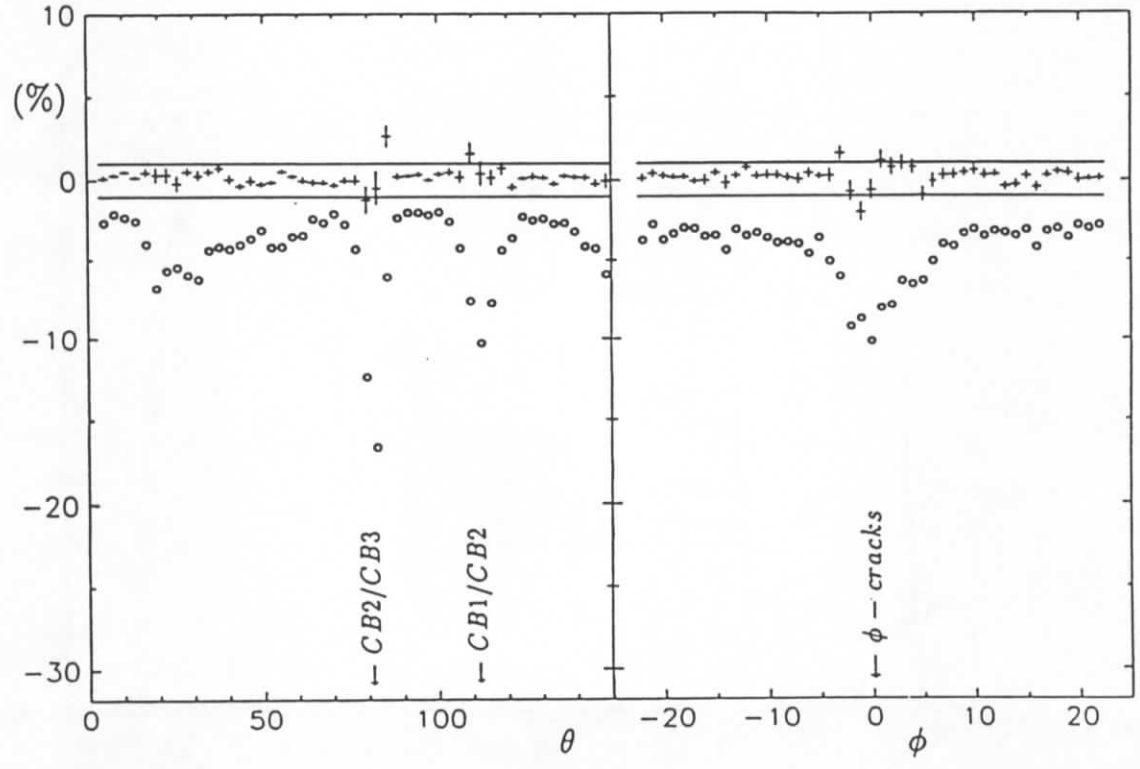

Figure 5.7: Performance of the dead material correction for simulated pions at 20 GeV. Ratios $(-E^{true}_{lost})/E^{true}_{tot}$ (circles) and $(E^{rec}_{lost} - E^{true}_{lost})/E^{true}_{tot}$ (crosses) are shown as function of θ and ϕ (both given in degrees). Before the correction a crack structure is clearly seen. Solid lines correspond to $\pm 1\%$ deviations from the true energy .

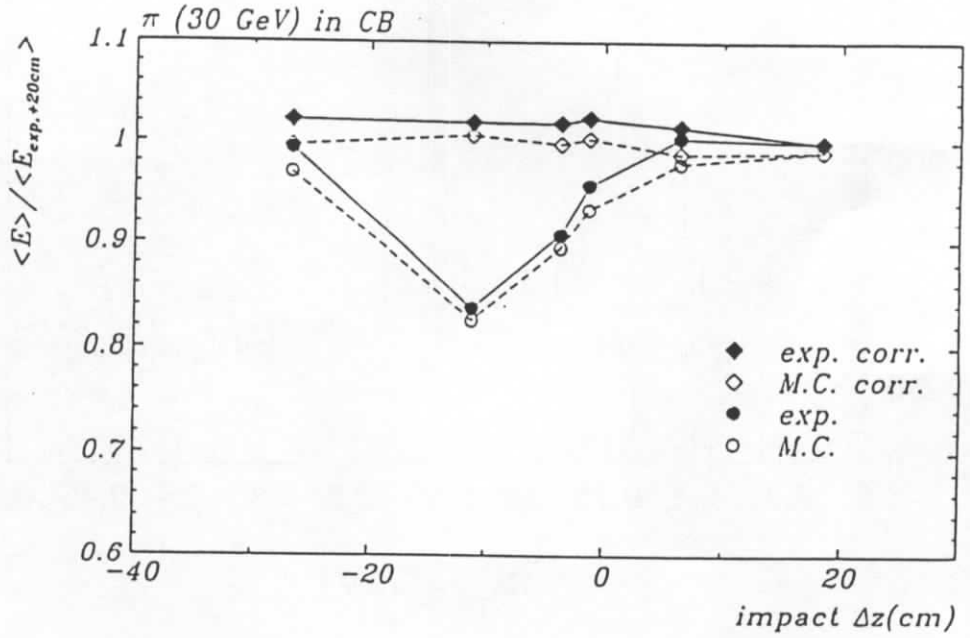

Figure 5.8: Response across the CB2/CB3 z crack in a pion test beam of 30 GeV at CERN.

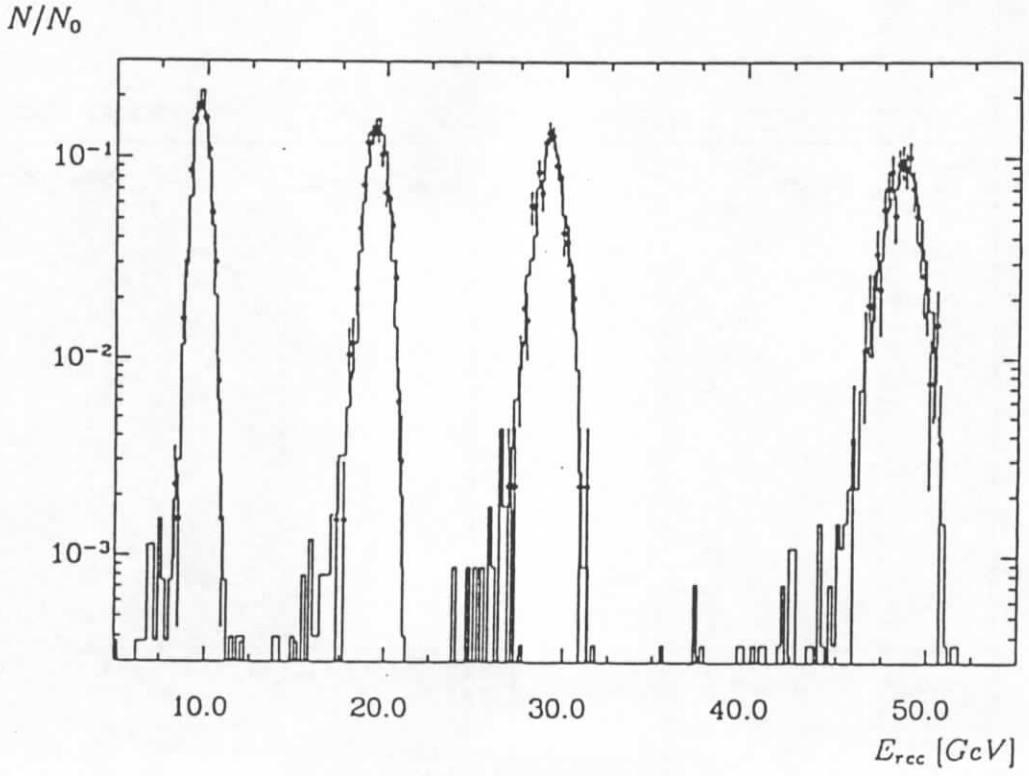

Figure 5.9: Reconstructed energy for data (histogram) and MC (points) for electron energies of 10, 20, 30 and 50 GeV (BBE Wheel).

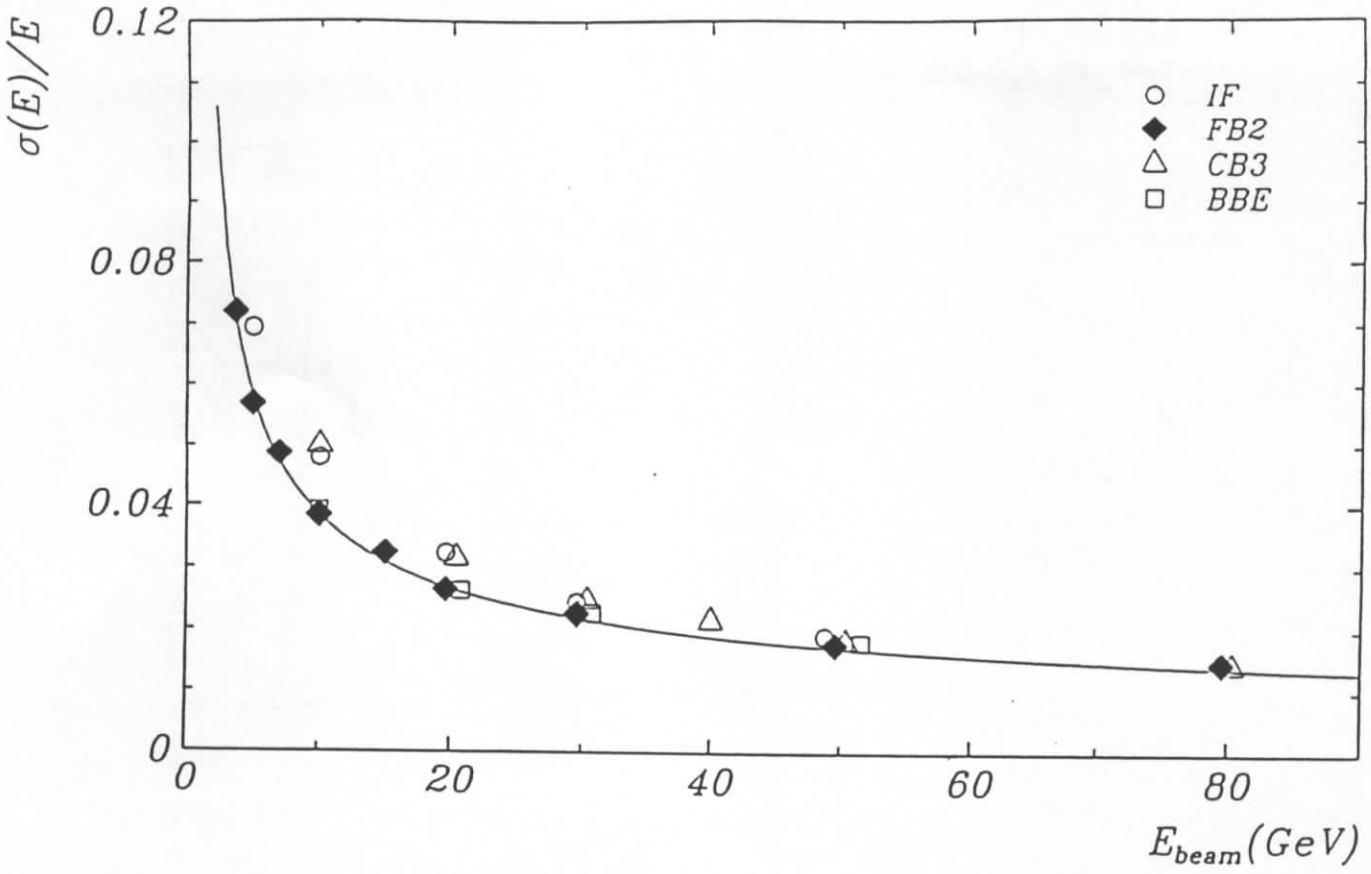

Figure 5.10: Energy resolution as function of electron energy for wheels BBE, CB, FB2 and IF. Solid line: parametrization for FB2.

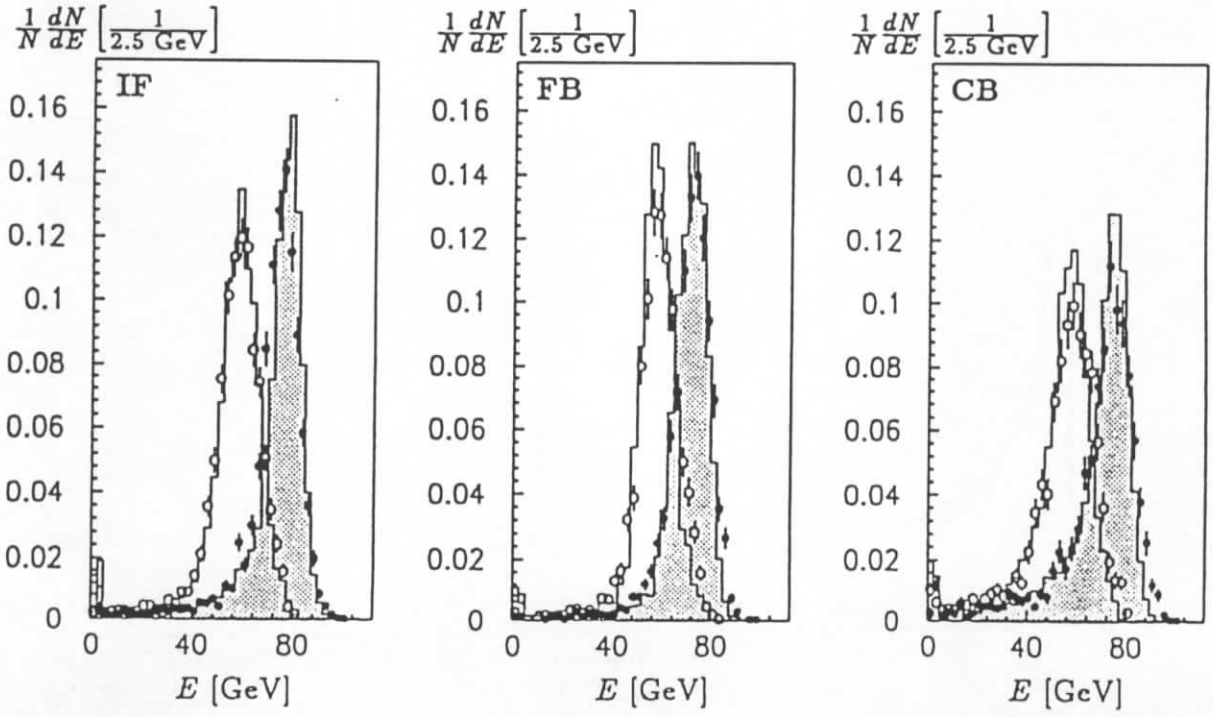

Figure 5.11: Energy reconstruction for pions at 80 GeV for wheels CB, FB and IF on the electromagnetic (open) and hadronic energy scale (closed, shadowed) for data (histogram) and MC (points).

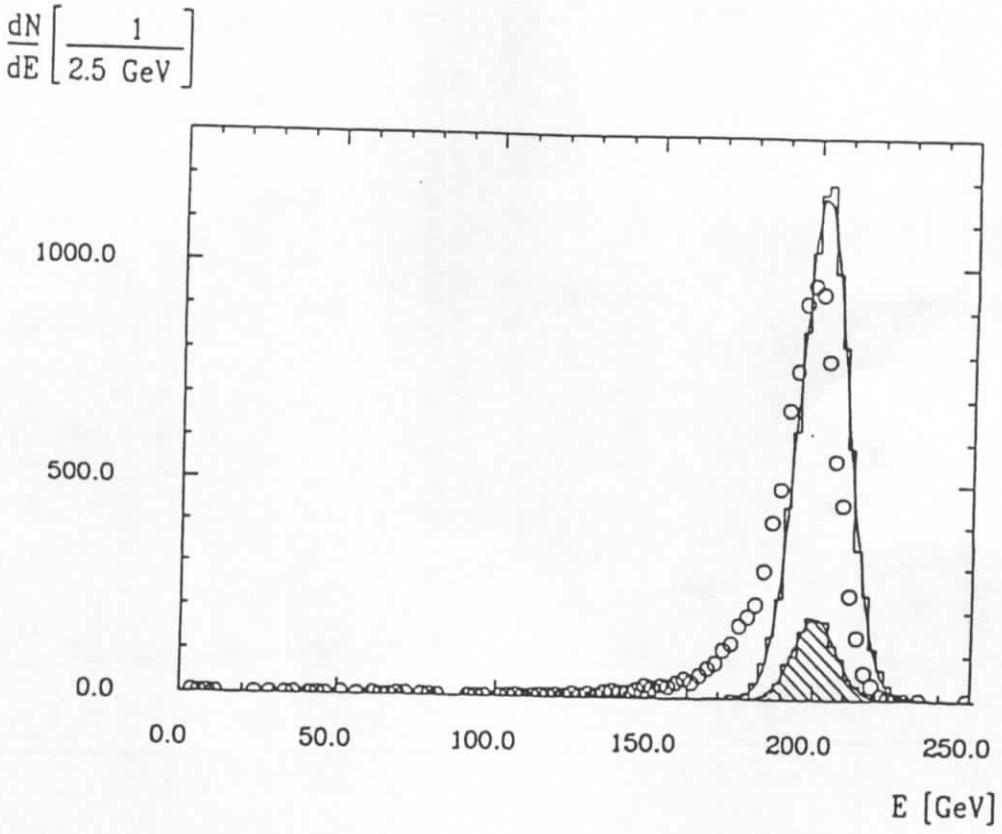

Figure 5.12: Energy reconstruction for pions at 205 GeV for wheel IF with tail catcher (open histogram), only IF (circles) and for events fully contained in IF. Solid lines: fitted Gaussian distributions.

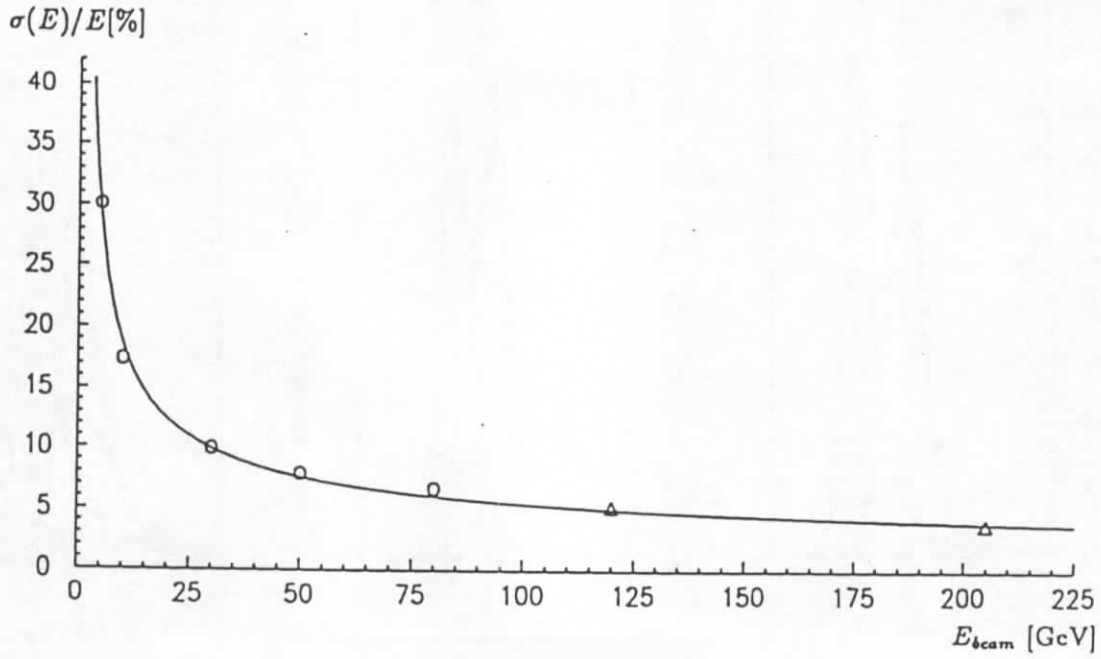

Figure 5.13: Energy resolution as function of pion energy for wheel IF. Circles: IF only , triangles: IF + iron tail catcher. Parametrization according to equation (2) with A = (50.7 ± 0.1)% [$\sqrt{GeV}$], B = 0.9 GeV and C = 1.6 ± 0.1%.

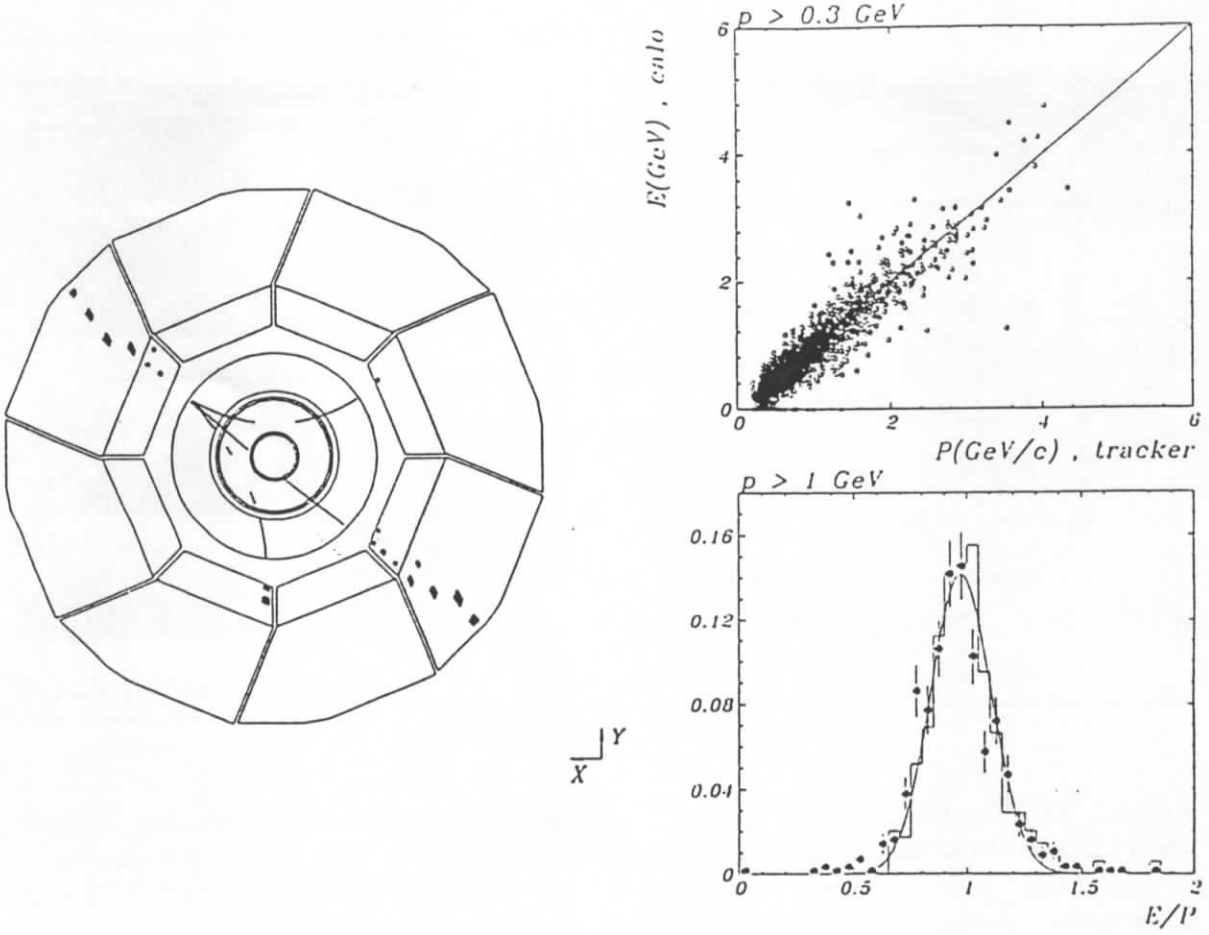

Figure 5.14: Energy/momentum match of electrons generated by cosmic muons measured in the CJC and LAr CB wheels.

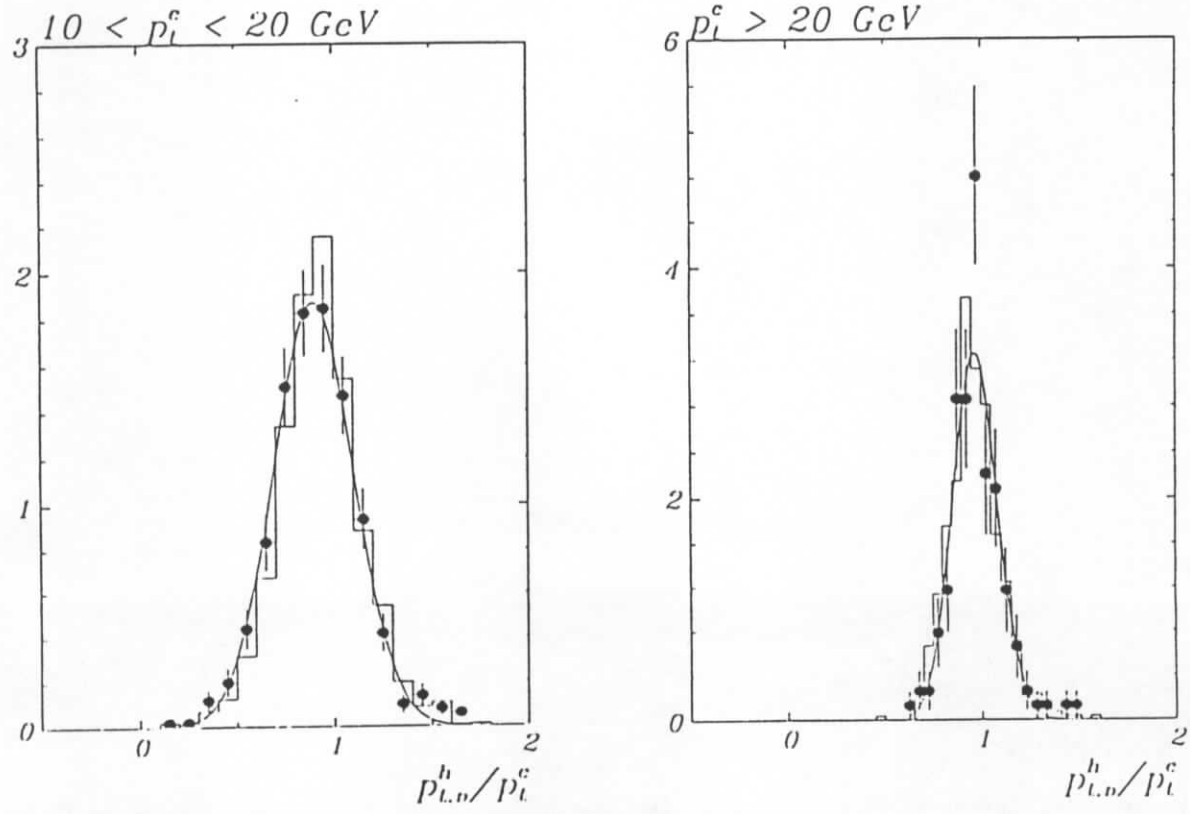

Figure 5.15: Transverse momentum balance p_{th}/p_{te} for both scattered electron and hadronic shower detected in the LAr calorimeter for data (open symbols) and Monte Carlo (histogram).

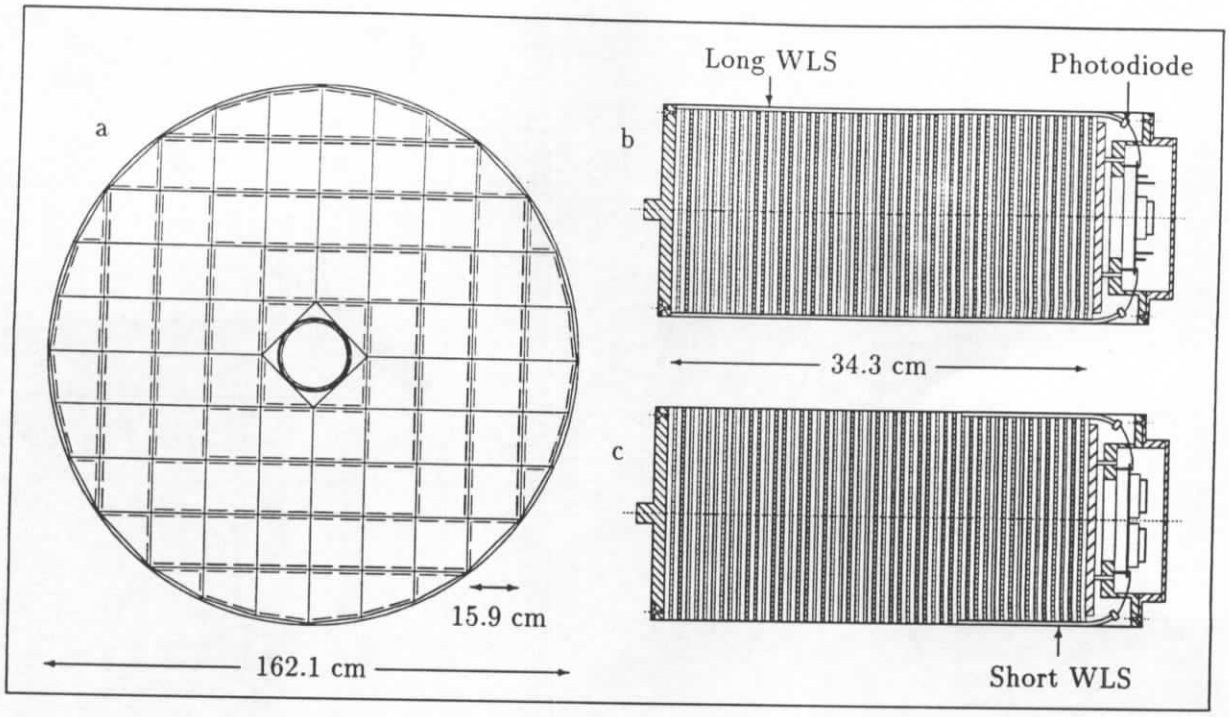

Figure 5.16: Transverse view of the BEMC barrel and longitudinal cross-sections of BEMC stacks, The positions of all long WLS in the BEMC are marked in (a). The scintillating light is read out transversely via long WLS covering the full length of the BEMC stacks (b). In square and trapezoid stacks the last 15 sampling layers are read out via short WLS (c).

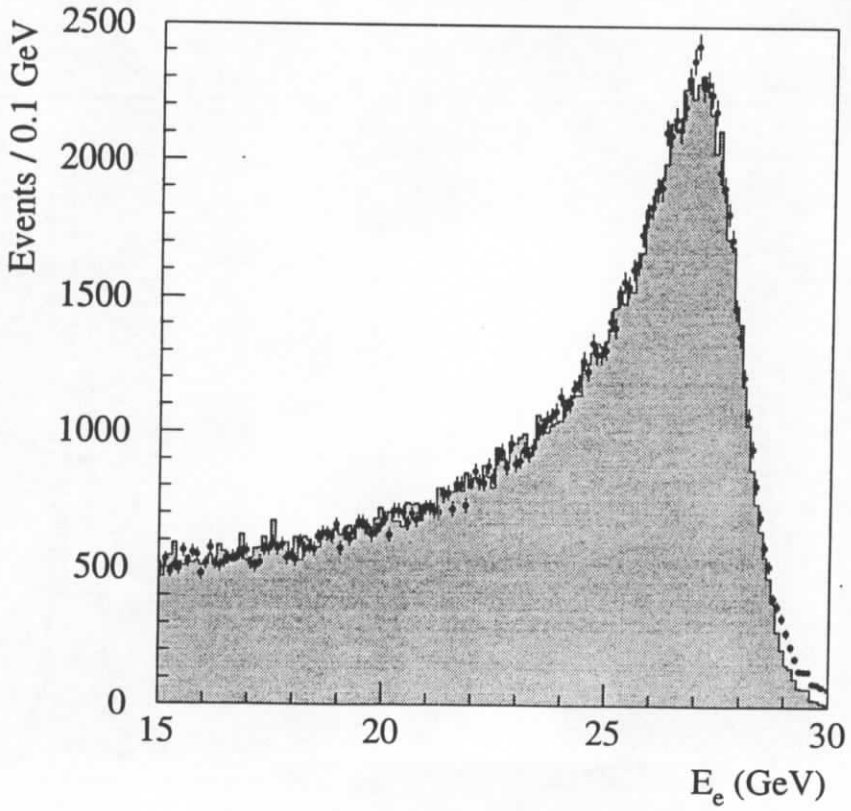

Figure 5.17: Energy spectrum of low Q^2 DIS electrons scattered in the region of square BEMC stacks. For simulation (shaded area) the structure function GRV is used.

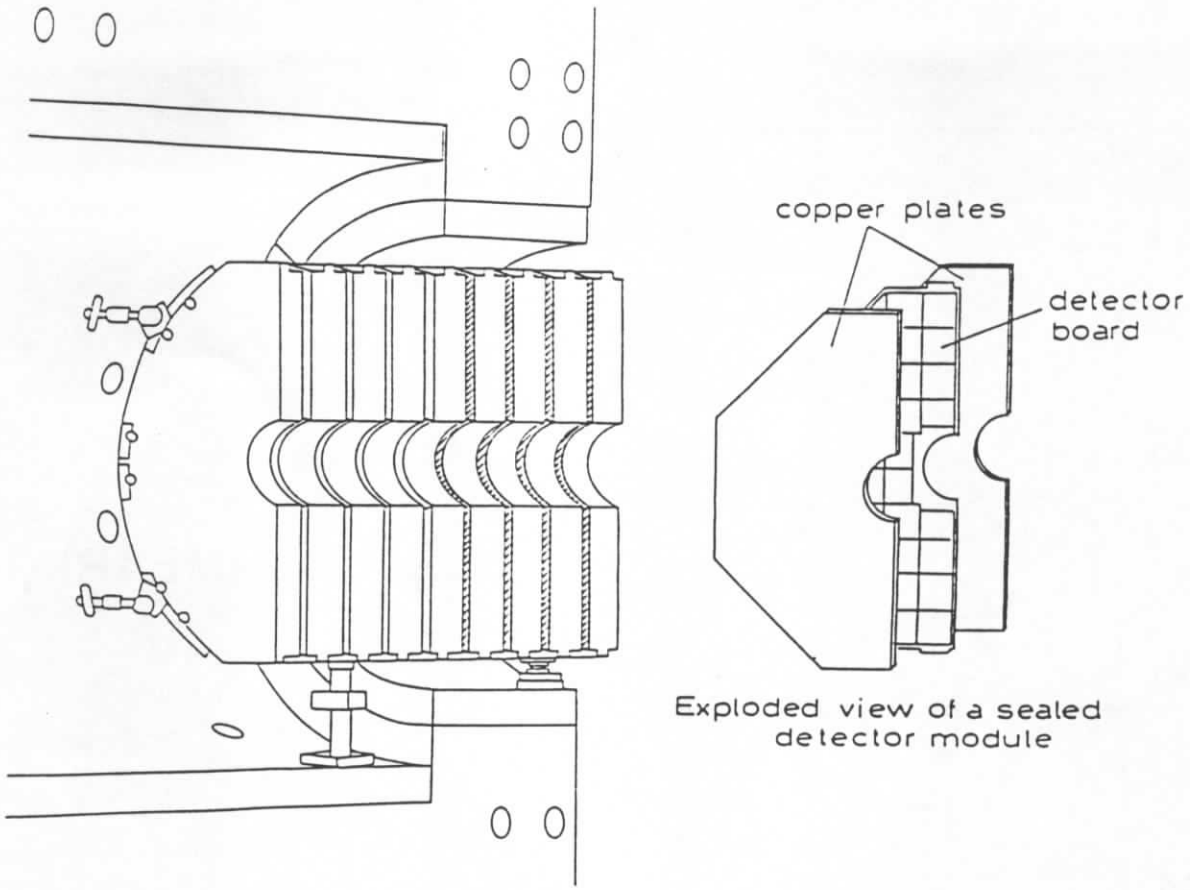

Figure 5.18: Cross sectional view of the PLUG calorimeter.

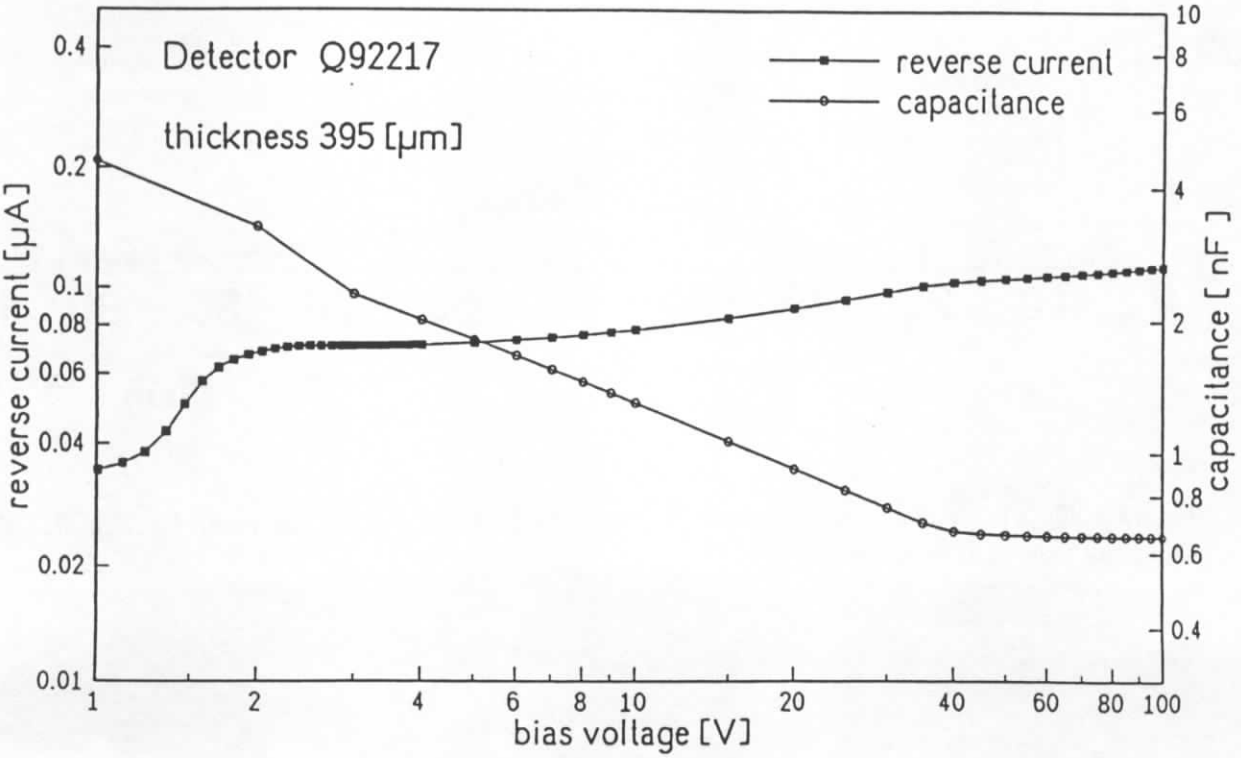

Figure 5.19: Typical $I/V-$ and $C/V-$characteristics of the PLUG Si-detectors.

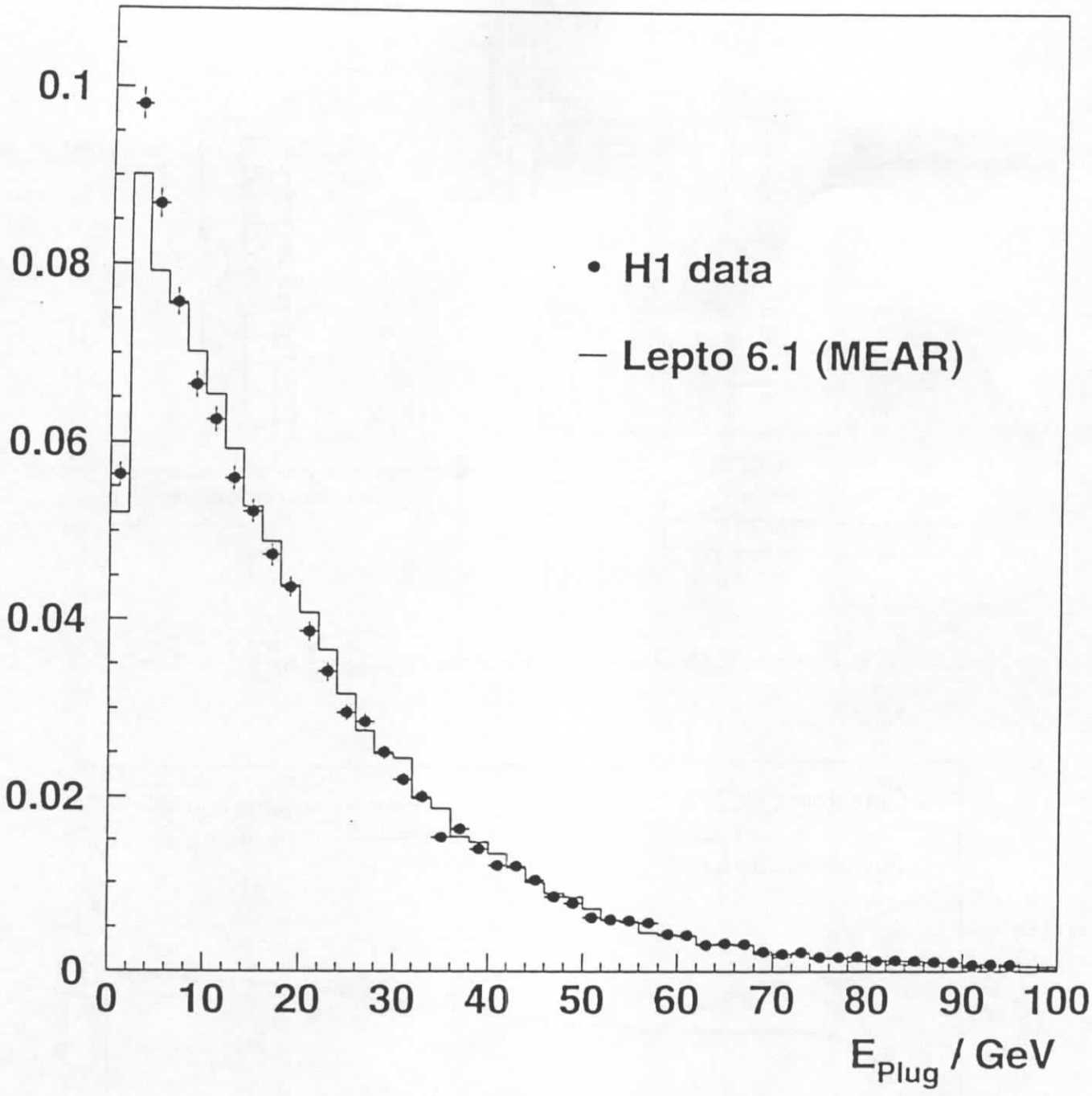

Figure 5.20: PLUG response to *ep* events compared to a MC simulation (solid line) produced using the Colour Dipole Model.

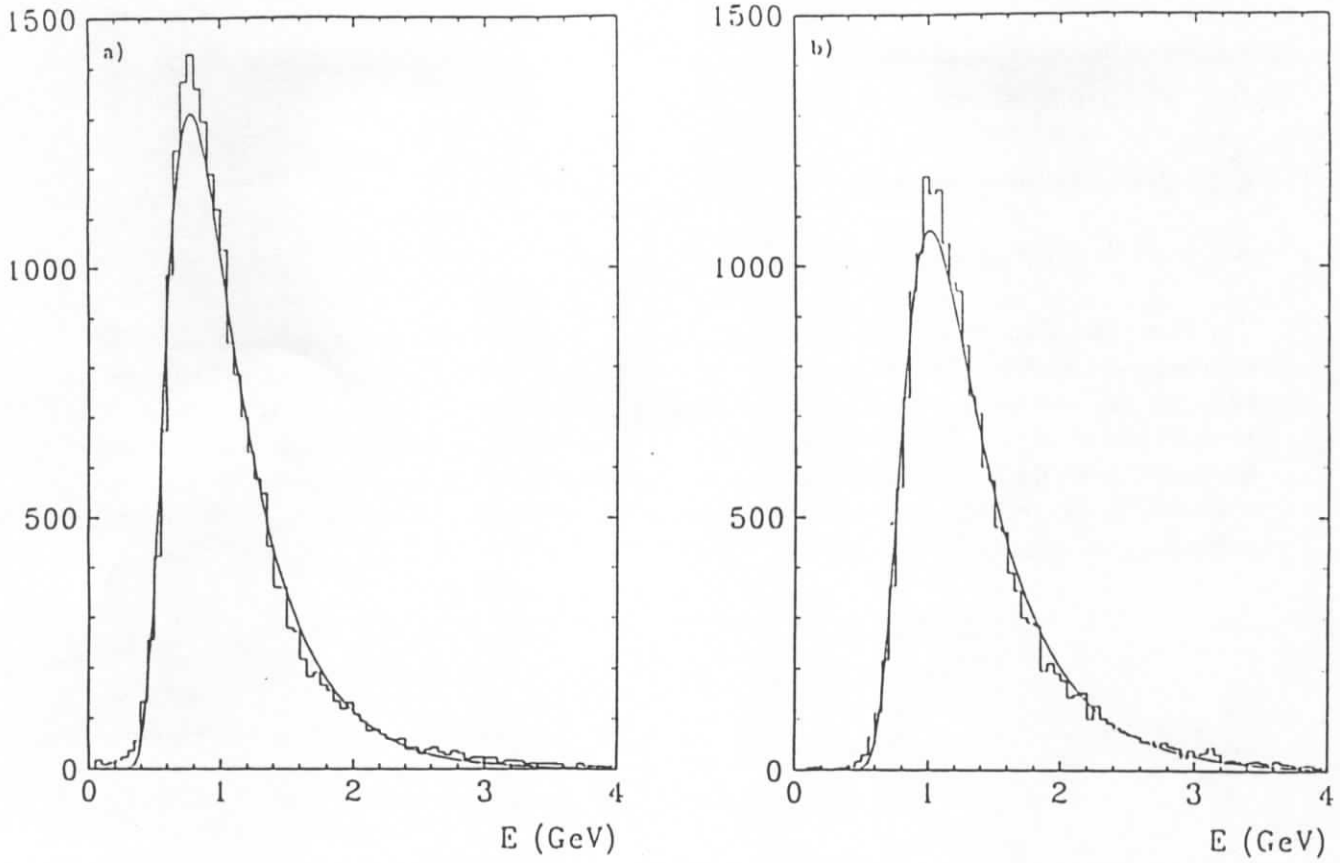

Figure 5.21: Muon spectra summed over a complete module for a) inner towers normalized to 4 planes, and b) outer towers normalized to 5 planes. The curves are fits to a Landau distribution.

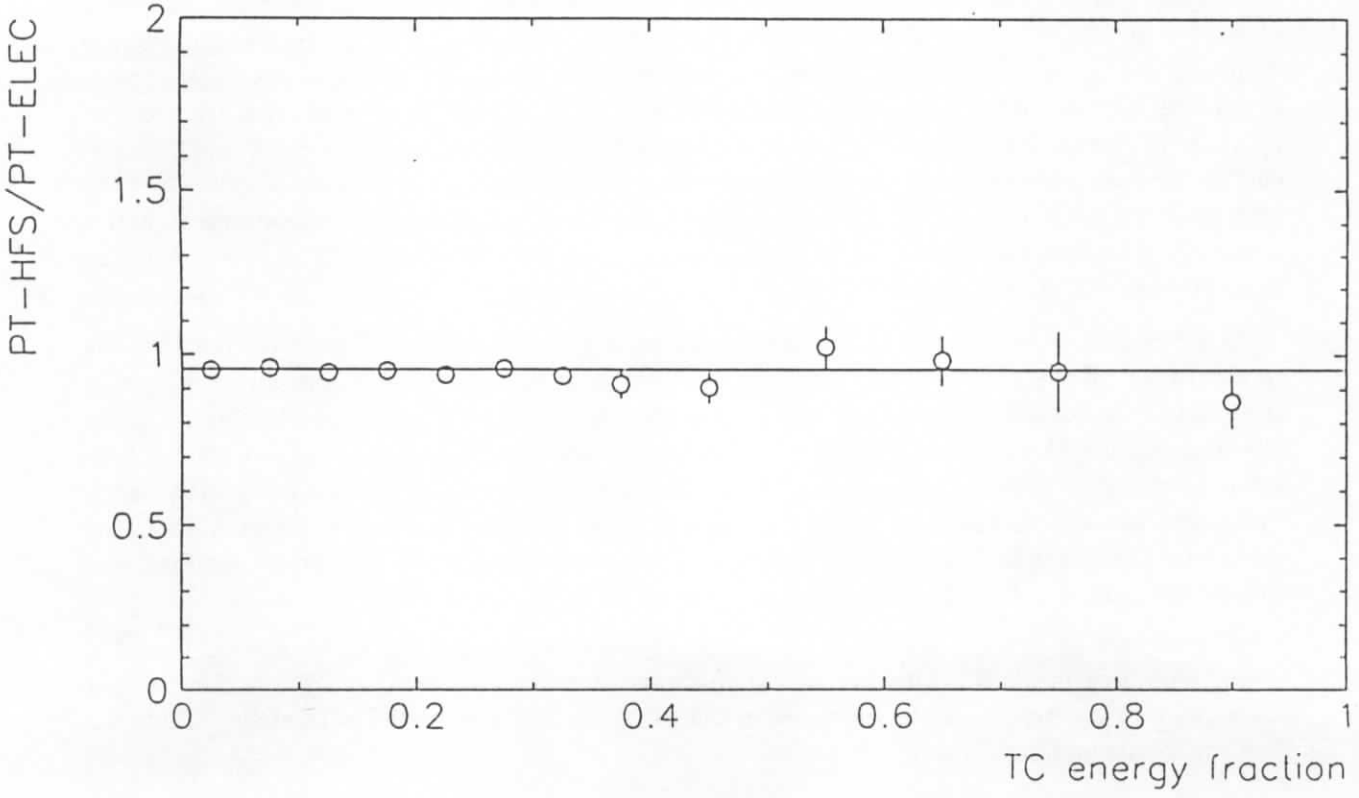

Figure 5.22: Ratio of the total transverse hadronic energy- including the corrected TC energy - and the transverse electron energy versus the energy fraction in the TC, for NC events. The line is a fit to the data.

6 Muon system

6.1 Iron instrumentation

6.1.1 The limited streamer tubes

The iron yoke of the main solenoid magnet surrounds all major detector components of H1. It is interleaved with slits which are equipped with limited streamer tubes (LST). They serve as hadronic tail catcher and for the measurement of penetrating tracks. Luranyl [130] was used to build the chambers since PVC tubes [131] were excluded for safety reasons [132]. Luranyl is a halogen free plastic material which can be extruded with sufficient precision. It can also be coated with the graphite paint needed to obtain the required surface resistivity. Some features are listed in Table 6.1.

Density	1.06 g cm^{-3}
Thermal expansion (23 - 80 °C)	$0.6 - 0.7 \times 10^{-4}$
Surface resistivity	$10^{14}\ \Omega$
Softening point	100 °C

Table 6.1: Basic properties of Luranyl [130].

The basic chamber elements are extruded eightfold profiles with a cell surface size of 10×10 mm^2. The mechanical precision achieved is 0.1 mm, the straightness of the profiles is better than 1 mm per m. The profiles are coated with graphite paint to yield a low surface resistivity of $\approx 10 - 30$ k$\Omega/\Box$. The HV is applied to this surface. A silver coated Cu-Be wire of 100 μm diameter is at ground potential. The wire is kept in place by spacers every 50 cm. The profiles are closed with a Luranyl cover with high resistivity of ≈ 10 M$\Omega/\Box$. The profiles are grouped by pairs in a gas tight box of Luranyl. All connections to the chamber are provided on one end of the box. Several boxes are put together to form a complete streamer tube layer. On the high resistivity side planes of either strips or pads are glued onto the boxes containing 16 active elements. The layers are put onto an aluminium plate and wrapped into a non conducting foil to guarantee electrical insulation.

A schematic view of the basic structure is given in Figure 6.1, while Figure 6.2 displays the configuration of the planes within the iron together with an indication where strips and pads are located. As an example, the instrumentation of a barrel octant is shown. Starting from the interaction point there is first a so-called muon-box installed in front of the iron containing three layers (two layers with strips perpendicular to the wire direction and a third layer with pads). Pad layers are also installed in the first three iron slits. The fourth slit is twice as wide as the others and houses a strip and a pad layer. Pad layers are inserted in the remaining five slits. Behind the iron is a second muon-box with three planes.

The signals of consecutive pads are added (5 inner + 6 outer layers) providing two-fold energy sampling in depth. All wire- and strip-signals are read out digitally. Three dimensional space-points from tracks can be obtained in the three chambers equipped with strips. Table 6.2 lists some parameters of the LST detector.

6.1.2 Gas system

Due to safety requirements the chambers are operated with a non-inflammable three component gas mixture of CO_2, argon and isobutane with relative volume fractions of 88 %, 2.5 %, and

Total size	4000 m^2
Nr. of profiles	13000
Nr. of wires	103000
Nr. of strips	28700
Nr. of analog channels	3888
Angular coverage	$6° \leq \theta \leq 172°$

Table 6.2: The LST detector.

9.5 %. The total gas volume amounts to 36 m^3. Different parallel circuits supply the detector with gas. The flow in each branch can be adjusted with needle valves and is measured with computer readable flow meters. 192 branches are used including some spare and test branches. The number of chambers connected serially was chosen such that the total gas volume per branch does not exceed $\approx$ 200 l. The gas composition, in particular the isobutane content, is controlled by two monitors. The gas flow is stopped and the HV is switched off if the fraction of isobutane is outside the range 8.5 % to 9.9 %

The gas quality is also monitored by two LST chambers equipped with a ^{90}Sr source, one in the incoming and one in the outgoing gas flow. The pulse height spectra of these chambers allow the monitoring of the gas composition and the HV regulation.

6.1.3 High voltage system

Five high voltage crates [133] with a total of 200 independent HV channels are used. Each channel supplies between 20 and 110 profiles. Chambers within one gas circuit are connected to the same HV channel. A passive distribution system allows to disconnect each single profile from HV in case of problems. All switches are computer readable, such that the HV configuration of each single 8–fold profile can be stored in a database.

Two different reference voltages can be applied to the detector. One is selected to be well below working conditions at $V_1 = 3000$ V. This setting is activated during unstable beam and injection conditions. The normal operating voltage is set to $V_0 = 4500$ V at normal pressure. Since the charge gain of streamer chambers depends on the pressure we adjust the high voltage accordingly. The gain variation amounts to $dQ/Q = -1.73\,\% \, dP/\mathrm{hPa}$. The high voltage V_0 is automatically adjusted by +2.75 V/hPa. In Hamburg one observes pressure changes of up to $\approx$ 6 hPa/h, and total variations of 80 hPa are possible.

Other relevant parameters such as temperature are monitored. They remain constant over long periods. The currents of all HV channels are constantly monitored. If a channel draws more than 5 μA, the corresponding voltage is automatically reduced until this current is below 5 μA. Channels are switched off, if this limit is exceeded for more than one minute.

6.1.4 Readout system

The readout of the analog information is incorporated as part of the LAr calorimeter and is discussed in Section 5.4. A digital readout system was developed for the wire- and strip-readout. Each wire (strip) is connected to a comparator, a synchronization circuit and a digital pipeline. The wire signal is digitized according to a computer adjustable threshold, synchronized with the HERA bunch crossing frequency and fed into a digital pipeline which has a depth of 32 steps corresponding to a total storage time of $\approx$ 3.1 μsec.

The front-end logic for eight data channels has been integrated in a gate array [134]. The leading edge of the input signal clocks the first flip-flop of a dead time-free synchronization circuit. The synchronized data patterns are buffered in a pipeline register. As soon as a trigger is accepted, the filling of pipelines is stopped. By means of a remotely controlled signal it can be decided whether the data pattern of one time slice, or the logical OR of two adjacent time slices is read out. This is necessary since the signal propagation within the chambers can exceed 96 ns, the time between two bunch crossings. In addition the eightfold OR of the stored data pattern is clocked into a separate flip-flop of the readout chain providing a signal for trigger purposes.

The electronics for 16 channels is housed on a readout card which is directly mounted onto the streamer chamber layers. This allows for early digitization and thus provides high noise resistance and a significant reduction in the number of cables needed. Multiple readout cards can be daisy chained. A layer of chambers is read out serially. The readout chains of a maximum of 24 layers are connected to special VME-based readout controllers (ROC) which provide zero suppression, data encoding, and submit all relevant steering signals to the readout cards.

Upon arrival of the first level trigger (L1), the ROCs start to collect the data from the electronics. The absolute position of the data corresponding to the triggered event within the front-end pipelines depends on the decision time of the trigger and the distance between the central trigger logic and the respective chambers. Due to the physical dimensions of the detector the delay is different for different areas.

One ROC serves up to 12300 digital channels corresponding to 24 chamber planes with 512 channels each. Since we operate 64 of these ROCs simultaneously less than 300 μs are needed to collect all data.

The architecture of the local DAQ environment is given in Figure 6.3. The VME crates are distributed in five clusters around the detector. The readout of these units starts after a second level trigger (L2). VME processors collect the data which are then stored locally. The data of up to 20 events can be stored before they are delivered to the central H1 data acquisition system.

6.1.5 Track reconstruction

The track reconstruction uses 16 wire, 5 strip and 11 pad layers, the latter being combined into 2 towers. The wires measure up to 16 points in the so-called 'wire plane' and the strips up to 3 points in the perpendicular 'strip plane'. The resolution for wire and strip hits is 3-4 mm and 10-15 mm respectively. The pads define coarse areas in space with a precision of about 10 cm.

The pattern recognition starts with the 16 wire layers. Track segments are parametrized by straight lines. To get curved track candidates several segments are connected. Then the pattern recognition selects track segments in the strips which have a matching wire track candidate. These matching wires and strips are then combined to a three dimensional track. In case of ambiguities the pad information is used to resolve them. The combination which fits best to the pads in space and amplitude (analog pad charge divided by number of wires hit) is chosen. The towers are then assigned to their matching wire and strip combination.

Due to crosstalk along the wires usually more than one pad gets a signal. With the centre of gravity of the pad charge the coordinate along the wires can be measured for both towers with an accuracy better than 10 % of the pad size. With these two additional points a direction in the strip plane can be determined even for very short tracks.

The magnetic field $\vec{B}(\vec{r})$ varies strongly inside the iron plates and in the gaps. The energy loss in one plate is on average 80 MeV for muons at perpendicular incidence. The track fit uses an average magnetic field for each plate and gap and performs a least square fit simultaneously to wire, strip and tower readings. The effect of the energy loss is accounted for by an iteration procedure.

6.1.6 Performance

During operation typically 0.1 % of the digital channels (wires, strips) are noisy and $1-2\,\%$ are dead.

Calibration data were taken during cosmic runs. One result is the efficiency of the chambers, which is shown in Figure 6.4. It agrees well with the expected values. Figure 6.5 shows the number of wires and strips per event for events triggered by the muon system. The wire data show a signal starting at a multiplicity of 13 which is roughly the mean number of wires expected for single penetrating muons with a plane efficiency of 80 %.

With cosmic muons the chambers of all modules have been aligned to each other with an accuracy of a few mm. In the barrel region cosmic muons can be used to determine the reconstruction efficiency by extrapolating jet chamber tracks. Geometrical acceptance limits this efficiency to 89 % in the plateau region above the threshold of 2 GeV as shown in Figure 6.6.

6.2 Forward muon spectrometer

6.2.1 General description

The purpose of the forward muon spectrometer is to measure high energy muons in the range of polar angles $3° \leq \theta \leq 17°$. The detector consists of drift chamber planes mounted on either side of a toroidal magnet. The design aim was to measure the momenta of muons in the range between 5 GeV/c and 200 GeV/c, the lower limit being given by the amount of material the muons have to penetrate and the influence on the momentum resolution of the multiple Coulomb scattering in the magnet iron. The upper limit is set by the magnetic field strength of the toroid together with the spatial resolution of the drift chambers. The expected momentum resolution at 5 GeV/c is 24% and deteriorates slowly to 36% at 200 GeV/c. Muon momenta below 5 GeV/c are measured in the forward tracker.

Figure 6.7a shows schematically the detector arrangement and the toroid magnet. The latter is described in Section 3.4. The drift chamber planes, which increase in size from about 4 m diameter for the first detector plane to 6 m diameter for the last, are all divided into octants of individual drift cells mounted on Al-frames. The orientation of the drift cells is such that four of the planes essentially measure the polar angle (θ) and thereby provide the momentum of the traversing muon while the remaining two measure the azimuthal angle (ϕ). Each plane consists of a double layer of drift cells staggered by half a cell width (Figure 6.7b). This arrangement enables the resolution of left-right ambiguities and also the determination of t_0 as will be explained below. The total number of drift cells is 1520.

6.2.2 Chamber design

All drift cells have a rectangular cross-section with a depth of 2 cm, a width of 12 cm and lengths between 40 cm and 240 cm. With a central sense wire the maximum drift distance is 6 cm. The cells have 50 μm thick Nichrome wires except for the inner short cells where the diameter is 40 μm. For cells longer than 1.5 m there is a wire support in the middle. More details can be found in reference [135].

The chamber signals are amplified, digitized and read out using the same components as all other drift chambers within the H1 detector (see Section 4.4).

6.2.3 The chamber gas and high voltage system

The choice of gas for the drift chambers was determined by several requirements. One is the desire to work in a drift voltage range where the drift velocity is constant. Further the gas has to be fast enough for the pulse to arrive in time for the trigger and finally it should be non-flammable for safety reasons. Currently a mixture of 92.5% argon, 5% CO_2 and 2.5% methane (FMS gas) has been chosen for the chambers. The gas is mixed and purified in a recirculator. The chambers have a total gas volume of 4 m^3, and with a small overpressure of about 0.2 hPa measured at the output, the return gas flow is typically 90% of the input and the oxygen content is of order 100 ppm. More details can be found in [135].

A 120-channel high voltage system [133] supplies distribution boxes on the detector with high voltage via 50 m long coaxial cables. Two different modules are used, one (6 kV, 1 mA) supplies the drift voltage and the other (8 kV, 200 μA) supplies the sense voltage. One drift channel supplies voltage to an entire octant, feeding 20-40 individual resistor chains. One sense channel supplies voltage to all but the 12 innermost cells of a θ-octant and the central section of the ϕ-octants. These cells have another sense channel, which can be set to a lower voltage in case of bad beam conditions. Additionally, for the ϕ-octants, the central section which is close to the beam tube can be moved outwards mechanically, if necessary.

There is a continuous monitoring of the gas composition and flow rates as well as of the high voltage and the toroid magnet, communicated via an Apple Macintosh II ci in the control room. From this work station it is also possible to control the high voltage of the detector.

6.2.4 The charge-time analysis

Only the rising edge and peak region of a pulse are used to get the time and charge information. A pulse is said to start when there are two successively rising digitizings above threshold (see also Section 4.4.5).

The end of a pulse is taken as the second successive digitizing after the peak which is below threshold, or eight 9.6 ns time bins from the start of the pulse, whichever occurs first. The arrival time of the pulse is obtained by extrapolating a line fitted to the steepest part of the leading edge back to the intercept with the background level. With a test set up, looking at cosmic muons, this method gave a resolution of < 200 μm. This result was obtained with a gas mixture of 90% argon and 10% propane providing a drift velocity of 4 cm/μs [135]. However, to satisfy the gas requirements specified in Section 6.2.3 we have chosen the FMS-gas with a drift velocity of $\sim$5 cm/μs, resulting in an expected resolution of $\sim$250 μm. Pairs of pulses which originate from the same hit are associated by requiring the difference of their arrival times to be less than the full propagation time through the two sense wires and the linking resistor.

The collected charge is found by integrating the digitizings of the pulses from the two wire ends over intervals of the same length, with subtraction of a constant background. A correction for fractional time bins was found to be important since the start times for the two pulses are subject to variable propagation delays. With cosmic muons in the test set up we found a charge-division versus distance characteristic linear to about 1%, which is well matched to the resolution.

6.2.5 Track reconstruction

The space points obtained from the charge-time analysis of the chamber hits are used in a three step procedure for track reconstruction which starts with the pairing of hits in each double

layer followed by association of pairs into straight track segments and finally the linking of track segments through the toroid to form full tracks and thus provide a momentum measurement. Pair finding in the double layers is decisive due to the displacements of cells which results in the sum of drift times being a constant (compare Figure 6.7b). A vertex pointing requirement is applied as selection criteria, but also unpaired hits are kept to be considered in the track segment finding where we demand 3 out of 4 hits in the θ-layers. The measuring errors of the space points for a pair define a cone which is extrapolated to the other θ-layer on the same side of the toroid. In the area defined by the cone, hits are tried for segment fits and are selected by a χ^2-cut.

For the linking procedure each pre-toroid segment is tracked through the magnetic field of the toroid, taking into account energy loss and multiple Coulomb scattering in the magnet iron. By doing this for a minimal reconstructible momentum of 2.5 GeV/c in the spectrometer and for either of the two muon charges possible, regions in the θ-layers after the toroid are defined inside which segment candidates for linking are considered. From the crossing angle of two linked segments an estimate of the momentum is made. Starting from the pre-toroid segment and the estimated momentum the tracking is repeated as the momentum is changed in small steps around the estimated value. Each post-toroid segment obtained from the tracking is compared to the actual segment found and a χ^2 is calculated. The minimum of the χ^2 variation with momentum defines the momentum corresponding to the best fit.

6.2.6 Drift velocity and t_0-determination

Beam halo muons are used to determine the drift velocity. From the uniform population of the total number of tracks (N) over the full drift distance (Δy), recorded in a run, a rectangular distribution is expected if the drift velocity is constant. However, due to field variations close to the sense wire, dependence on the angle of the track, the possibility of tracks traversing only the corner of a cell etc., the drift velocity will be altered and cause a smearing of the distribution.

t_0 is determined from the specific geometry of the detector, making true specific check sums for each track, as detailed in reference [135]. The widths of the check sum distributions can be used to find the spatial resolution of the chambers.

6.2.7 Chamber alignment

The drift chambers must be aligned with respect to each other and to the rest of the detector. The cells of a θ-layer are positioned on its supporting Al-frame to a precision of $\sim$50 μm along the drift direction and to $\sim$1 mm in the two other directions. This is better than the achievable resolution and therefore we only have to consider the alignment of the full octants.

Simulation studies and analysis of a small sample of real data have shown that beam halo tracks are suitable for providing the two translational and one rotational quantities which are needed to specify the position of the octant in the plane transverse to the beam direction. Further studies with angle tracks together with the survey will determine the relative positions of the octants along the direction of the beam.

Basic structure of instrumentation chambers and outside endcap muon chambers

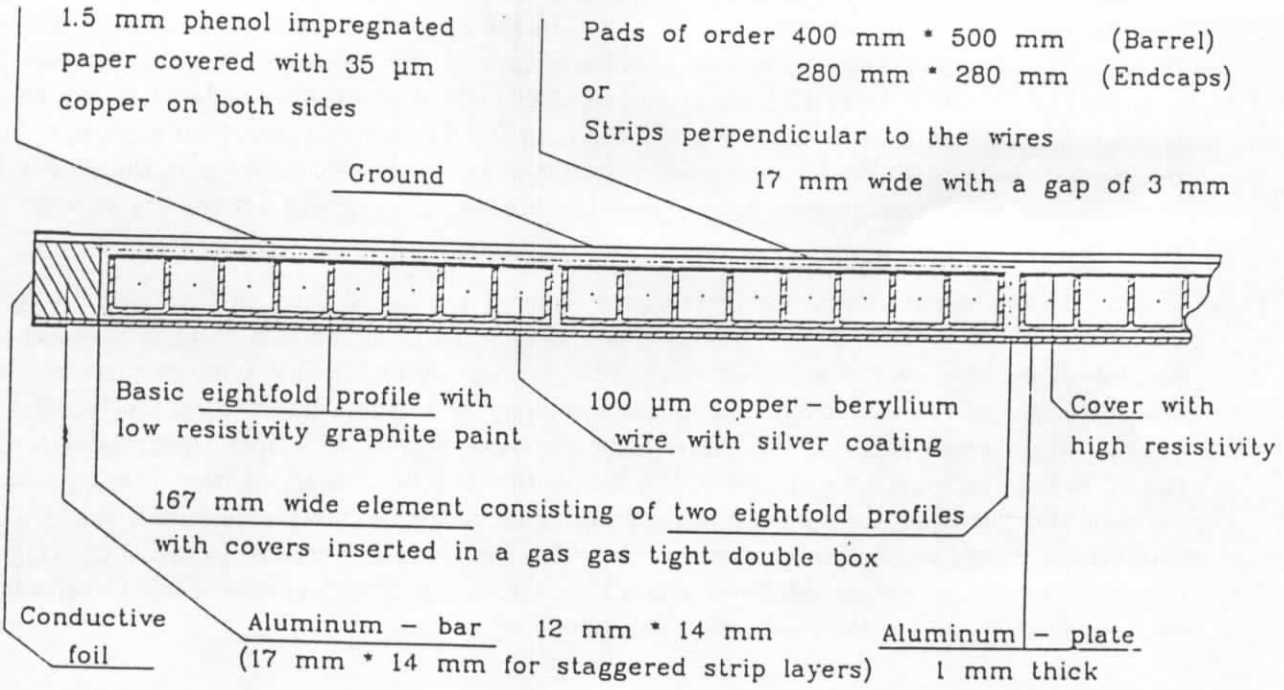

Figure 6.1: Structure of LST chambers.

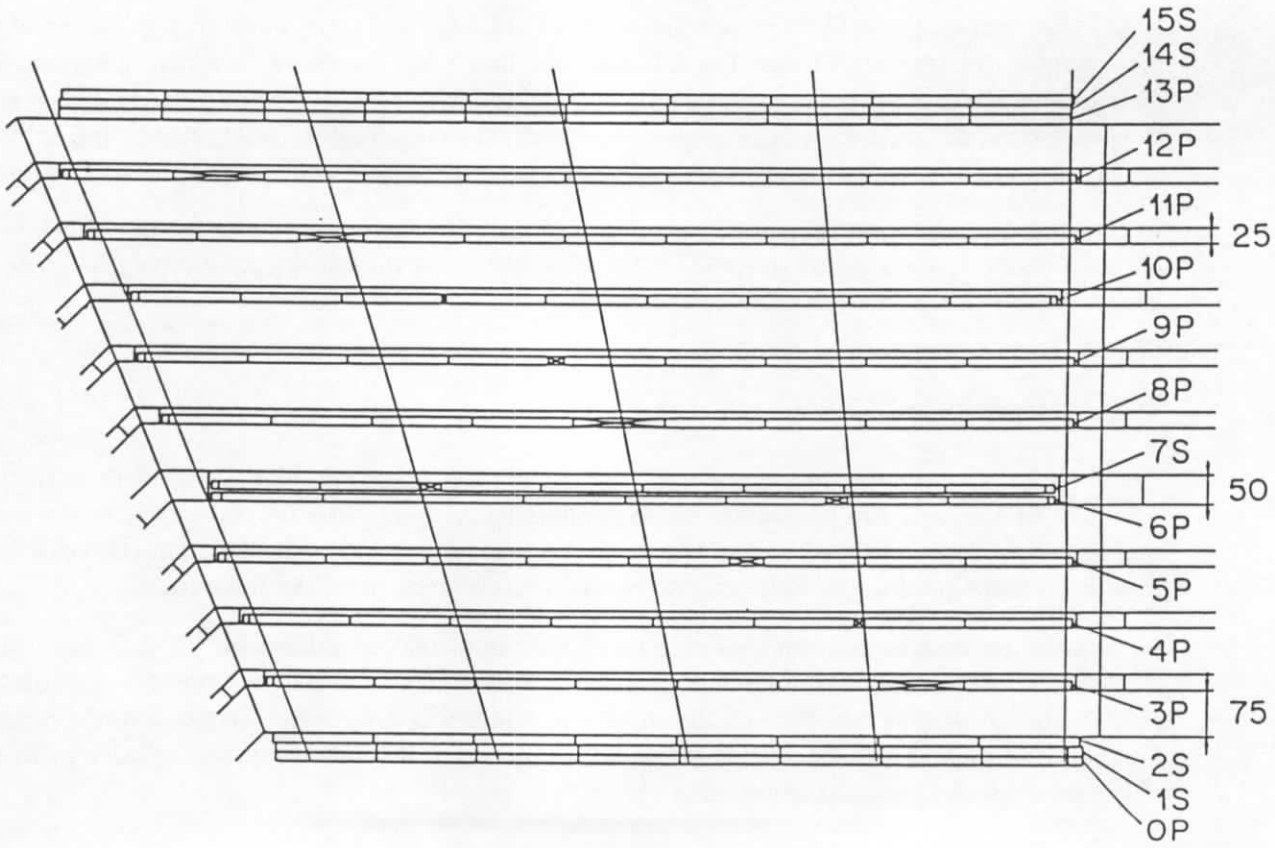

Figure 6.2: Iron instrumentation showing the pointing pad structure of the barrel region. The crossed elements represent dummy modules which fill the space not occupied by the chambers in a way to ensure that the dead areas are not aligned for tracks from the vertex region (P=pads; S=strips).

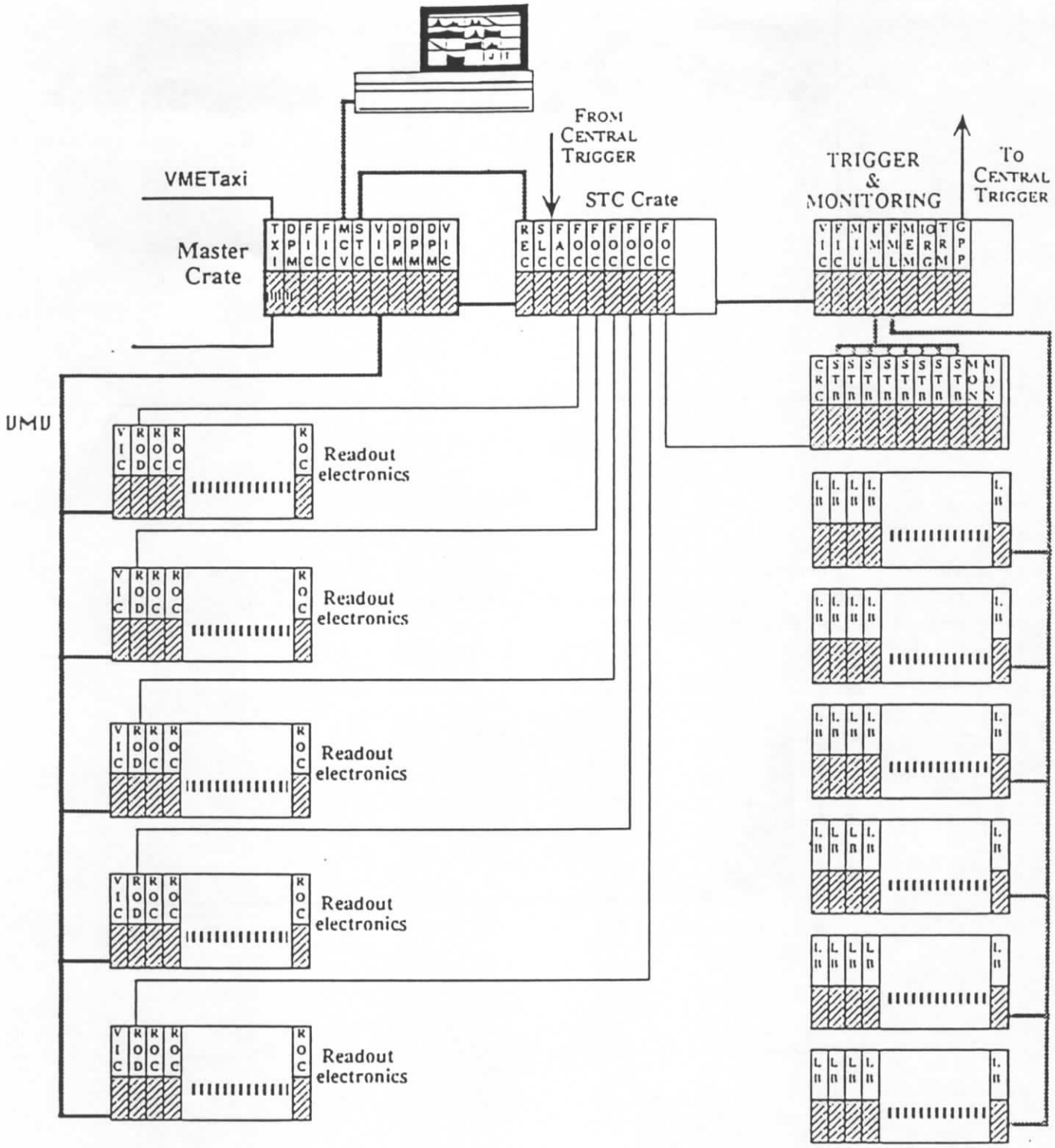

Figure 6.3: The local data acquisition system.

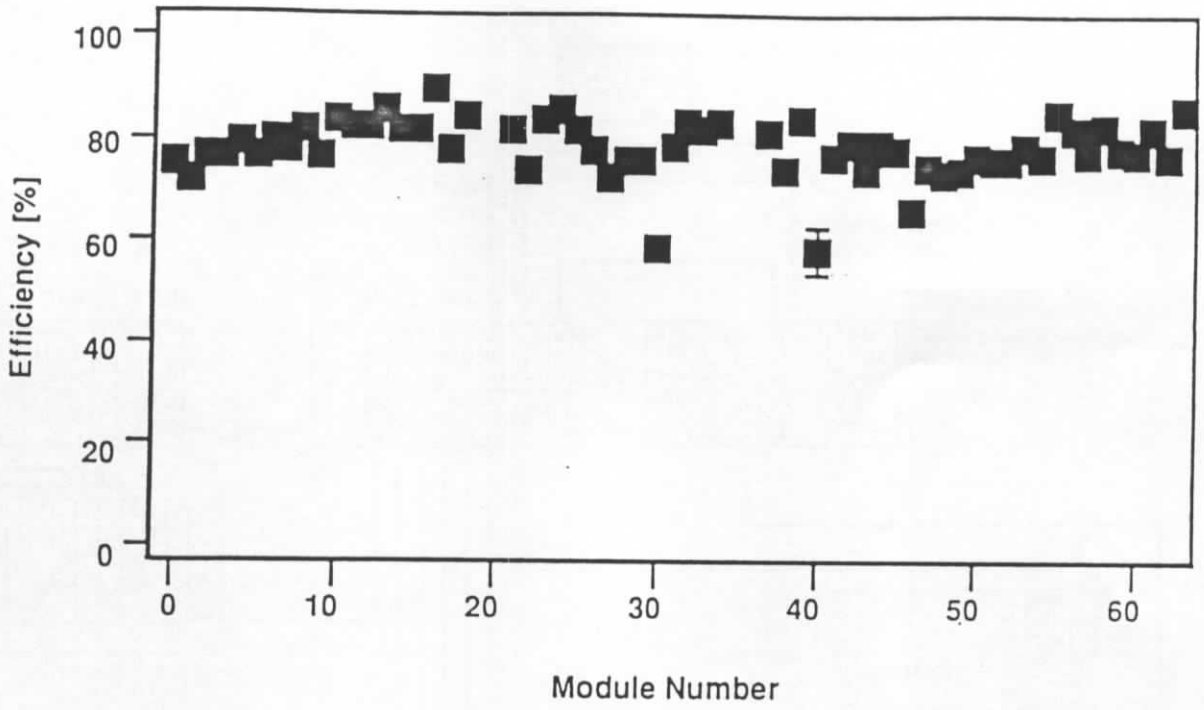

Figure 6.4: Efficiency of chamber planes . The following numbering scheme is used: 0 - 15 backward endcap (from bottom to top), 16 - 31 backward barrel, 32 - 47 forward barrel, 48 - 63 forward endcap (from bottom to top).

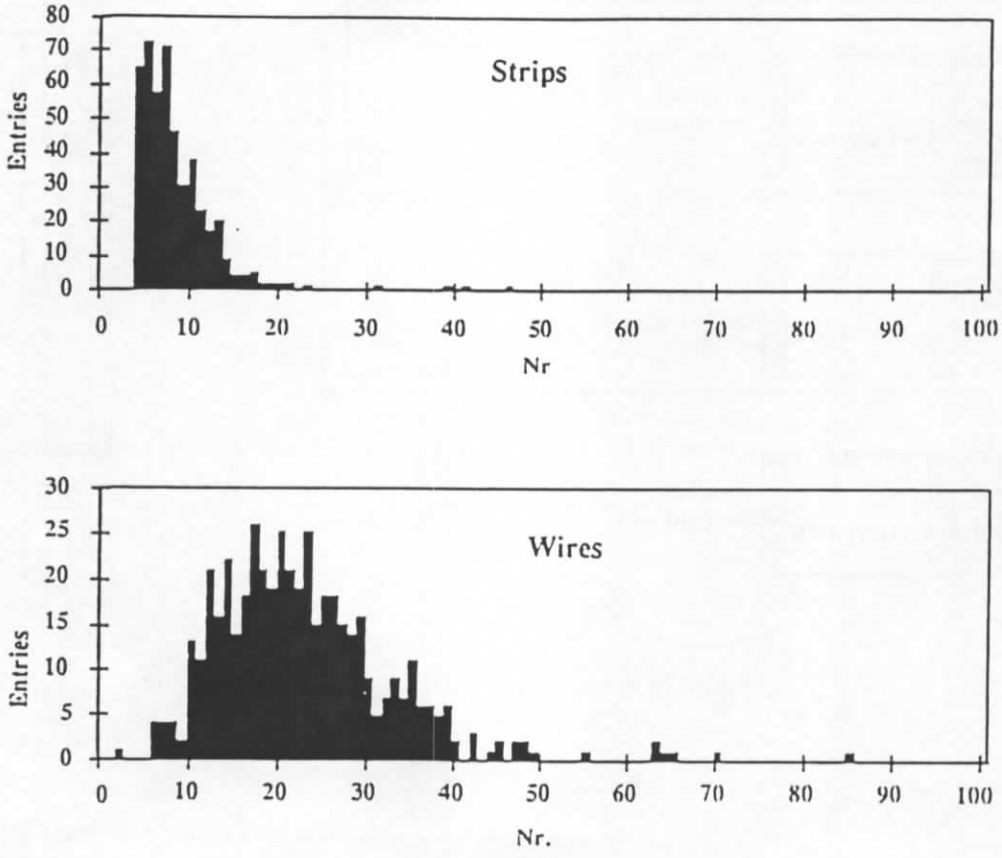

Figure 6.5: Wire and strip multiplicity per event.

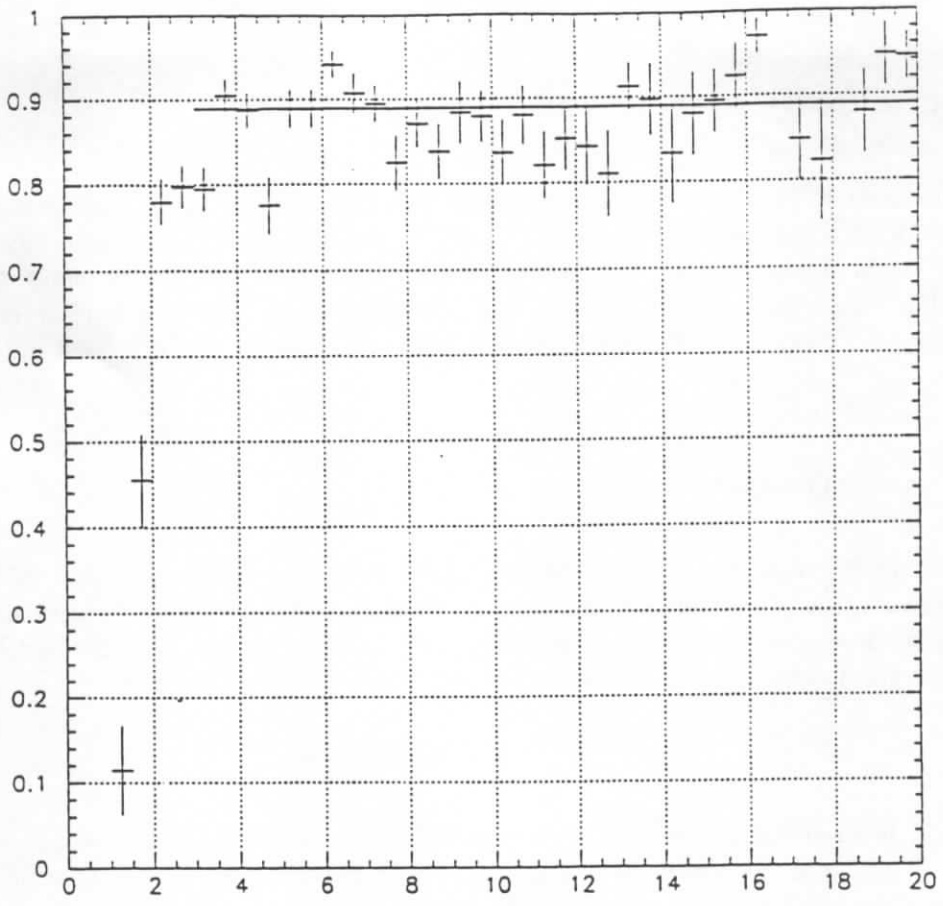

Figure 6.6: Muon reconstruction efficiency in the barrel region as function of the muon energy [GeV] determined from cosmic muons. The average efficiency in the plateau region is 89 % and is determined by geometrical acceptance.

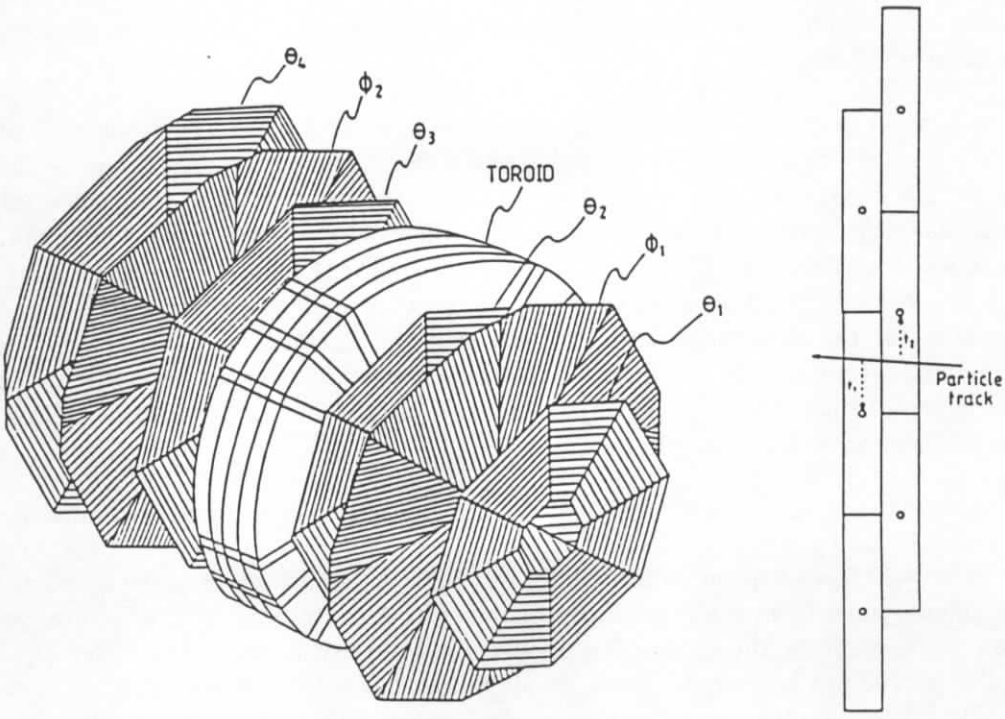

Figure 6.7: a) A schematic view of the forward muon spectrometer and b) the cell structure of a double layer.

7 Luminosity system and electron tagger

The luminosity system serves several purposes. Its main task is a fast relative luminosity measurement with a statistical precision of $\sim$ 2% at nominal beam conditions. It also provides electron beam monitoring for the HERA machine, absolute luminosity measurement in the interaction region with an accuracy of $\sim$ 5%, tagging of photoproduction events and energy measurement for electrons scattered under small angles and for photons from initial state radiation.

7.1 System Overview

The luminosity is determined from the rate of Bethe-Heitler events $et \rightarrow ep\gamma$ [136]. The main source of background is bremsstrahlung from the residual gas in the beam pipe, $eA \rightarrow eA\gamma$. At design luminosity these events are expected at 10% of the $ep \rightarrow ep\gamma$ rate, but can be subtracted using data from electron pilot bunches. The luminosity is calculated as

$$L = \frac{R_{tot} - (I_{tot}/I_0)R_0}{\sigma_{vis}}$$

where R_{tot} is the total rate of the bremsstrahlung events, R_0 is the rate in the electron pilot bunches, I_{tot}, I_0 are the corresponding electron beam currents and σ_{vis} is the visible part of the $ep \rightarrow ep\gamma$ cross-section with acceptance and trigger efficiency included.

The luminosity monitor detects scattered electrons and outgoing photons in coincidence. It contains therefore two arms: the electron tagger (ET) and the photon detector (PD). Since the angular distributions for both the electrons and photons are strongly peaked in the direction of the primary e-beam – at 30 GeV polar angles are of the order of $\theta \simeq O(m/E) \simeq 17$ μrad – the detectors have to be placed close to the beamline and from the interaction region in order to cover these small angles.

The general view of the luminosity system is shown in Fig. 7.1. Scattered electrons are deflected by a set of low-beta quadrupoles and a bending magnet located in the region 5.8 m $< -z <$ 23.8 m, pass an exit window at $-z$ = 27.3 m and hit the ET at $-z$ = 33.4 m. The photons leave the proton beam pipe through a window at $-z$ = 92.3 m, where the beam pipe bends upward, and hit the PD at $-z$ = 102.9 m. A Pb filter (2 X_0) followed by a water Čerenkov (1 X_0) veto counter (VC) protects the detector from the high synchrotron radiation flux. From the p-beam side the PD is shielded by an iron wall of 2 m thickness. The VC eliminates events with photons interacting in the filter. Both the ET and PD can be remotely moved from the median plane of the e-beam during injection. This operation can be reversed within 1 – 2 min with a position accuracy of $\sim$ 100 μm.

The acceptance of the luminosity system for nominal electron beam conditions (E_e = 30 GeV, zero tilt) and the expected rates at the design luminosity of 1.5×10^{31} cm^{-2}s^{-1} are given in the Table 7.1. One of the main contributions to the systematic error in the absolute luminosity measurement comes from the dependence of the system acceptance on possible variations of the electron beam angle in the interaction region. This tilt, typically of the order of 100 μrad, is controlled by the position of the beam profile at the PD with high precision, of the order of 10 μrad. The corresponding corrections to σ_{vis} are taken into account already online and can be further improved during the offline analysis.

Quasi-real photoproduction events with $Q^2 < 0.01$ GeV^2 can be tagged by the ET in the energy interval $0.2 < E_{e'}/E_e < 0.8$ using both the PD and VC as a veto.

	unit	ET	PD
Energy interval, $E_\gamma/E_e = 1 - E_{e'}/E_e$		0.2 – 0.8	0.004 – 1.0
Polar angle acceptance interval	mrad	0 – 5	0 – 0.45
Average acceptance for $ep \rightarrow ep\gamma$	%	48	98
Average acceptance for photoproduction	%	36	–
σ_{vis}	mb	28	174
$ep \rightarrow ep\gamma$ rate for $E > E_{thr} = 4$ GeV [1]	MHz	0.4	1.3
Photoproduction event rate [1]	Hz	20 – 30	–
Aperture $x \times y$ (granularity)	mm^2	154 × 154 (7 × 7)	100 × 100 (5 × 5)
Chemical composition		TlCl(78%) + TlBr(22%)	
Radiation length (Moliere radius)	cm	0.93 (2.10)	
Crystal length (radiation hardness)	cm (Rad)	20 ($> 6 \cdot 10^7$)	
Energy resolution, σ_E/E [2]	%	$1 \oplus 10/\sqrt{E}$, (E in GeV)	
Position (time) resolution, $\sigma_{x,y}$ (σ_t) [2]	mm (ns)	0.3 – 1.2 (< 3)	

Table 7.1: Parameters of the luminosity system. [1] at design luminosity; [2] values reached at HERA.

7.2 Detectors

The design goals – high radiation resistance, good energy, coordinate and time resolution and compactness – were best met by a hodoscope of total absorption KRS-15 crystal Čerenkov counters. Their properties are summarized in Table 7.1.

Each calorimeter cell is viewed by a FEU-147 photomultiplier [137] with a 20 mm diameter cathode coupled to the crystal with an optical contact. The veto counter is viewed by two phototubes operating in different regimes, the first for photon detection, the second operating with increased voltage and reaching full efficiency for charged particles with a range exceeding 35 cm. Taking into account the material in front of VC, this corresponds to full efficiency for e. m. showers initiated by the photons with $E_\gamma > 1.5$ GeV.

Since the luminosity detectors operate at high rates up to few MHz, which may vary within one beam filling by a factor of 3 to 10, they are permanently calibrated during data taking using the energy constraint $E_{ET} + E_{PD} = E_{e-beam}$. Although the calibration coefficients may change within 5 – 20%, this method allows an absolute calibration with a precision of better than 1%. Figure 7.2 illustrates this energy correlation between the two arms.

7.3 Trigger and data acquisition

The different functions of the luminosity system required a special trigger and data acquisition concept, based on the two completely independent branches. The photomultiplier signals pass first differential preamplifiers close to the detectors and then, after 170 m or 100 m of fast coaxial cable pairs, respectively, are again shaped and amplified at the trigger electronics crate. This solution reduces noise and compensates for signal attenuation in the cables. Then the signals are split and analysed in two groups of FADCs (2 × 80 channels).

The first FADC group operates in a standard mode, similar to all other subdetector trigger systems (see Section 8.3.4). The trigger electronics discriminates the analog energy sums against the individually set thresholds, producing a dead time free trigger bit synchronized to the HERA beam crossing. Three basic trigger signals are available from the electron arm ($E_{ET} > E_{ET}^{thr}$), the photon arm ($E_{PD+VC} > E_{PD+VC}^{thr}$), and the veto counter. The main TE used so far for

Based on the offline γ - rate method				
Contribution to $\delta\mathcal{L}$	1993	1994		
	e^-p	e^-p	e^+p	shifted I.P.
1. Theoretical value for σ_{BH}	0.5%		0.5%	
2. Trigger efficiency	2.0%		0.3%	
3. Statistics, e-gas bgrd. subtraction	1.5%	1.3%	0.4%	3.3%
4. γ-energy scale (calib & resol.)	1.7%	1.1%	0.9%	1.7 %
5. Geometrical acceptance of γ-arm	0.7%		0.5%	
6. Multiple photon effect (pileup)	0.2%	0.3%	0.4%	0.3%
7. Counting and rounding errors	1.1%		0.5%	
Total error from lumi system	3.4%	2.0%	1.4%	3.8%

Table 7.2: Systematic error for the absolute luminosity measurement.

tagged γp physics was eTAG = ET$*\overline{\text{PD}}*\overline{\text{VC}}$. The front end readout and the data transfer to the central data acquisition are done by a program running on the FIC8230 master processor [53].

The second FADC group is controlled locally and completely decoupled from the H1 trigger system. Two triggers are used for the luminosity calculation and online detector calibration: ET$*$PD and ET$*$PD$*\overline{\text{VC}}$. Any combination of 5 TEs can be permanently stored without dead time for each of the 220 bunches in a fast histogramming memory of 32×220 channels. This memory contains the full information on all bunch related trigger statistics, e. g. the level of accidental coincidences. The online event processing includes fast reconstruction, calibration, trigger verification and calculation of the current luminosity and is performed on a second FIC8230 processor.

7.4 Performance

The system has been working successfully since April 1992. A typical example of the information provided by the luminosity system during $e-p$ collisions is shown in Fig. 7.3. For safety reasons lead-scintillator calorimeters were used in 1991 [138] during the running in phase of HERA. In the early phase, when HERA operated at 1% of the design luminosity, the detectors were active even during injection and ramping of the electron beam, which allowed the machine crew to better understand the beam dynamics and to adjust for collisions quickly.

The total integrated luminosity measured in 1993 and 1994 by H1 is shown in Fig. 2.5. The present understanding of the systematic error is summarized in the Table 7.2. Due to the redundancy in the trigger, the systematic error can be further reduced by combining the present method with other possible triggers (e.g. with the total photon flux measurements [139] etc.). The data sample taken with the help the eTAG trigger of the luminosity system was the starting point for all photoproduction results presented by H1 so far [140, 141].

Based on the bremsstrahlung process:

$$ep \rightarrow e\gamma p$$

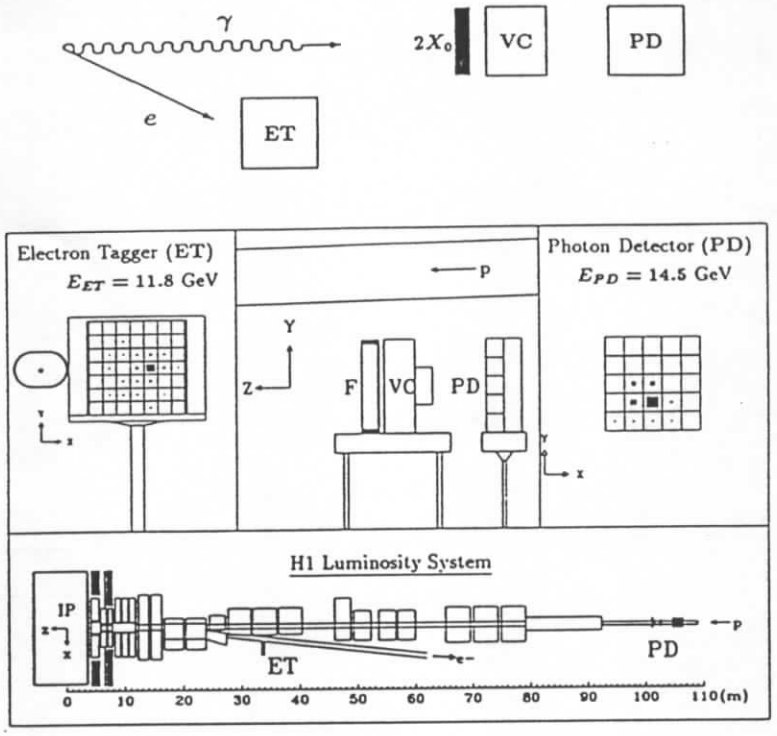

Figure 7.1: The layout of the luminosity system.

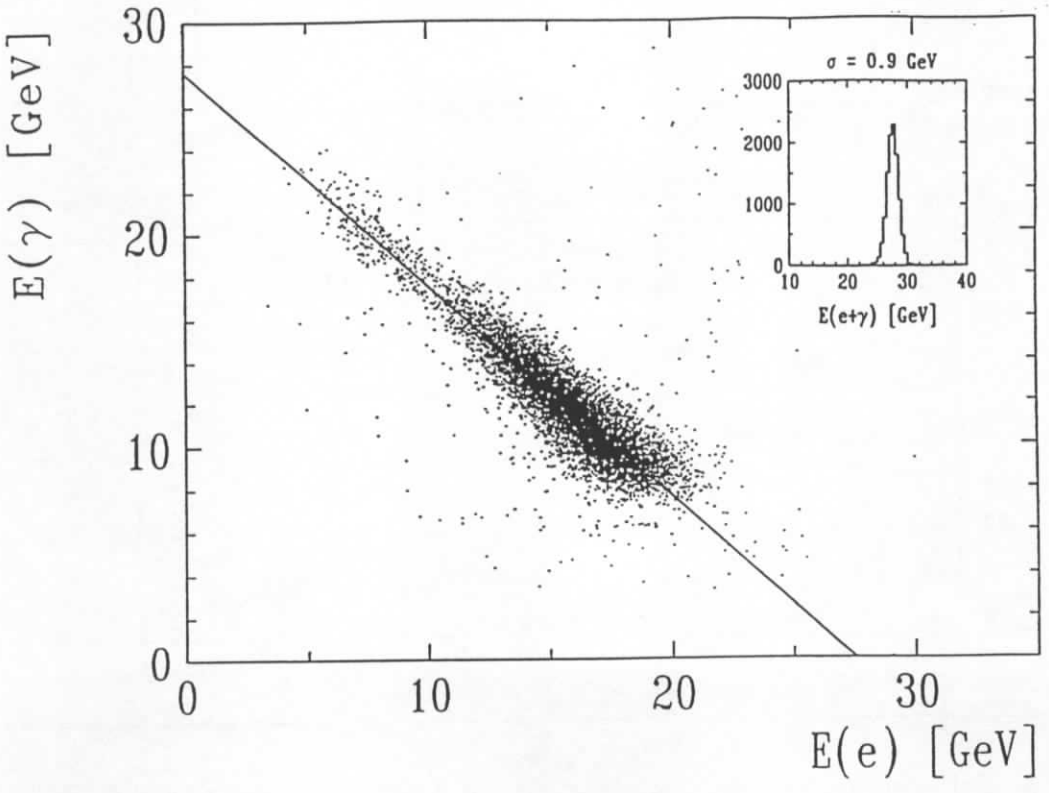

Figure 7.2: $e - \gamma$ energy correlation for bremsstrahlung events detected by the luminosity calorimeters. In the upper right corner the total reconstructed energy is shown. These data are from the beginning of the 1994 HERA e^-p run at 27.5 GeV $\times$ 820 GeV collision energy.

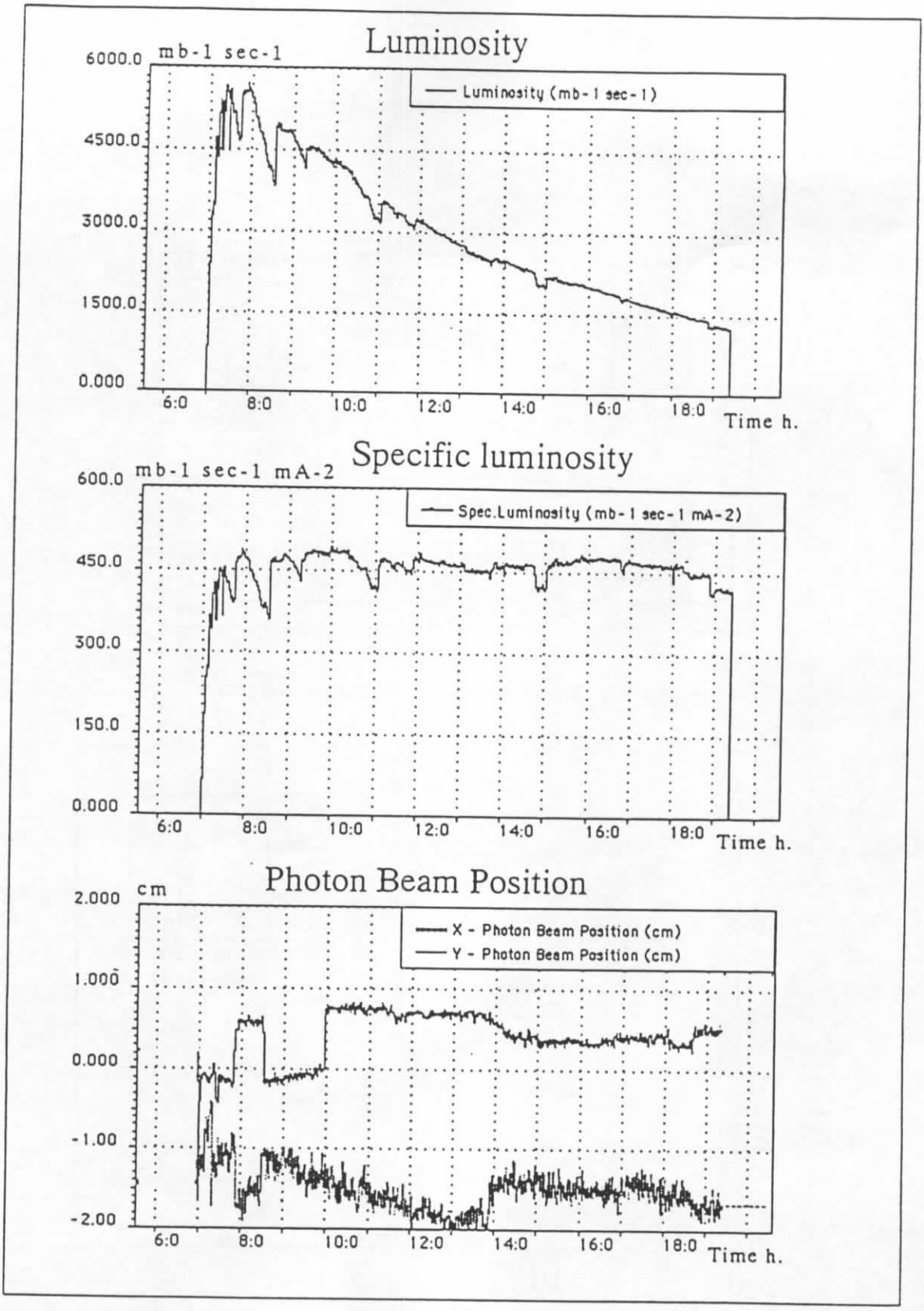

Figure 7.3: Data provided by the luminosity system during the $e - p$ collisions at HERA. Statistical fluctuations correspond to one measurement every 10 s.

8 Trigger

8.1 Introduction and trigger requirements

The task of the trigger system is to select out of the flow of signals registered in the multitude of detector channels those for permanent recording that originate from a given $e-p$ interaction of physics interest and to reject background events. The common background sources of other accelerator experiments are also present at HERA: synchrotron radiation from the electron beam, proton gas interaction in the beam pipe vacuum of about 10^{-9} hPa and stray protons, which produce particle showers by hitting the beam tube and other materials around the accelerator. Beam halo muons and muons from cosmic radiation play a rôle, too.

The variety of physics processes under study in $e-p$ collisions covers a wide range of cross-sections and of rates, respectively. It extends from photoproduction, where the visible $e-p$ cross section of several μb implies an event rate of 20–30 Hz at design luminosity ($\mathcal{L} = 1.5 \cdot 10^{31} \mathrm{cm}^2 \mathrm{s}^{-1}$), towards W production expected to occur a few times per week. (See Table 8.1.)

beam gas interactions			50	kHz
cosmic μ in barrel			700	Hz
tagged γp	1.6	μb	25	Hz
$c\bar{c}$ total	1	μb	15	Hz
DIS low Q^2	150	nb	2.2	Hz
DIS high Q^2 (e in LAr)	1.5	nb	1.4	min^{-1}
Charged current DIS p_T >25 GeV	50	pb	3.0	h^{-1}
W production	0.4	pb	0.5	d^{-1}

Table 8.1: Cross sections and rates (at design luminosity).

The high luminosity mandatory for the measurement of the rare processes could only be achieved with a large number of proton and electron bunches in the machine (see section 2.4). With a basic proton RF frequency of 52 MHz (208 MHz) 210 bunch positions have been foreseen along the circumference of the storage ring; consequently the bunch crossing interval is 96 ns.

This time span has to be compared to typical signal formation times in the detector: the largest drift times in the central jet chamber (CJC) amount to 1 μs and the calorimeter preamplifier has an integration time of about 1.5 μs. (see Table 8.2.)

The probabilities per bunch crossing for accidental tracks, calorimeter energy deposits or electron tagger signals are at or below the percent level. However, when integrated over the detector sampling times, the pile-up probability is no longer negligible. Therefore it is mandatory that the trigger identifies the bunch crossing ("t_0") associated to the event under consideration.

Most subdetectors of H1 generate signals that can be used for the first level trigger. Some examples are: tracks in certain ranges of curvature, energy depositions with their topology, interaction vertex positions, particle arrival times. Local coincidences between MWPC 'rays' and calorimeter 'towers' are also formed. While fast detectors like MWPCs and scintillators intrinsically provide time resolution within a bunch crossing, "t_0" information can be obtained from calorimeter signals using constant fraction methods, or from the drift chambers by requiring special track configurations. In contrast, threshold-like signals extend over several bunch crossings and have to be put into coincidence with external "t_0" bits.

The first level trigger thus provides a decision for each bunch crossing. The fully pipelined system runs deadtime free at 10.4 MHz and is phase locked to the RF signal of HERA. The

width of proton bunch	1.4 ns
distance to next satellite bunch	5 ns
flight time to backward ToF	6 ns
flight time to barrel muon system	20 ns
bunch crossing interval	**96 ns**
longest drift time in CJC	1 μs
integration time of LAr preamplifier	1.5 μs
delay of first level trigger	2.5 μs
front end readout time	$\approx$1 ms

Table 8.2: Time scales at HERA and H1.

decision delay of 2.5 μs determines the minimum pipeline length needed to store the full detector data at the front end.

The asymmetric beam energies of HERA give rise to strongly forward-directed event topologies that are hard to discriminate against background from proton interactions with residual gas atoms. Already at first level, the trigger system has to provide a sophisticated identification of the characteristics of an event and to trigger on the complex signatures of physics processes. To this end, the trigger subsystems of H1 deliver information on distinct properties of the event. In several different ways, use is made on the track origin information that uniquely distinguishes $e-p$ interactions from the beam gas background. Early arrival times in the ToF system indicate that the origin of the event is upstream the proton beam, a large distance of closest approach to the beam axis of CJC measured tracks in the (x, y) plane, or along the beam axis (from the z drift chambers) distinguishes against events not produced in the fiducial volume of the interaction region. In addition, a fast estimate of the z vertex position along the beam axis based on histogramming techniques of signals from the central and forward proportional chambers, constrains the vertex even further.

For some $e-p$ events the vertex information may not be the best requirement at the first trigger level. The signature of the scattered electron can be exploited where appropriate. Depending on the Q^2 region under consideration, it is detected in the electron tagger of the luminosity system, in the backward electromagnetic or in the main LAr calorimeter. Next, the topology of the hadronic final state is widely used. Charge current (CC) events are identified by the imbalance of transverse component of the hadronic energy deposition. Jet signatures spot hard photoproduction events, and the requirement of a positive muon signal serves as a tag for heavy quark production. It has even been possible to trigger on heavy quark production events without detection of the scattered electron, relying just on the topology of the registered charged tracks.

An obvious possible extension of the system is to make use of local correlations between the trigger "objects" of different subsystems. "Some track" together with "some muon signal" is more likely being randomly produced than a "track pointing to a muon signal" in space. Probabilities for accidental coincidences are reduced with increasing granularity.

While at first trigger level only the MWPC and LAr calorimeter data are correlated in such a way, full use of the detailed, high granularity trigger data of most subsystems is being made in the intermediate trigger levels 2 and 3. With decision times of 20 μs and 800 μs, respectively, they work within the primary dead time. The level 2 decision is made using purpose built hardware. A *KEEP* decision at level 2 initiates the readout of the front end under processor control. In parallel, a flexible level 3 system with software algorithms running on a RISC microprocessor can refine the trigger and potentially abort the readout.

8.2 Front end pipelining

The time interval between two consecutive bunch crossings of 96 ns is used as the time unit (1 BC) in the following. The time needed to run trigger signals even through a few electronics circuits performing simple logical calculations is usually longer than that. Moreover the large size of the experiment introduces cable delays of several BC. Finally certain subdetectors have a long detector response time which means that the information of these detectors is only available some BC after the event (LAr: 13 BC due to long integration time of the preamplifiers, central drift chamber: 11 BC due to a longest drift time of 1 μs). Such long response times can only be tolerated because, due to the relatively low event rate (compared to a $p-p$ collider), the probability for an $e-p$ interaction per bunch crossing is small (of order 10^{-3}).

The L1 trigger decision (called L1keep signal) is available centrally 24 BC after the real $e-p$ interaction. Further time is needed to distribute this signal to stop the various subdetector pipelines, otherwise the information which belongs to the relevant BC would be lost. The pipeline length varies between 27 and 35 BC depending on the subdetector, which is just long enough to operate the system. For future system designs we would advise to increase this pipeline length to gain more flexibility in the timing of such a system or - even better - to perform signal processing and zero suppression before entering the pipelines and store the information dynamically.

This concept of a pipelined front end system also avoids a huge amount of analog cable delays and allows to reconstruct offline the history of the event over several BC for timing studies and to identify signal pile up.

H1 uses four different types of pipelines (For a more detailed description of the electronics see the chapters of the respective detectors):

- Fast random access memory (RAM) is used to store the digitized information of the drift chambers (central and forward tracker, forward muon system) as well as of the LAr calorimeter for trigger purposes. The analog to digital converters operate at a frequency of 10.4 MHz for the LAr calorimeter and 104 MHz for the drift chambers. They are synchronized to the HERA clock which is also used to increment the 8-bit address of the RAM, operating as a circular buffer. At L1keep time writing into the RAMs is disabled to save the information for the readout process. In addition RAM buffers are used to pipeline information in the drift chamber trigger and in the central trigger.

- Digital shift registers are used to store the single bit information, generated by threshold discriminators followed by a special HERA clock phase synchronization circuit, in the instrumented iron system, the multiwire proportional chambers, the drift chamber trigger branch, the BEMC trigger branch and the ToF and Veto wall scintillator systems. A custom designed gate array contains the clock synchronization circuit and a 8 channel 32 stage pipeline realized as D-Flip-flops. See the chapter 6.1.4 for a description of this gate array.

- Analog delay lines are used to store the pulse height of the BEMC. The L1keep signal is used to stop a sample and hold circuit from which the digitization takes place during the dead time of the readout.

- Signal pulse-shaping of the LAr and TC is adjusted such, that the signal's maximum occurs at L1keep time. The same type of sample and hold and digitization is used as in the BEMC case.

The timing of the synchronization step and the analog to digital conversion clocks is critical. The information has to be uniquely attributed to the BC the event originated from. The

adjustment of the HERA clock phase, which defines this synchronization time in each subsystem, is therefore a major task, which required several iterations of delay curves combined with offline analysis, and it turned out to be a much more complex operation than expected. Online bunch and clock phase monitors ensure stable operation at the correct timing values.

8.3 Trigger level 1

The trigger level 1 system [142] consists of nine different trigger systems each based on the information of a subdetector. The outputs of these systems are called trigger elements (TE). These TE are fed to the CTL where they are combined to various so-called subtriggers. Each single subtrigger suffices to produce a L1keep signal to stop the pipelines and initiate the event readout.

In the following paragraphs the nine systems and the CTL are described.

8.3.1 Vertex position oriented trigger systems

The geometrical origin of the event is the main handle to suppress background at a HERA experiment. Vertices which lie outside the nominal $e-p$ interaction region identify uniquely background events. These TE are therefore in one or the other way used for almost all subtriggers, with the exception of the higher threshold triggers of the calorimeters.

8.3.1.1 The backward time-of-flight system Beam-wall and beam-gas events originating from the proton beam produce showers, which mostly penetrate both scintillator walls (see Section 4.7) behind the BEMC. A background (BG) and an interaction (IA) timing window (derived from the HERA clock signal) define for each scintillator whether the hits belong to particles arriving directly from upstream or via the longer path from the nominal interaction region. The signals from the single scintillator sheets of each wall are logically 'ORed' together to form a signal for each plane, and the two planes are then put into coincidence forming the trigger elements `ToF-BG` and `ToF-IA`.

The `ToF-BG` signal is the simplest and most effective background rejection criterium and is therefore applied to most of the physics subtriggers as a veto condition. The logic is realized in conventional NIM electronics.

8.3.1.2 The $z-$vertex trigger The central and the first forward proportional chamber are used to estimate the event vertex position along the beam axis ($z-$axis) (for a more detailed description see [143]). A particle originating from the beam passes four layers of chambers (either the double layers of CIP and COP or CIP and first forward proportional chamber). The first step of the vertex estimator, the so-called rayfinder, therefore combines the four cathode pad signals (see Section 4.5.2) which lie on a straight line into an object called ray. In the plane perpendicular to the beam a 16 fold segmentation (ϕ - sectors) is used, such that the rays of each segment are treated separately. A total of 34'400 different rays are examined for each bunch crossing simultaneously.

A histogram with 16 bins along z with a bin width of 5.4 cm is filled according to the $z-$coordinate of the origin of each ray. The rays formed by the correct combinations of pads all enter in the same bin and consequently form a significant peak above the background generated by rays from wrong combinations of pads which are more or less randomly distributed (see Figure 8.1(a)). Events which have their vertex far outside from the nominal interaction region

do not develop significant peaks, in this case the histogram contains only the background from accidentally formed rays.

From this histogram various TE are derived. The `zVTX-t0` TE is activated if there is at least one entry in the histogram. `zVTX-t0` indicates a minimum of activity in the central region of H1 and also serves for bunch crossing identification in combination with low threshold energy triggers of the calorimeters. The two TE `zVTX-sig1` or `zVTX-sig2` are activated if the histogram peak exceeds a given significance threshold (two different threshold settings are available in parallel). For events with a few tracks only, a special TE indicates that there were only few entries in the histogram albeit in a single cluster. The histogram analysis is fully programmable, such that the meaning of the TE can easily be changed.

The rayfinder is based on a custom designed gate array (1.5 μm CMOS technology), of which 2112 pieces are in use. It contains the logic to examine the signals of 45 cathode pads and to form 30 rays (allowing a flexible 3 out of 4 logic), the adder tree to count the active rays, the grouping of these rays into big rays (see below) and some pipeline structure for delays. For the final histogram building and the peak analysis programmable logic cell arrays (XILINX family 3000 [144]) and a 22 bit look up table realized with 4 MByte of fast static RAM are used (see Figure 8.1(b) for a block diagram).

8.3.1.3 The forward ray trigger The cathode pad signals of the FPC and the CIP are fed into a logic circuit which finds rays originating from the nominal interaction region and pointing in the forward direction (for more detailed description see [145]). A ray here is a set of impacts on three or four chambers, compatible with a track coming from the interaction region in one $2\pi/16$ ϕ-sector. Out of the 6 or 8 chamber planes (2 planes per chamber) which are hit by the track, only one is allowed to be absent. For each of the 16 ϕ-sectors there are 32 possible rays corresponding to radial bands for impacts on the second FPC. The width of these bands increases in geometrical progression, the lowest radius is 21 cm, and the largest one 75 cm, corresponding to angles of 5.63° and 24.72° respectively.

These rays are counted and a TE is activated if at least one road is found. Other TE indicate active rays in adjacent ϕ-sectors (the xy plane is divided into 16 ϕ-sectors as in the $z-$vertex trigger above). Furthermore, special topology conditions in the 16 ϕ-sectors can be used to activate a TE, e.g. a back to back of all rays.

This system is realized by a total of 320 RAMs, which are used as hierarchically organized look up tables.

8.3.1.4 Other MWPC triggers Additional TE are derived from the CIP to trigger on cosmic rays passing through the beam pipe.

If more than three sectors in the backward quarter of the CIP are set, the TE `CIP-backward` might indicate an upstream p beam-gas event. The TE is used as a veto for certain subtriggers which are derived from tracking information only.

8.3.1.5 Big rays The rays found by the forward ray trigger and the $z-$vertex trigger (in the latter case only the rays originating from the highest peak in the $z-$vertex histogram, fig. 8.1(b)) are extrapolated and combined to 224 "regions of interest" so-called 'big rays', which have the same geometrical division as the 'big towers' of the liquid argon calorimeter trigger (see below and fig. 8.4). They 'rays' can both be put into coincidence with the 'towers' (fig. 8.3) but also be used in a stand alone manner by demanding topological conditions (e.g. back-to-back configuration or minimal multiplicity in backward region) on the pattern of MWPC rays.

8.3.1.6 The central jet chamber trigger This trigger [146] finds tracks in the CJC, which have a distance of closest approach to the nominal beam line of less than 2 cm from the nominal beam axis and therefore suppresses beam-wall events as well as synchrotron radiation background. To keep the number of channels at a manageable level without degrading the performance 10 selected layers out of 56 radial signal wire layers of the CJC are used in the trigger.

In a first step (fig. 8.2) the signals from the CJC are digitized by a threshold comparator (independent of the normal readout branch) and synchronized to the HERA clock. This way the drift time information is kept with an accuracy of 96 ns corresponding to about 5 mm of position resolution. For the innermost two drift cells this resolution is improved by doubling the clock frequency.

In a second stage the hits are serially clocked into shift registers. Hit masks are defined according to track position in drift space and track curvature in the magnetic field. A total of 10000 different masks are applied in parallel to the outputs of the shift registers to mark the active roads. Tracks with low or high transverse momentum can be distinguished as well as the charge of low momentum tracks (< 1 GeV/c). The number of roads found in each of the 15 ϕ-segments and in the two momentum bins for each charge are counted separately in 3 bit numbers.

In the final step these track counts are processed to generate the TE. Three different thresholds on the total number of tracks are implemented. In addition a topological analysis in the xy plane is performed, for instance back to back tracks in ϕ can be recognized.

Most of the digital logic is programmed into about 1200 programmable logic cell arrays (XILINX [144] family 3000).

8.3.1.7 The z−chamber trigger The z−chamber trigger [34] uses the signals of the drift chambers CIZ and COZ in a way similar to the central $r\phi$ jet chamber trigger, utilizing the relatively high spatial resolution obtained from the drift chambers. Signals are synchronized with twice the HERA bunch frequency and stored in shift register pipelines. Their parallel outputs are fed into coincidence circuits used as look up tables for all possible tracks coming either out of the interaction region of 50 cm length (vertex tracks), or from the upstream proton beam region with $20° \leq \theta \leq 90°$ with respect to the beam line (background tracks).

In a first step tracks are found with a granularity of 2.4 mm within the individual CIZ and COZ systems. For tracks originating from the vertex signals from CIZ and COZ are combined in a 96 bin vertex histogram using an analog technique. By gating the system with an OR of the central proportional chambers the search for a peak in this histogram can optionally be further restricted. A resolution of 5 mm for the vertex reconstruction is achieved. The drift cells associated with a vertex track (both left and right solutions in drift space) are stored thus providing a fast θ measurement of a track.

Tracks not associated with the fiducial volume of the interaction region are counted as upstream background, a signal that can be used as an effective veto.

The shift registers and the look up tables are configured in 1060 logic cell arrays (XILINX [144] family 3064 and 3090).

8.3.2 Calorimetric triggers

The selection of deep inelastic $e-p$ reactions is based primarily on calorimetric triggers. These events are characterized by large transverse energy depositions originating from jets and eventually the primary scattered electron. Certain physics channels "beyond the standard model" are expected to lead to similar event signatures. Correspondingly, the calorimeter triggers have to cope with a wide spectrum of trigger observables, from narrow, localized energy depositions (e.g. electrons) to global energy sums such as transverse or missing transverse energy. Even photoproduction events with heavy quarks, with energy deposits as small as 1-2 GeV, should be efficiently detected, when the calorimeter signal is locally put into coincidence with big rays from the MWPC system.

8.3.2.1 The liquid argon calorimeter trigger The liquid argon trigger [147] system is designed to calculate the energy deposited in various parts of the calorimeter as well as the total energy and other global energy sums which can be weighted by position-dependent weighting factors.

The realization of this system contains an analog and a digital part (fig. 8.3). In the analog part the signals from the calorimeter cells are split off the readout chain after the preamplifier and are separately amplified and shaped to a pulse width of about 600 ns FWHM. Signals within a Trigger Tower (TT) are summed. The TTs are approximately pointing to the vertex and are segmented in 23 bins in θ and in 32 bins or less in ϕ. While the electromagnetic and hadronic signals are still separated in the TTs, the sum of the two is fed into an analog discriminator which turns both signals off for later summing, if the level is below an adjustable threshold ("AGM threshold") as determined by the electronic noise. The same signal is used to determine the time of the signal (t_0) by a constant fraction type method. The boolean number of $t_0 > 0$ is available as a TE (`LAr-T0`). Using the trigger for low threshold photoproduction physics requires a precise adjustment of thresholds already at the analog stage. This is possible by cross calibrating the trigger to the more precise ADC readout [148].

Depending on the θ region, either one, two or four TTs are summed up to 'big towers' (BT), providing finer granularity in the forward direction (fig. 8.4). A total of 240 such BT's are formed from the $\approx$ 45000 LAr cells, another 12 BT's are derived in a similar way from the signals of the BEMC and the PLUG calorimeter.

The electromagnetic and hadronic signals of each BT are digitized separately by analog to digital converters running at the HERA clock frequency of 10.4 MHz. The digital outputs are calibrated by a RAM look up table and two threshold discriminators are used to look in each BT for a potential electron signature defined by high electromagnetic and low hadronic energy in the respective sections of the tower. Another discriminator look up table marks all BT's to be transferred to the higher trigger levels. The electromagnetic and hadronic parts of each BT are summed and the total BT energies are then available for further processing. A threshold is set on the total BT signal in coincidence with the 'big rays' as derived from the MWPC triggers (see Section 8.3.1.5). The number of these towers is counted, discriminated and provided as a trigger element to the CTL.

The total BT energy is fed into a set of look up tables producing the weighted energy of this big tower for the global sums: For the total transverse energy a weight of $\sin\theta$ is used, the transverse components E_x and E_y are obtained by multiplication with $\sin\theta\cos\phi$ and $\sin\theta\sin\phi$, respectively, to build the missing energy signal. A further channel can be used for arbitrary purposes, e.g. for generating a trigger with uniformly distributed rates over the polar angle by weighting each BT with the inverse of the background rate of its angular region. A 'topological' channel allows to sum up separately the energies in five predefined topological regions (BEMC,

central barrel (CB), forward barrel (FB), inner forward (IF), and PLUG). For these regions, the total energy as well as the energies in each of the contributing quadrants are calculated. Furthermore the total energies are calculated for the total barrel (CB+FB) and the forward (IF+PLUG) and backward (FB+CB+BEMC) regions. For the summing of the weighted BT energies, custom specific gate arrays are used with 8 bit accuracy (7 bit plus sign for E_x, E_y).

In the last step further RAM-based look up tables are used to encode the various global and topological sums into two-bit threshold functions provided as TE to the CTL. One such look up table also builds the missing energy from the two signed components E_x and E_y with subsequent discrimination and encoding into two bits.

More details about this trigger and its performance in 1994 can be found in reference [149].

8.3.2.2 The BEMC single electron trigger The purpose of the BEMC Single Electron Trigger (BSET) (see [112, 150]) is to identify scattered electrons from DIS processes in the angular acceptance of the BEMC. The basic concept of this trigger is to provide cluster recognition and to place energy thresholds on the sum of all energy clusters in the BEMC. The trigger is based on energies deposited in BEMC stacks which have a granularity well matched to the transverse spread of electromagnetic showers.

Analog signals from preamplifiers of single wavelength shifters are first added to form stack sums representing a high granularity TE. The summed analog stack signals are then adjusted in their gain and timing in order to provide an equal analog response to energy and to uniquely assign the energy depositions in all stacks to a single HERA bunch crossing. Two thresholds are applied to these signals. A low threshold just above noise level and a medium threshold to be used as a cluster seed. Typical values are 1.3 GeV for the low threshold and 2.3 GeV for the medium one. A cluster identification module then detects the cluster seeds and assigns neighboring stacks to define clusters. Two TE reflect the cluster multiplicity (one or more clusters, exactly one cluster). The energy of all clusters is summed up and three possible thresholds (CL1, CL2 and CL3) can be placed on this sum, which activate the respective TE. The total energy summed over all stacks exceeding the low threshold is also compared to a threshold and activates another trigger element. Finally the cluster energy and the total energy sum is digitized into an eight-bit number to be used for correlations with other quantities at the CTL.

The trigger has been able to operate in coincidence with a timing veto from the time-of-flight system (see Section 8.3.1.1) and a cluster threshold of 2.5 GeV during the first data taking period. The threshold curve for the cluster energy is shown in figure 8.5.

8.3.3 Muon triggers

Both the instrumented iron system and the forward muon spectrometer deliver level 1 trigger information, as described below.

8.3.3.1 The instrumented iron muon trigger The instrumented iron system is logically divided into 4 subdetectors (front end cap, forward barrel, backward barrel and backward end-cap) [151]. Each subdetector consists of 16 modules. The wire signals of layer numbers 3, 4, 5, 8 and 12 of each module are used for the level 1 trigger. The pipeline gate arrays used in this system have this output available after the synchronization step, but before the entry into the pipeline. The "OR" of 16 wires of these signals is called an element and all elements of one chamber are again ORed together to form a single layer signal. Any condition on the 5 trigger layer signals of one module can be requested by means of RAM look up tables (e.g. 3 out of all 5) for each module independently. Two signal lines per module are used. One of

these contains the system's t_0 information, the second is used for the coincidence condition. The latter is transferred to the level 1 trigger after its timing has been set correctly by means of the t_0 signal from the first hit trigger layer in the module. This determines the correct BC with a resolution of about 20ns. On level 1 only 8 TE are left distinguishing between exactly one or more than one module trigger in different regions of the polar angle. The 64 coincidence bits as well as additional information on the multiplicity per module is then ready for use in the level 2 and level 3 trigger systems.

The instrumented iron muon trigger has been used up to now for two main purposes: in combination with other H1 triggers (especially from the tracking system) to trigger on muons from heavy quark decays or from $\gamma\gamma$ interactions or as stand alone trigger for monitoring : either on cosmic muons or on muons in the proton beam halo.

8.3.3.2 The forward muon trigger The signals from the drift chambers of the forward muon spectrometer are discriminated and fed into an electronic system which extracts the appropriate t_0 and the coordinate within the drift space of chamber hits which correspond to tracks [152]). This is achieved by making use of the staggered arrangement of two adjacent drift cells as shown in fig. 8.6. For correct t_0 the sum of the drift times of the two cells is defined for any track coming from the collision point, while the difference of the two drift times gives the coordinate within the drift space. A field-programmable 32×32 coincidence array with serial-load shift register axes, built in a 1.5 μm CMOS custom specific chip is used to make the correlations between the two drift times and thus identify bunch number and track position.

A similar coincidence matrix with parallel-loaded axis is then used to define pairs of track segments which correspond to tracks in the chambers before the toroid and separately in the chambers after the toroid. A variable width road may be applied to require that the tracks point to the interaction vertex. In the third step of this trigger processor pre-toroid and post-toroid tracks are fed into a further coincidence matrix which finds pairs of tracks which have traversed the toroid. The momentum selection of the trigger is made by varying the widths of the roads.

The trigger deals with each octant of the forward muon chambers separately. The track candidates found in each octant are allocated to eight regions at different polar angles relative to the beam. The 8-bit hit patterns from all eight octants are fed into a RAM based look up table which counts the number of muon candidates and allows programmable topological correlations to be made . Eight bits of trigger information are then sent to the CTL as TE.

8.3.4 Triggers derived from the luminosity system

The luminosity system runs with an independent data acquisition and triggering system as described previously in chapter 7. However the trigger signals derived from the three detectors of this system are available also to the main trigger system: independent thresholds can be set on the electron energy, the photon energy and the calibrated sum of both. Together with the signals of the veto counter located in front of the photon detector this information is fed into a look up table to form logical combinations. The outputs are connected to the CTL as TE.

So far mainly the electron signal was used to tag photoproduction events.

8.3.5 Central trigger level 1 decision

The information generated by the subdetector trigger systems described above consists of 16 groups of 8 TE, which are connected to the CTL inputs [153, 142]. The 16 groups of TE are fed into pipelines realized as dual ported RAM based circular buffers, which allows to adjust the

delays of all incoming signals to the proper BC. In addition the RAMs can be used to study the time evolution before and after the actual event.

The TE are logically combined to generate a level 1 trigger signal. Up to 128 different subtriggers are formed by applying coincidence and threshold requirements. (Lookup tables are used to form 16 fold coincidences of arbitrary logic expressions from up to 11 predefined input bits). A compact trigger description language (TDL) has been developed to keep up with the ever changing demands for new subtriggers and to properly log the logic and the status of the triggers loaded.

The subtriggers are assigned to a given physics event class (physics trigger), to experimental data needed e.g. for measuring the efficiency of a given detector (monitor trigger) or to cosmic ray events for calibration purposes (cosmics trigger).

The possibility to gate the logic with beam information is also useful; cosmic or calibration triggers should only fire when both bunches are empty, physics triggers only, when both are filled.

The rate of each subtrigger is counted separately and can be prescaled if needed. The final L1keep signal is defined by the logical OR of all subtriggers after prescaling and is distributed to the front end electronics of all subsystems to stop the pipelines. Only at this point the primary dead time starts to accumulate.

8.4 Intermediate trigger levels

The two intermediate trigger levels 2 and 3 operate during primary dead time of the readout and are therefore called synchronous. The calculations which are performed in these systems and the decision criteria applied depend on the subtrigger derived in the level 1 system, which acts in this way as a rough event classification.

During the level 2 latency time (a fixed time of typically 20 μs) the level 2 trigger system evaluates a larger number of detector signal correlations typically in a mixed serial/parallel manner. Depending on the outcome of the analysis a fast *KEEP* or *REJECT* signal is issued at decision time. For the level 2 decision various hardware solutions are under construction including a complex topological correlator [154] and a neural network approach to exploit the correlations between the trigger quantities from the various subsystems in a multidimensional space [155]. The massively parallel decision algorithm of these systems makes them ideally suited for fast trigger applications.

Only if the event is accepted at level 2, the time consuming readout tasks such as zero-suppressing of the drift chamber digital signals and the calorimeter analog to digital conversion and DSP processing are initiated. During this time the trigger level 3 system based on a AM 29000 RISC processor performs further calculations [156]. The level 3 decision is available after typically a few hundred μs, in case of a reject the readout operations are aborted and the experiment is alive again after a few μs.

The calculations of both level 2 and level 3 triggers are based on the same information prepared by the trigger level 1 systems described in the previous section: MWPC (Big Rays, $z-$vertex histogram), central drift chamber (number of tracks found in each ϕ-sector by the level 1 trigger), BEMC (individual stack information, energy sums built in the trigger level 1 system), LAr calorimeter (individual big tower electromagnetic and hadronic energies and the global sums, as built in the trigger level 1 system) and intermediate information generated by the main and forward muon triggers. Topological and other complex correlations between these values are the main applications for the intermediate trigger systems.

The events which survive the level 2 and 3 triggers are taken over by the central data acquisition system with a typical maximum rate of 50 Hz (see chapter 10 for upgrading state of this limit). Since this system works asynchronous to the primary trigger system, there is no further dead time involved as long as the level 3 accept rate stays safely below these 50 Hz. The decision times of these systems (level 2: 20 μs, level 3: assume 100 μs average) and the total primary dead time of about 1.5 ms for fully accepted events imply, that the level 1 (level 2) trigger accept rate must not exceed 1000 Hz (200Hz) to be able to run the experiment with an overall dead time below 10 %.

Fig. 8.7 indicates the front end response time as a function of the instantaneous input rate. The time is independent of the "distance" between two events until at high input rates 2^{nd} order limitations come into play. One such effect has been identified in the drift chamber readout and been cured by introducing deeper buffering at the front end.

At present the level 2 and 3 processing systems have not yet been in use. (However, all accept and reject control signals were available and the system can be run by arbitrarily forcing level 2 and level 3 accept/reject decisions for each event.) The level 1 accept rate had therefore to meet the central data acquisition limitation of 50 Hz. Since the "physics content" of the TE information is already appreciable this can typically be done in a straight forward manner. Special caution, however, is appropriate when the background conditions of the beams change dramatically, which may happen from time to time.

8.5 The level 4 filter farm

The level 4 filter farm is an asynchronous software trigger based on fast MIPS R3000 based processor boards [157]. It is integrated into the central data acquisition system and has the raw data of the full event available as a basis for its decision making algorithms. This allows for online trigger selections with the full intrinsic detector resolution. In 1992 fourteen in 1993/1994 thirty two processor boards ran in parallel. Each board processes one event completely until a decision is reached. The hardware layout is described in detail in chapter 10.

In order to reach a decision in the shortest possible time, the L4 algorithm is split into various logical modules, which are run only if a quantity calculated by the respective module is needed to reach this decision. The L4 modules use either fast algorithms designed specifically for the filter farm, or contain parts of the standard offline reconstruction program. The execution of the modules is controlled by a steering bank containing text in a steering language written explicitly for this purpose. The final decision is based on statements containing logical combinations of numerical or logical values. The event is either accepted or rejected if the statement is true.

Execution of the statement is terminated and the next statement is executed as soon as a sub-condition is false. It is possible to run any statement in test mode without influence on the actual decision. This allows the evaluation of the effect of new statements with high statistics prior to activation and the flagging of particularly interesting events, e.g. for the online event display. In most cases, the first condition in a statement is simply a mask of L1 trigger bits. This scheme allows for high flexibility without changes in the program code and facilitates book-keeping as the steering bank is automatically stored in the H1 database.

A small fraction - typically 1 % - of all rejected events is always kept for monitoring purposes.

In the 1993 runs the filter farm was mainly used to reject events with vertices outside of the nominal interaction region along the beam axis, which survived the relatively weak conditions set in the first level trigger. The largest reduction was achieved using charge division information from the trackers: In a first statement, a histogram of $z-$intercepts is evaluated. These are derived from the projection of straight lines defined by pairs of well separated wire hits in cells

of the central jet chamber (CJC). If more than 50 % of all entries are below $z = -75$ cm, the event is rejected. This condition rejects upstream beam-gas and beam-wall interactions. A similar algorithm evaluates multiple hits on neighboring CJC wires. If the ratio of hit pairs with an absolute angle of less than 10° vs the beam direction to all hit pairs is greater 1/2, the event is rejected. Events with this topology are predominantly due to electron induced background originating from synchrotron radiation. These algorithms are very fast: both tests combined need an average of 8 ms on the processor boards and rejected 50-80 % of the events triggered by tracker triggers in 1992. The full track reconstruction in the CJC is run on events passing the above criteria. Events with only positive charged tracks or no tracks at all in the beam interaction region are rejected. Three or more well reconstructed tracks originating from $z < -1$ m also lead to rejection of the event.

The BSET trigger described in Section 8.3.2.2 suffers from a large background due to particles hitting a single photo diode (mainly synchrotron radiation related). Events with a disproportionate fraction of the total stack energy in just one of the four photo diodes are rejected. In addition false BSET triggers from upstream proton beam background are rejected by the tracker cuts described previously. Muon triggers in the instrumented iron are verified by requiring a reconstructed track in the iron.

As can be seen in the above examples, the L4 filter farm has been rejecting background events based primarily on technical quantities. It has rejected an average of 70% of the input events. At higher luminosity rejection of beam-gas events in the nominal interaction region will become necessary. In addition, the increased number of filled bunches will necessitate the rejection of cosmic ray events.

The filter farm is not only used for event filtering purposes. As reconstructed data of the whole detector merges there for the first time, it is also well suited for monitoring and calibration. The reconstruction modules fill monitor histograms which can be inspected online. Warning messages can also be sent to the central control console, informing the shift crew immediately of potential problems. Calibration data are sent to the data base for immediate use by the online reconstruction process.

8.6 Performance and outlook

With the above described system we reduced the high background rate at trigger level 1 to typically 26 Hz at the present luminosities delivered by HERA. 70 % of these events were rejected by the level 4 event filter, so we ended up with a tape recording rate of 8 Hz at a overall dead time of the system of 8 %.

The total rate of background events into the experiment due to proton beam losses from upstream was expected to be of order 50 kHz. In fact we measured at a total proton beam current of 0.8 mA (0.5 % of the design value) an event rate of 225 Hz in the ToF scintillator wall, which scales with this expectation.

A proton-residual gas interaction rate of about 1 kHz/m can be calculated from the observed vacuum of 10^{-9} hPa and at design luminosity. This scales to 5 Hz within the interaction region (± 25 cm) and at the reduced luminosity condition mentioned above. We effectively observed a rate of about 2 Hz of such beam-gas events triggered with the central tracking triggers.

The rate of synchrotron radiation background turned out to be a bigger problem than expected. However by using the DC track trigger these events can easily be suppressed. For the low Q^2 deep inelastic neutral scattering events with the scattered electron observed in the BEMC this background is a more serious problem, only spatial correlation between BPC and

BEMC and relative signal distributions in the BEMC photo diodes (see previous section) give a significant reduction of this type of background.

Offline studies based on the data taken during the first year of HERA operation show that it is possible by setting more stringent coincidence requirements for the level 1 subtriggers to run the system in the same manner (only level 1 and level 4 triggers) at 10 times higher beam currents without cutting significantly into physics acceptance and with the same performance concerning rates and dead times. However at design luminosity (100 times higher than our first year experience) we will have to tighten the requirements on the events in level 2 and 3 trigger systems. But it looks still possible to trigger with high acceptance for physics events, perhaps with the exception of the heavy quark production of which a large fraction of events have not enough transverse energy for the calorimetric triggers to fire and no or only low energy electrons or muons in the final state. Therefore they have to be triggered in the first level by central tracking information alone resulting in a high beam gas background from the nominal $e - p$ interaction region. We will have to use topological criteria in the level 4 or even in level 2 or 3 to recognize these events.

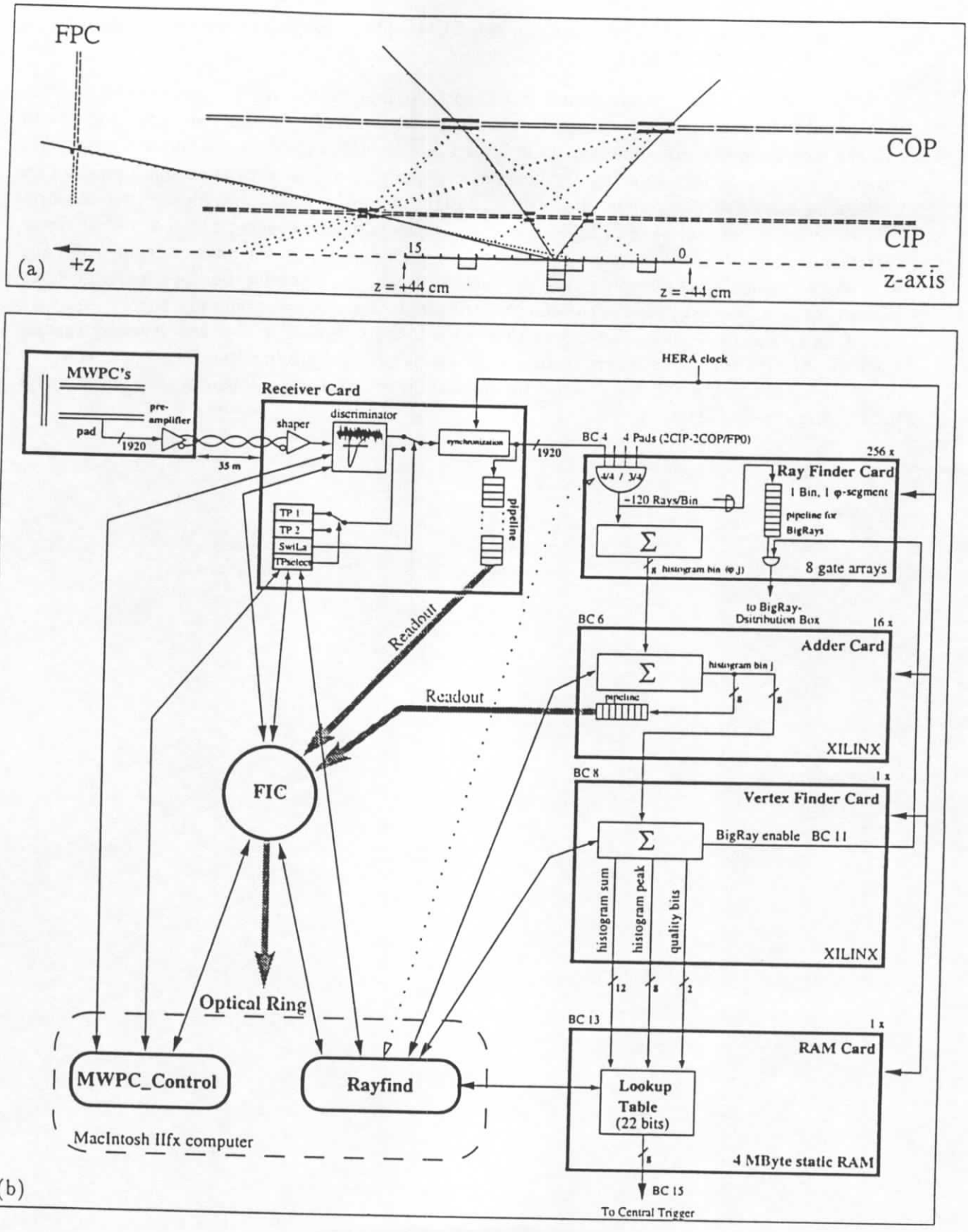

Figure 8.1: (a) $z-$vertex reconstruction by building a histogram, which displays a peak at the true vertex location. (b) Block diagram of the $z-$vertex trigger.

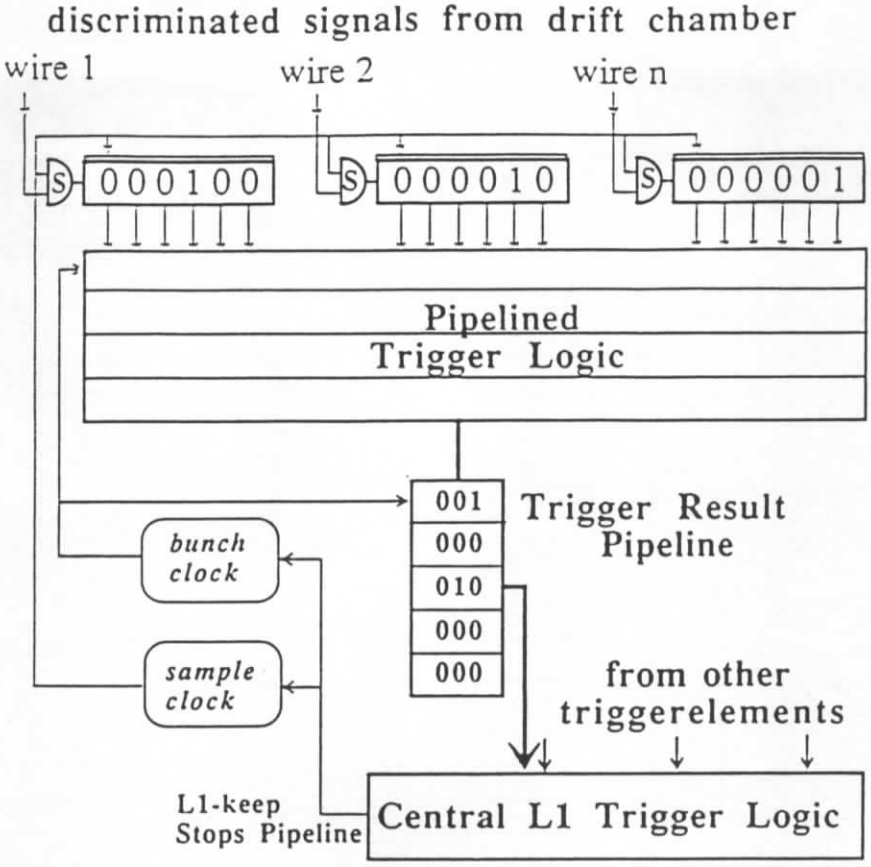

Figure 8.2: Block diagram of the drift chamber trigger.

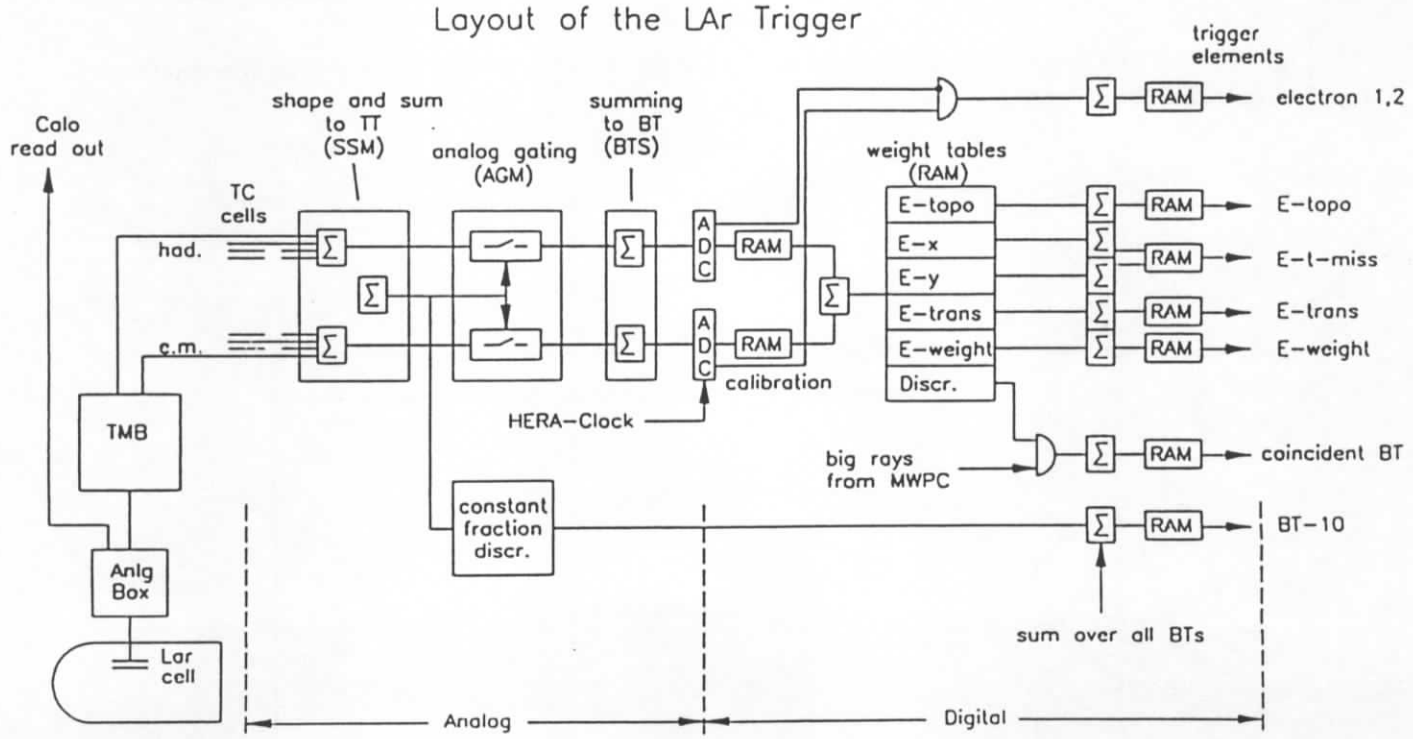

Figure 8.3: Block diagram of the liquid argon calorimeter trigger.

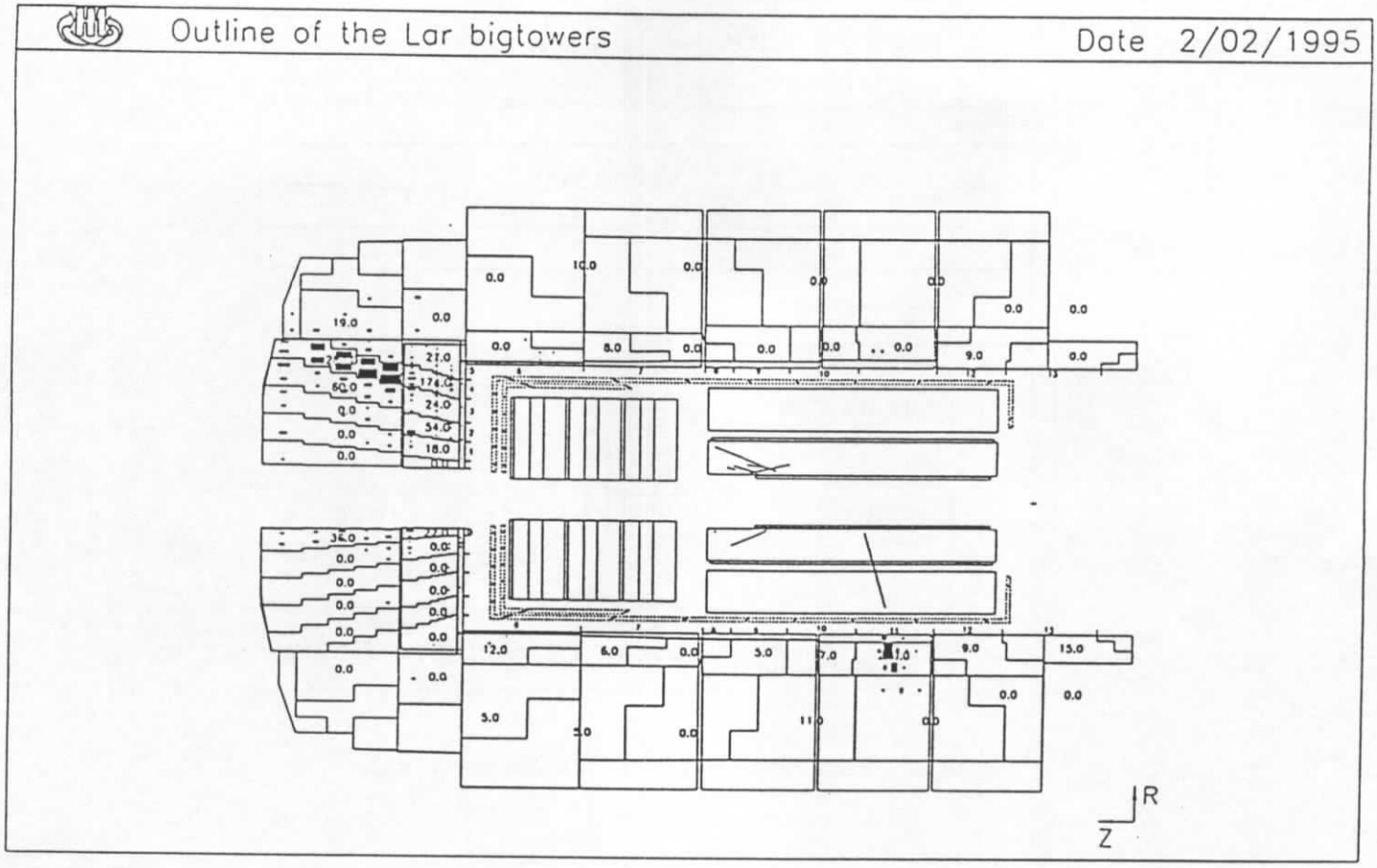

Figure 8.4: Cross section through the θ plane of the liquid argon calorimeter showing the pointing geometry of the trigger big towers.

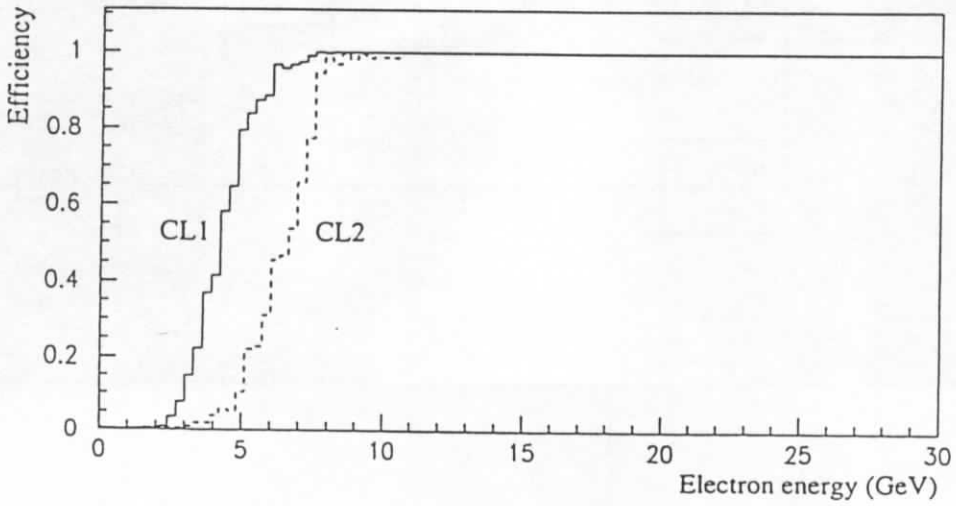

Figure 8.5: BEMC single electron trigger efficiency for thresholds CL1 and CL2.

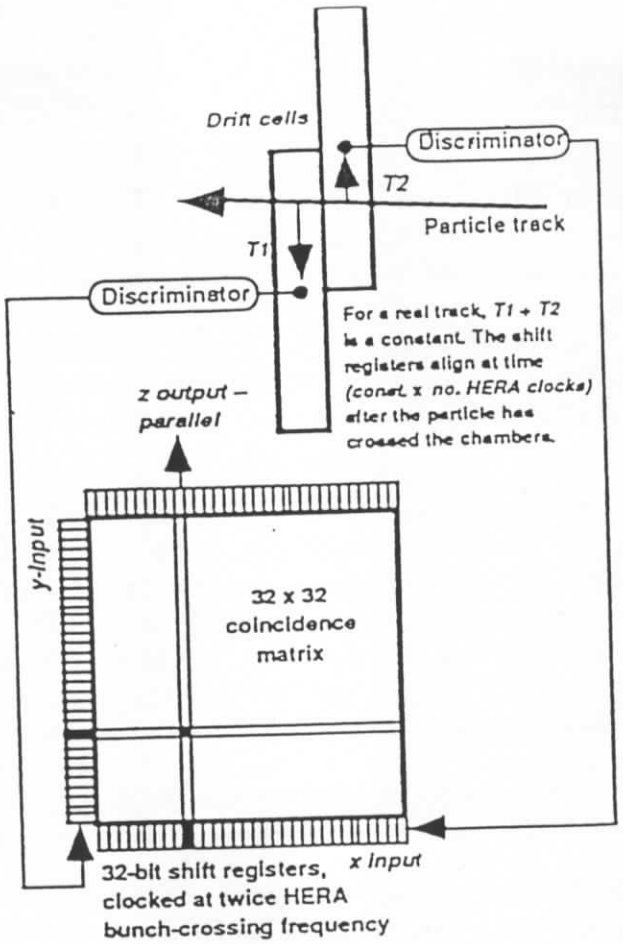

Figure 8.6: Principle of track recognition in the forward muon trigger.

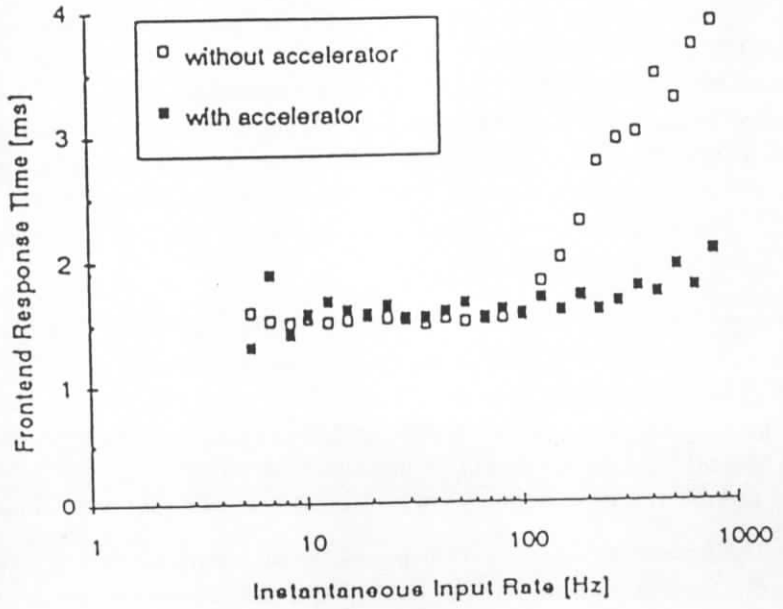

Figure 8.7: The frontend response time as a function of the instantaneous input frequency (=1/time between consecutive events). The increase at rates above 100 Hz is related to a buffering limitation in the drift chamber readout, which has subsequently been cured.

9 Slow control

The slow control system of H1 [158] is designed to take care of all parameters of the experiment which would be constant in an ideal world. Except for central control and monitoring of all VME crates, all subdetectors described above are equipped with a slow control system of their own. All systems use VME crates controlled by Macintosh or OS-9 computers and some of them use a VME-controlled multichannel slow control system developed at H1 [159]. The integration of subsystems is achieved in two ways, a simple hardware alarm system and a computer control network (CCN). A combined database is used for maintenance of static data and storage of measurements.

Throughout the slow control system we use the notions of slow channel (SC) and slow event (SE) [160]. A slow channel is a single measurable quantity of a single signal type of a single physical channel (e.g. a real setting of a high voltage power supply channel, or the value loaded into this channel). Each SC is uniquely identified by its code (ID). All slow channels are first initialized by their subsystem computer according to the central database. A microevent occurs when a significantly new result is obtained from the measurement on a SC. Microevents are accumulated in their slow event buffer until the status of some SC has changed, the time allowed for a SE accumulation has expired, the command to send a SE was received or the maximum number of microevents within a SE has been reached. As a result of any of the above conditions (SE triggers) a slow event is sent to the central slow control computer.

We use a relational database management system for the maintenance of slow control data. We use the structured query language (ANSI SQL) for the purpose of data integrity, control of access and commitment, and for queries. The complete history of the databases is kept. Any set of reports from queries can be automatically formatted into H1 standard records suitable for production programs. Slow events are stored in two standard files. The slow event archive file uses keyed access to SEs. Both of these history files are zero-suppressed in the sense of microevent definition. We have a good interactive access to slow control data stored on the mainframe IBM computer. A menu tree can be used to guide casual users. Remote access to all databases and history files is made transparent by a TCP/IP database server.

The control network consists of subsystem control computers (Macintosh and OS-9) attached to different detector parts (Figure 9.1). They are connected via Ethernet (TCP/IP). CCN is used to monitor all parameters of H1. All slow control computers produce SEs and transfer them to the central slow control (CSC) computer. The CSC computer provides data for the online display of the detector status [161] running on Macintosh computers. SEs are also injected into main data acquisition event data stream. On the mainframe IBM computer they are copied to the history files. The CSC computer itself monitors some 200 VME-crates and other devices not linked to a particular subdetector.

Hardware alarms do not depend on computers. Only hardwired combinatorial logic is involved to handle critical situations immediately (e.g. to switch off high voltage power supplies). The central logic [162] uses open/close switch signals. It is connected to the experiment via a routing array which makes it possible to receive input from or deliver output to any location within H1. The central logic drives an alarm signalization panel in the control room and provides status flags read out by the data acquisition and included into the event data.

In summary, the hardware alarm system presently monitors some 170 signals. It works reliably and can readily accommodate new input or output anywhere within the whole experiment. The only change foreseen is automatic interaction with the accelerator.

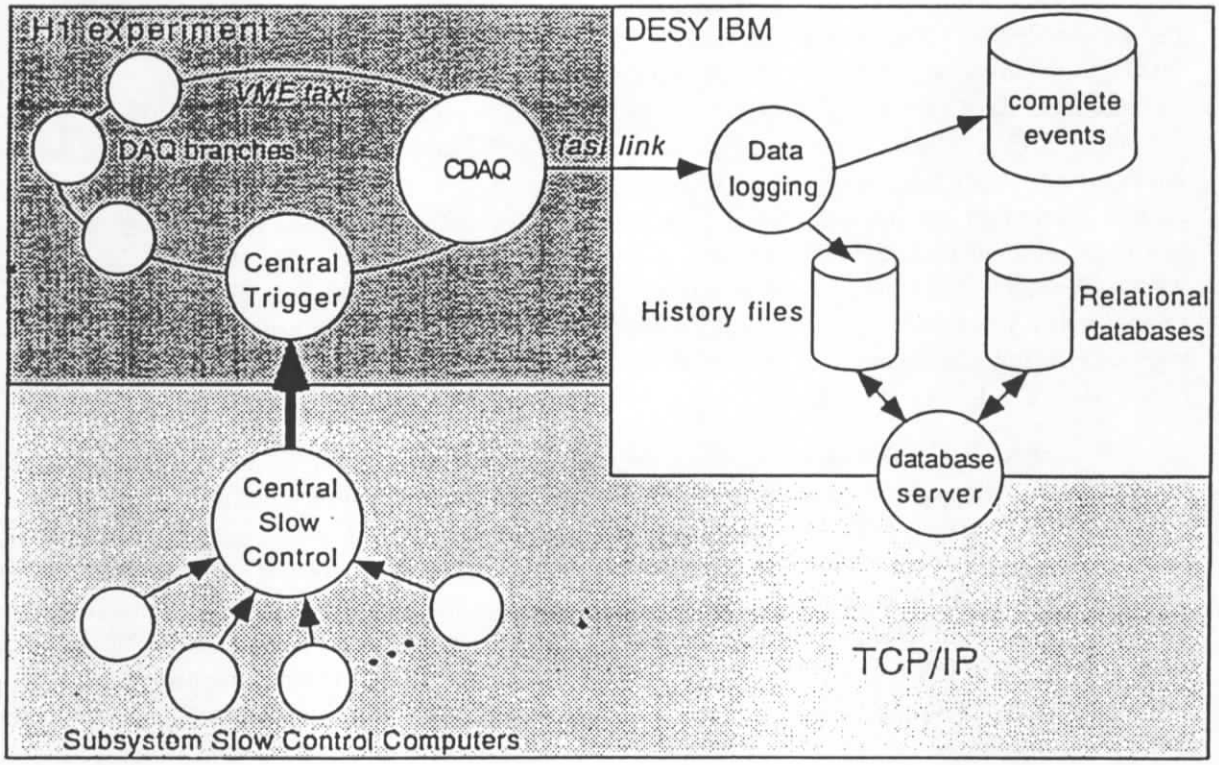

Figure 9.1: Flow of slow control data within H1. The data flow between the database server and slow control computers over TCP/IP has been omitted.

10 The data acquisition system

This section concentrates on the central part of the H1 data acquisition system, the front-end readout and triggering subsystems having been dealt with extensively in previous chapters.

From the real-time computational point of view, a total of over a quarter of a million analogue channels are read-out and digitized, resulting in some 3 Mbyte of raw digitized information for a triggered event. As the time between successive electron-proton bunch crossings is just 96 ns, various levels of hardware triggering, software filtering and digital compression are employed before reducing final data sizes to acceptable storage- media recording rates. For the data acquisition several hundred processing elements are embedded largely within the IEEE VMEbus standard [163]. Descriptions of the system also exist elsewhere [164, 165].

Figure 10.1 summarises the overall data acquisition system and the key rates at full HERA design luminosity. Information is digitized and read-out in parallel from many subdetector partitions before being finally merged. Four main levels of hardware triggering and software filtering can be enabled on all or part of the various detector partitions. In parallel data compression and formatting reduce the 3 Mbyte of raw data to event sizes of between 50 Kbyte and 100 Kbyte so that final data recording rates are restricted, at present, to a maximum 1.2 Mbyte/s. The first level (L1) pipelined triggering system selects initial candidates for data processing from the background. After a L1 accept the front-end pipelines are held. Dead-time then begins. A more refined hardwired L2 decision, based on combined information, can then be activated within 20 μs. Front-end electronics readout is not initiated until an early-level triggering decision is made whereupon each component has a maximum digitization time of 800 μs before the pipelines are re-enabled; a large amount of the data compression also takes place during this phase. A third level of filtering can be enabled so that should readout commence the pipelines are immediately reactivated if a L3 reject occurs.

In logical structure the detector components are merged, in parallel, into individual subdetector VMEbus crates which each contain a readout controller and memory buffer plus a fibre optic link to a coordinating event management task. A parallel array of RISC processors provides the fourth level of software-coded filtering once all of the full-event information is combined over the fibre-optics [157]. At all stages workstation intervention provides for data monitoring and detector control. To avoid saturation on global VMEbusses, extensive use is made of the local VSB specification [55]. To minimise any further dead time contributions, memory buffering is provided at the key data processing stages. Finally a local area network (Ethernet) caters for the relatively slow exchange of general operating conditions, files and even event-records between different subsystems. This also serves the external international community with current status and event information over wide-area networks.

10.1 System components

To provide a coherently managed system, between over 200 electronics crates, a baseline set of standards was established to ease maintenance and software development overheads.

10.1.1 Basic hardware components

For general-purpose real-time control within VMEbus, a common 68020/30/40 series processor card was selected [53]. On-board memory is dual-ported so that it can be accessed externally from the VMEbus (for communication) as well as internally from the processor itself. VSB local bus access can be extended to memory boards in adjacent crates but is never used as an

inter-crate connection. For even more calculation-intensive applications RISC processor-based modules are employed. The RAID 8235/8239 is a single-width VMEbus/VSB board based on the MIPS R3000 processor (25/40 MHz clock) and the R3010 Floating-Point Accelerator with up to 32 Mbyte of onboard DRAM [166]. To enhance memory bandwidths and reduce instruction access times, up to 128 Kbyte of independent data and instruction cache ensure that each board has an equivalent computing power of up to 80 % of an IBM 3090 mainframe. The DPM 8242 is the basic memory module and can be equipped with up to 16 Mbyte of 70 ns static RAM, having equal priority in arbitration from the VME and VSB ports [167]. A broadcast mode selection allows any VMEbus master to write to several memories simultaneously. Both the VMEbus and VSB memory base addresses are software programmable via VME accessible registers, permitting a managing Event Coordinator task (see later) to switch units between different events. Due to their graphics-user-interface and open NuBus architecture, Macintosh computers are used extensively for the purpose of software development and operator control. A maximum of 24 VMEbus crates can be mapped directly onto each Macintosh via MacVEE and Micron, MacVEE interface card resident on NuBus [168]. No sophisticated protocol needs to be initialised, unlike other DMA-based connections.

10.1.2 VMEtaxi

In many of the front-end subsystems the standard VICbus is used to interconnect crates [51]. However for coordinating the fast data acquisition transmission protocol between the different readout subsystems, VMEtaxi modules are employed [169]. These can connect VMEbus crates up to several kilometres with fibre-optics. Figure 10.2 illustrates the basic philosophy. All boards are interconnected with multimode optic fibres to form a ring, using AMD 7968/7969 TAXI-chip transmitter/receiver pairs. Because of this, there is theoretically no limit on the number of such devices which can be interconnected within a single ring; in practice one is limited by the software overhead in setting up transfers. Each single- width board has a CPU controller and single level VMEbus arbiter. The software protocol, discussed further in the following sections, is purpose-written and optimised for speed and efficiency in a data acquisition environment; no FDDI or similar networking protocol is adopted. In setting up transfers between any two crates, an initial description packet is sent around the ring; those modules not engaged in the subsequent activity can enable by-pass registers so as to establish a direct connection between the two VMEtaxis that are involved, analogous with SCI [170]. During the early stages of data-taking, a 25 MHz 68020-based board was used with 125 MHz taxi chips. Upgraded Mark-2 modules are now installed which exploit 50 MHz 68030 processors and either 175 MHz or 250 MHz taxi chips. By driving double-links in parallel there is the potential for 55 Mbyte/s point-to-point data transfers between crates up to distances of several km. The link reliability has been tested to a bit error rate of less than 1 in 10^{13}. Program memory is provided for by 128 Kbyte of on-board fast static RAM with an additional 2 Mbyte of on-board extension static RAM accessible over the VMEbus by external processors. On-board EPROM and EEPROM provide for firmware storage and configuration parameters. VME64 and VSB block transfer modes are realised on the Mark-2 modules with XILINX gate arrays.

10.1.3 Software

The architectural structure of the hardware, discussed in the following section, defines how the software is written and developed. Dedicated tasks run on dedicated processors throughout the VMEbus system with operator intervention provided for via graphics-orientated computers such as Macintosh. Different languages and approaches are used depending on the application being developed. Much of the online data acquisition systems code which executes on 68000 series microprocessors, within the VMEbus, is written in either C or Assembler. Final-level filtering

algorithms, which execute on the R3000 boards, have large code resources originating offline and written in Fortran [157]. Control programs which run on the Macintosh computers exploit the latest object- orientated and graphics-based packages currently on the market [171]. It can be seen that the Macintosh provides a convenient integral component in both software development and operator-control. In order to encompass the framework of VMEbus, extra tools have been developed to ease the integration into the VMEbus [172]. As a result, no formal operating system is required to run on the VMEbus boards; all basic functions can be controlled from a Macintosh via external directives through dual-ported mailbox memories. In order to enhance information exchange between control computers a dedicated package has been written based on international networking protocols [173]; this has the added advantage of enabling the complete system to be monitored from external laboratories and institutes.

10.2 System Integration

By convention the data acquisition system breaks down into three main categories for the purpose of central coordination and management. First there are the front-end "producers" of data; the end result of extensive electronics digitization from the subdetectors or "branches". Second, the data are merged and distributed to several full-event "consumers"; subsystems which monitor and record the data onto permanent storage media. Third, the system is initiated and controlled via external processes for overall system supervision and operator intervention. Figure 10.3 shows the physical layout of the complete system, managed centrally through several layers of software protocol, purpose-written around the VMEtaxi fibre-optic ring [174]. Common, shared, memory blocks provide for the communication between all system processors and external computer stations. The master of the ring executes the "Event Coordinator" task, controlling the whole sequence of management processes. A separate object module provides a software library to interface the individual subsystem elements, with features ranging from full module testing and control through to basic buffer management and system coordination.

10.2.1 The architecture of the front-end producers

The readout system of each branch is autonomous up to and including a central subdetector VMEbus crate. Each central subdetector crate contains a dedicated supervisory readout controller, a multi-event buffer (MEB), a VMEtaxi and any input drivers necessary to access the data (Figure 10.4). Consequently the design allows a particular subdetector to be decoupled from the rest of the system, during installation and test phases, and does not exclude the use of other busses for front-end digitization. Data are placed into the multi-event buffer over VMEbus and then extracted by the VMEtaxi either over VSB or locally, depending on whether the buffer uses a DPM or exploits the extension RAM of the VMEtaxi. The Event Coordinator management task runs on the master VMEtaxi of the ring and interacts with each readout controller via shared memory blocks. Before commencing data acquisition, the Event Coordinator is responsible for hardware recognition and initialization of the various branches. During acquisition, when it is free for event building, it searches the subdetector multi-event buffers for the next event. When all branches are ready with the same event number, the separate banks are transferred via the optical ring into a full-event buffering system. On completion, each corresponding buffer is released. A subdetector crate may also contain additional processors for data reduction, an interface to a subdetector monitoring computer and a subsystem trigger controller (STC). All STCs are interfaced to a dedicated central trigger controller which, in turn, coordinates the sequence of all hardware triggering levels together with obtaining information from the HERA machine [54]. Each STC provides signal ports for the component electronics and communicates with the readout through VMEbus read-write cycles and interrupts. A consequence of this is that the Event Coordinator needs no hardwired connection with the central trigger controller

itself; all management sequences are handled by software, so providing a portable solution to any large multi-crate VMEbus system [174].

At the subdetector branch level, the software library provides multi-event-unit routines catering for initialization, accessing status information, requesting buffers and signalling when event data are ready for merging. Readout error codes are normally indicated as standard parameters, but messages can be sent through the system in standard ASCII format to describe branch- specific anomalies. Figure 10.4 also shows how the protocol has been transparently mapped from a main branch through to a sub-branch structure by incorporating standard VIC links to merge smaller subsystem components.

10.2.2 The management of full-event consumers

As the Event Coordinator VMEtaxi builds full-event records it simultaneously broadcasts them along its VMEbus to dual-ported memories associated with parallel sets of " full-event units ". Event tasks are performed by connecting the unit processors with their respective full- event buffer (FEB) memories via VSB in order to minimise any bandwidth overheads (Figure 10.5). Since the memory has read/write access from both the event task processors and the Event Coordinator, full-event units need not only be "consumers" of data. An event unit can also become a "producer" of data, "feeding-back" data into the system. Consumers are able to determine which data they wish to receive, i.e. directly built events from the front-end branches or data fed-back into the system from, for example, a parallel filter farm. All this is handled modularly by the software protocol and its associated library of routines.

Typical full-event tasks are local data-logging, event display, data monitoring and histogramming. A more sophisticated form of unit is the fourth level filter "farm" consisting of many MIPS series processor "nodes" working in parallel. Each node executes the same algorithm independently on different events. This provides not only a final level of triggering but a further stage of data processing and online reconstruction, used for online event display [175].

Event records are passed to the different nodes under control of 3 filter input controllers, which communicate with the Event Coordinator as normal consumer full-event tasks. When a node is free it signals this to its filter input task which waits for an event ready in its full-event buffer. The data are then extracted over the VSB and sent to the free node, releasing that particular buffer and enabling a further node to be serviced. When a node has finished processing an event it signals completion to the filter output controller (a "feedback" event task). The latter then decides whether to pass the event back into the central system managed by the Event Coordinator and frees the node buffer for further processing. As a full-event unit, the parallel filter can be easily enabled or disabled. The filter output controller in addition handles output to permanent mass storage.

Final event records are sent to an SGI Challenge computer some 3 km distant [176].

The data is transferred via 4Mbyte VIC8251F crate interconnects to FORCE VMEbus based UNIX single board computers with SBUS FDDI cards to a Netstar Gigarouter in the 3 km distant central DESY computer centre, from where the data is finally transferred via HIPPI to a SGI Challenge mainframe and via SCSI to an Ampex DST800 tape robot. In case of link failure a backup event task, that drives a storage device directly from VMEbus, can be enabled.

10.2.3 System supervision and operator-control

The H1 system is capable of running entirely in VMEbus; Figure 10.6 illustrates the composition of the central part where dedicated processors run dedicated tasks so that the net result is one

of a conventional multi-tasking system. This leads to a natural division of tasks and processes. The primary tasks of data acquisition are performed by the subsystem readout controllers, event builders, filter control tasks and event units, all managed by the Event Coordinator. All fast processing and readout is done within VMEbus. An exhaustive software library caters for external control by providing a full set of routines for system configuration, testing, system-status and monitoring [174]. NuBus-based Macintosh computers take over the responsibility of program development and run- time operator-control. The System Supervisor Mac [177] initialises the readout and checks the status of all elements by initiating VMEbus tasks such as the Event Coordinator. To provide a central focus of monitoring it also communicates with event tasks and subsystems either through VMEbus or over Ethernet. Additionally it serves the network with status information for external monitoring. The graphics-based philosophy of the Mac ensures that the operator is presented with, arguably, one of the most human-interactive interfaces, available today, to a complex real-time system.

10.3 Observations and performance

The H1 data acquisition system was initially commissioned during cosmic-ray tests in Spring 1991 and then used to read out the complete detector during first HERA operation in Summer 1992. Its advanced preparation, and relatively stable operation, was in no small measure due to the choice of an open, industrial bus- standard and the incorporation of modern commercially-available hardware and software where suitable. Of particular note has been the extensive use of the networking facilities in addition to the main data flow. The ability to control and monitor the system externally, even from the latest generation of portable note-book computers, has been extensively capitalised upon.

From the master VMEtaxi the system can manage up to 32 branches and 16 full-event units, including the parallel filter farm, providing status information and accepting control command sequences from the System Supervisor Macintosh. Presently events of up to 100Kbytes can be coordinated from 12 branches at rates up to 200 Hz using the Mark-2 VMEtaxi modules, depending on the filter farm rejection rate. The primary sources of dead time remain at the front-end, where future injections of greater processing and refined triggers are made more comfortable by working within an international bus standard.

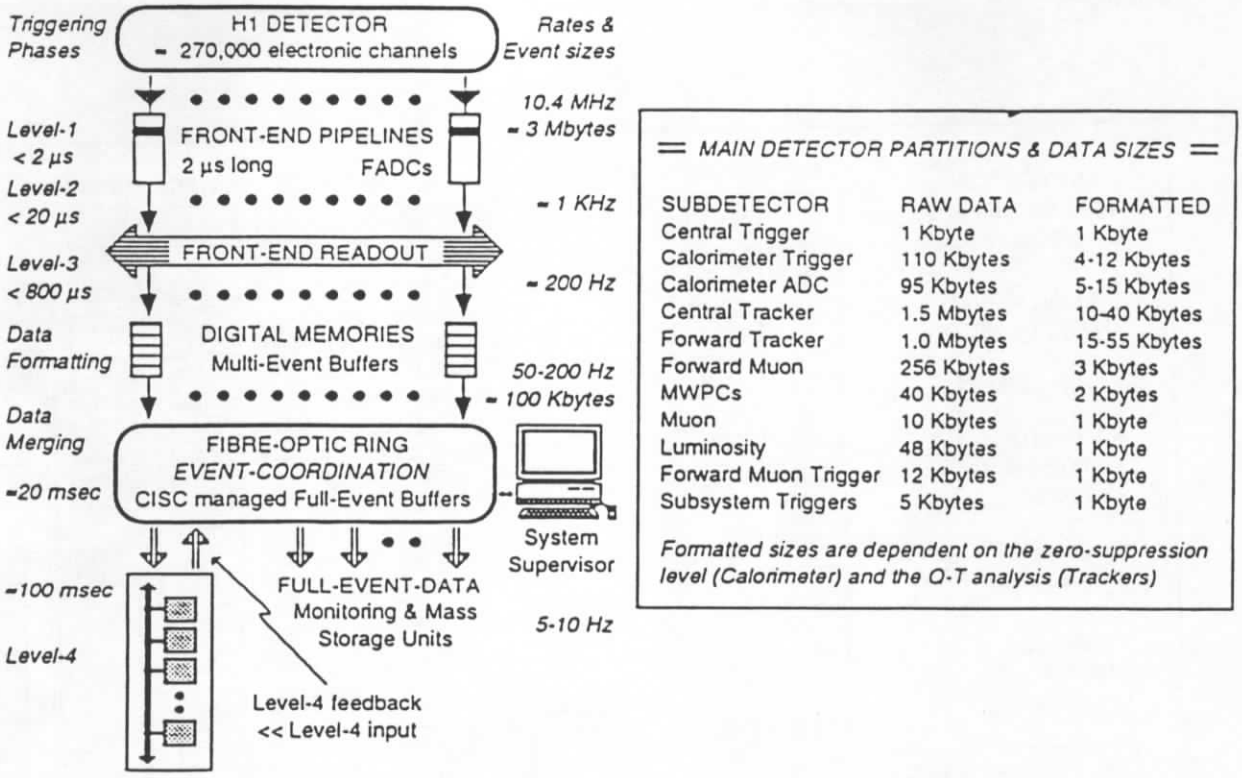

Figure 10.1: Overview of the H1 data acquisition system.

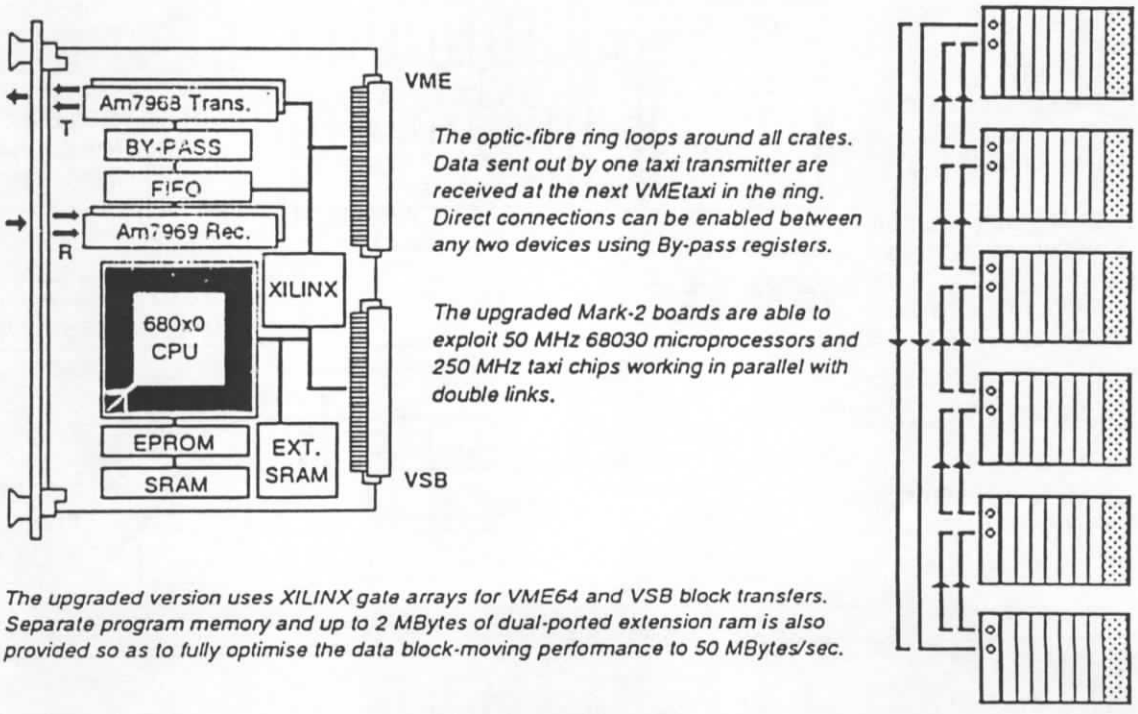

Figure 10.2: VMEtaxi fundamentals.

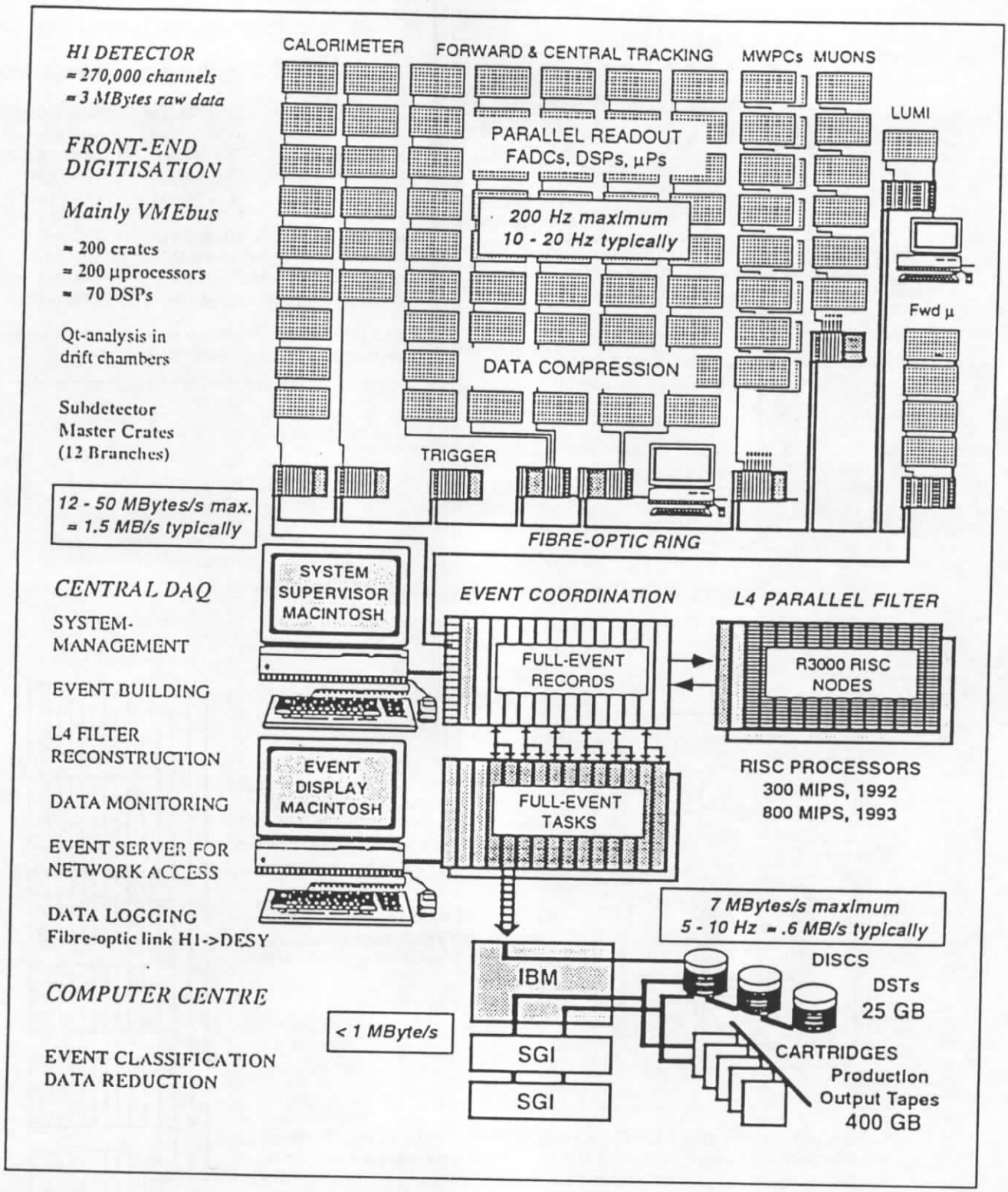

Figure 10.3: Physical layout of the key features of the H1 data acquisition system. See text for details.

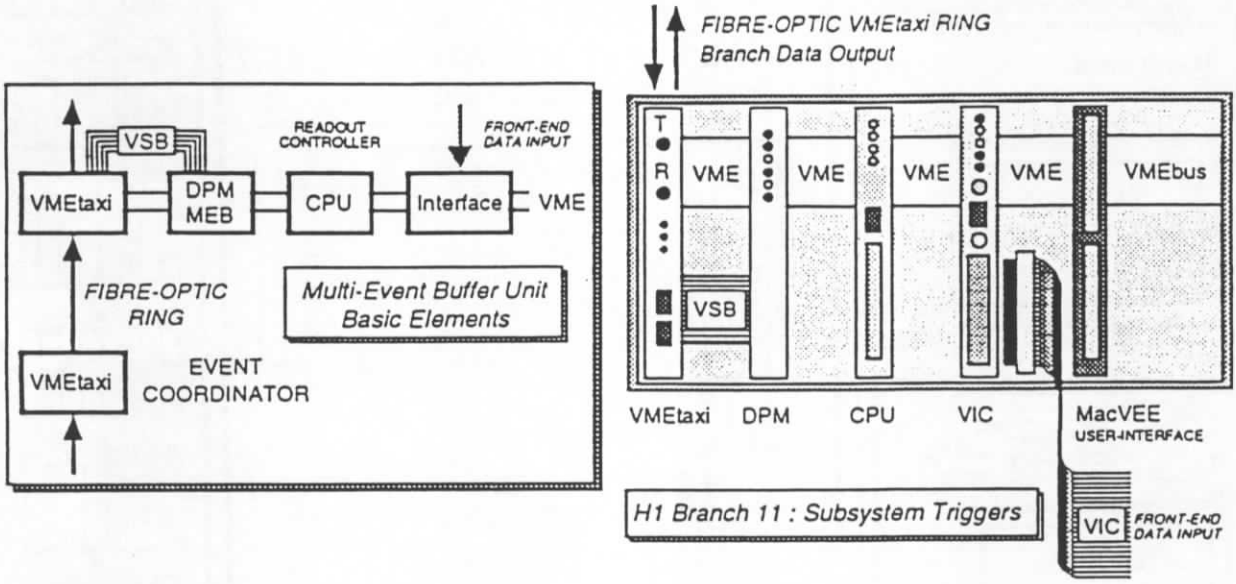

Figure 10.4: Multi-event buffer units.

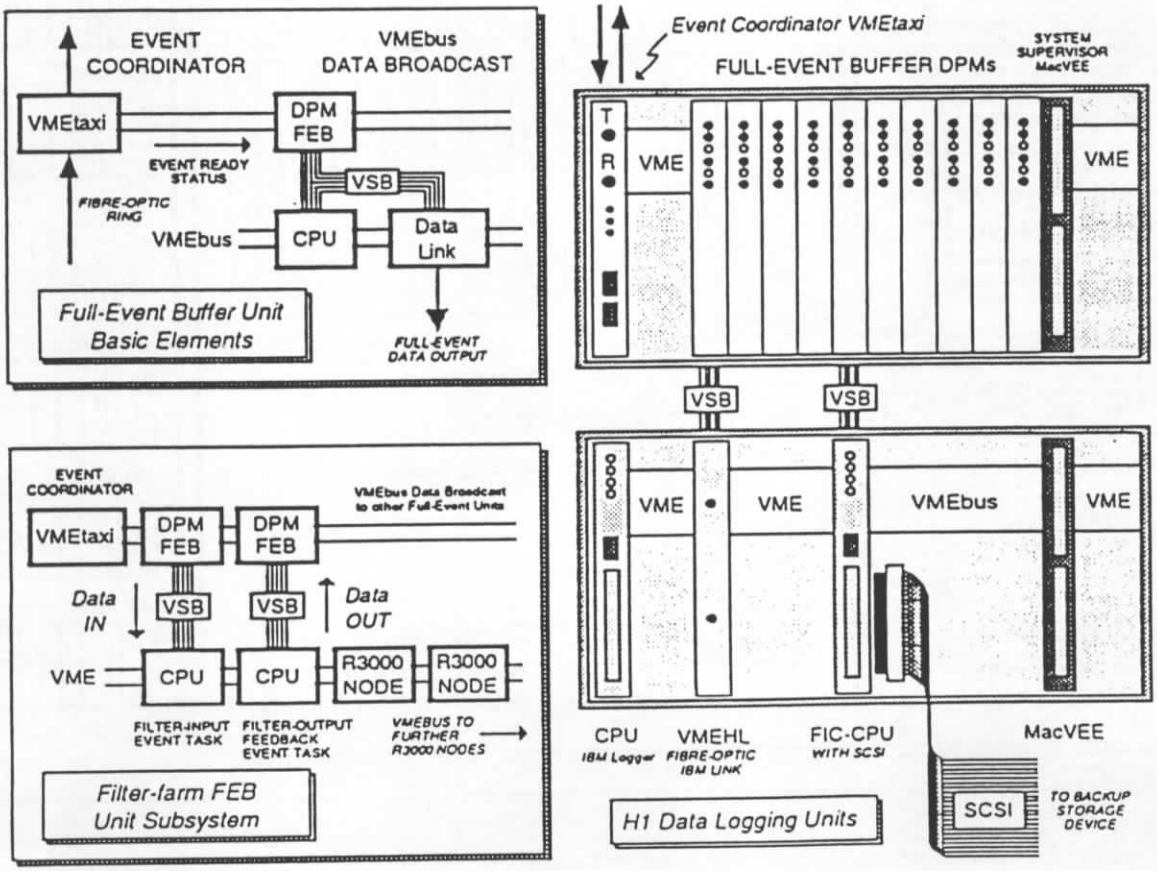

Figure 10.5: Full event buffer units.

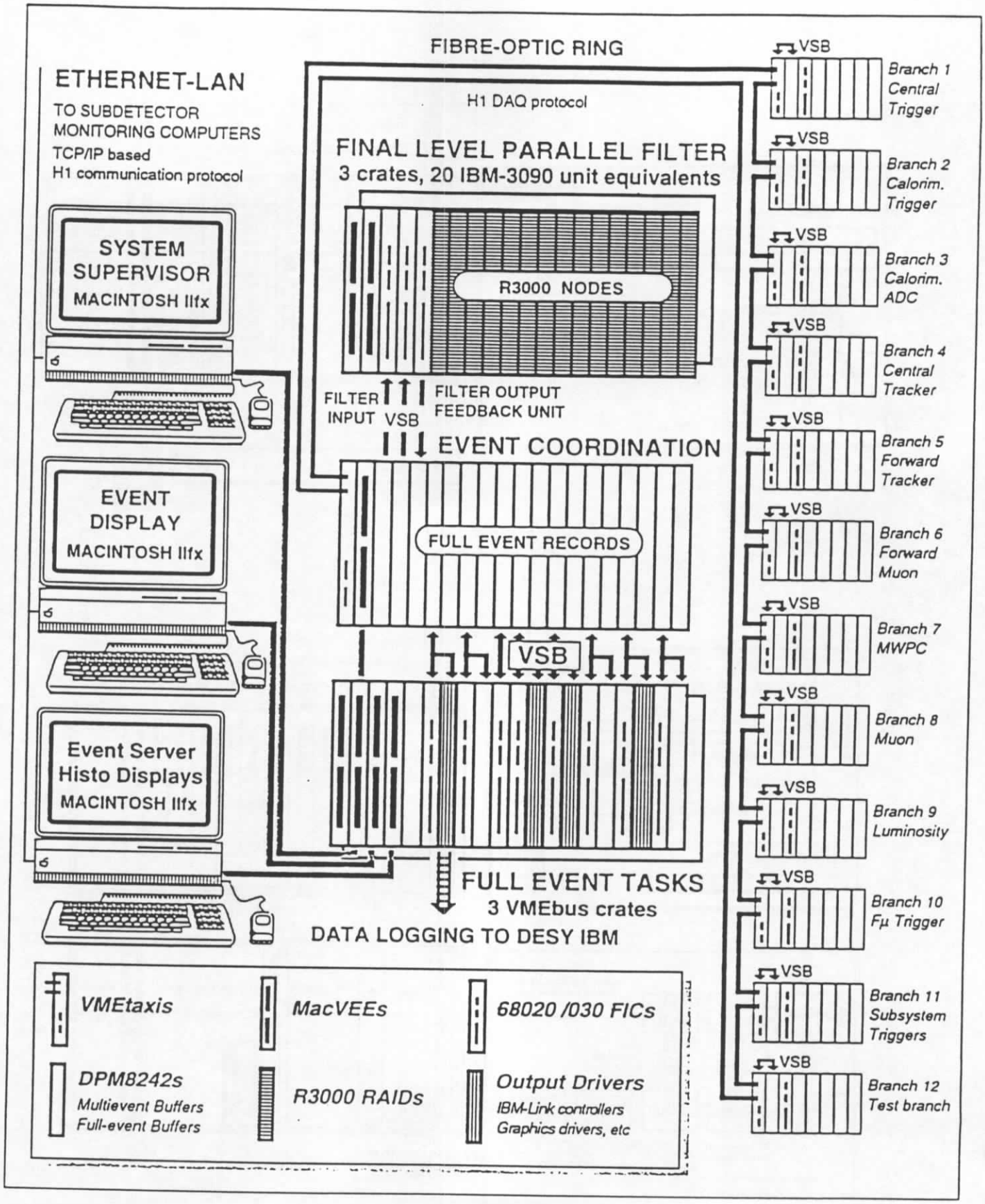

Figure 10.6: Physical composition of the central part of the H1 data acquisition system as during the data taking periods of 1993 and 1994.

11 Off-line data handling and simulation

This section concentrates on the off-line data handling, quasi-online data reconstruction, event simulation and the H1 analysis environment.

11.1 Off-line computing

An overview of the H1 offline computing environment is given in Figure 11.1. The H1 experiment is using two multiprocessor SGI Challenge series computers for all computing purposes [178] They are connected to the DESY computing infrastructure via fast UltraNet, HIPPI, and FDDI links as well as Ethernet. Fast access to data both on disks and tapes is provided. The disk space amounts to about 500 GB connected via SCSI interfaces. The access to the data stored on disk allows many users to analyze the data simultaneously, thus offering an efficient environment for physics analysis. Major tape service is provided by four Storagetek Automatic Cartridge Systems with a total capacity of about 35 TB, directly accessible from the SGI Challenge using the Open Storage Manager software. Mass data are also kept on an Ampex TeraStore mass storage system, equipped with 3 helical scan D2 recorders and connected to the SGI Challenge via SCSI interfaces. The total capacity of the Ampex system amounts to 6 TB. Multi-user access to data on tape is also offered by an efficient staging mechanism. Export of data is performed via 3490 and Exabytes cartridges.

During data taking, one of the SGI computers is dedicated to the data logging and online reconstruction tasks. The analysis of data is performed on the second SGI Challenge computer and partly on the IBM mainframe. Several institutes have also installed RISC processor based workstations at DESY for analysis purposes, connected to the local network facilities.

Care has been taken from the beginning that all offline processing of the data and simulation was portable between DESY and external institutes. Meanwhile many of these institutes have installed the complete offline program chain and participate in simulation and data analysis. More than half of the detailed detector simulated data were produced in external institutes. Furthermore, most institutes are connected to DESY via fast network links.

H1 uses the dynamic memory management package BOS [179] for its software. A general input/output package, FPACK [180], was written in order to have a simple and unique system for all data transfer in the experiment. It contains automatic wordformat conversions between different machine representations (IBM,VAX,DEC,IEEE), includes record selection options and supports event directory based fast access to data. A database package was developed and is used to store run dependent data and Monte Carlo information. Further, the code manager CMZ [181] is used for the H1 software packages. A set of simple but solid rules, complemented by the necessary subdivision of responsibilities and the imposing of discipline, has created a successful and efficient environment for code development in this large collaboration. Details on code management with CMZ in H1 can be found in [181].

An important aspect of the software is the concept of modularity [182]. Modules are self-contained sets of routines with clear I/O interfaces. They take care of their own initialization upon first call. Modules communicate to each other only via BOS banks. A larger program, such as the reconstruction program, consists of a simple series of module calls. Purpose written utility software performs automatic bookkeeping of used input and created output BOS banks and guarantees the internal consistency of the data after reprocessing of modules. The dynamic memory management package BOS includes modularity oriented functions to support this scheme.

H1 also uses an entity relationship model as a basis for data structures of all event data. A data management tool DATMAN [183] provides an easy and userfriendly access to the data.

11.2 Data reconstruction and reduction

The H1 data are reconstructed quasi-online [176] on an 18 processor SGI Challenge computer. The reconstruction task runs in parallel up to 25 identical and independent processes, whereby a set of shared memory areas and semaphores is used to share data among the processes. The raw and reconstructed data are stored on D2 tapes on a dedicated tape robot. During normal operation, the data taking proceeds with an average rate of about 500 KB/s, leading to an expected yearly data volume of about 5 TB. A part of the event information is stored on disk (DST) for physics analysis for the full data taking period.

The reconstruction of an event takes on average 1.5 s on a SGI Challenge processor. Thus the reconstruction task can cope with the data logging rate of 10 Hz of the experiment. In all, the reconstructed data become available to the users typically a few hours after the raw data are recorded by the experiment. The amount of recorded data by experiments at HERA is large. During the 1994 data taking period about 7×10^7 triggers were recorded by H1. The total integrated luminosity in that period was about 3.5 pb^{-1}. Off-line event classification and background rejection filters, based on reconstructed energies and tracks, reduce the amount of background presently by a factor 3 to 5 during reconstruction. Background rejection filters include cosmic muon and muon-halo filters, recognition of coherent noise patterns and filters for beam-wall and beam-gas collisions originating from outside the detector.

11.3 Event simulation

A complete detector simulation program has been assembled within the GEANT [110] framework. The geometry of the full detector and the beamline within ± 100 m around the interaction region is implemented with two different levels of detail, called fine and coarse granularities. For the fine granularity the longitudinal structure of all calorimeter stacks is implemented layer by layer, whereas for the coarse geometry a calorimeter stack is implemented as a block of properly mixed homogeneous material with no longitudinal structure. For the tracking detectors separate volumes are implemented for each active cell (wire) for the detailed geometry, whereas for the coarse geometry an entire gas volume is treated as one volume. For accurate detector response, particularly in the detailed geometry option, the tracking cutoff parameters for the kinetic energies have to be set as low as 1 MeV. This leads to simulation times of the order of 200 s for a typical low Q^2 deep inelastic event on a SGI Challenge processor. Three strategies were followed to tackle this large CPU time consumption for event simulation:

- The time consuming part of the actual tracking of particles through the geometry was strictly separated from the digitization part of the detector response. Run dependent detector effects and the actually achieved resolutions can easily be adjusted by reprocessing the digitization part only, using only a fraction of a second per event. A similar scheme was used for the simulation of the trigger response.
- A book-keeping is made of all energy depositions in the detector, both for visible and invisible (nuclear breakup, neutrinos, slow neutrons) energies, and both in active and dead detector regions [184]. This allows to reconstruct the calorimeter response after simulation with simple response functions, which are basically sums over the smeared true energy depositions. The absolute energy scale can thus be reconstructed correctly, which gives an important handle for testing the reconstruction programs and also to understand the behaviour of a non-compensating calorimeter.
- A fast but accurate energy shower parametrization [103, 108] was developed. This so-called H1FAST mode was included into the GEANT framework. The main idea is sketched in

Figure 11.2. The time consuming part of the full shower development in the detailed geometry is replaced by a shower parametrization in the coarse geometry leading to reduction of the CPU time consumption by a factor 10. Showers which cross crack boundaries are simulated in detail, in order to keep accuracy.

11.4 Physics analysis

The visual aspect of the physics analysis is mainly handled by a purpose written general system for graphics applications, baptized LOOK [179]. The aim is to have one –and only one– graphics package for all graphical applications: event display, histogramming, analysis, etc. LOOK can be considered as a layer between the user application and low level graphics functions, for which at present GKS functions are used. LOOK organizes the management of the display and e.g. hardcopy devices. It further contains a histogram package and a powerful command processor and is portable to many platforms. The H1 event display program, H1ED, is an application based on LOOK. Figure 11.3 shows an example of an event display and histogram analysis combined in one session. LOOK can be used for interactive analysis, e.g. n-tuple analysis of data. Also PAW ([185]) is used for interactive analysis.

The program H1PHAN is a tool to access event data and simplify physics analysis programs. The data are filled in internal event buffers called Q-vectors, which are accessible in simple Fortran DO-loops. Thus the user does not need to know the –sometimes complicated– underlying bank structure of the data. H1PHAN further contains tools for particle identification, secondary vertex fitting, jet finding and analysis, determining kinematic variables of deep inelastic event candidates, etc.

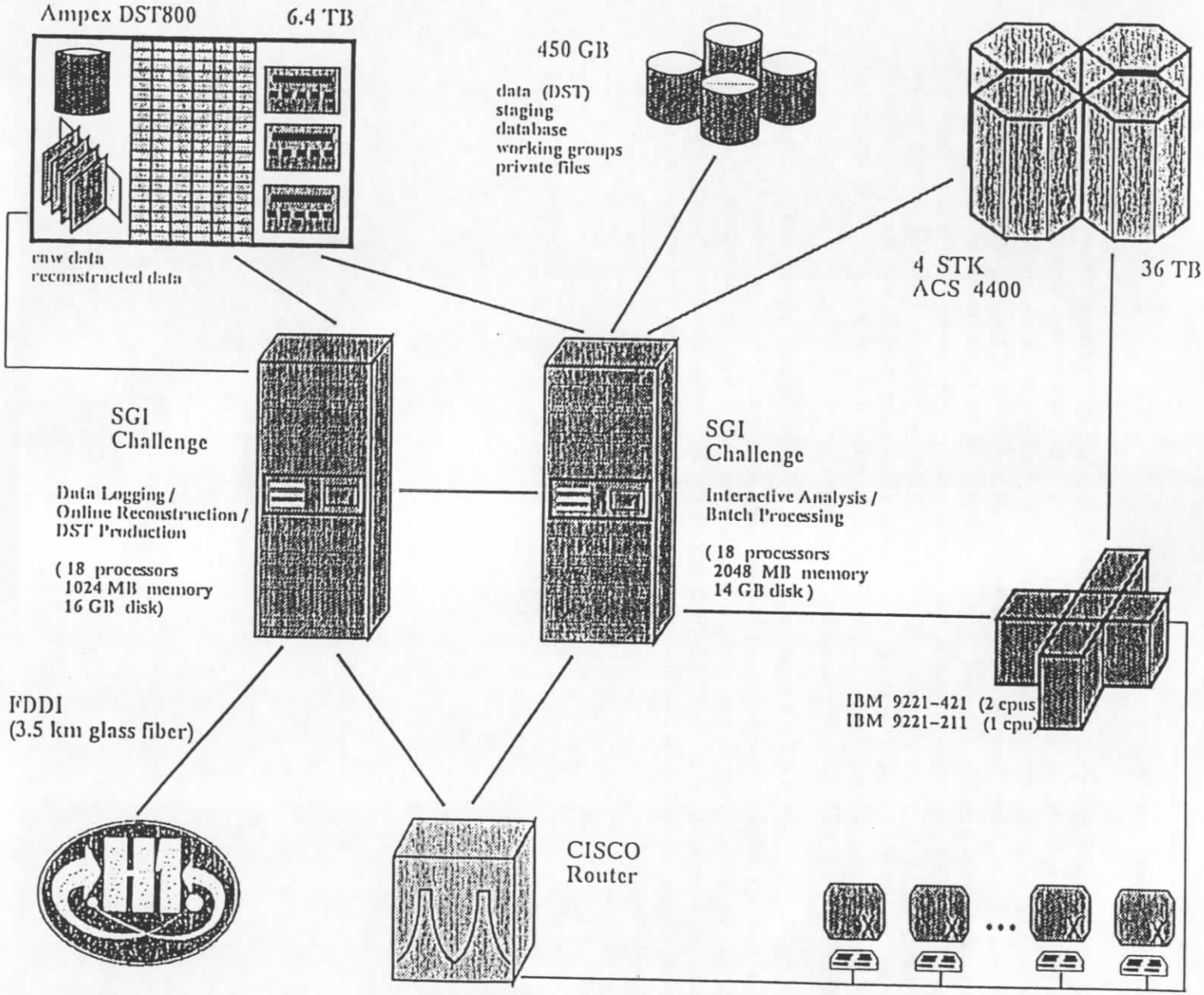

Figure 11.1: H1 off-line computing environment

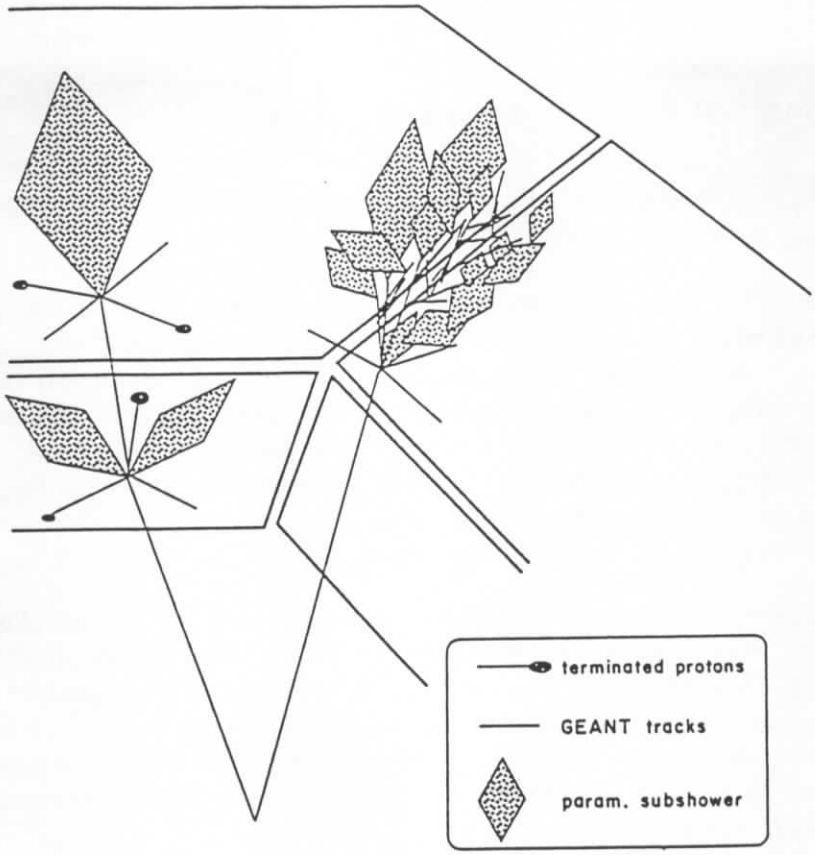

Figure 11.2: Schematic view of the parametrized shower simulation in a coarse geometry.

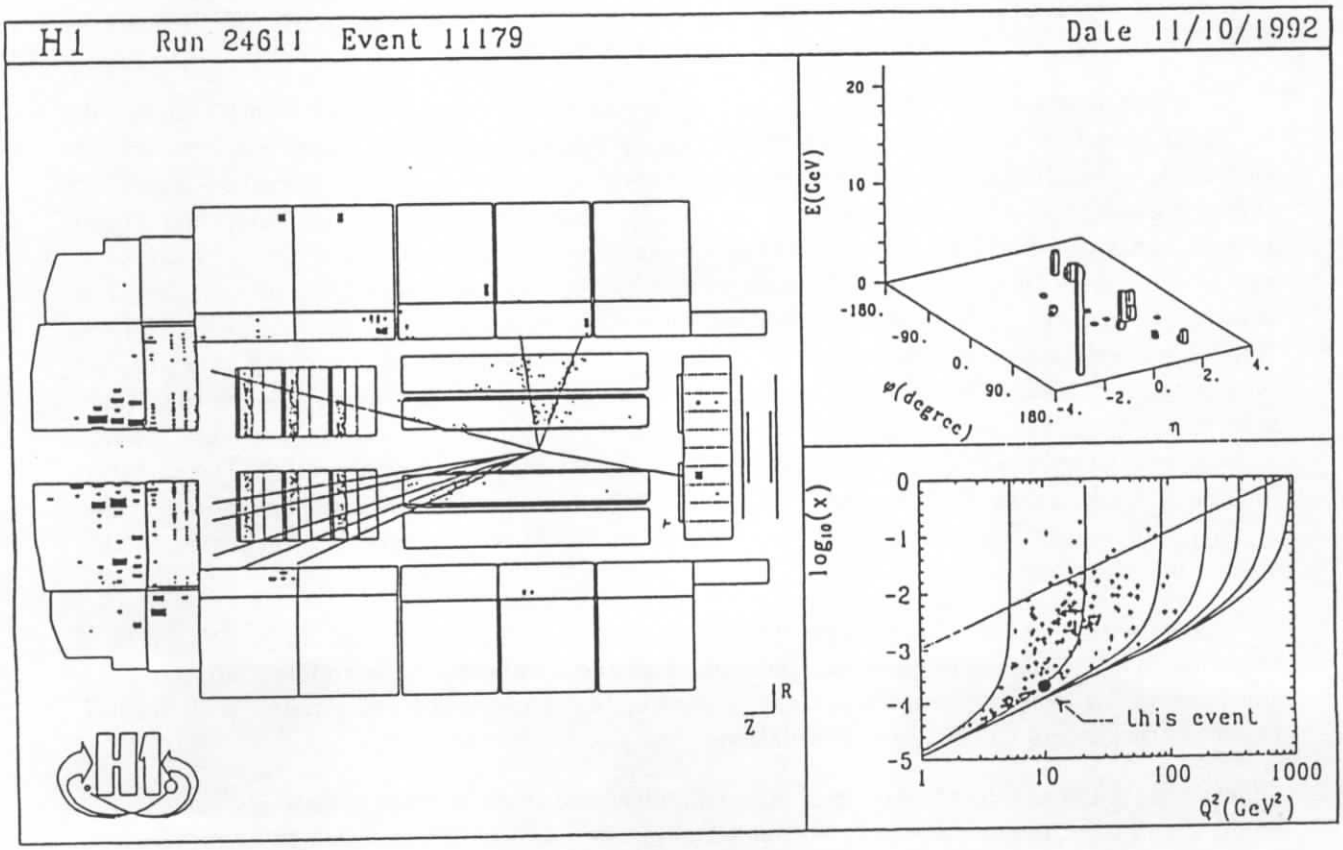

Figure 11.3: Physics analysis with LOOK

12 Summary of first operation at HERA

The successful operation of the H1 detector during the first years of HERA is evidenced by the many publications [186] which resulted from it.

The measurement of the total photoproduction cross-section [140] relied mainly on the luminosity monitor and electron tagger. It showed that the novel technique of monitoring luminosity via the $ep \rightarrow ep\gamma$ bremsstrahlung process combined with on-line background subtraction using electron pilot bunches can be used meaningfully. The electron tagger signal alone provides a fairly clean trigger for all photoproduction physics. Supplemented with tracker and calorimeter information at the trigger and reconstruction level the prominent beam gas background can be removed completely, as demonstrated in the analysis for hard photon scattering [141]. Figure 12.1 shows an event typical of this type of processes.

The total cross-section measurement with the electron tagger was cross-checked with data triggered only by the $z-$vertex trigger (see Section 8.3.1.2), which required a minimum number of tracks from a common vertex in the interaction region. Though photoproduction events from a different range of Q^2 and y are accepted by this trigger, a detailed understanding of this trigger and its dependence on chamber efficiency, noise, crosstalk, track transverse momentum p_t and energy loss is need, as is also a subtraction of proton pilot bunch data. The results are found to nicely confirm the electron tagger analysis.

The above examples were cited to emphasize again one of the stronger points of the H1 detector, which has been explained in more detail in the trigger section above, namely the ability to trigger on the soft physics while not loosing the deep inelastic events or vice versa. The use of topological information rather than thresholds on individual detectors, is a major step forward and will ease data taking at higher luminosities.

The first measurement of deep inelastic scattering in the new kinematic domain accessible to HERA required an understanding of the energy response of the backward electromagnetic calorimeter (BEMC) and the backward and central parts of the LAr calorimeter. Figure 12.2 shows the spectrum of energy clusters in the BEMC. Without additional constraints the trigger rate amounts to a few Hz/GeV even at the low beam intensities achieved so far. The observed rate is dominated by proton induced background hitting the rear part of the calorimeter. The rate can be reduced by almost two orders of magnitude by a simple timing requirement in the time-of-flight detector. In the analysis simple event topology and track matching cuts produce an almost background free electron spectrum for energies exceeding 15 GeV. Below that value fake electron signatures from photoproduction hadronic final states become dominant. These can be rejected by active electron identification tools (like shower shape analysis). The so-called kinematic peak, a feature discussed in our first publication on deep inelastic scattering at low x [187], and also in Section 5.2 in the context of the BEMC calibration, is clearly seen in this spectrum.

Events with a hadronic final state [188] are of the type shown in Figure 12.3. The check of the balance in transverse momentum (see Figs. 5.15 and 5.22) entails the understanding of both the hadronic as well as the electromagnetic part of the liquid argon calorimeter, and the link between tracker and calorimeter information.

On the technical side, the high stability, reliability and small number of dead channels in the liquid argon calorimeter deserve to be singled out. The noise level was found to be low enough to extend its use down to quite low energies.

The digital muon system and the muon trigger behave as expected. Fig. 12.4 shows the invariant $\mu^+\mu^-$ mass spectrum for elastic and inelastic photoproduction of J/Ψ mesons, with a

prominent peak at the mass of the J/Ψ meson. These events were mostly triggered and identified by the muon system.

Figure 12.5 shows the resolution of the K^0_s peak in the $\pi^+\pi^-$ mass spectrum and of the $\Lambda(\bar{\Lambda})$ signal. This may serve as evidence, that the isolation of J/Ψ, D^*-tagging etc. is feasible, once sufficient statistics is available. The $J/\Psi \rightarrow \mu^+\mu^-$ candidates found prove that the tracker muon link can be made.

On the software side the online filtering and reconstruction concepts have permitted a fast access to the data, and also their quick reduction and dissemination to the various analysis centres.

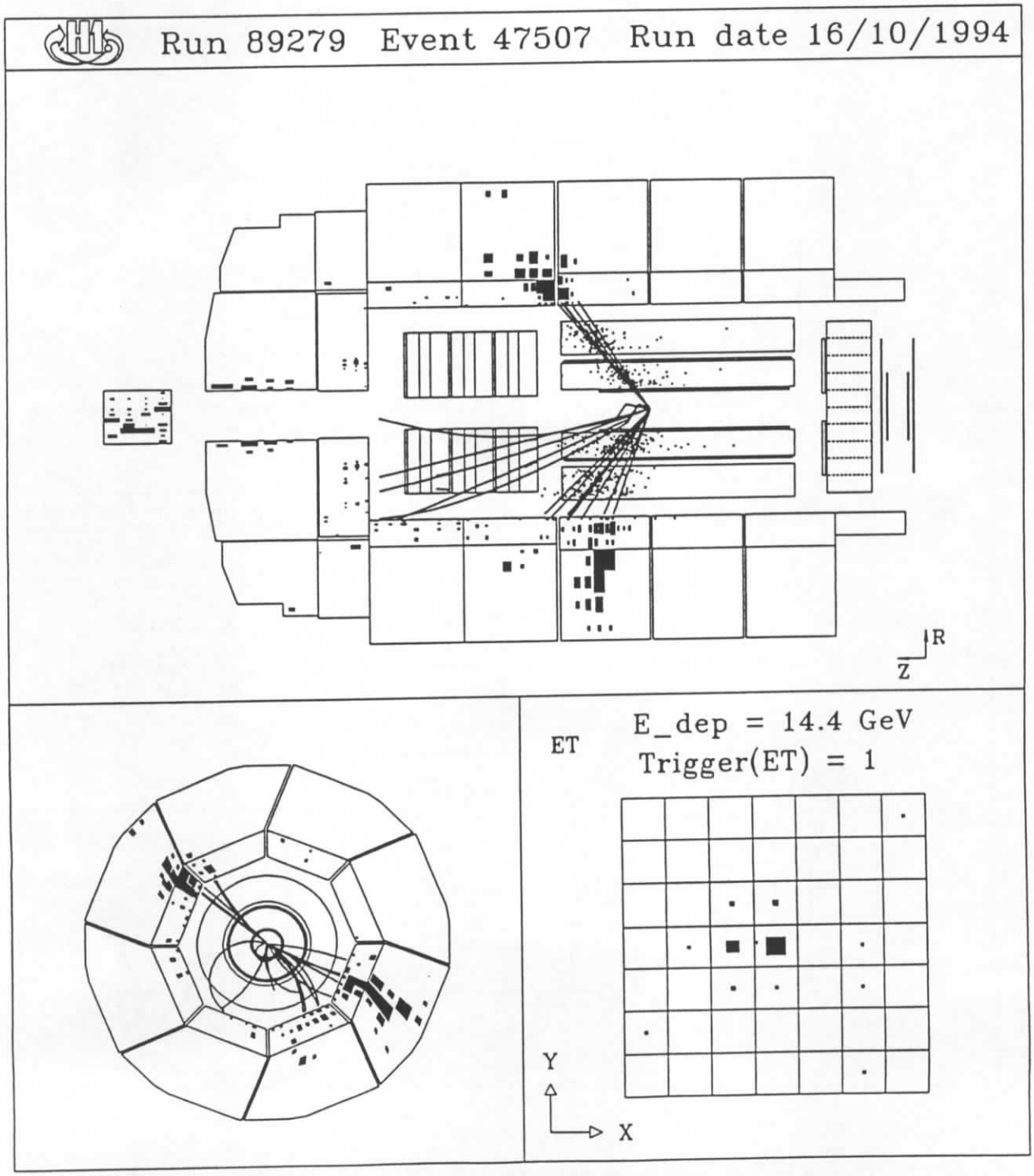

Figure 12.1: Typical two jet event from $\gamma - g$ fusion tagged by an electron in the tagger.

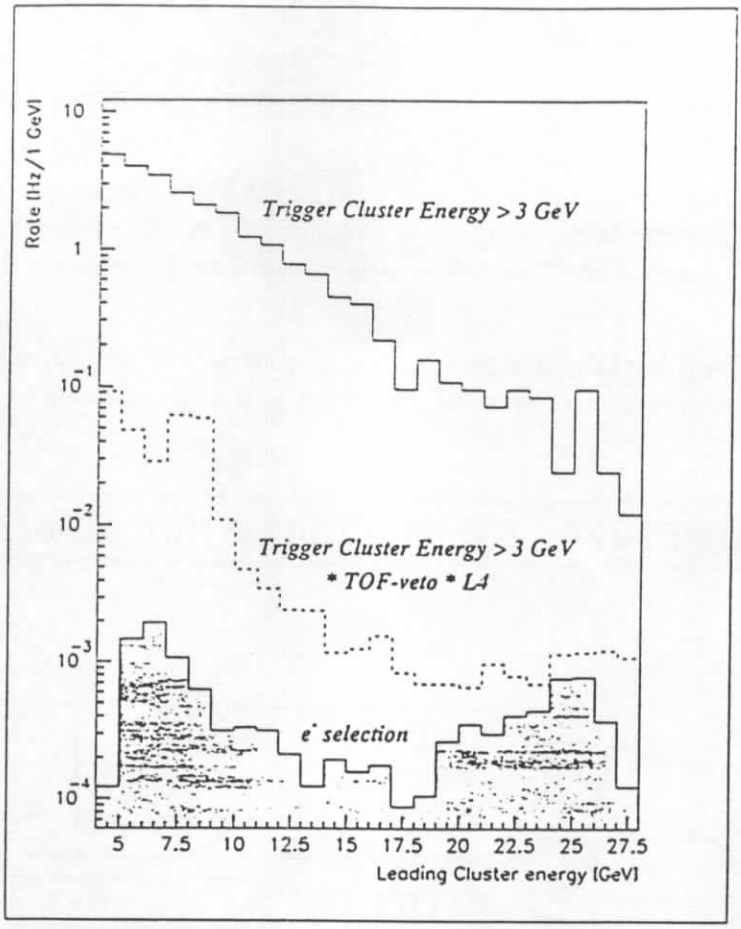

Figure 12.2: Absolute trigger rates recorded in the backward electromagnetic calorimeter in function of cluster energy at different trigger and reconstruction levels.

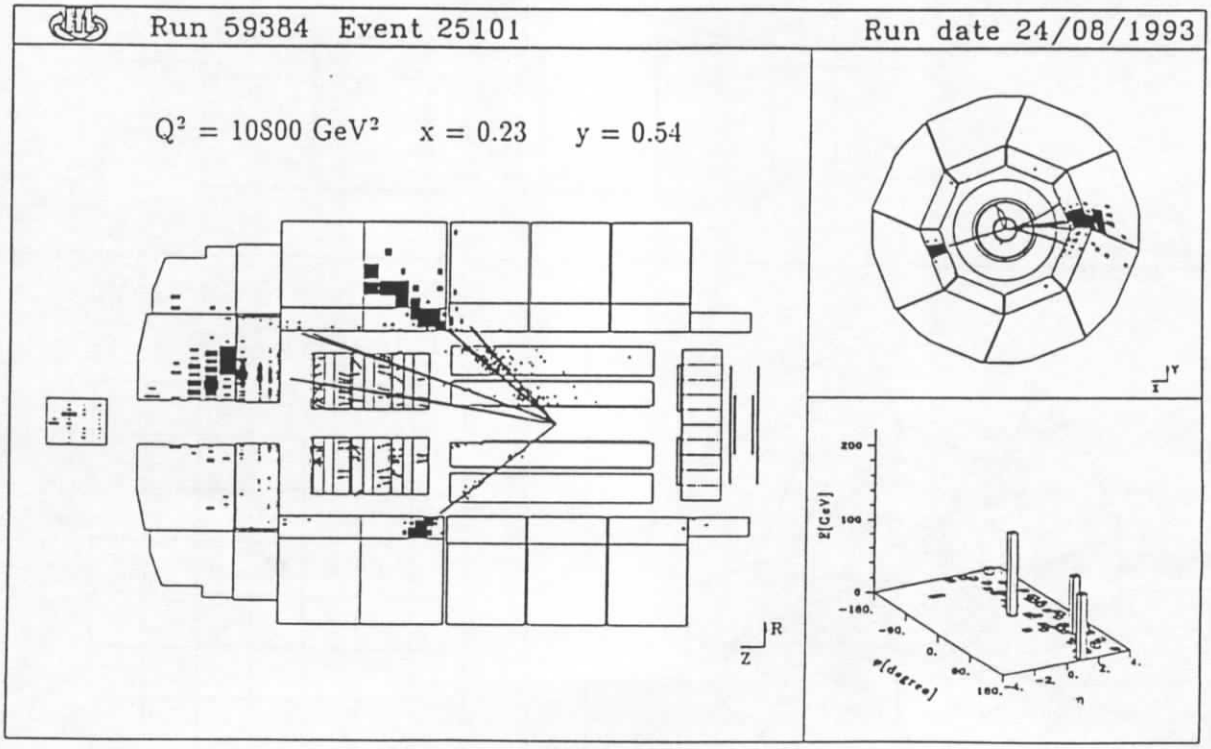

Figure 12.3: Typical high Q^2 event with both the scattered electron and the hadronic recoil jet observed in the LAr calorimeter.

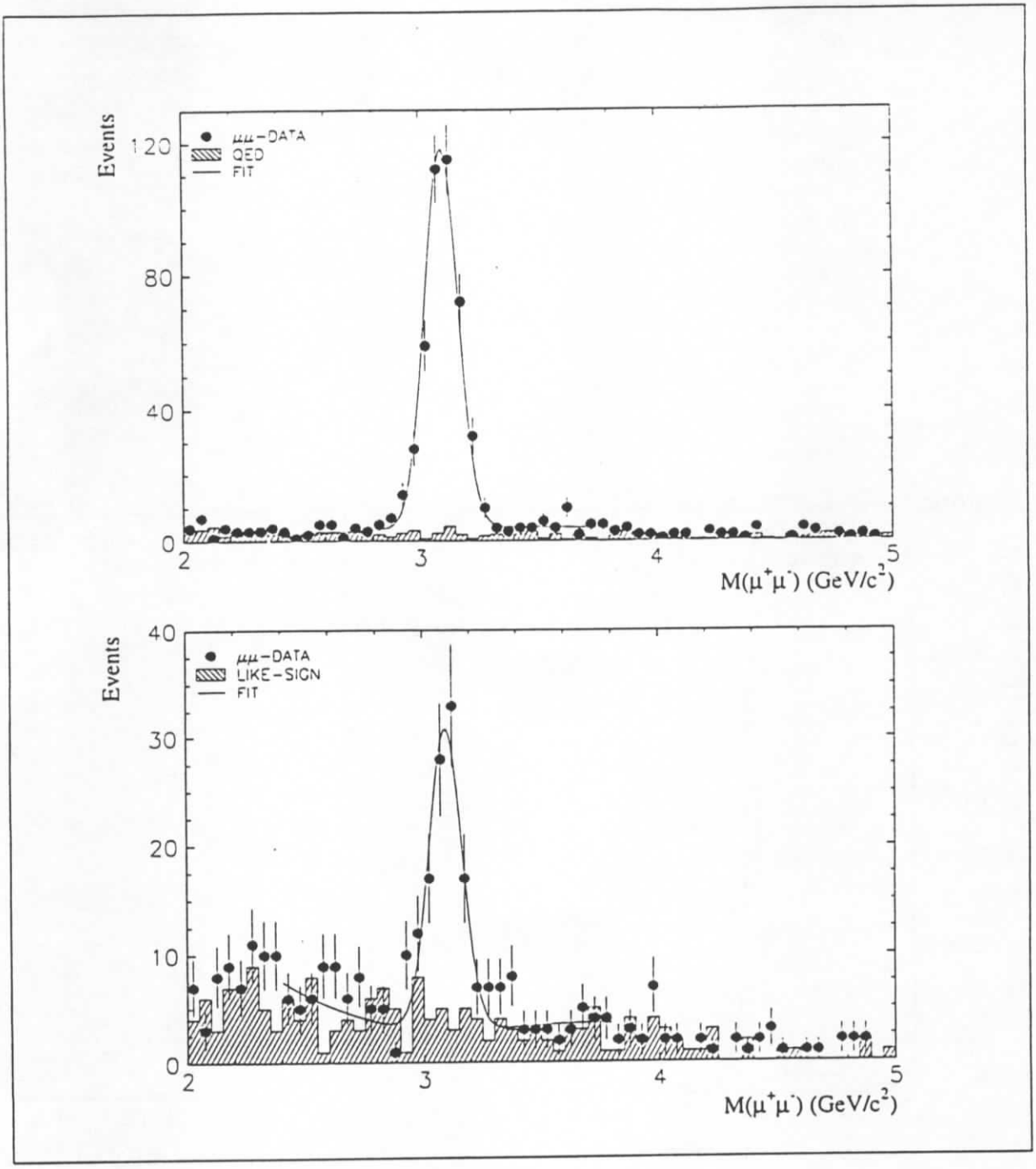

Figure 12.4: Invariant mass distribution of elastically (top) and inelastically (bottom) produced $\mu^+\mu^-$ pairs in J/Ψ photoproduction. The curve is a fit of a Gaussian plus a polynomial background to the J/Ψ mass region. The shaded histogram shows the contribution of QED lepton pairs (top figure) and the contribution of like sign muon pairs (bottom figure). The maximum of the fit is at 3.10±0.01 GeV with a width of 76 MeV, and at 3.10±0.01 GeV with a width of 65 MeV for the top and bottom distributions respectively, the detector simulation yielding in each case a width of respectively 65 MeV and 60 MeV.

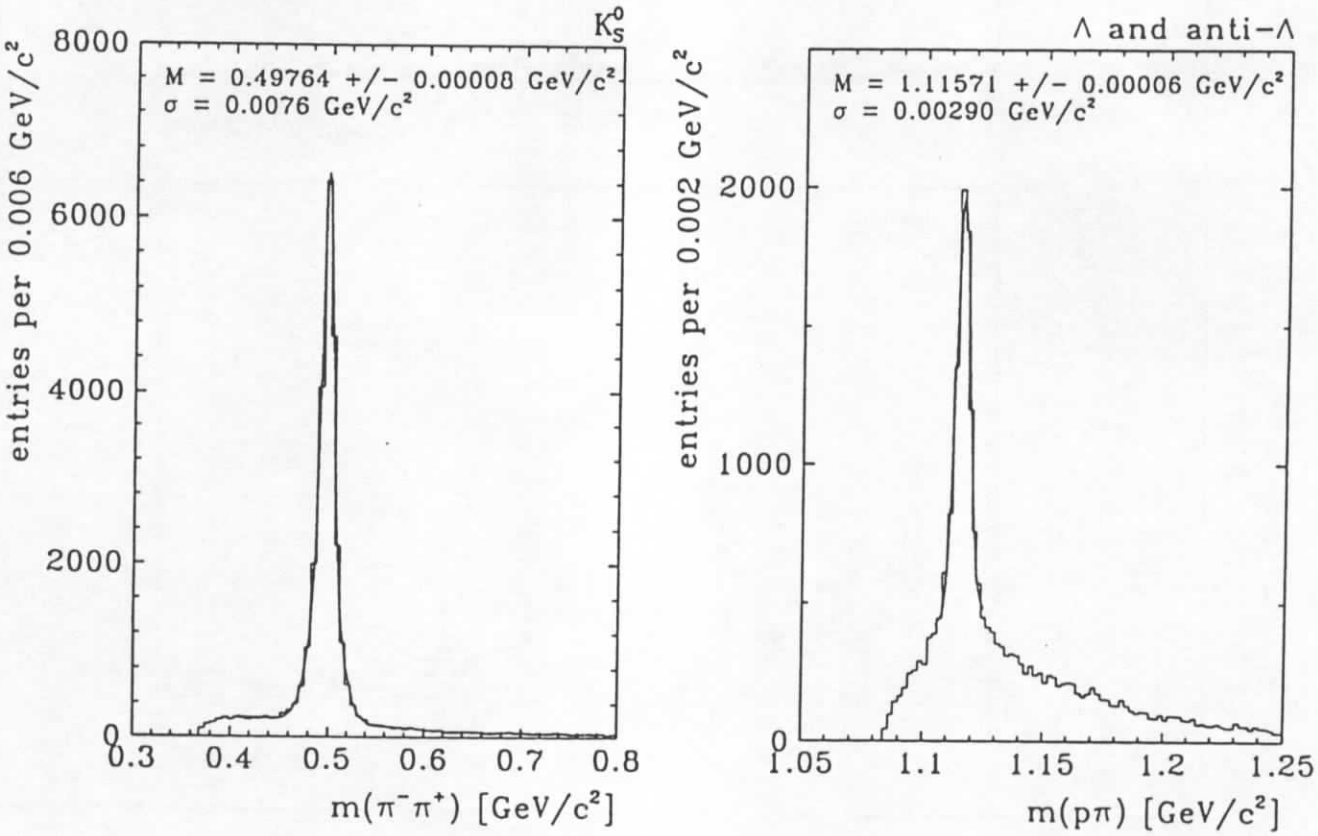

Figure 12.5: K^0_s (left) and $\Lambda(\bar{\Lambda})$ (right) signal observed in the central jet chamber.

13 Upgrade program

During the winter shutdown 1994-1995 the detector was moved out of the beam and several upgrade operations were performed, as listed below:

- the beam pipe was replaced by one of smaller diameter (Ø9 cm) made of Aluminum, 2% of X_0 at 90 °.
- a set of trackers made of silicon detectors (CST and BST) was installed between the beam-pipe and the CTD, the CST (see [14, 189, 190]) covering the central angular region for improved vertex detection and the BST (see [14, 189, 191, 192, 193]) covering the rear angular region to improve reconstruction of rear-going small angle tracks.
- the BWPC was replaced by a drift chamber (Backward Drift Chamber BDC) made of eight layers. The layers are arranged in four different stereo views. It has a much improved resolution capability and furthermore provides trigger information for the H1 level 1 trigger. For details see [189].
- the BEMC was replaced by a lead-scintillating fiber calorimeter (SpaCal) providing improved energy and spatial resolution for electrons down to angles of 177 °. This calorimeter consists of two sections, each $\sim 1\lambda$ deep, the first one for detection of electromagnetic showers and the second one for measuring the electromagnetic energy leakage from the e.m.section as well as a determining the hadronic energy flow in the backward region. Furthermore, the latter section provides the H1 detector with a time-of-flight veto on proton beam induced background from upstream, replacing the ToF system described above in 4.7.1. Fast signals are used for triggering. For more details see references [189, 194, 195, 196, 197, 198, 199].
- downstream of the proton beam a forward proton spectrometer (FPS) was added. It consists of stations at 81 m and 90 m, where scintillating fibre hodoscopes can be moved close to the circulating beam by employing the Roman Pot technique. Protons which cross both stations generate a trigger signal which is added to the H1 trigger mix. Two more stations at 63 m and 80 m are planned for 1997. More details can be found in [200, 201, 202].
- the second level triggers mentioned in section 8.4 were installed and tested using real data.

14 Acknowledgement

We appreciate the immense effort of the engineers and technicians of the participating laboratories who designed, constructed and maintain the detector. We are grateful to the HERA machine group whose outstanding efforts contribute to making this experiment possible. We thank the funding agencies for financial support. The non-DESY members of the collaboration also express their thanks the DESY directorate for the hospitality extended to them. We acknowledge the help of DESY and CERN in providing test beam time for the many calibration runs. The help of the computing centres at DESY and at CERN in the test and running phases is highly appreciated.

References

[1] M. Breidenbach et al., Phys. Rev. Lett. **23** (1969), 935; 1990 Nobel prize lectures: R. Taylor, Rev. Mod. Phys. **63** (1991), 573; H. W. Kendall, ibid. p. 597; J. Friedman, ibid. p. 615.

[2] EMC: J.J. Aubert et al., Nucl. Phys. **B259** (1985), 189, ibid. **B293** (1987), 740; BCDMS: A.C. Benvenuti et al., Phys. Lett. **B223** (1989), 485, ibid. **B237** (1990), 599; NMC: P. Amaudruz et al., Phys. Lett. **B294** (1992), 120, ibid. **B295**, 159.

[3] Proc. of the study for an *ep* facility for Europe (1979), U. Amaldi ed., DESY preprint 79-48 (1979).

[4] Proc. of the HERA workshop, Hamburg (1987), R.D. Peccei ed., DESY, Hamburg (1988), vol. I, II.

[5] Proc. of the workshop on Physics at HERA, Hamburg (1991), W. Buchmüller and G. Ingelman eds., DESY, Hamburg (1992), vol. I, II, III.

[6] A. Jacquet, and F. Blondel, in ref. [3], p. 391.

[7] S. Bentvelsen, J. Engelen, and P. Kooijman, in ref. [5], vol. I, p. 23.

[8] W. Bartel et al., Prospects for charm physics with the H1-Detector at HERA, pres. by F. Ould-Saada, Proc. 4^{th} Int. Symp. on Heavy Flavour Physics, Orsay, France (1991), eds. M. Davier and G. Wormser (Editions Frontières, Gif-sur-Yvette, 1992), p. 515; see also ref. [203].

[9] G. Bernardi, W. Hildesheim, A detailed simulation of F_2 measurability at HERA, LPNHE-Paris report LPNHE-92-01 (1992); in ref. [5], vol. I, p. 79.

[10] B.H. Wiik, HERA status, in ref. [5], vol. I, p. 1.

[11] F. Willeke, in ref. [204], p. 28.

[12] G. Lopez et al., in ref. [204], p. 251.

[13] D. Pitzl et al., A silicon vertex detector for H1 at HERA, Proc. IEEE Nuclear Science Symp., Orlando, Florida (1992); Paul-Scherrer Institut report PSI-PR-92-35, Villigen (1992).

[14] H.J. Behrend et al., Technical proposal to build silicon tracking detectors for H1, H1 report 07/92-226, DESY, Hamburg (1992), unpublished.

[15] UA5-Collaboration: G.J. Alner et al., Zeit. f. Phys. **C32** (1986) 153; ibid. **C33** (1986) 1; R.E. Ansorge et al., Zeit. f. Phys. **C33** (1986) 175; D.P. Johnson, Beam gas background at HERA, H1 report 07/87-65, DESY, Hamburg (1992), unpublished.

[16] D. Pitzl, Diploma thesis, University of Hamburg (1987), unpublished.

[17] D. Decamps et al., Nucl. Instr. and Meth. **A294** (1990) 121.

[18] P. Aarnio et al., Nucl. Instr. and Meth. **A303** (1991) 233.

[19] Vakuumschmelze, D-6450 Hanau.

[20] P.T.M. Clee, and D.E. Baynham, Towards the realisation of two 1.2 Tesla superconducting solenoids for particle physics experiments, Proc. 11^{th} Int. Conf. on Magnet Technology, Tsukuba (1989), T. Sekiguchi, and S. Shimamoto eds., Elsevier Applied Science (London, 1990), p. 206.

[21] D. Barber and J. Rossbach, Some analytical and numerical calculations of the effects of the H1 and ZEUS solenoids on the HERA optics, DESY preprint HERA 86-13, Hamburg (1986), unpublished.

[22] ASEA Brown Boveri, CH-8050 Zürich.

[23] W. Beckhusen et al., Field measurements of the compensating solenoids in the HERA e-p storage ring, Proc. 12^{th} Int. Conf. on Magnet Technology, Leningrad (1991), IEEE Trans. Magn. **28** (1992) 801.

[24] J. Bürger et al., Nucl. Inst. and Meth. **A279** (1989) 217.

[25] J. Bürger, Tracking at H1 in the environment of HERA, Proc. 4^{th} Topical Sem. on Exp. Apparatus in High Energy Particle Physics and Astrophysics, San Miniato, Italy (1990), eds. P. Giusti et al. (World Scientific, Singapore, 1991), p. 272.

[26] H. Drumm et al., Nucl. Instr. and Meth. **176** (1980) 333.

[27] Glass fiber reinforced epoxy: Stesalit AG, Zullwil, Switzerland; and Permali, F 54320 Marseille, France.

[28] S. Prell, Z-Kalibration und $dE/dx-$Kalibration der zentralen Spurkammer des H1 Detektors, Diploma thesis, University of Hamburg (1992), H1 report FH1T-92-04, DESY, Hamburg (1992), unpublished.

[29] V. Karimäki, Fast code to fit circular arcs, Helsinki University report HU-SEFT-1991-10 (1991), unpublished.

[30] V. Lioubimov, Particle separation by likelihood analysis of dE/dX measurements in H1 tracking chambers, H1 report 11/93-329, DESY, Hamburg (1993), unpublished.

[31] C. Ley, Untersuchungen zur Rekonstruktion des radiativen D^{*0} Zerfalls im H1 Detektor, Ph. D. thesis, RWTH Aachen (1994), unpublished; RWTH Aachen report PITHA-91-10 (1991).

[32] N. Sahlmann, Reconstruction of Λ and K^0_s with the H1 detector, H1 report 04/93-281, DESY, Hamburg (1993), unpublished.

[33] R. Luchsinger, and C. Grab, Comp. Phys. Comm. **76** (1993) 263.

[34] H.J. Behrend and W. Zimmermann, A hardwired trigger processor using logic cell arrays (XILINX), in ref. [205], p. 237.

[35] Rohacell 51: Roehm GmbH, Darmstadt, Germany.

[36] S. Egli et al., Nucl. Instr. and Meth. **A283** (1989) 487.

[37] P. Robmann et al., Nucl. Instr. and Meth. **A277** (1989) 368.

[38] P. Robmann, The central inner $z-$chamber of the H1-experiment at HERA, Ph. D. thesis, University of Zürich (1994).

[39] California Fine Wire Company, Grover City, Cal. 93433.

[40] K. Esslinger, and P. Robmann, A sensitive current monitor for drift chambers, Nucl. Instr. and Meth. **A334** (1993) 649.

[41] H. Bärwolff et al., Proc. 4^{th} San Miniato Topical Seminar on Experimental Apparatus for High-Energy Physics and Astrophysics (1990), P. Giusti et al. eds., World Scientific 1990, p. 284.

[42] H. Bärwolff et al., Nucl. Instr. and Meth. **A283** (1989) 467.

[43] H. Bärwolff et al., Nucl. Instr. and Meth. **A294** (1990) 117.

[44] S. Burke et al., Track Finding and Fitting in the H1 Forward Track Detector, DESY preprint 95-132, Hamburg (1995), submitted to Nucl. Instr. and Meth.

[45] NOMEX: Eurocomposites, L 6401 Echternach, Luxembourg.

[46] G.A. Beck et al., Nucl. Inst. and Meth. **A283** (1989) 471.

[47] H. Graessler et al., Nucl. Inst. and Meth. **A283** (1989) 622.

[48] H. Graessler et al., Nucl. Inst. and Meth. **A310** (1991) 535.

[49] J.M. Bailey et al., Nucl. Inst. and Meth. **A323** (1992) 184.

[50] H. Graessler et al., Nucl. Inst. and Meth. **A323** (1992) 401.

[51] VICbus, VME Inter-Crate Bus, ISO/IEC JTC 1/SC26.

[52] W. Zimmermann et al., A 16 channel VME flash ADC system (F1001-FADC), H1 internal report, DESY, Hamburg (1989), unpublished; manufacturer: Struck, Tangstedt/Hamburg.

[53] Creative Electronics Systems SA, Fast intelligent controller FIC 8230/8232, Geneva, CH, 1987/1992.

[54] H. Krehbiel, H1 trigger control system, H1 report 12/88-101, DESY, Hamburg (1988), unpublished.

[55] The VME Subsystem Bus (VSB) specification, IEEE standard 1096.

[56] M. de Palma et al., Nucl. Instr. and Meth. **216** (1983) 393.

[57] J. Boucrot et al., Nucl. Instr. and Meth. **176** (1980) 291.

[58] DAG and Electrodag graphite solutions: Acheson Colloiden, Scheemda, Netherlands; Deutsche Acheson Colloids, Ulm, Germany.

[59] K. Müller et al., Nucl. Instr. and Meth. **A312** (1992) 457.

[60] Araldit: epoxy glue manufactured by CIBA-Geigy AG, Basel, Switzerland.

[61] R–4825 Johnson Mathey, Conductive Adhesives and Coatings.

[62] G. Bertrand-Coremans et al., Nucl. Phys. B (Proc. Suppl.) **16** (1990) 518.

[63] P. Huet, A VMEbus-based Data Acquisition System for the MWPCs of the H1 Detector at the HERA Collider, Ph. D. thesis, Université Libre de Bruxelles (1993), unpublished.

[64] BASF AG, Ludwigshafen, Germany.

[65] G. Kemmerling, Untersuchungen zur Beimischung von Alkoholdampf in geschlossene Gaskreisläufe für den Betrieb von Drift- und Proportionalkammern, Diploma thesis, RWTH Aachen (1990), unpublished.

[66] S. Masson, Ph. D. thesis, RWTH Aachen (1993), unpublished.

[67] J.A. Kadyk, Nucl. Instr. and Meth. **A300** (1991) 436.

[68] R. Etienne, Diploma thesis, RWTH Aachen (1993), unpublished.

[69] Messer Griessheim AG, Griessheim, Germany.

[70] BAYER AG, Leverkusen (Vertrieb Hamburg), Germany.

[71] H.B. Dreis, Bau einer automatisierten Gaschromatographie Messtation für den H1 Detektor, Diploma thesis, RWTH Aachen (1991), unpublished.

[72] W.A. Dietz, Response factors for gas chromatography, Esso Res. and Eng. Co., Analytical Res. Div., Linden, New Jersey, 68 (1967).

[73] V. Commichau, RWTH Aachen III. Physik. Inst. Lehrstuhl B, internal report, unpublished.

[74] P. Göttlicher, Entwicklung und Bau eines rechnergesteuerten Gassystems für eine Präzisionsdriftkammer, Ph. D. thesis, RWTH Aachen (1993), unpublished.

[75] C. Leverenz, Aufbau und Test eines Szintillationszählersystems zur Bestimmung des Strahluntergrundes am H1 Experiment sowie erste Strahlstudien an HERA, Diploma thesis, University of Hamburg (1991), unpublished.

[76] V. Korbel, Erste HERA - Strahluntergrundstudien in der H1 Wechselwirkungszone im November 1991, DESY preprint HERA 92-07, Hamburg (1992), unpublished.

[77] K. Flamm, Messungen von Strahluntergrund bei HERA für den Betrieb von H1, H1 report FH1K-92-03, DESY, Hamburg (1992), unpublished.

[78] H1 Collaboration, C. Berger et al., Technical proposal for the H1 detector, DESY report PRC 86-02, Hamburg (1986), unpublished.

[79] H1 calorimeter group, B. Andrieu et al., The H1 liquid argon calorimeter system, Nucl. Instr. and Meth. **A336** (1993) 460.

[80] H1 calorimeter group, B. Andrieu et al., Electron/Pion Separation with the H1 LAr Calorimeter, Nucl. Instr. and Meth. **A344** (1994) 492.

[81] J. Stier, Kalibration des H1 Flüssig-Argon Kalorimeters mit kosmischen Myonen, DESY FH1K-92-04, Diploma thesis, University of Hamburg (1992), unpublished.

[82] R. Bernier et al., Pedestal drift and cable pickup problems in multiplexed analog signal transmission, NS Symposium 34, San Francisco, IEEE. Transactions on Nuclear Science **34** (1988) 131.

[83] K. Djidi, DSP readout of ADCs for the H1 calorimeter, Proc. 2^{nd} Int. Conf. on Advanced Technology and Particle Physics, Como (1990), E. Borchi et al. eds., Nucl. Phys. B (Proc. Suppl.) **23A** (1991) 186.

[84] N. Huot, Estimation et Réjection de l'Empilement pour la Mesure des Fonctions de Structure par les Calorimètres de H1, Ph. D. thesis, University of Paris 7 (1992), unpublished.

[85] H. Abramowicz et al., Nucl. Instr. and Meth. **180** (1981) 429.

[86] H1 Collaboration, W. Braunschweig et al., Nucl. Instr. and Meth. **A265** (1988) 419.

[87] H1 Collaboration, W. Braunschweig et al., Nucl. Instr. and Meth. **A275** (1989) 246.

[88] H. Greif, Untersuchung zur kalorimetrischen Messung von Jeteigenschaften in hochenergetischen Elektron - Proton Speicherring - Experimenten, Ph. D. thesis, Technical University of München (1990), unpublished.

[89] H1 calorimeter group, H. Oberlack, Compensation by software - single particles and jets in the H1 calorimeter, Proc XXV. Int. Conf. on High Energy Physics, Singapore, (1990) vol.2, p. 1377.

[90] P. Loch, Kalibration des H1 Flüssig-Argon Kalorimeters unter Berücksichtigung der Gewichtungsmethode für Teilchen-Jets, H1 report FH1K-92-02, DESY, Hamburg (1992); Ph. D. thesis, University of Hamburg (1992), unpublished.

[91] H.P. Wellisch et al., MPI-PhE/94-03 (1994).

[92] W. Braunschweig et al., Results from a test of a Pb-Fe liquid argon calorimeter, DESY preprint 89-022, Hamburg (1989).

[93] H1 calorimeter group, B. Andrieu et al., Results from pion calibration runs for the H1 liquid argon calorimeter and comparisons with simulations, Nucl. Instr. and Meth. **A336** (1993) 499.

[94] H1 calorimeter group, B. Andrieu et al., Beam tests and calibration of the H1 liquid argon calorimeter with electrons, Nucl. Instr. and Meth. **A350** (1994) 57.

[95] F. Zomer, Energy Correction Procedure for Electrons in CB2-CB3 ϕ-crack region, H1 report 09/93-316, DESY, Hamburg (1993), unpublished.

[96] M. Korn, Untersuchungen zur Messung der Energie von Elektronen und geladenen Pionen mit dem Flüssig Argon Kalorimeter des Detektors H1, Ph. D. thesis, University of Dortmund (1994), unpublished.

[97] M. Huette and M. Korn,Energy Correction Procedure for Electrons in FBE ϕ-crack region, H1 report 11/94-400, DESY, Hamburg (1994), unpublished.

[98] H1 Collaboration, W. Braunschweig et al., Nucl. Instr. and Meth. **A270** (1988) 334.

[99] R. Grässler, Kalibration eines elektromagnetischen Kalorimetermoduls für den H1 Detektor, Diploma thesis, RWTH Aachen (1991), unpublished.

[100] J.-F. Laporte, Diffusion Profondément Inélastique à HERA et Calibration Absolue de la Mesure en Energie d'un Electron dans le Calorimètre à Argon Liquide de l'Expérience H1, Ph. D. thesis, University of Paris-Sud (1991), unpublished.

[101] K. Borras, Aufbau und Kalibration eines Flüssig-Argon Kalorimeters im H1 Detektor, Ph. D. thesis, University of Dortmund (1992), unpublished.

[102] M. Flieser, Untersuchungen zur Energieauflösung eines Flüssig-Argon-Kalorimeters für Elektronen und Pionen im Energiebereich von 3.7 - 170 GeV, MPI-Phe/92-08, H1 report 07/92-231, DESY, Hamburg (1992), unpublished; Diploma thesis, Technical University of München (1992), unpublished.

[103] S. Peters, Die parametrisierte Simulation elektromagnetischer Schauer, MPI-PhE/92-13, Ph. D. thesis, University of Hamburg (1992), unpublished.

[104] P. Hartz, Kalibration eines Blei-Flüssigargon Kalorimeters mit Elektronen für das H1 Experiment, Ph. D. thesis, University of Dortmund (1993), unpublished.

[105] R. Haydar, Test et Calibration du Calorimètre Hadronique de l'Expérience H1 à HERA, Ph. D. thesis, University of Paris-Sud (1991), unpublished.

[106] J. Gayler, Proc. Workshop on Detector and Event Simulation, K. Bos and B. van Eijk eds., NIKHEF-H report, Amsterdam (1991), p. 312.

[107] B. Delcourt et al., Comparison of pion calorimeter test data with simulation for CB2/CB3 period, H1 report 04/92-220, DESY, Hamburg (1992), unpublished.

[108] M. Rudowicz, Hadronische Schauersimulation fuer den H1 Detektor, MPI-PhE/92-14, Ph. D. thesis, University of Hamburg (1992), unpublished.

[109] H. Fesefeldt, Nucl. Instr. and Meth. **A263** (1988) 114.

[110] R. Brun et al. GEANT long write-up, CERN Program Library, W5103, 1989.

[111] H. Bergstein, Eichung des H1 Tail Catchers als stand-alone Kalorimeter und in der Kombination mit dem H1 Flüssig Argon Kalorimeter, Ph. D. thesis, RWTH Aachen (1993), unpublished.

[112] H1 BEMC group, J. Ban et al., DESY preprint 95-177, Hamburg (1995), to be published in Nucl. Instr. and Meth.

[113] Kyowa Gas Chemical ind. Co. Ltd., Nihonbashi, 3-8-2, Chuo-ku, Tokyo 103, Japan.

[114] HAMAMATSU Photonics K.K., Ichino-cho, Hamamatsu City, Japan.

[115] Floeth Electronic, Landsberg a. Lech, Germany.

[116] C. Brune et al., BEMC Calibration in 1993, H1 report 04/94-352, DESY, Hamburg (1994), unpublished.

[117] E. Fretwurst et al., Nucl. Instr. and Meth. **A288** (1990) 1.

[118] M. Eberle et al., Electromagnetic MC-simulations with EGS4 and GEANT – How to make them work for thin detectors, H1 report 05/89-113, DESY preprint 89-104, Hamburg (1989).

[119] M. Eberle et al., Test Experiment und Monte-Carlo-Simulationen für Silizium-Instrumentierte Kalorimeter, Annual report 1990/1991, I. Inst. Phys., University of Hamburg (1991), unpublished; M.Eberle, Ph. D. thesis, University of Hamburg, in preparation.

[120] I. Fedder, Untersuchungen an Silizium-instrumentierten Test-Kalorimetern für elektromagnetische und hadronische Schauer, Ph. D. thesis, University of Hamburg (1991), unpublished.

[121] M. Ruffer, Implementierung des Silizium-instrumentierten PLUG-Kalorimeters in den H1-Detektor, Ph. D. thesis, University of Hamburg (1992), unpublished.

[122] E. Panaro,M. Krüger and M. Seidel, Calibration of the H1 Plug calorimeter and comparison of data with Monte-Carlo simulations, H1 report 09/95-455, DESY, Hamburg (1995), unpublished.

[123] R. Wunstorf, Systematische Untersuchungen zur Strahlenresistenz von Silizium-Detektoren für die Verwendung in Hochenergiephysik-Experimenten, Ph. D. thesis, University of, Hamburg (1992), unpublished; H1 report FH1K-92-01, DESY, Hamburg (1992), unpublished.

[124] W. Hildesheim and M. Seidel, An investigation into the radiation damage of the silicon detectors of the H1 Plug calorimeter within the HERA environment, DESY preprint 95-139, Hamburg (1995), unpublished.

[125] G. Ingelman, Proc. of the workshop on Physics at HERA, Hamburg (1991), W. Buchmüller and G. Ingelman eds., DESY, Hamburg (1992), vol.III, p. 1366.

[126] J. Ebert, The H1 Tail Catcher hardware and software performance, H1 report 08/95-448, DESY, Hamburg (1995), unpublished.

[127] F. Niebergall, Calibration and data correction for the TC calorimeter, H1 report 02/91-163, DESY, Hamburg (1991), unpublished.

[128] H. Bergstein et al., Beam calibration of the H1 tail catcher at CERN, H1 report 10/91-197, DESY, Hamburg (1991), unpublished.

[129] L. Büngener, Interkalibration der Türme des H1 Tailcatchers, Diploma thesis, University of Hamburg (1992), unpublished.

[130] Luranyl: BASF, Ludwigshafen, Germany.

[131] G. Battistoni et al., Nucl. Instr. and Meth. **152** (1978) 423; ibid. **176** (1980) 297.

[132] F. Ferrarotto, R. Kotthaus, and B. Stella, Study of alternative materials for streamer tubes, H1 report TR-406, DESY, Hamburg (1987), unpublished.

[133] CAEN High Voltage System SY 127, Costruzioni Apparecchiature Elettroniche Nucleari S.p.A., I-55049 Viareggio.

[134] K. Geske, H. Riege, and R. van Staa, The digital electronics of the H1 streamer tube detector, H1 report H1LSTEC 90-8, DESY, Hamburg (1990), unpublished.

[135] I. Cronström et al., Nucl. Instr. and Meth. **A340** (1994) 304.

[136] H. Bethe, and W. Heitler, Proc. Roy. Soc. **A146** (1934) 83.

[137] FEU-147, MELZ, Moscow, Russia.

[138] S. Levonian, DESY preprint HERA 92-07, Hamburg (1992) 247.

[139] C. Bini et al., Nucl. Instr. and Meth., **A306** (1991) 467.

[140] H1 Collaboration, S. Aid et al., Zeit. f. Phys. **C69** (1995) 27.

[141] H1 Collaboration, T. Ahmed et al., Phys. Lett. **B297** (1992), 205.

[142] F. Sefkow et al., IEEE Trans.Nucl.Sci. **42** No 4 (1995) 900-904.

[143] S. Eichenberger et al., Nucl. Instr. and Meth. **A323** (1992) 532; see also ref. [206], p. 214.

[144] XILINX, The Programmable Gate Array Company, 2100 Logic Drive, San Jose, CA 95124, USA.

[145] R. Eichler et al., The first level MWPC trigger for the H1 detector, H1 report 04/87-61, DESY, Hamburg (1987), unpublished.

[146] T. Wolff et al., Nucl. Instr. and Meth. **A323** (1992), 537.

[147] H. Brettel et al., Calorimeter event t_0 and trigger elements for CTL and DSP, MPI-Munich report H1-MPI-140, Munich (1990), unpublished.

[148] F. Sefkow, Calibration of the H1 Liquid Argon Calorimeter Trigger Analog Thresholds, H1 report 10/94-394, DESY, Hamburg (1994), unpublished.

[149] T. Carli et al., Performance of the H1 Liquid Argon Calorimeter Trigger in 1994, Contributed paper to EPS-HEP 1995 Int. Europhysics Conf. on HEP, EPS-0644, Bruxelles (1995), and H1 report 07/95-455, DESY, Hamburg (1995), unpublished.

[150] J. Ban et al., The BEMC single electron trigger, H1 report 07/92-235, DESY, Hamburg (1992), unpublished.

[151] J. Tutas, A level 1 trigger from the limited streamer tube system, H1 report 07/91-185, DESY, Hamburg (1991), unpublished.

[152] T. Ahmed et al., A pipelined first level forward muon drift chamber trigger for H1, Nucl. Instr. and Meth. **A364** (1995) 456.

[153] H. Krehbiel, The H1 trigger decider: from trigger elements to L1-keep, H1 report 09/92-239, DESY, Hamburg (1992), unpublished.

[154] J.-C. Bizot et al., Hardware study for a topological level 2 trigger, H1 report 09/92-240, DESY, Hamburg (1992); J.-C. Bizot et al., Status of simulation for a topological level 2 trigger, H1 report 09/92-212, DESY, Hamburg (1992), unpublished.

[155] J. Fent et al., A level 2 calorimeter trigger using neural networks, H1 report 04/91-172, DESY, Hamburg (1991), unpublished.

[156] E. Barrelet et al., The hardware implementation of L3 triggers in H1, H1 report 12/88-100, DESY, Hamburg (1988), unpublished.

[157] A. Campbell, A RISC multiprocessor event trigger for the data acquisition system of the H1 experiment at HERA, Int. Conf. Real Time '91, Jülich, FRG (1991).

[158] S. Guenther, P. Skvaril, and J. Strachota, Slow control on the H1 experiment at HERA, in ref. [206], p. 769.

[159] R. van Staa, A slow control system for the H1 streamer tube detector, University of Hamburg II. Inst. of Physics internal report (1990), unpublished.

[160] J. Strachota, S. Guenther, and P. Skvaril, A model of minimal traffic monitoring, to be published.

[161] J.M. Le Goff et al., ARGUS: a graphic user interface package to monitor the slowly changing parameters of a physics experiment on a Macintosh II, CERN report ECP 91-31, Geneva (1991).

[162] J. Pothier, BBL3, CERN report EF/L3, Geneva (1989); and private communication.

[163] The VMEbus specification, IEEE standard 1014.

[164] W.J. Haynes, Bus-based architectures in the H1 data acquisition system, VITA Int. Conf. Open Bus Systems '92 in Research and Industry, Zürich, Switzerland, (1992) 27; Rutherford Appleton Laboratory report RAL 92-048 (1992).

[165] W.J. Haynes, Experiences at HERA with the H1 data acquisition system, in ref. [206], p.151; DESY preprint 92-129, Hamburg (1992).

[166] Creative Electronics Systems SA, RAID 8235, R3000 VMEbus controller, Geneva, CH, 1990.

[167] Creative Electronics Systems SA, VME/VSB Dual ported memory DPM 8242, Geneva, CH, 1989.

[168] B.G. Taylor, MICRON: VMEbus and CAMAC access from Macintosh, Conf. VMEbus in Research, Zürich, CH (1988).

[169] E. Pietarinen, VMEbus cross interface processor module with high speed fibre-optic links: VMExi, Univ. of Helsinki Report HU-SEFT-1991-14, Helsinki, Finland (1991).

[170] The scalable coherent interface (SCI), IEEE standard 1596.

[171] J. Coughlan, D. Düllmann, M. Savitski, M. Zimmer, Object orientated programming for online systems at H1, in ref. [206], p. 519.

[172] W.J. Haynes, VME_TOOLS, VMEbus interaction from the MPW shell, DESY, Version 3.2, February 1994.

[173] E. Deffur, P. Fuhrmann, M. Zimmer, Communication on the H1 local area network, H1 internal report, DESY, Hamburg (1991), unpublished.

[174] W.J. Haynes, VMEXI_SSP : VMEtaxi system software package, DESY, Version 4.2, July 1993.

[175] P. Hill, MacEvLook Online version of H1 event display, DESY internal report (1991), unpublished.

[176] P. Fuhrmann et al., Data logging and online reconstruction in H1, Proc. Int. Conf. on Computing in High Energy Physics, San Francisco (1994), p. 482.

[177] M. Zimmer, Graphics-orientated operator interfaces at H1, in ref. [205], p. 269.

[178] R. Gerhards et al., Experience with a UNIX based batch facility for H1, Proc. Int. Conf. on Computing in High Energy Physics, San Francisco (1994), p. 162.

[179] V. Blobel, BOS and related packages, Proc. 14. Workshop of the INFN Eloisatron Project: Data Structures for Particle Physics Experiments: Evolution or Revolution, Erice, Sicily, Italy (1990),
R. Brun, P. Kunz and P. Palazzi eds., World Scientific (Singapore, 1991), p. 1.

[180] V. Blobel, The F-package for input-output, in ref. [206], p. 755.

[181] M. Brun, R. Brun and A.A. Rademakers, CMZ - a source code management system, Proc. Int. Conf. on Computing in High Energy Physics, Oxford (1989),
R. C. E. Devenish, T. Daniels eds., Comp. Phys. Comm. **57** (1989) 235.

[182] S. Egli, BOS modules in H1 software - A set of rules and recommendations H1-software note 12, DESY, Hamburg (1990), unpublished.

[183] U. Berthon et al. A data management tool package for H1 reconstruction and analysis, H1-software note 8, DESY, Hamburg (1990), unpublished.

[184] M. Kuhlen, The fast H1 detector Monte Carlo, in ref. [207].

[185] R. Brun et al., PAW long write-up, CERN Program Library, Q 121, Geneva.

[186] H1 Collaboration, publication list in WWW file:
http://dice2.desy.de/h1/www/publications/pub_list.html.

[187] H1 Collaboration, T. Ahmed et al., Phys. Lett. **B299** (1993), 385.

[188] H1 Collaboration, T. Ahmed et al., Phys. Lett. **B298** (1993), 469.

[189] H1 Collaboration, Technical proposal to upgrade the backward scattering region of the H1 detector, DESY report PRC 93-02, Hamburg (1993), unpublished.

[190] D. Pitzl et al., Nucl. Instr. and Meth., **A348** (1994) 454.
W. Erdmann et al., Nucl. Instr. and Meth., to be published.
J. Bürger et al., Nucl. Instr. and Meth., **A367** (1995) 422.

[191] H1 Collaboration, Upgrade of the H1 Backward Silicon Tracker, DESY report PRC 96-02, Hamburg (1996), unpublished.

[192] J. Bürger et al., Design of a Silicon Backward Tracking Detector and Trigger for the H1 Experiment at the ep Collider HERA, DESY preprint 93-002, Hamburg (1993), unpublished.

[193] H. Henschel et al., A Silicon Backward Tracking Detector and Trigger for the H1 Experiment at the ep Collider HERA, IEEE Trans. on Nucl. Sci., Vol. 40, Nb. 4 (1993).

[194] G. Müller, A Spaghetti Calorimeter for the H1 Detector, Proc. of the Vth Int. Conf. on Calorimetry in HEP, Brookhaven (1994) 355.

[195] M. Weber, The new Spaghetti Calorimeter of the H1 Experiment, Proc. of the '94 Beijing Calorimetry Symposium, Beijing (1994) and DESY preprint 95-067,Hamburg (1995), unpublished.

[196] H1 SpaCal group, Performance of an Electromagnetic Lead/Scintillating-fibre Calorimeter for the H1 Detector DESY preprint 95-165, Hamburg (1995), submitted to Nucl. Inst. and Meth.

[197] H1 SpaCal group, Hadronic Response and e-π Separation with the H1 Lead/Fibre Calorimeter, DESY preprint 95-250, Hamburg (1995), submitted to Nucl. Instr. and Meth.

[198] H1 SpaCal group, H1 Backward Upgrade with a SpaCal Calorimeter: the Hadronic Section, DESY preprint 96-013, Hamburg (1996), Hamburg (1995), to be submitted to Nucl. Instr. and Meth.

[199] E. Eisenhandler et al., Spacal Time to Digital Converter System, IEEE Tran. Nucl. **42** No 4 (1995) 688.

[200] H1 Collaboration, Technical proposal for Roman pots, DESY report PRC 93-02, Hamburg (1993), unpublished.
Proposal for a Forward Proton Spectrometer for H1, DESY report PRC 94/03, Hamburg (1994), unpublished.

[201] J. Bähr et al., Nucl. Instr. and Meth. **A 324** (1993) 145; Nucl. Instr. and Meth. **A 330** (1993) 103.

[202] J. Bähr et al., Beam Tests of Prototype Fibre Detectors for the H1 Forward Proton Spectrometer, DESY preprint 94-130, Hamburg (1994).

[203] S. Egli et al., in ref. [5], vol. II, p. 770.

[204] Proc. XVth Int. Conf. on High-Energy Accelerators, Hamburg (1992), J. Rossbach ed., Int. J. Mod. Phys. A (Proc. Suppl.) **2A** (1993).

[205] Proc. Int. Conf. on Computing in High Energy Physics, Tsukuba, Japan (1991), Universal Academy Press,(1991).

[206] Proc. Int. Conf. on Computing in High Energy Physics 92, Annecy, France (1992), eds. C. Verkerk and W. Wojcik, CERN-Report 92-07, Geneva (1992).

[207] Proc. 26th Int. Conf. on High Energy Physics, Dallas, Texas, (1992).